University of Naples Federico II Polytechnic and Basic Science School Department of Chemical Sciences



Ph.D. in Chemical Sciences

A microstructural insight in polyethylene based bioriented mono-materials: from fundamental to processing

Adriano Guida

Advisor: Finizia Auriemma Roberta Cipullo **Examiner:**Andrea Correa

XXXVII Cycle 2022 – 2025 Coordinator: prof. Angela Lombardi

Abstract

The primary objective of this PhD project is to generate new knowledge on the structural transformations of polyethylene (PE) during biaxial stretching, focusing on the relationship between chain microstructure, crystallization behaviour, processing conditions and final properties of biaxially oriented PE (BOPE) films. This study aims to investigate how different PE grades, including HDPE, LLDPE and their blends, perform during the stretching process, aiming to optimize their use as mono-materials for next-generation packaging applications. The innovative aspects of the thesis lie in providing insights into the structural mechanisms at play during the biaxial orientation process, offering potential breakthroughs in expanding PE application as a sustainable alternative to multilayer films. The work is structured to build a systematic and interdisciplinary chain of knowledge, linking microstructural characteristics with processing conditions and the resulting properties of BOPE.

To achieve this goal, three universities and three industrial partners have collaborated synergistically, under the coordination of the DPI. Indeed, the PhD project brings together the Soft Condensed Matter Lab from University of Naples Federico II (which this PhD candidate belongs to), the Zernike Institute for Advanced Materials from University of Groningen for structure and properties investigation, and the Department of Industrial Engineering from University of Salerno for rheology and modeling part. The ex-situ comprehensive characterization of the selected PE grades is coupled with in-situ structural analysis performed using synchrotrons within EU facilities (ESRF in Grenoble, ALBA in Barcelona) with a new device for lab scale biaxial stretching suitably developed by the engineering group from Salerno. The commercial PE grades investigated have been supplied by Borealis, DOW and SABIC, which have been helpful in providing an industrial perspective during the development of the thesis.

Chapter 2 is dedicated to the description of all the experimental procedures and techniques employed in this work. The starting basic characterization of the samples, presented in Chapter 3, includes microstructural analysis to check molecular mass and distribution, branch type and branching concentration and corresponding distribution. Tensile tests have been carried out on compression molded films of the samples for a mechanical characterization of the PE grades. In addition, the characterization of thermal properties, crystallization behaviour and thermal fractionation are illustrated. In Chapter 4 phenomena induced by temperature examined through the application of a thermal protocol are discussed. They have been investigated using DSC, coupling the results with structural (WAXS, SAXS) and morphological (POM, SEM) analysis. In Chapter 5, are reported the results achieved by performing in situ experiments aimed at gaining a better understanding of the phenomena induced by temperature and the thermal protocol adopted for ex-situ analysis in conditions emulating the stages preceding tentering. Further in-situ analysis aimed at understanding the complex structuring process that occur during biaxial stretching in the semi-solid state of cast sheets of selected grades produced at Karo Brukner facility, using the biaxial stretching device, are illustrated in Chapter 6. In situ experiments are performed by collecting 2D-WAXS and 2D-SAXS data while heating/cooling/stretching the PE samples. The results will be laid out in detail and discussed in depth in each Chapter, allowing for a comprehensive interpretation of the findings. In Chapter 7, the main conclusion of this work will be illustrated.

Index

| Chapt | er I - Introduction 4 |
|-----------------|--|
| 1.1 | Plastic Packaging: Market Growth and Environmental Challenges. 4 |
| 1.2. | Polyethylene7 |
| 1.2.1. | Role in Global Markets and Environmental Sustainability 7 |
| 1.2.2. | Synthesis and Classification |
| 1.2.3. | Structure and Morphology11 |
| 1.2.4. | General Properties |
| 1.2.5. | Industrial Processing and Application20 |
| 1.3. | Biaxially Oriented Polyethylene (BOPE)24 |
| 1.3.1. Packa | Polyethylene Film Manufacturing Processes for Flexible ging Applications |
| 1.3.2. | Tenter-Frame Biaxially-Oriented Polyethylene (TF-BOPE) 25 |
| 1.3.3. | Structure Evolution During Biaxial Stretching26 |
| 1.4. | The Interdisciplinary Approach: Objective and Layout of the Work 31 |
| Biblio | graphy of chapter I34 |
| Chapt | er II - Experimental40 |
| 2.1. | Materials40 |
| 2.2. | Microstructural characterization |
| 2.2.1. | Solution 13C NMR40 |
| 2.2.2. | Gel Permeation Chromatography (GPC)41 |
| 2.3. | Thermal analysis and fractionation41 |
| 2.3.1. | Differential scan calorimetry (DSC)41 |
| 2.3.2. | Melt memory effect |
| 2.3.3. | Self-nucleation and annealing (SNA) |
| 2.3.4. | Thermal fractionation (SSA) |
| 2.4. | Structural characterization |

| 2.4.1. | Wide-Angle X-ray scattering (WAXS) | 49 |
|----------------|---|-----|
| 2.4.2. | Small-Angle X-ray scattering (SAXS) | 50 |
| 2.5. | Compression-molding | 50 |
| 2.6. | Mechanical characterization | 51 |
| 2.7. | Morphological characterization | 53 |
| 2.7.1. | Polarized Optical Microscopy (POM) | 53 |
| 2.8. | Thermal protocol | 53 |
| Biblio | graphy of chapter II | 56 |
| Chapt | ter III – Characterization of commercial PE grades | 57 |
| 3.1. | Microstructural characterization | 57 |
| 3.2. | Thermal and Structural characterization | 59 |
| 3.3. | Melt memory effect | 68 |
| 3.4. functi | Mechanical, structural and morphological characterization of cooling conditions | |
| 3.5. | Characterization of blends of selected grades | 85 |
| 3.6. | Thermal fractionation of selected samples | 92 |
| 3.7. | Conclusion | 110 |
| Biblio | graphy of chapter III | 117 |
| Chapt | ter IV – Thermal protocol | 119 |
| 4.1. | Effect of thermal treatment on the sample H-C4 | 123 |
| 4.2. | Effect of thermal treatments on the sample L-C8 | 137 |
| 4.3. | Effect of heat treatments on the blend 50L-50H | 149 |
| 4.4. | Conclusion | 159 |
| Biblio | graphy of chapter IV | 161 |
| Chapt | ter V – Annealing in situ analysis | 162 |
| 5.1. | Experimental | 163 |
| 5.2. | Results and discussion | 165 |
| 53 | Conclusion | 188 |

| Chaj | pter VI – Biaxial stretching in situ analysis | 190 |
|-------------|---|----------------|
| 6.1. | Biaxial stretching device | 190 |
| 6.2 | Experimental | 197 |
| 6.3. | 2D-SAXS/1D-WAXS analysis on samples stretched u 198 | ntil breakage |
| 6.4 drav | 2D-SAXS/1D-WAXS analysis on samples stretched uv ratio and successive cooling | - |
| 6.5. | 2D-WAXS analysis on samples stretched until a speci 221 | fic draw ratio |
| 6.6. | Conclusions | 230 |
| Bibli | iography of Chapter VI | 232 |
| Chaj | pter VII - Conlcusions | 233 |
| App | endix A1 | 241 |
| App | endix A2 | 242 |
| App | endix A3 | 248 |
| App | endix A4 | 256 |
| App | endix A5 | 264 |
| App | endix A6 | 278 |
| App | endix A7 | 280 |
| App | endix A8 | 298 |
| Ann | endix A9 | 304 |

Chapter I

Introduction

1.1 Plastic Packaging: Market Growth and Environmental Challenges

Over the past century, one of the most significant revolutions in the field of materials is definitely represented by the development of plastics. Their versatility and remarkable properties have allowed these materials to replace the traditional ones as metal, wood, ceramic and glass in a wide range of applications. As the research has advanced and production processes have been optimized, it has become possible to manufacture increasingly specialized products at a relatively low cost. This cost-effectiveness, combined with the intrinsic durability of plastic materials is the mayor driver behind the exponential growth of production volume: from just 2 million tons in 1950, the global plastics production surged to 400 million tons in 2022¹. However, this intrinsic durability and resistance to degradation of plastics represents also a drawback at their end-oflife, because the leakage of plastics in the environment entails that plastics also persist there for very long time. Furthermore, the production of plastic waste is strongly related to how the plastic is used, meaning that some sectors can generate more waste stream than others. This is the case of packaging, which lifespan is extremely short (often discarded immediately after use) compared to other plastic products² (Figure 1). Consequently, packaging waste represents a substantial portion (about 42%³) of total plastic waste.

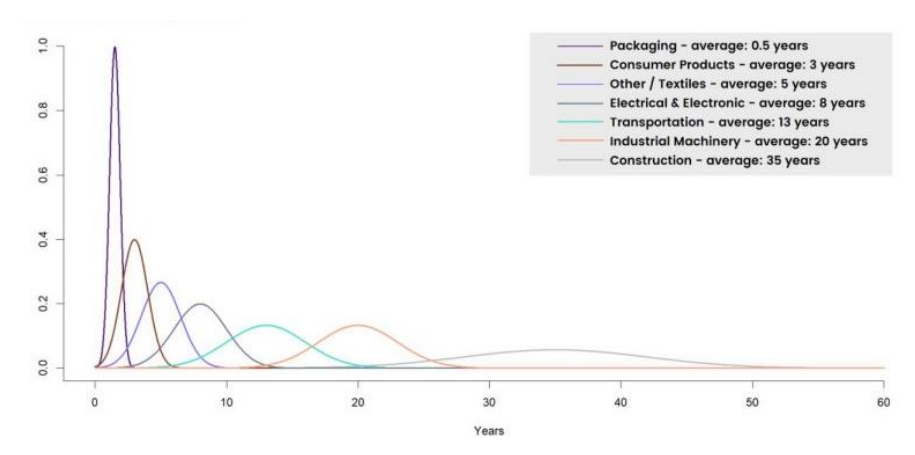


Figure 1 plastic product life stream

The significant percentage of packaging waste is directly correlated with the high production volumes⁴ within the packaging sector (Figure 2), which account for around 26% of the total plastics production⁵.

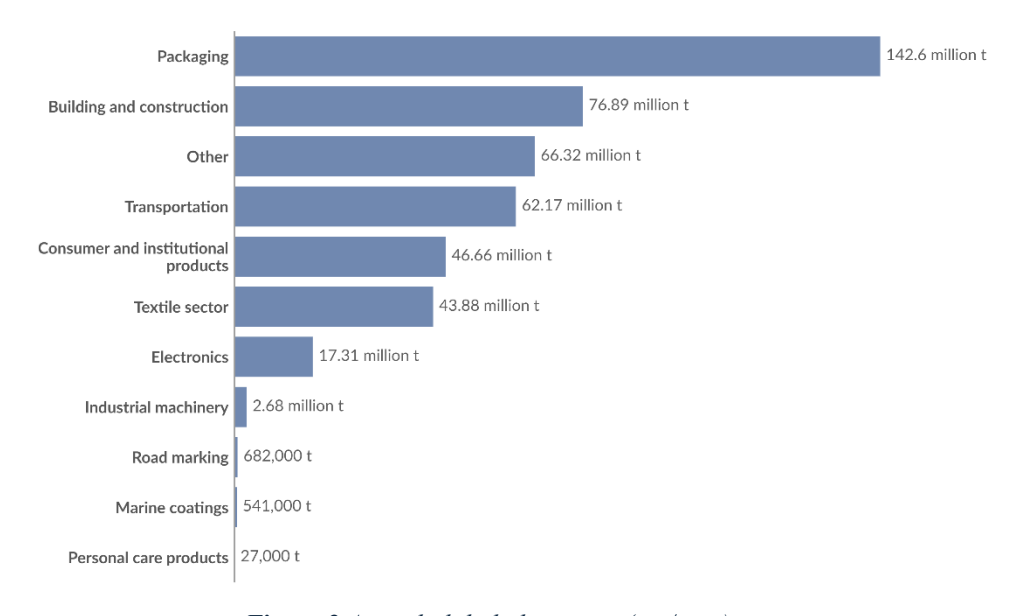


Figure 2 Annual global plastic use (ton/year)

This sector is largely dominated by polyolefins⁶; in particular, polyethylene (PE) and polypropylene (PP) represent approximately 78% of global packaging market⁷ (Figure 3).

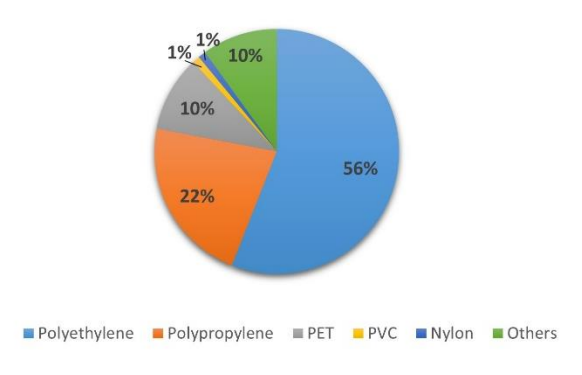


Figure 3 global plastic packaging market

However, the environmental issue related to plastic waste has become currently a central concern for worldwide institutions. The European Parliament recently approved updates to the Packaging and Packaging Waste Regulation (PPWR)⁸ in 2023, with a strong focus on minimizing single-use packaging and promoting recycling and reuse. By 2029, the regulation aims to ensure that 90% of all packaging materials, including those made from polyethylene, are collected separately. This ambitious target reflects the growing institutional recognition of the urgent need to address the environmental impacts associated with plastic packaging waste.

Among the innovation actions launched to improve circularity of the plastics economy in the packaging sector, the design of new materials leading to improvement of separation and reprocessing technologies is a key point. It includes initiatives intended at proposing mono-material packaging containers⁹ to replace multi-material film packaging, and in particular using mono-material laminates entirely based on PE¹⁰. Indeed, the identification of an efficient recycling strategy for polyolefin-based packaging systems is hampered by the fact

that PP and PE are often used in multilayer films comprising different materials glued together, separation of which at the end-of-life turns out to be particularly challenging.

1.2. Polyethylene

1.2.1. Role in Global Markets and Environmental Sustainability

Polyethylene stands out as one of the most widely produced plastics globally, with an annual production capacity exceeding 110 million tons. Since its widespread adoption in the 1950s, polyethylene has remained the most prevalent industrial polymer, owing to its versatility and outstanding properties and it still holds a dominant position as the primary material used in packaging applications. As the global demand for PE continues to grow¹¹, gaining a comprehensive understanding about all the aspects of the industrial processes behind so widely used products is mandatory. If on the one hand a better insight into structure-properties relationship of PE materials is essential to optimize the processing protocols in terms of both cost and product quality, on the other hand it is no longer possible to neglect the environmental issues related to this market.

Scientific research must move along this dual path, by striving to continuously advance the quality and performance of products, while maintaining a strong focus on their environmental footprint. It is crucial to develop cutting-edge technologies for material separation and efficient recycling processes, ensuring that innovation aligns with sustainability. Balancing these goals will allow for progress that not only improves product functionality but also mitigates long-term ecological impacts.

1.2.2. Synthesis and Classification

PE is classified as a thermoplastic due to its structure, which consists of linear or branched macromolecules held together primarily by intermolecular forces. These forces weaken as the temperature increases, allowing the material to soften and eventually melt at relatively high temperatures. As a thermoplastic, PE is first synthesized and then molded into its final shape during subsequent processing stages, making it highly adaptable to a wide range of applications. Its ability to be reheated and remoulded without significant degradation is a key feature that distinguishes it from thermosetting plastics.

PE is the product of the polymerization of ethylene, typically occurring in the gas phase under high-pressure or low-pressure conditions (Figure 4).

Figure 4 Polymerization reaction of PE

The resulting structure consists of a long carbon backbone, where each carbon atom is bonded to two hydrogen atoms, except at the chain ends (terminated with methyl groups) and branching points. The general formula of chemically pure PE is C_{2n}H_{4n+2}, with n representing the degree of polymerization, namely the number of ethylene monomers in the polymer chain. A characteristic shared by all plastic materials is the variability in the length of polymer chains, that leads to a distribution of molecular mass within the material. The degree of polymerization typically varies from 100 and can reach values as high as 125,000 or more, corresponding to molecular weights ranging from approximately 1,400 to over

3,500,000. When polymerization degree is in between 8 and 100, PE tend to form waxy solids that lack the characteristic properties of plastics.

Depending on the polymerization process, such as free radical polymerization ¹², Ziegler-Natta catalysis ¹³, metallocene catalysis ¹⁴, polyethylene can exhibit a range of molecular architectures, including linear or branched structures. The reaction conditions like temperature, pressure, and the choice of catalyst, greatly influence the molecular mass, degree of branching and density, ultimately determining the final properties. Chain ends and branching represent defects in polymer backbone and limits the crystallization of the chains in the solid state. Since the chains are more densely arranged in the crystalline regions rather than in the amorphous one, the density critically depends on the achieved degree of crystallinity. Based on these structural features, polyethylene is classified into different ^{15–17} types (Figure 5):

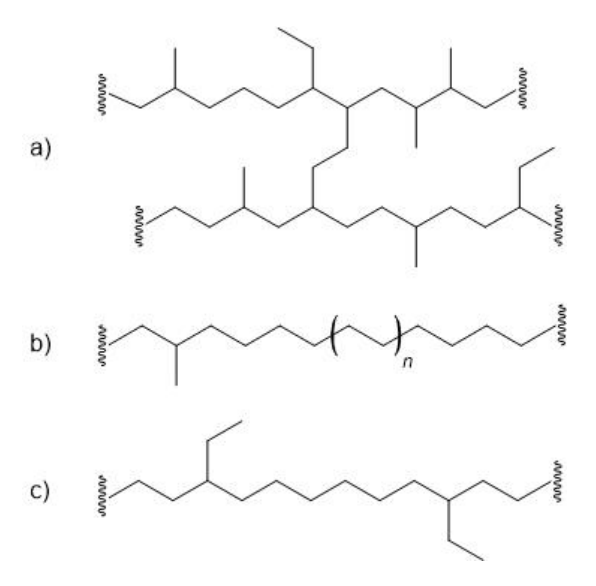


Figure 5 Typical molecular structures of different PE types: a) LDPE b) HDPE c) LLDPE

• Low-Density Polyethylene (LDPE): produced via free radical polymerization, typically at high pressure and temperature. Due to

- extensive branching, LDPE exhibits a major fraction of amorphous phase and, as a consequence, low density. It is flexible, transparent, and has good resistance to impact and moisture.
- High-Density Polyethylene (HDPE): formed through Phillips catalyst,
 Ziegler-Natta or metallocene catalysis, HDPE has a linear structure with minimal branching. HDPE is in general highly crystalline and shows higher density, greater mechanical resistance and stiffness, than LDPE. It is also resistant to chemicals and impacts.
- Linear Low-Density Polyethylene (LLDPE): exhibits a linear structure with short, controlled branching, offering a balance between flexibility and strength. It is obtained by copolymerization of ethylene with α-olefines using catalysts similar to those used for HDPE. The type of comonomers selected determines the length of the branching.
- *Ultra-High Molecular Weight Polyethylene* (UHMWPE): obtained through a synthesis process based on metallocene catalysts. It is characterized by extremely long polymer chains with number average molecular mass around 3.5-7.5 MDa, resulting in a very tough material, with high impact strength.
- Cross-Linked Polyethylene (PEX): produced by modifying HDPE or LDPE through a chemical or radiation-induced cross-linking process. The presence of covalent bonds between polymer chains determines an increased heat and chemical resistance and durability with respect to the non-cross-linked PEs.

1.2.3. Structure and Morphology

To fully understand the macroscopic properties of polyethylene, it is essential to first explore its structural organization across different length scales, ranging from Angstrom to millimetres. This involves understanding how the polymer chains are arranged relative to each other, and the types of structures they form, ranging from the atomic to the macroscopic level (Figure 6). On the molecular scale, the polymer crystalline and amorphous regions play a key role in determining its physical properties. As we move up in scale, phenomena such as chain entanglement, crystallization, and crystalline/amorphous phase separation emerge, influencing the material mechanical strength, flexibility, and thermal behaviour.

In the solid state PE presents a semi-crystalline morphology in which regions with short-range order are interspersed with regions having little or no short-range order. When a polymer chain is left unrestrained, it forms a random coil configuration, representing its state of maximum entropy. This random conformation occurs in the molten state or when dissolved in an ideal solvent. According to chain lengths and branching concentration, random coils overlap leading to chain entanglements, which significantly increase viscosity. Upon solidification, parts of the chains crystallize into small regions (crystallites) while disordered segments surround them, resulting in the semicrystalline structure. A single polyethylene molecule can link multiple crystallites through disordered segments. These disordered regions are not truly random due to the constraints from their connections to crystallites and potential alignment caused by external deformation during processing. In general, the term "amorphous" refers not only to the disordered regions located in between the lamellae (intra-lamellar amorphous phase), but also to the disordered regions sometime located outside the lamellar stacks (interlamellar amorphous phase), regardless of the degree of conformational disorder and segmental dynamics. In this respect, semicrystalline

polymers are considered bi-phasic systems, simply consisting of a crystalline and an amorphous phase. However, the disordered phase placed at the interface between lamellar crystals and the intra-lamellar amorphous phase may be characterized by a different set of conformations and reduced segmental dynamics compared to the bulk amorphous phase. The existence of this third phase may emerge in some experiments, which are sensitive to local conformation and/or to local dynamics.

The fundamental building block of the crystalline structures is the unit cell, which represents the smallest repeating arrangement of chain segments in three dimensions (Figure 7). The unit cell contains all the necessary crystallographic information to describe the entire crystallite. Within the crystalline regions, the PE polymer chains are fully extended in a conformation known as the "zig zag" transplanar allowing the chains to achieve their maximum length. The absence of possible configurational defects explains why PEs usually achieve larger crystallinity compared to other polyolefins.

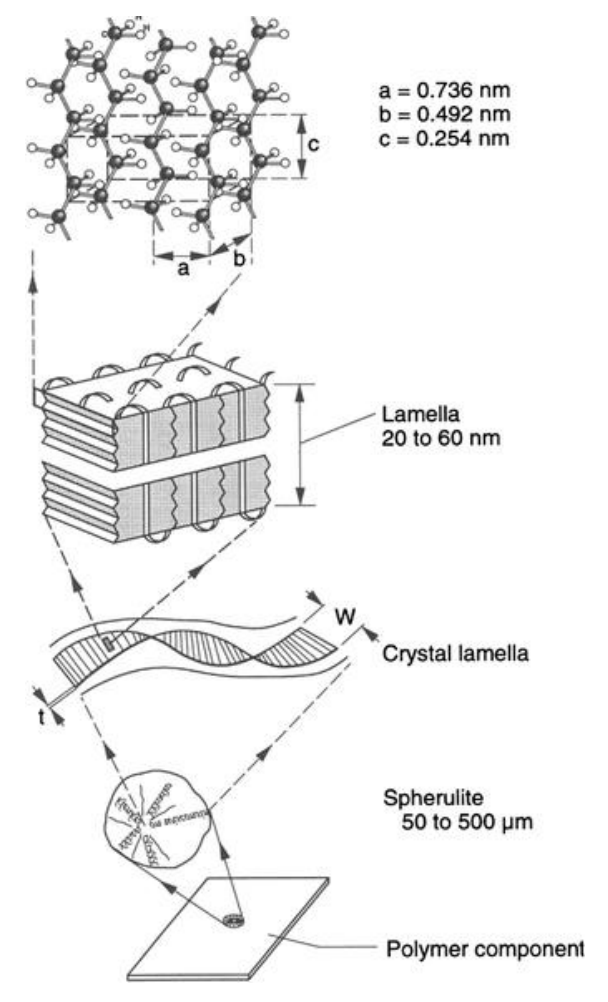


Figure 6 Structural hierarchy of crystallized PE¹⁸

The following polymorphic forms of PE are known (Figure 7):

Orthorhombic form.

The crystal structure of polyethylene was first determined by Bunn¹⁹, who identified the most stable form as characterized by an orthorhombic unit cell (Figure 7a). This unit cell, with space group symmetry $Pnam-D_{2h}$, contains four CH₂ groups, and two polymer chains arranged in a parallel, all-trans zig zag planar conformation, in which the zig zag planes have

different orientations. At 23°C, the dimensions of the unit cell for linear polyethylene in the orthorhombic form²⁰ are approximately a = 0.74069 nm, b = 0.49491 nm, c (chain axis) = 0.25511 nm ($\alpha = \beta = \gamma = 90^{\circ}$), for a crystal density of 996.2 kg/m³. The angle between the zig zag planes and the b-axis of the unit cell is $45^{\circ 21}$. In branched polyethylene^{22,23}, the unit cell expands slightly along the a and b axes, resulting in a larger setting angle of 49–51°. Short branches, like methyl and ethyl groups, can be incorporated into the crystal near kinks²⁴, while butyl groups cause negligible cell expansion²⁵. The extra space provided by the kinks is not sufficient to house larger pendant groups. In any case incorporation of defect in the crystal phase is negligible, causing the difference in crystallinity degree between HDPE and the low-density PEs.

• Monoclinic form.

This polymorph (Figure 7b) with space group symmetry C2/m- C_{2h}^{26} is less stable and arise by effect of mechanical stress^{27,28}. At 23°C, the unit cell parameters²⁹ are a=0.809 nm, b=0.253 nm (chain axis), c=0.479 nm, ($\alpha = \gamma = 90^{\circ}$, β =107.9°). It corresponds to 4 CH₂ groups (2 chains)/unit cell, for a crystal density of 998 kg/m³. Also in this case the chains are in the zig zag trans-planar conformation, and they have an identical azimuthal orientation around the chain axes. The monoclinic form of PE transforms into more stable orthorhombic form at temperature close to the melting point.

In addition a third crystalline polymorph is also known, that is the high-pressure hexagonal form, discovered by Bassett et al³⁰.

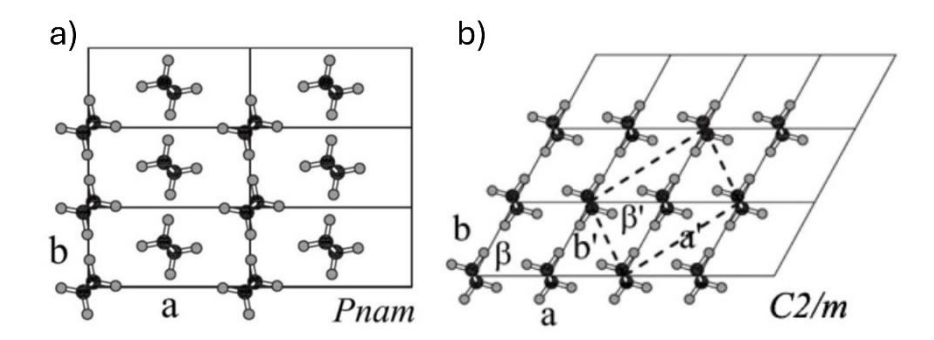


Figure 7 Crystal unit cells³¹ of PE: a) Orthorhombic b) Monoclinic

The most common crystal growth habit of polyethylene crystals obtained both from solution^{32,33} and melt^{34,35} corresponds to "lamellae" (Figure 8), meaning that the lateral crystallite size are much greater than the size along the third axis, normal to the lamellar plane. Typically, PE lamellae show a thickness ranging from 50 to 200 Å, while the lateral dimensions can span several orders of magnitude, from a few hundred angstroms to millimetres. The chains axis of molecules within the lamellae are usually slightly tilted to the basal plane of the crystal. Related to the lamellar crystal habit is the concept of chain folding.^{32,36,37} The chains, instead of stretching out in a fully extended conformation, "fold" back and forth to fit within the lamellar crystals. This occurs because the chains are too long to pack completely straight into the crystalline regions, so that when "the lamellae are isolated single entities, as in solution crystallization, then given that the chains are perpendicular, or at a large angle to the basal plane, folding is a straightforward necessity as the chains have nowhere else to go."³⁸

Upon crystallization from the melt, stacks of almost parallel crystal lamellae with amorphous layers sandwiched between adjacent crystals are obtained. In addition, lamellae can adopt different formats, such as curved, fragmented and bifurcating, and they can associate in large scale structures

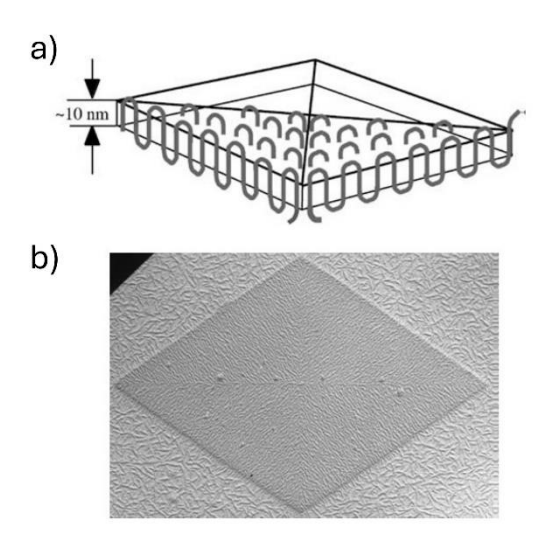


Figure 8 PE lamellae: a) Schematic representation b)Transmission electron micrograph of a replicate of a single crystal of polyethylene³⁹

Common super-structure comprising crystalline and noncrystalline regions are the spherulites⁴⁰, in which the growth habit is approximately spherical. From nucleation site, lamellae grow radially outward. For PE, the sheaves of lamellae, often twisted or bifurcate, present their crystallographic *b*-axis (the direction in which growth occurs) mainly aligned with the radii of the spherulite while chain axes are preferentially oriented in the direction normal to spherulite radii^{41,42}. The growth of the spherulite super-structures can stop with impingement with other spherulites, giving birth to irregular polyhedrons, the size of which can vary from a few nanometres to millimetres depending on the concentration of nucleation sites. In these structures higher molar mass (or less branched) chains crystallize first producing dominant lamellae, while low molar mass chains (or more branched) segregate between them and crystallize in later stage as subsidiary lamellae. When crystallization (typically of branched PEs) occurs at low temperature, banded spherulites⁴³ can be observed: these structures show optical micrographs in polarized light characterized by textures made of concentric rings

overlapping the typical Maltese cross (Figure 9). This feature is related to the periodic twisting of the lamellae^{34,44} during crystallization, in which the *b*-axis runs along the radius, while the *c*-axis exhibits a periodic twisting within the transverse plane along the spherulite radius.

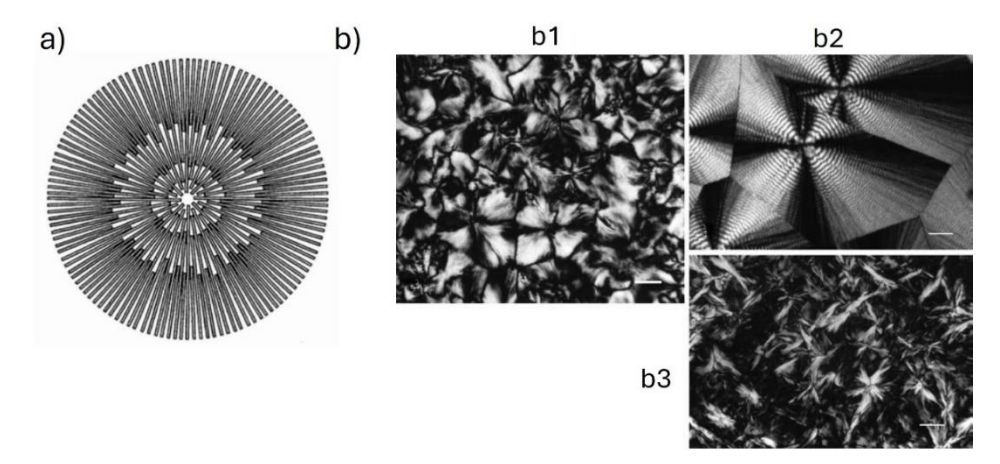


Figure 9 PE spherulites: a) Schematic representation b) Polarized light optical micrographs⁴⁵ of differente PEs showing b1) Non banded spherulites b2) Banded spherulites b3) Axialites (Scale bars represent 20 µm)

When lamellar aggregates lack the full spherical symmetry, they generate another kind of super-structures named axialites⁴⁶, usually observed in low molar mass linear polyethylenes (Figure 9b3).

1.2.4. General Properties

The properties of polyethylene (PE) are influenced by several interrelated factors, including its molecular mass, molecular structure, morphology, processing conditions, and the additives used during manufacturing. Table 1 provides an overview of the typical ranges of some key solid-state properties of various PE types⁴⁷, underscoring the significant variability in their characteristics and illustrating how each variant possesses unique attributes tailored to specific

applications. This wide spectrum of properties not only reflects the versatility of polyethylene as a material but also highlights its capability to meet the demands of various industries, enabling innovative solutions across multiple sectors, including packaging, automotive, and construction.

Table 1 General properties of PE different types

| Property | HDPE | LDPE | LLDPE |
|------------------------------|-----------|-----------|-------------|
| Density (g/cm ³) | 0.94-0.97 | 0.91-0.94 | 0.90-0.94 |
| Degree of crystallinity | 62-82 | 42-62 | 34-62 |
| (% from density) | | | |
| Degree of crystallinity | 55-77 | 30-54 | 22-55 |
| (% from calorimetry) | 33-77 | 30-34 | 22-33 |
| Flexural modulus | 100-1550 | 240-330 | 280-1100 |
| (MPa @ 23°C) | 100-1330 | 240-330 | 280-1100 |
| Tensile modulus (MPa) | 1070-1380 | 170-350 | 260-900 |
| Tensile yield stress (MPa) | 18-31 | 9-19 | 8-19 |
| Tensile strength at break | 22-31 | 8-31 | 13-49 |
| (MPa) | 22-31 | 0-31 | 13-49 |
| Tensile elongation at break | 10-1,500 | 100-650 | 100-950 |
| (%) | 10-1,500 | 100-030 | 100-930 |
| Shore hardness (type D) | 66-73 | 44-50 | 35-70 |
| Izod impact strength | 70-700 | No break | 60-No break |
| (J/m of notch) | | | |
| Melting temperature (°C) | 125-132 | 98-115 | 100-125 |
| HDT (°C @ 455 Pa) | 80-90 | 10-44 | 35-80 |
| Heat of fusion (kJ/kg) | 159-222 | 88-155 | 63-180 |
| Thermal expansivity | 1525-2795 | 2540-5590 | 1780-3810 |
| (µm/m/°C) | 1323-2193 | 2370-3390 | 1700-3010 |

Generally, higher molecular mass enhances mechanical strength and toughness, whereas lower molecular mass improves melt processability thanks to the decrease of viscosity, at the expense of mechanical strength. The degree of crystallinity is crucial as it affects clarity, density, and thermal stability; typically, increased crystallinity leads to enhanced strength and thermal resistance. Variations in chain architecture, such as those occurring in linear low-density

polyethylene (LLDPE) and branched low-density polyethylene (LDPE), significantly impact flexibility, toughness, and impact resistance. Additionally, processing conditions such as temperature, pressure, and cooling rates are vital in shaping the crystallization behaviour and the resultant mechanical properties of the polymer. The use of additives also plays a significant role; for instance, stabilizers protect against degradation, fillers enhance specific mechanical properties, plasticizers increase flexibility, and colorants provide aesthetic appeal. Furthermore, environmental factors like moisture and chemical exposure can affect the mechanical properties and overall durability of the material. Ultimately, the interplay among these various factors enables the tailoring of polyethylene properties, making it suitable for a broad range of applications across different industries.

1.2.5. Industrial Processing and Application

The industrial processing of polyethylene involves a variety of methods that convert the raw polymer into a wide range of products, each one designed to meet specific functional and performance requirements. Many studies have been carried out on PE⁴⁸ highlighting its great properties like good heat resistance, molding and processing performances. This aspect makes PE easily processable using various methods allowing the production of both flexible and rigid products with several complex shapes and structures. The choice of the PE type and processing method plays a crucial role in determining the material final properties, such as strength, flexibility, and durability.

Polyethylene is generally processed in the molten or semi-solid state, using methods that often involve shear forces or stretching, such as extrusion, injection molding, blow molding⁴⁹, rotational molding, calendering, and the tenter-frame process⁵⁰. Each of these techniques, which includes steps of melting, homogenizing, shaping and cooling, enable the production of specific products, from films and packaging materials to structural components and storage

containers. It is well known that the specific processing parameters employed during the manufacturing processes directly impact the polymer structure and morphology, which are related to the final properties of the material^{51,52}.

Below the main processing methods and the typical industrial products associated are illustrated.

• Extrusion

Extrusion is a key process in polyethylene manufacturing, where polyethylene pellets are melted, homogenized, and transported to produce a continuous supply of molten resin. This resin is then forced through a die to create continuous shapes. Commonly, the extruded material is processed into films, which are created using techniques like bubble blowing for tubular film and chill roll casting for flat film and sheet production. Extruded polyethylene can also be formed into profiles like pipes and conduits through shaped dies, or applied as coatings onto substrates such as paper, cardboard, and wire for insulation purposes. Thus, extrusion serves as a fundamental method for producing intermediate polyethylene forms that are further processed into packaging materials, structural components, and insulation.

• Injection Molding

Injection molding is a versatile method primarily used to produce a variety of intricate and precise shapes. This process is well-suited for making commodity items as rigid containers, caps, automotive parts, and household goods that require high dimensional accuracy and complex geometries. HDPE is commonly chosen in this method for its stability and rigidity, making it ideal for items needing resilience and a defined structure. In contrast, LDPE and linear low-density LLDPE are often used for items that require flexibility and resilience.

• Blow Molding

Blow molding is a versatile process used to produce a wide range of plastic items by inflating a molten polymer tube inside a mold. Common products made through this technique include containers, tanks, and toys. The primary types of blow molding are extrusion blow molding and injection blow molding. While injection blow molding tends to be more costly, it creates reusable containers with precise shapes and fewer weak points. High-density polyethylene (HDPE) is the most widely used resin for blow molding, particularly for producing durable containers and storage tanks. Lower molecular weight HDPE is used for smaller items, while higher molecular weight HDPE is reserved for large, heavy-duty products due to its increased strength and durability. For items that need flexibility, such as squeeze bottles or certain toys, low-density polyethylene (LDPE) is used, providing a softer and more impactresistant material. Linear low-density polyethylene (LLDPE) can also be used for products requiring flexibility with added resistance to environmental stress cracking.

• Rotational Molding

Rotational molding, or "rotomolding," is a process used to create medium to large hollow plastic items by heating and rotating a mold containing polyethylene powder. The main products made through this process include storage tanks, trash containers, playground equipment, kayaks, and even boat hulls. The process is popular for producing items with uniform wall thickness and high resistance to environmental stress cracking, making it ideal for large-scale chemical storage, agricultural tanks, and fuel containers. Polyethylene is the primary resin used in rotomolding, making up about 85% of all products produced with this method. HDPE is frequently chosen for these applications due to its

impact resistance and stability, which are essential for large and durable products.

• Calendering

Calendering is a less common process for polyethylene that involves passing the molten polymer between rollers to create thin sheets with precise thickness. This process is used to produce sheeting for liners and protective packaging. The smooth and uniform sheets produced through calendering are often utilized in applications that require consistent surface quality and material thickness, typically used in protective and lining materials.

• Tenter Frame Process

The tenter frame process is used to stretch polyethylene film both longitudinally and transversely, producing biaxially oriented films with enhanced mechanical and barrier properties. In this method, the polymer film is heated and stretched in both directions while being held in place by clips along the edges, which move along a guided frame. Tentering may be simultaneous or sequential. In both cases, the tentering process is particularly useful for producing high-strength films that are commonly used in packaging applications, wrapping materials, and industrial films. The biaxial orientation achieved in tenter frame processing improves the film's toughness, clarity, and resistance to puncture, making it suitable for demanding applications such as food packaging and protective films where durability and clarity are critical

1.3. Biaxially Oriented Polyethylene (BOPE)

My PhD thesis work is focused on the study of phenomena occurring at molecular and supra-molecular length scales by effect of bi-axial stretching of polyethylene, before and during the simultaneous tentering process. For this reason, the following paragraphs describe in some detail the tentering frame process of PE and the state of the art on the topic.

1.3.1. Polyethylene Film Manufacturing Processes for Flexible Packaging Applications

In the production of polyethylene films for flexible packaging, two primary technologies are utilized: the melt blowing 53,54 process (Figure 10a) and the tenter-frame process 55,56 (Figure 10b). As mentioned above, in the melt blowing process, a molten PE tube is blown in a circular orientation, with different roller speeds controlling the longitudinal orientation. This process, known for its cost-effectiveness and higher productivity, is widely used in the industry. The tenter-frame process, on the other hand, involves drawing a cast sheet in two mutually perpendicular directions either through sequential biaxial stretching (two successive steps) or simultaneous biaxial stretching (a single step). These industrial processing methods, involving the use of biaxial shear/elongation forces in the melt or in the (semi)solid state, impart different degrees of orientation to the polymers that enhance mechanical strength, impact and barrier resistance and transparency.

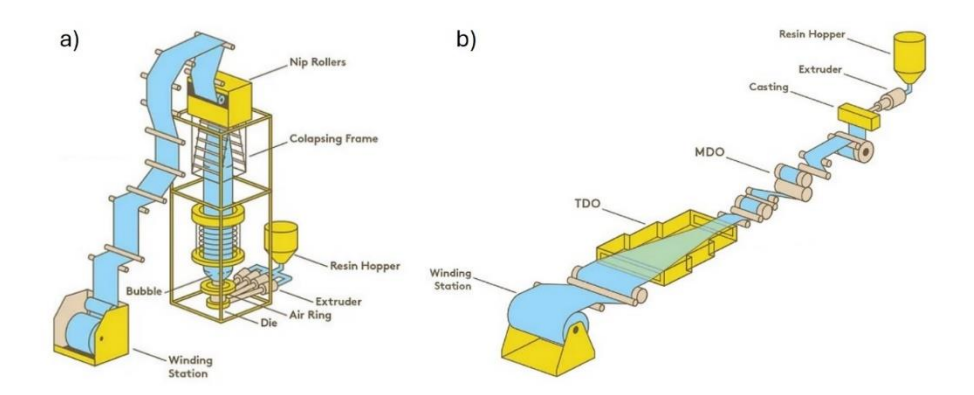


Figure 10 Schematic representation of a) Melt blowing process b) Tenter-frame process.

MDO = Machine Direction Orientation; TDO = transverse direction orientation.

The resulting films are biaxially oriented, meaning that stretching is applied in both directions⁵⁷ in order to improve the film characteristics in the machine (MD) and transverse (TD) directions. Flexible packaging must balance protection (in terms of mechanical and barrier properties), product appeal, economic efficiency and environmental responsibility. When subjected to biaxial orientation, both crystalline and amorphous phase in the film can achieve a high degree of orientation, creating a structural network capable of limiting the passage of low molecular weight gaseous substances, like water vapour, O₂ and CO₂. In addition, orientation can improve the final degree of crystallinity, leading to a significant increase in mechanical properties. Moreover, the increase in crystallinity can enhance optical properties as haze and gloss.

1.3.2. Tenter-Frame Biaxially-Oriented Polyethylene (TF-BOPE)

Tentering has recently attracted great attention as the resultant biaxially oriented films can achieve values of tensile modulus and strength, impact and puncture resistance up to two-three times greater than those of the corresponding conventional blown film⁵⁶. Compared to melt blowing film, tenter-frame process presents some advantages: higher chain orientation and more flexible processing

conditions, which lead to superior mechanical property, optical property, and processability⁵⁸. Due to the excellent low-temperature toughness and puncture resistance, TF-BOPE films are extremely suitable for the field of frozen food packaging^{59,60}. Despite the intrinsic good performance in terms of optical and mechanical properties^{61–63}, BOPE is usually combined with biaxially oriented polyamide (BOPA), biaxially oriented polyethylene terephthalate (BOPET) or biaxially oriented polypropylene (BOPP) to produce multi-layered films^{64,65}, helping in reducing the thickness of films without affecting mechanical strength⁶⁶. Although this technology helps in improving the final properties of the films, separation of the constituent materials is still very challenging, affecting so the recyclability at their end-of-life. Therefore, nowadays, research points out toward the study of the main transformations occurring at molecular and supramolecular length scales by effect of frame tentering, with the aim to identify the basic parameters that allow obtaining PE-based mono-materials with high performance, without resorting to the multi-layered technology.

1.3.3. Structure Evolution During Biaxial Stretching

While uniaxial deformation of PE had been extensively investigated^{67–71}, the mechanisms involved in the structure evolution for TF-BOPE are still unclear. Many factors must be taken into account, starting from the type of stretching (sequential or simultaneous), the selection of the resin and the processing conditions. In Figure 11 sequential and simultaneous biaxial stretching are shown.

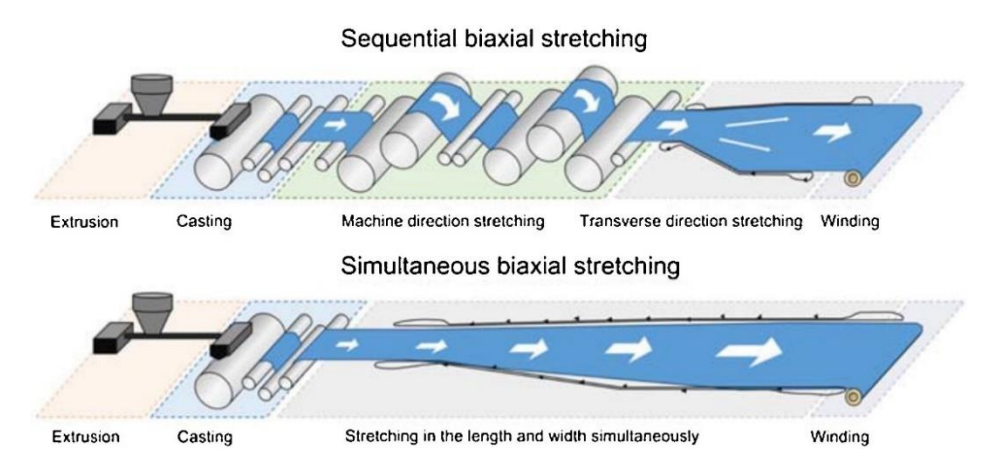


Figure 11 Schematic representation of the two types of biaxial stretching in tenter frame process⁷²

Commonly, techniques as wide-angle X-ray diffraction (WAXD), atomic force microscope (AFM) and scanning electron microscopy (SEM) have been employed to investigate the morphology of BOPE films. Previous studies⁶³ revealed that the stretching HDPE in MD determines a crystalline morphology changes from the spherulite structure into lamellar stacks trough occurrence of local melting and recrystallization phenomena, bulk melting, or a combination of the above ways. Chen *et al.*⁵⁶ investigated the sequential biaxial stretching of LLDPE and proposed that the lamellar fragments obtained by the destruction of spherulites incorporate in a fibrillar structure. The subsequent stretching in TD leads to the separation of the single fibrils and the development of nanosized fiber-like network. Similar results have been found for biaxial stretching of BOPP^{73,74}. While a general orientation reaches a balanced state in the two directions after a certain value of biaxial ratio in the case of sequential biaxial stretching, the simultaneous biaxially stretching leads to films that commonly exhibit a more uniform orientational distribution of lamellae in the MD-TD plane (Figure 12).

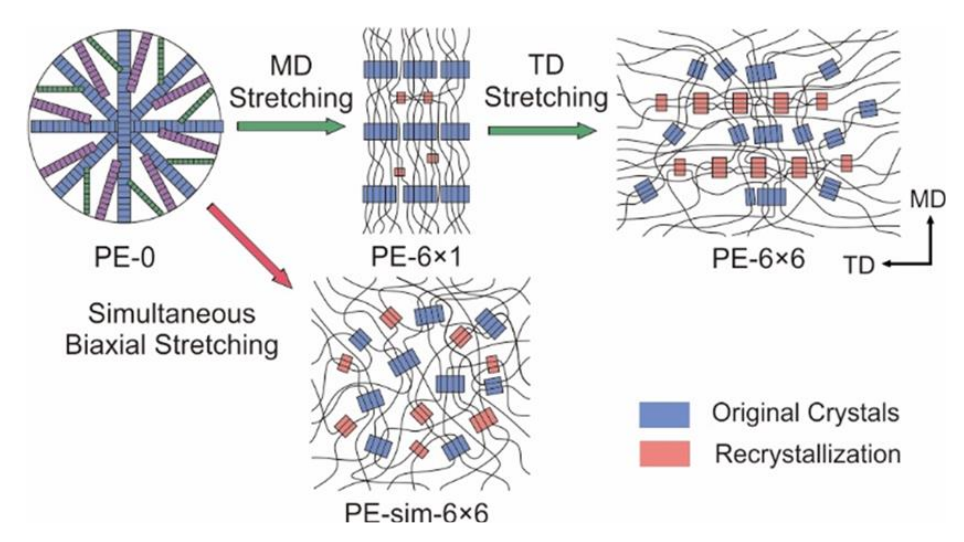


Figure 12 Mechanism of structure evolution during sequential and simultaneous biaxial stretching (Reprinted with permission from Ref. 55, American Chemical Society, 2019).

Molecular structure and molecular weight distribution also play a key role in the structural evolution and, more generally, in the success of biaxial stretching. In another work, Chen et al. 55 investigated sequential biaxial stretching on two types of LLDPE, with similar melt flow rate but different dispersity D and comonomer content and distribution. This study demonstrates that the PE grade with less content and uniform distribution of comonomer, owing to the presence longer crystallizable chain segments, developed thicker chain-folded lamellae during stretching in the first direction. Moreover, the lower comonomer content provide a lower probability of exclusion of comonomer from the growing crystals, leading to a thinner interphase layer in the stacked lamellae morphology, larger lateral dimensions of lamellae and a higher content of fibrils after stretching. During the stretching some of these lamellae can cross adjacent lamellar stacks, increasing lateral tie connection. In addition, the presence of shorter methylene sequence lengths (MSL), due to the heterogeneous distribution of comonomer, determine the formation of fine lamellae that after deformation at high temperature turned into thick lamellae by melting and re crystallization processes and act as additional

lateral connection during the stretching in the second direction. Coexistence of lamellae of different size, in terms of Thomson-Gibbs equation⁷⁵, is suggested by the presence of multiple melting peaks in DSC curves recorded after drawing. Figure 13 give a schematic representation of the difference between structural evolution for the two PE grades.

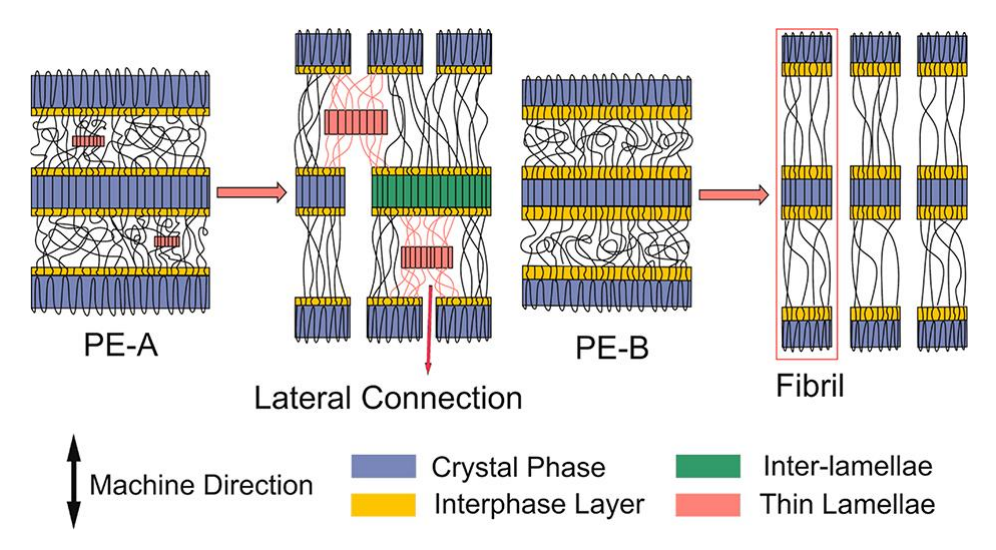


Figure 13 Proposed structural evolution during stretching in the first direction for two different PE grades. PE-A has less comonomer content and less uniform distribution of comonomer with respect to PE-B (Reprinted with permission from Ref. 55, American Chemical Society, 2019).

Comonomer content and high molecular weight tails have an important effect also on the orientation⁶¹ reached in the BOPE films. Lower branching content and higher molecular weight determine an increased orientation, owing to a relatively slower relaxation rate of molecular chains. Indeed, a slower relaxation rate facilitates the orientation of molecular chains, and the increased relaxation time is desirable for the biaxial stretching process⁷⁶.

Commonly, polyethylene shows a narrow stretchable temperature range and not all the PE grades are suitable for biaxial stretching. In addition, the fast crystallization rate and high crystallinity do not contribute to obtain an even thickness, causing breakage of the film upon wrinkling. This problematic aspect can be overcome by blending⁷⁷ different PE grades. Several patents^{78,79} for the production of BOPE films include this solution to improve biaxial stretchable properties. Uehara^{80,81} investigated the structural requirements for BOPE resin, finding that a wider or even bimodal molecular weight distribution (MWD) is better for stretchability and in particular determines a wider stretchable temperature range. However, there is still no extensive study on the selection of polyethylene in terms of chain microstructure and condensed structure, so there are not yet established criteria for selecting the polyethylene to be used for biaxial stretching.

Another aspect to explore is the stretching temperature. It is known that a proper temperature is between the glass transition temperature (Tg) and the melting point $(T_{\rm m})$ of materials^{82–84}. However, the temperature experienced by the polymer affect chain mobility⁸⁵ and can promote several phenomena as self-nucleation⁸⁶, secondary crystallization⁸⁷ or crystals perfectioning by annealing⁸⁸, melting and recrystallization processes^{89,90}. All these phenomena result in structural and morphological changes in both the crystalline and amorphous phase. Previous studies have demonstrated that self-nucleation can accelerate the crystallization process⁹¹ and, for low crystallization rate polymers, the overall crystallization degree can be increased⁹², affecting properties such as mechanical performance and barrier and optical properties. Secondary crystallization, representing a further increase in crystallinity consisting in additional crystallization of uncrystallized material or in further development of the already formed crystalline structure⁹³, has the same effect: this phenomenon is observed in systems incapable of complete crystallization 94,95 and cause an increase in crystallinity beyond that which can be fit by the Johnson-Mehl-Avrami (JRIA) equation 96,97. Annealing process occurs when a polymer solid is heated to temperatures approaching its

melting point⁹⁸ and is frequently used in both fundamental research and industrial processing to improve specific properties^{99–101}. The effect of annealing has been extensively investigated and many interesting phenomena such as lamellar thickening, lamellar doubling, and chain diffusion have been observed ^{102–106}. It is clear from all these considerations that, although the biaxial stretching process is currently used in the packaging industry, our understanding of the structural transformations that polyethylene undergoes during biaxial stretching remains limited. Similarly, the parameters required to optimize the process, including the selection of the most suitable type of PE and the ideal operating conditions, are still not fully defined to maximize the potential of BOPE.

1.4. The Interdisciplinary Approach: Objective and Layout of the Work

This thesis work originates from the project #847 "PER-MANENT- A microstructural insight in PolyEthylene based bioriented mono-MAterials: from fuNdamENTal to processing", promoted by the Dutch Polymer Institute (DPI). The primary objective of this thesis is to generate new knowledge on the structural transformations of polyethylene (PE) during biaxial stretching, focusing on the relationship between chain microstructure, crystallization behaviour, processing conditions and final properties of biaxially oriented PE (BOPE) films. This study aims to investigate how different PE grades, including HDPE, LLDPE and their blends, perform during the stretching process, aiming to optimize their use as mono-materials for next-generation packaging applications. The innovative aspects of the study lie in providing insights into the structural mechanisms at play during the biaxial orientation process, offering potential breakthroughs in expanding PE application as a sustainable alternative to multilayer films.

The work is structured to build a systematic and interdisciplinary chain of knowledge, linking microstructural characteristics with processing conditions and the resulting properties of BOPE.

To achieve this goal, three universities and three industrial partners have collaborated synergistically, under the coordination of the DPI. Indeed, the project brings together the Soft Condensed Matter Lab from University of Naples Federico II (which this PhD candidate belongs to), the Zernike Institute for Advanced Materials from University of Groningen for structure and properties investigation, and the Department of Industrial Engineering from University of Salerno for rheology and modeling part. The ex-situ comprehensive characterization of the selected PE grades is coupled with in-situ structural analysis performed using synchrotrons within EU facilities (ESRF in Grenoble, ALBA in Barcelona) with a new device for lab scale biaxial stretching suitably developed by the engineering group from Salerno. The commercial PE grades investigated have been supplied by Borealis, DOW and SABIC, which have been helpful in providing an industrial perspective during the development of the project.

Chapter 2 is dedicated to the description of all the experimental procedures and techniques employed in this work. The starting basic characterization of the samples, presented in Chapter 3, includes microstructural analysis to check molecular mass and distribution, branch type and branching concentration and corresponding distribution. Tensile tests have been carried out on compression molded films of the samples for a mechanical characterization of the PE grades. In addition, the characterization of thermal properties, crystallization behaviour and thermal fractionation are illustrated. In Chapter 4 phenomena induced by temperature examined through the application of a thermal protocol are discussed. They have been investigated using DSC, coupling the results with structural (WAXS, SAXS) and morphological (POM, SEM) analysis. In Chapter 5, the results achieved by performing in situ experiments aimed at gaining a better understanding of the phenomena induced by temperature and the thermal protocol adopted for ex-situ analysis in conditions emulating the stages preceding tentering

are reported. Further in-situ analysis aimed at understanding the complex structuring process that occur during biaxial stretching in the semi-solid state of cast sheets of selected grades produced at Karo Brukner facility, using the biaxial stretching device, are illustrated in Chapter 6. In situ experiments are performed by collecting 2D-WAXS and 2D-SAXS data while heating/cooling/stretching the PE samples. The results will be laid out in detail and discussed in depth in each Chapter, allowing for a comprehensive interpretation of the findings. In Chapter 7, the main conclusion of this work will be illustrated.

Bibliography of chapter I

- (1) Plastic Europe. *Plastics the Fast Facts (2023)*; 2023.
- (2) Geyer, R.; Jambeck, J. R.; Law, K. L. Production, Use, and Fate of All Plastics Ever Made. *Sci. Adv. 3* (7), e1700782. https://doi.org/10.1126/sciadv.1700782.
- (3) OECD. Global Plastics Outlook, 2022. https://www.oecd-ilibrary.org/content/publication/de747aef-en.
- (4) Global Plastics Outlook Plastics Use by Application, 2022. https://www.oecd.org.
- (5) *Https://Www.Ellenmacarthurfoundation.Org.*
- (6) Galli, P.; Vechellio, G. Polyolefins: The Most Promising Large- Volume Materials for the 21st Century. *J Polym Sci* **2004**, *42*, 396-415.
- (7) *Https://Www.Woodmac.Com.*
- (8) European Parliament. European Parliament Approves Updates to Packaging and Packaging Waste Regulation (PPWR). **2023**.
- (9) Https://Corporate.Dow.Com/En-Us/News/Press-Releases/Dow-Launches-Game-Changing-Fully-Recyclable-Polyethylene-Packaging-Solution-in-India.
- (10) Www.Borealisgroup.Com.
- (11) OECD. Global Plastics Outlook; 2022. https://doi.org/10.1787/de747aef-en.
- (12) Kissen, Y. Y. Kirk-Othmer. *Encyclopedia of Chemical Technology*, 4th ed.; Howe-Grant, M., Ed.; Wiley-Interscience: New York. 1996.
- (13) Boor, J. Ziegler-Natta. *Catalysts and Polymerizations*; New York, 1979.
- (14) Christoph Janiak. Metallocene Catalysts ECT, 5th ed.; Vol. Vol. 16.
- (15) Whiteley, K. S. *Ullman's Encyclopedia of Industrial Chemistry*, 5th ed.; Schulz, G., Ed.: New York, 1992.
- (16) Sirota, A. G. *Polyolefins, Modification of Structure and Properties*; Keter Press: Jerusalem, 1971.
- (17) Peacock, A. J. *Handbook of Polyethylene*; Marcel Dekker, Inc.: New York, 2000.
- (18) Schönherr, H.; Vancso, G. J. Visualization of Macromolecules and Polymer Morphology. In *Scanning Force Microscopy of Polymers*; Schönherr, H., Vancso, G. J., Eds.; Springer Berlin Heidelberg: Berlin, Heidelberg, 2010; pp 79–187. https://doi.org/10.1007/978-3-642-01231-0 3.
- (19) Bunn CW. Trans. Faraday Soc. 1939, 35:428.
- (20) Busing WR. *Macromolecules* **1990**, No. 23, 4608.

- (21) Chatani Y, Ueda Y, Tadokoro H. Annual Meeting of the Society of Polymer Science. Japan, Tokyo 1977.
- (22) Swan PR. J Polym Sci. **1962**, *56*, 409.
- (23) Holdsworth PJ, Keller A. J Polym Sci, Polym Lett. 1967, 5, 605.
- (24) Martinez Salazar FJ, Balt Calleja FJ. J Cryst Growth. 1979, 48, 282.
- (25) Preedy JE. Br Polym J. **1973**, No. 5, 13.
- (26) Teare PW, Holmes DR. J Polym Sci. 1957, 24, 496.
- (27) Yamada M., Miyasaka K., Ishikawa K. Redrawing of Oriented of Polyethylene Film. *J. Polym. Sci.* **1971**, *9*, 1083–1096.
- (28) L.Fontana, d.q. Vinh, M. Santoro, S. Scandolo, F.A. Gorelli, R. Bini, and M. Hanfland; Phisical Review. 75th ed. 2007.
- (29) Seto T, Hara T, Tanaka K. Japanese J Phys. 1968, 7, 31.
- (30) Bassett DC, Block S, Piermarini GJ. J Appl Phys. 1974, 45, 4146.
- (31) L.Fontana, d.q. Vinh, M. Santoro, S. Scandolo, F.A. Gorelli, R. Bini, and M. Hanfland; Phisical Review. **2007**, *B* 75, 174112–1.
- (32) Keller A. Phil Mag. **1957**, No. 2, 1171.
- (33) Till PH. J Polym Sci. 1957, No. 24, 301.
- (34) Fischer EW. Z Naturf. 1957, No. 12a, 753.
- (35) Kobayashi K. Kagaku Chem. **1962**, No. 8, 203.
- (36) Williams T, Blundell DJ, Keller A, Ward IM. J Polym Sci A-2. 1968, No. 6, 1613.
- (37) Blundell DJ, Keller A, Connor T. J Polym Sci. **1967**, *A-2* (5), 991.
- (38) Keller, A. Faraday Discuss. Chem. Soc. Faraday Discuss. Chem. Soc. 1979, 68, 145.
- (39) Wittmann JC, Lotz B. J Polym Sci, Polym Phys. 1985, No. 23, 205.
- (40) Bunn CW, Alcock TC. Trans Faraday Soc. **1945**, No. 41, 317.
- (41) Point J. J Bull Acad R Belg. 1955, No. 41, 982.
- (42) Keller A. J Polym Sci. **1955**, No. 17, 351.
- (43) Keller A. J Polym Sci. 1955, No. 17, 291.
- (44) Keith HD, Padden FJ. J Polym Sci. **1963**, No. 39, 101.
- (45) Rego Lopez JM, Gedde UW. Polymer. **1988**, No. 29, 1037.
- (46) Bassett DC, Keller A, Mitsuhashi S. J Polym Sci A. 1963, No. 1, 763.

- (47) Peacock, A. Handbook of Polyethylene, 1st ed.; CRC Press, 2000.
- (48) X. Lu, B. Norman. Abnormal Slow Crack Growth in Polyethylene. *Polymer* **1997**, *38* (23), 5749–5753.
- (49) Xiuhua Zhong, et al. Polyethylene Plastic Production Process. **2017**, *1* (1), 1–11.
- (50) Benning, Calvin J. Plastic Films for Packaging: Technology, Applications, and Process Economics. 1983.
- (51) Mandelkern L, Peacock AJ. Stud Phys Theor Chem. 1988, No. 54, 201e17.
- (52) Popli R, Mandelkern L. J Polym Sci Polym Phys. 1987, No. 25, 441e9.
- (53) Yu, T. H.; Wilkes, G. L. Orientation Determination and Morphological Study of High-Density Polyethylene (HDPE) Extruded Tubular Films: Effect of Processing Variables and Molecular Weight Distribution. *J. Plast. Film Sheeting* **1997**, *13*, 299.
- (54) Pazur, R. J.; Prud'Homme, R. E. X-Ray Pole Figure and Small Angle Scattering Measurements on Tubular Blown Low-Density Poly(Ethylene) Films. *Macromolecules* **1996**, *29*, 119.
- (55) Chen, Q.; Chen, D.; Kang, J.; Cao, Y.; Chen, J. Structure Evolution of Polyethylene in Sequential Biaxial Stretching along the First Tensile Direction. *Ind. Eng. Chem. Res.* **2019**, *58* (27), 12419–12430. https://doi.org/10.1021/acs.iecr.9b01733.
- (56) Chen, Q.; Wang, Z.; Zhang, S.; Cao, Y.; Chen, J. Structure Evolution and Deformation Behaviour of Polyethylene Film during Biaxial Stretching. *ACS Omega* **2020**, *5* (1), 655–666. https://doi.org/10.1021/acsomega.9b03250.
- (57) Briston, J. H.; Katan, L. L. *Plastic Films*; 3rd ed., Ed.; Longman Scientific & Technical: Harlow, 1989.
- (58) Yuksekkalayci, C.; Yilmazer, U.; Orbey, N. Effects of Nucleating Agent and Processing Conditions on the Mechanical, Thermal, and Optical Properties of Biaxially Oriented Polypropylene Films. *Polym. Eng. Sci.* **1999**, *39*, 1216.
- (59) Strangl, M.; Ortner, E.; Buettner, A. Evaluation of the Efficiency of Odor Removal from Recycled HDPE Using a Modified Recycling Process. *Resour. Conserv. Recycl.* **2019**, *146*, 89–97.
- (60) Moreno, D. D. P.; Saron, C. Low-Density Polyethylene/Polyamide 6 Blends from Multilayer Films Waste. *J. Appl. Polym. Sci.* **2019**, *136*, 47456–47464.
- (61) Ajji, A.; Auger, J.; Huang, J.; Kale, L. Biaxial Stretching and Structure of Various LLDPE Resins. *Polym. Eng. Sci.* **2004**, *44*, 252–260.
- (62) Ajji, A.; Zhang, X.; Elkoun, S. Biaxial Orientation in HDPE Films: Comparison of Infrared Spectroscopy, X-Ray Pole Figures and Birefringence Techniques. *Polymer* **2005**, *46*, 3838–3846.

- (63) Ratta, V.; Wilkes, G. L.; Su, T. K. Structure-Property-Processing Investigations of the Tenter-Frame Process for Making Biaxially Oriented HDPE Film. I. Base Sheet and Draw along the MD. *Polymer* **2001**, *42*, 9059–9071.
- (64) Wu, J.; Feng, R.; Zhang, G.; N., N. [Nota: I. cognome dell'autore è stato indicato solo con "N. "]. [Titolo Non Specificato Nell'informazione Fornita]. *Chem. Mater.* **2013**, *41*, 182.
- (65) Bobovitch, A. L.; Ajji, A.; Tkach, R.; Elkoun, S.; Nir, Y.; Unigovski, Y.; Gutman, E. M. [Titolo Non Specificato Nell'informazione Fornita]. *J. Appl. Polym. Sci.* **2010**, *100*, 3545.
- (66) Tamura, S.; Kuramoto, I.; Kanai, T. [Title Not Provided]. *Polym. Eng. Sci.* **2012**, *52*, 1383.
- (67) Peterlin, A. Drawing and Extrusion of Semi-Crystalline Polymers. *Colloid Polym. Sci.* **1987**, *265*, 357.
- (68) Hiss, R.; Hobeika, S.; Lynn, C.; Strobl, G. Network Stretching, Slip Processes, and Fragmentation of Crystallites during Uniaxial Drawing of Polyethylene and Related Copolymers. A Comparative Study. *Macromolecules* **1999**, *32*, 4390.
- (69) Peterlin, A. Molecular Model of Drawing Polyethylene and Polypropylene. *J. Mater. Sci.* **1971**, *6*, 490.
- (70) Adams, W. W.; Yang, D.; Thomas, E. L. Direct Visualization of Microstructural Deformation Processes in Polyethylene. *J. Mater. Sci.* **1986**, *21*, 2239.
- (71) Jiang, Z.; Tang, Y.; Rieger, J.; Enderle, H. F.; Lilge, D.; Roth, S. V.; Gehrke, R.; Heckmann, W.; Men, Y. Two Lamellar to Fibrillar Transitions in the Tensile Deformation of High-Density Polyethylene. *Macromolecules* **2010**, *43*, 4727.
- (72) Wang, D.; Dang, Z.-M. 12 Processing of Polymeric Dielectrics for High Energy Density Capacitors. In *Dielectric Polymer Materials for High-Density Energy Storage*; Dang, Z.-M., Ed.; William Andrew Publishing, 2018; pp 429–446. https://doi.org/10.1016/B978-0-12-813215-9.00012-9.
- (73) Elias, M. B.; Machado, R.; Canevarolo, S. V. Thermal and Dynamic-Mechanical Characterization of Uni-and Biaxially Oriented Polypropylene Films. *J. Therm. Anal. Calorim.* **2000**, *59*, 143–155.
- (74) Lüpke, T.; Dunger, S.; Sänze, J.; Radusch, H.-J. Sequential Biaxial Drawing of Polypropylene Films. *Polymer* **2004**, *45*, 6861–6872.
- (75) Włochowicz, A.; Eder, M. Distribution of Lamella Thicknesses in Isothermally Crystallized Polypropylene and Polyethylene by Differential Scanning Calorimetry. *Polymer* **1984**, *25*, 1268–1270.
- (76) Xu, J.; Xu, X.; Zheng, Q.; Feng, L.; Chen, W. [Title Not Provided]. Eur. Polym. J. 2002, 38, 365.
- (77) Wang, T.; Li, H.; Wang, F.; Schultz, J. M.; Yan, S. [Title Not Provided]. *J. Polym. Sci. Part Polym. Chem.* **2011**, *2*, 1688.

- (78) Okura Industrial Co., Ltd. J. P. Patent 2001026684, 2001.
- (79) Larter, J. A.; Poirier, R. V. U. S. Patent 6689857, 2004.
- (80) Uehara, H.; Sakauchi, K.; Kanai, T.; Yamada, T. [Title Not Provided]. *Int. Polym. Process.* **2004**, *19*, 172.
- (81) Uehara, H.; Sakauchi, K.; Kanai, T.; Yamada, T. [Title Not Provided]; 2004.
- (82) Bobovitch, A.; Gutman, E. M.; Henning, S.; Michler, G. H. [Title Not Provided]. *Mater. Lett.* 2003, 57, 2597.
- (83) Demeuse, M. T. *Biaxial Stretching of Film*; Elsevier: Cambridge, 2011.
- (84) Poirier, R. V.; Su, T. K.; Corporation, M. O. U. S. Patent 6168826, 2001.
- (85) Hedesiu, C.; Demco, D. E.; Kleppinger, R.; Buda, A. A.; Blümich, B.; Remerie, K.; Litvinov, V. M. The Effect of Temperature and Annealing on the Phase Composition, Molecular Mobility and the Thickness of Domains in High-Density Polyethylene. *Polymer* **2007**, *48*, 763–777.
- (86) Fillon, B.; Wittmann, J.; Lotz, B.; Thierry, A. [Title Not Provided]. *J. Polym. Sci. Part B Polym. Phys.* **1993**, *31*, 1383.
- (87) Schultz, J. M.; Scott, R. D. Temperature Dependence of Secondary Crystallization in Linear Polyethylene. *J. Polym. Sci. -2 Polym. Phys.* **1969**, *7*, 659–666.
- (88) Moyses, S.; Zukermann-Schpector, J. Annealing in Low Density Polyethylene at Several Temperatures. *Polym. J.* **2004**, *36*, 679–683.
- (89) Jackson, J. B.; Flory, P. J.; Chiang, R. [Title Not Provided]. *Trans. Faraday Soc.* 1963, 59, 1906.
- (90) Roe, R.-J.; Gieniewski, C.; Vadimsky, R. G. [Title Not Provided]. J. Polym. Sci. Part B Polym. Phys. 1973, 11, 1653.
- (91) Jiang, J.; Zhuravlev, E.; Hu, W.-B.; Schick, C.; Zhou, D.-S. The Effect of Self-Nucleation on Isothermal Crystallization Kinetics of Poly(Butylene Succinate) (PBS) Investigated by Differential Fast Scanning Calorimetry. *Chin. J. Polym. Sci.* **2017**, *35*, 1009–1019.
- (92) Sangroniz, L.; Cavallo, D.; Müller, A. J. [Title Not Provided]. *Macromolecules* **2020**, *53*, 4581–4604.
- (93) Rybnikř, F. Mechanism of Secondary Crystallization in Polymers. *J. Polym. Sci. Gen. Pap.* **1963**, *1*, 2031–2038.
- (94) Avrami, M. [Title Not Provided]. J. Chem. Phys. 1939, 7, 1103.
- (95) Johnson, W. A.; Mehl, R. F. [Title Not Provided]. *Trans. Am. Inst. Min. Eng.* **1939**, *135*, A16.
- (96) Mandelkern, L. [Title Not Provided]. J. Appl. Phys. 1955, 26, 443.

- (97) Mandelkern, L.; Quinn, F. A. Jr.; Flory, P. J. [Title Not Provided]. J. Appl. Phys. 1954, 25, 830.
- (98) Song, S.; Feng, J.; Wu, P. Annealing of Melt-Crystallized Polyethylene and Its Influence on Microstructure and Mechanical Properties: A Comparative Study on Branched and Linear Polyethylenes. *J. Polym. Sci. Part B Polym. Phys.* **2011**, *49*, 1347–1359.
- (99) Blackadder, D. A.; Lewell, P. A. [Title Not Provided]. *Polymer* **1970**, *11*, 147–164.
- (100) Drozdov, A. D.; Yuan, Q. [Title Not Provided]. J. Polym. Sci. Part B Polym. Phys.
- (101) Shan, C. L.; Soares, J. B. P.; Penlidis, A. [Title Not Provided]. *Polymer* **2002**, *43*, 7345–7365.
- (102) Uehara, H.; Yamanobe, T.; Komoto, T. [Title Not Provided]. *Macromolecules* **2000**, *33*, 4861–4870.
- (103) Spells, S. J.; Hill, M. J. [Title Not Provided]. *Polymer* **1991**, *32*, 2716–2723.
- (104) Rastogi, S.; Spoelstra, A. B.; Goossens, J. G. P.; Lemstra, P. J. [Title Not Provided]. *Macromolecules* **1997**, *30*, 7880–7889.
- (105) Matsuda, H.; Aoike, T.; Uehara, H.; Yamanobe, T.; Komoto, T. [Title Not Provided]. *Polymer* **2001**, *42*, 5013–5021.
- (106) Men, Y. F.; Rieger, J.; Lindner, P.; Enderle, H. F.; Lilge, D.; Kristen, M. O.; Mihan, S.; Jiang, S. C. [Title Not Provided]. *Polymer* **2007**, *48*, 2464–2469.

Chapter II

Experimental

2.1. Materials

The samples investigated in the present thesis work consist in a set of four commercial polyethylene (PE) grades, in form of pellets, provided by partner industries: one high-density polyethylene (HDPE) and three linear low-density polyethylene (LLDPEs). The HDPE is produced by Borealis under the trade name BOR PURE MB5568, has a very low content (0.5%mol) of 1-butene. Borealis provided also the LLDPE grade FX1003 which contains the 0.5%mol of 1-butene and 1.2%mol of 1-hexene. The LLDPE that contains 2.6%mol of 1-octene as comonomer is the INNATE TF80 produced by Dow and the one with 3.1%mol of 1-hexene is produced by SABIC with the trade name SUPEER VM006.

To extend the study to PE blends, the HDPE by Borealis and the LLDPE by Dow have been selected to produce blends of different weight ratio at the Department of Industrial Engineering (DIIn) of the University of Salerno, using the twin-screw extruder Collin GmbH. The selected ratios are 20/80, 40/60, 50/50, 60/40, 80/20. For the in-situ analysis, cast film (with thickness close to 0.75 mm) of the PE grades and blends have been produced at Karo Bruckner facility.

2.2. Microstructural characterization

2.2.1. Solution 13C NMR

Solution ¹³C NMR spectra have been recorded using a Bruker Avance III 400 spectrometer equipped with a 5 mm high-temperature cryoprobe, on 45 mg mL⁻¹ polymer solutions in tetrachloroethane-1,2-d₂, with 0.40 mg mL⁻¹ of 4-methyl-2,6-di-tert-butyl-phenol (BHT) added as a stabilizer. Acquisition conditions were: 45° pulse; 2.3 s acquisition time; 5.0 s relaxation delay; 1.5K

transients. Broad-band proton decoupling has been achieved with a modified WALTZ16 sequence (BI WALTZ16 32 by Bruker).

2.2.2. Gel Permeation Chromatography (GPC)

Gel Permeation Chromatography (GPC) analysis has been performed using a Freeslate Rapid-GPC setup, with a set of two mixed-bed Agilent PLgel 10 μ m columns and a Polymer Char IR4 detector. Calibration has been performed with the universal method, using 10 monodisperse polystyrene samples (M_n between 1.3 and 3700 kDa).

2.3. Thermal analysis and fractionation

2.3.1. Differential scan calorimetry (DSC)

Calorimetric measurements have been performed with a heat flux differential scanning calorimeter DSC-Mettler822. Thermal properties have been obtained, on pellets as well as on cast films, recording the differential heat flux in 3 consecutive temperature ramps (I heating-cooling- II heating) in the range 25°C-180°C with scanning rate of 10°C/min, in a flowing N₂ atmosphere. The weight fraction extent of crystallinity is defined as $x_c(DSC)=\Delta H_m(T_m)/\Delta H_m^{\circ}(T_m^{\circ})$, where $\Delta H_m(T_m)$ is the enthalpy of fusion measured at the melting point, T_m , and $\Delta H_m^{\circ}(T_m^{\circ})$ ($\Delta H_m^{\circ}(T_m^{\circ}) = 293 \text{ J/g}$)³ is the enthalpy of fusion of the totally crystalline polymer measured at the equilibrium melting point T_m° ($T_m^{\circ}=141^{\circ}C$)³. For the integration procedure, a linear baseline covering the entire temperature range of each exothermic/endothermic peak was considered.

In the calculation of the crystallinity fraction x_c , it is assumed that the enthalpy of melting for a perfect crystal ΔH_m° does not vary significantly with temperature, i.e., $\Delta H_m^{\circ}(T_m^{\circ}) = \Delta H_m^{\circ}(T_m)$. This assumption is reasonable as T_m is not far from T_m° , minimizing the impact of differences in heat capacities between the crystalline and molten phases.

2.3.2. Melt memory effect

The possible occurrence of memory effect in the melt has been explored resorting to a method devices by Alamo⁴. "Melt memory" refers to the ability of a polymer melt to retain structural information from its crystalline state even after being heated above its melting temperature. This phenomenon enhances crystallization, as evidenced by a shift of the crystallization temperature recorded during subsequent cooling scan. Unlike heterogeneous nuclei, which can produce a fixed number of crystal nuclei, melt memory nuclei originate from the "nonisotropic" structure of the melt. In this context, the term nonisotropic refers to a not-fully relaxed melt. These nuclei form through the aggregation of polymer chains and represent a unique type of homogeneous nucleation, driven by the retained organization within the melt.

The method consists in performing a DSC thermal protocol that includes several heating and cooling cycles, carried out by randomly varying the maximum temperature achieved in the melt between 2 limit values, $T_{\rm maxI}$, where self-nuclei are surely extinct, and $T_{\rm maxII}$, corresponding to the incipient melting temperature. In particular, the Alamo's procedure (Figure 1) includes:

- 1. Erasure of previous thermal history and crystalline memory: the sample is kept in the melt for 5 min at a T_{maxl} =200°C
- 2. Cooling from the melt at a constant rate (10 °C/min) down to a minimum temperature (25°C), low enough to allow the sample to crystallize until saturation.
- 3. Heating to a random value of temperature comprised in between T_{maxI} and T_{maxII} , followed by an isotherm of 5 min at the selected T.
- 4. Cooling at same rate of step (2) to 25°C, followed by an isotherm of 5 min.

5. Steps (3) and (4) are repeated a number of times by varying the temperature in step 3 at random in the range comprised in between T_{maxI} and T_{maxI} .

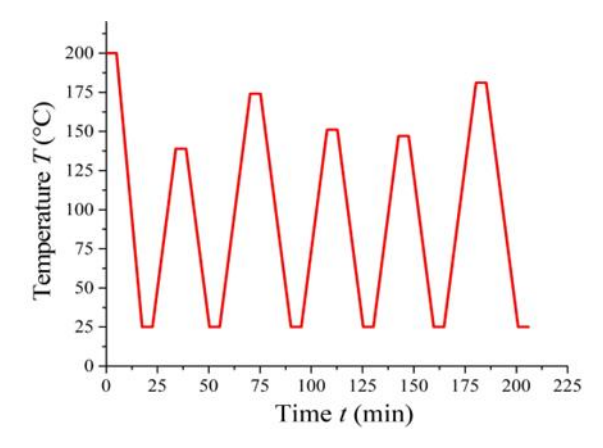


Figure 1 Schematic representation of Alamo's method.⁴

The relevant parameters of this protocol are the values of the crystallization temperatures achieved in the cooling step 4. The occurrence of melt memory effects emerges in the plot of the maximum temperatures reached in the melt $T_{\rm max}$ in the cooling step 3 as a function of the corresponding crystallization temperatures $T_{\rm c}$, as deviations from a straight vertical line at low $T_{\rm max}$, toward greater $T_{\rm c}$ values. (vide infra) To verify that the melting temperature and latent heat of fusion were independent of the initial melt temperature, the melting endotherms recoded in the step 4 have been also analysed.

2.3.3. Self-nucleation and annealing (SNA)

To investigate self-nucleation behavior of the samples, the SNA method has been employed. Self-nucleation and annealing (SNA) is a technique to produce self-seeds or self-nuclei within a polymer melt, so that its nucleation can be greatly enhanced. Fillon et al. devised a thermal protocol to induce and study self-nucleation by DSC⁵. The SNA procedure is schematically shown in Figure 2. It includes the following steps:

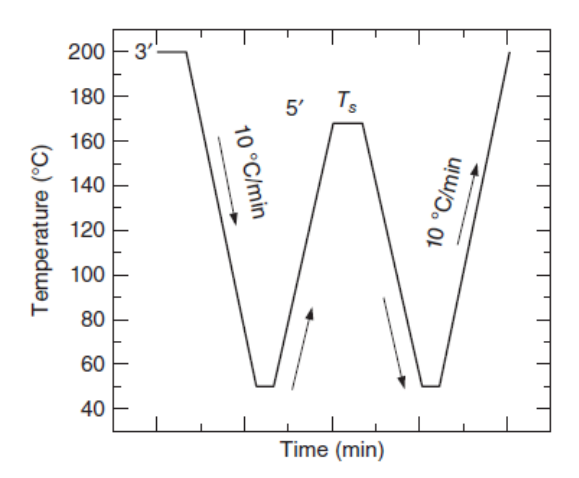


Figure 2 Schematic representation of a self-nucleation treatment.

- 1. Erasure of previous thermal history and crystalline memory: the sample is kept in the melt for 5 min at a high enough temperature ($T_{\text{max}} = 200$ °C). All thermally sensitive nuclei must be destroyed in this first step, leaving only temperature-resistant heterogeneous nuclei of unknown nature.
- 2. Creation of the initial standard semicrystalline state: the sample is cooled from the melt at a constant rate (10 °C/min) down to a temperature ($T_{\rm min}$ =25°C) low enough to allow the sample to crystallize until saturation. The peak crystallization temperature recorded during this cooling scan is the standard crystallization temperature (or standard $T_{\rm c}$). The sample is held at $T_{\rm min}$ for 5 min.
- 3. Thermal conditioning at a specific temperature T_s , where the sample could melt completely or in part, being subjected, depending on T_s , either to complete destruction of self-nuclei, or to survival of self-nuclei, or to survival of self-nuclei and annealing of residual crystals, or mere annealing. In particular, the sample is heated at a constant rate (the same rate employed in step (2)) from the minimum temperature chosen in step $2 (T_{min})$ up to T_s , and then held at T_s for 5 min.

- 4. Subsequent cooling at a constant rate from T_s down to the minimum temperature T_{\min} chosen in step (2).
- 5. Subsequent heating at a constant rate of 10 °C/min) from T_{\min} up to the maximum melting temperature established in step (1), T_{\max} .
- 6. Steps 2 5 are repeated a number of times, by gradually changing the value of T_s , in step 3.

Plotting the values of T_c extracted from the cooling steps (4) vs T_s used in steps (3) it is possible to recognize 3 self-nucleation regimes^{5,6}:

- I. **Domain I.** T_s is high enough to completely destroy self-nuclei, so no difference in T_c are observed.
- II. **Domain II.** It occurs when T_s is high enough to melt the majority of the polymer crystals but low enough to leave some self-nuclei, that accelerate crystallization in the cooling step, as evidenced by the increase of T_c with decrease in T_s Low T_s values in this domain leads to an increase of the number of self-seeds, up to achieve saturation at T_s ideal. The self-nucleation domain encompasses two sub-domains, depending on the mechanism of self-nucleation. In **sub-domain IIa** (higher temperature range of domain II) all crystals are fully melted, with self-nuclei originating from crystalline memory effects. **Sub-domain IIb** (lower temperature range of domain II) is characterized by the retention of small crystalline fragments in the melt, which act as self-seeds.
- III. **Domain III.** If T_s is lower than a threshold, it will only produce partial melting. The surviving crystals undergo annealing.

The value of $T_{\rm s~ideal}$ obtained is crucial for the fractionation technique SSA (successive self-nucleation and annealing).

2.3.4. Thermal fractionation (SSA)

Müller et al. designed and implemented SSA (successive self-nucleation and annealing) to resolve the melting peak of polymers, in terms of elementary melting events, at temperatures which reflect the distribution of lamellar crystals, the size of which, (namely the value of lamellar thickness) depends on the distribution of methylene sequence length (MSL)⁷⁻⁹. After a suitable thermal protocol aimed at inducing fractional crystallization of the samples, the broad endothermic peak of the pristine (unfractionated) samples is replaced, in the final DSC heating scan, by multiple endothermic peaks. This multiplicity of peaks corresponds to the melting of the crystals with different lengths that form during the SSA protocol. In practice, the distribution of the melting temperatures of the different peaks induced by SSA, reflects the presence of MSL of different length, delimited by defects along the chains (e.g., comonomers) that are excluded from the lamellar crystals.

Figure 3 shows a schematic representation of the thermal protocol involved in SSA. The first two steps are identical to all SNA protocols.

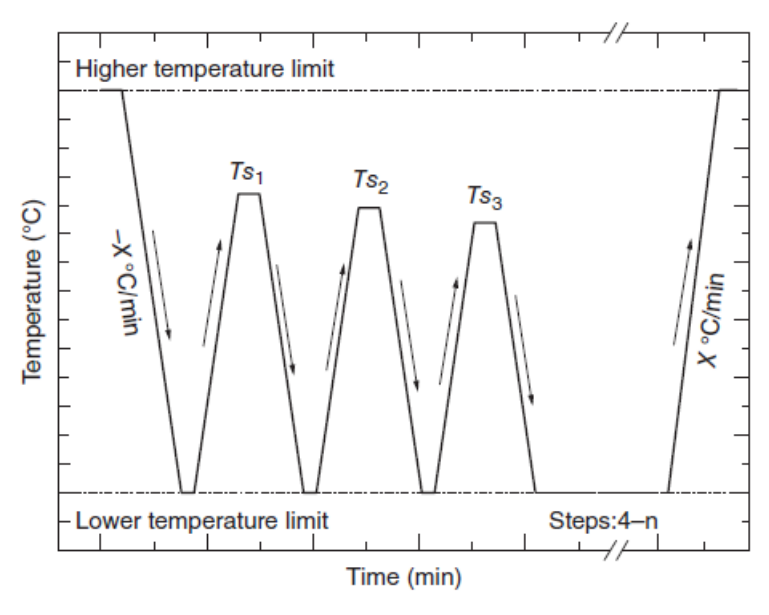


Figure 3 SSA thermal protocol schematic representation.

- 1. Erasure of previous thermal history and crystalline memory by heating the samples up to T_{max} (=200°C), and successive holding the samples at to T_{max} for 10 min.
- 2. Creation of an initial standard semicrystalline state by cooling the melt from T_{max} to T_{min} ($T_{\text{min}} = 25$ °C) and successive beholding the samples at T_{min} for 5 min.
- 3. The sample is heated from the T_{\min} to the ideal self-nucleation temperature $(T_{\text{s ideal}})$ determined in SNA experiments. In Figure 3, this first T_{s} temperature is denoted as $T_{\text{s}1}$.
- 4. The sample is held at the $T_{\rm s}$ ideal for 5 min. This is the isothermal fractionation time and it is kept constant in every cycle. During this step, the sample experiences self-nucleation ($T_{\rm s1}$ is in Domain II) and no annealing or fractionation occur.
- 5. Cooling from $T_{\rm s1}$ down to the $T_{\rm min}$ chosen in step (2), to ensure the crystallization of the ideally self-nucleated polymer.
- 6. Steps (3), (4) and (5) are repeated at progressively lower T_s value, with a fractional window ΔT_s of 5°C. The number of repetitions (cycles) is selected to cover the entire melting range of the sample. All the T_s after T_{s1} are in Domain III, so they produce in each step annealing of the unmolten crystals and self-nucleation of the molten polymer when cooling to T_{min} . During the isotherm at T_{s2} the first thermal fraction is generated in the sample due to isotherm crystallization and annealing. This fraction will be eventually refined by the subsequent thermal cycles.
- 7. Final melting. The sample is heated at the chosen constant rate up to the melt state. In this step, the fractionation is revealed by the splitting of the melting endotherms in multiple peaks centered at different temperatures T_{mi} , corresponding to the melting of crystallites with different lamellar thickness formed and annealed in each step (at particular T_s).

To obtain the percentage of each thermal fraction i, the final multi-peaked melting endotherm (step 7) of the SSA procedure can be analyzed. After a subtraction of a common baseline, the final heating scan is fitted to a sum of Gaussian peaks functions, each one centered at a certain value of T_{mi} . The area of each Gaussian peak A_{Gi} is then normalized to the sum of the areas of all the Gaussian peaks (ΣA_{Gi}) (equation 1).

$$A(T_{mi}) = \frac{A_{Gi}}{\sum_{i=1}^{n} A_{Gi}} \tag{1}$$

Thermal fractionation can be employed to qualitatively determine the distribution of lamellar thickness and short chain branching (SCB)⁷. Indeed, previous studies have shown that PE crystals that incorporate longer Methylene Sequence Lengths (MSL) possess thicker lamellae and melt at increasingly higher temperatures¹⁰. In addition, it has been proved¹¹ that lamellar thickness calculated through the measured $T_{\rm mi}$ of the final SSA endotherm, by employing the Gibbs-Thomson¹² equation (equation 2), are in good agreement with values obtained by other techniques as SAXS analysis.

$$T_{mi} = T_m^0 \left(1 - \frac{2\sigma_e}{l_{ci}\Delta H_m^0} \right) \tag{2}$$

Here, $T_{\rm m}^0$ is the equilibrium melting point (=141°C), $\Delta H_{\rm m}^0$ is the melting enthalpy of the defect-free PE orthorhombic crystals (=293 J/g), $\sigma_{\rm e}$ is the corresponding fold surface energy (=90 mJ/m2, valid for extended chain crystals of PE or 44 mJ/m2, valid for folded chain crystals of PE.), $I_{\rm c}$ is the lamellar thickness. MSLi values can be obtained as the ratio between $I_{\rm ci}$ and the chain periodicity c of PE in the orthorhombic form (0.254 nm), multiplied by 2.

2.4. Structural characterization

2.4.1. Wide-Angle X-ray scattering (WAXS)

Wide angle X-ray scattering (WAXS) data have been collected using the diffractometer Empyrean (PANalytical) in the reflection geometry, with Ni-filtered CuK α radiation (wavelength $\lambda = 0.15418$ nm). The index of crystallinity (x_c (WAXS)) has been evaluated, after subtraction of the background, approximated by a straight line, from the X-ray powder diffraction profiles as the ratio between the crystalline diffraction area (A_c) and the total area of the diffraction profile (A_t), that is xc(WAXS) = A_c/A_c . To obtain the diffraction areas, a fitting of the diffraction profiles with a pseudo-Voigt function has been used for the crystalline and amorphous contributions.

2.4.2. Small-Angle X-ray scattering (SAXS)

SAXS patterns have been collected at room and high temperatures with a compact small angle apparatus Anton Paar (SAXSess) in a linear collimation geometry, using the Cu Kα radiation. SAXS images have been recorded on film BAS-MS "Imaging Plate" (FUJIFILM) and digitalized by a digital reader Cyclone Plus (Perkin Elmer). The analysis has been performed on the compression-molded specimens. The SAXS data have been deconvoluted with the primary beam profile with help of the SAXSquant2D and SAXSquant1D software by Anton Paar, to calculate the equivalent mono-dimensional profiles that would be collected using a point collimation geometry (desmearing). After careful subtraction of the dark current, the empty sample holder, and of a constant background due to thermal density fluctuations, the SAXS data have been elaborated to extract lamellar parameters such as lamellar periodicity and thickness of the amorphous and crystalline layers, resorting to the calculation of the interface distribution function (IDF) and of the mono-dimensional self-correlation function of electron density fluctuations (CF). It is worth noting that the processing of SAXS data, such as the calculation of CF and IDF is typically derived for isotropic samples. However, in certain cases, this approach has also been applied to oriented samples (e.g., after biaxial stretching, Chapter 6) as the degrees of orientation has been assessed to be sufficiently low.

2.5. Compression-molding

The samples, initially in the form of pellets, have been forged into a film by melting them between the plates of a press and then cooling to room temperature. The equipment used was a Carver 4122 hydraulic press with heated plates. Films with average thickness ($\sim 100\text{--}300~\mu m$) have been obtained by melting about 5-6 g of pellets placed between two sheets of PTFE. The maximum temperature achieved in the melt was 200° C, ~ 70 degrees higher than the melting

temperature of the sample obtained from the DSC analysis. This ensures that the thermal and mechanical history of the material is erased, effectively eliminating the effects of previous treatments. The procedure involves maintaining the sample between the plates at 200°C for 10 minutes before applying a pressure of about 9-10 MPa for 2-3 minutes to reduce the occurrence of defects in the film, such as the presence of bubbles. In most cases, cooling occurred slowly by circulating water through the cooling system of the press plates (estimated cooling rate ~20°C/min), while in others, the film was quenched at 0°C by quickly transferring the films, sandwiched between PTFE sheets, and carefully wrapped in aluminium foils, from the press to an ice water bath. The so-obtained films have been used for determining mechanical properties and for structural and morphological analysis.

2.6. Mechanical characterization

Mechanical properties of the samples have been determined through uniaxial tensile tests, deriving the stress-strain curves at room temperature, using an Instron 5566H1543 electro-mechanical machine and following the standard test method for tensile properties of thin plastic sheeting ASTM D882-83. Specimens has been cut from compression-molded films obtained with different cooling conditions. The specimen, with a known cross-section A_0 , is vertically placed between two, one fixed and the other movable, clamps, positioned at an initial distance L_0 . As the clamps move apart at a constant selected speed, the load cell records the applied force F, while the corresponding elongation ΔL is simultaneously measured. The stretching rate v (mm min⁻¹) has been set equal to $10 L_0 \, \text{min}^{-1}$ per to measure the mechanical properties up to the break, namely stress and strain at yielding, σ_y and ε_y , and stress and strain at break σ_b and ε_b . The engineering strain ε is defined as $\varepsilon = \Delta L/L_0 = (L - L_0)/L_0$. Young's modulus E has been measured using a mechanical tester by Zwick Roell, setting the stretching

rate v (mm min⁻¹) equal to $0.1 L_0$ min⁻¹. Stress-strain curves and the values of the mechanical parameters have been obtained as a result of at least five independent, reproducible experiments and successive averaging.

2.7. Morphological characterization

2.7.1. Polarized Optical Microscopy (POM).

Morphological features at micrometric length scale have been investigated via polarized optical microscopy, on compression-molded films obtained in the same condition of the films used for mechanical characterization. POM micrometric images have been collected by Zeiss Axio Imager with objectives Zeiss Neofluar 10x, 20x, 40x and 50x.

2.8. Thermal protocol

A thermal protocol (Figure 4) has been set to investigate the effect of thermal treatment as a function of time and $T_{\text{treatment}}$ for HDPE with 0.5% mol butene (C4) content, LLDPE with 2.6 mol% octene (C8) content and the corresponding 50/50 wt/wt blends. This procedure is meant to identify phenomena that happens to the polymers when subjected to heat treatment at temperatures below the melting point. It consists of precise step cyclically repeated that, once $T_{\text{treatment}}$ is selected, allow to follow the effect of thermal treatment as a function of time. The protocol includes:

- a) The creation of a standard crystalline state: the sample is first heated (10°C/min) and kept for 10 minutes at a maximum temperature T_{max} , to erase any thermal/mechanical memory, then fast cooled to 25°C (40°C/min) .
- b) The actual treatment: the sample is fast heated (40° C/min) to the chosen $T_{\text{treatment}}$ and kept for a certain amount of time at this temperature, before fast cooling (40° C/min) to room temperature. The choose of this heating/cooling rate is dictated by instrumental limitations.

Steps a and b are then cyclically repeated for increasing values of $T_{\text{treatment}}$, in the DSC apparatus.

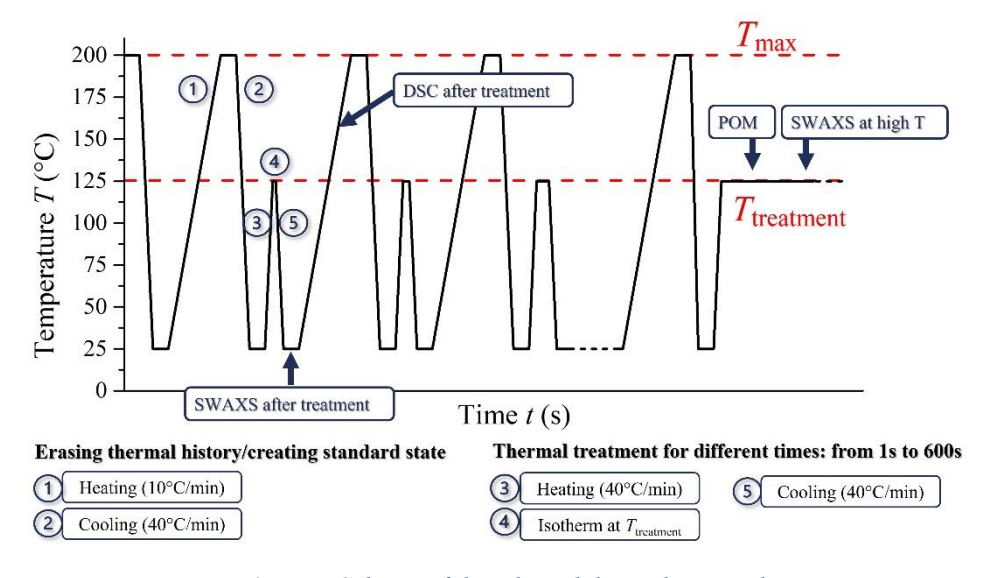


Figure 4 Scheme of the adopted thermal protocol

The subsequent heating scans (recorded from 25 °C until 200°C at 10°C/min) after the thermal treatment have been collected and analysed.

To investigate changes at lamellar length scale, small angle X-ray scattering measurements have been carried out, after subjecting the samples to the thermal protocol a+b using a THMS600 Linkam temperature control system and the scattering profiles have been recorded at room temperature. To gain more details about the effect of the high temperature on the samples, SAXS-WAXS profiles have been recorded at $T_{\text{treatment}}$ too. For room temperature measurements an acquisition time of 30 minutes has been selected, while for measurements at high temperature the acquisition time, after an equilibration of the sample at the selected T of 10 min, was of 5 min. Lamellar parameters have been determined in 3 different ways: by using direct application of Bragg's law on Lorentz corrected Intensity, and obtaining from experimental data the Interface distribution function (IDF) and self-correlation function of electron density fluctuations (CF). To get a

more comprehensive information SAXS-WAXS date have been collected onto image plates (range of 2θ from 0° to 40°), simultaneously. In this way, the structural transformations occurring at lamellar and unit cell length scales have been probed at once.

Polarized light microscopy has been employed to monitor morphological changes (at micrometric scale) occurring after each thermal treatment. In particular, a THMS600 Linkam has been used to collect in situ POM images as a function of time, on samples subjected to step a, during the heat-treatment at $T_{\text{treatment}}$ (step b) for 300 s.

Bibliography of chapter II

- (1) Randall, J. C. A Review Of High Resolution Liquid 13carbon Nuclear Magnetic Resonance Characterizations Of Ethylene-Based Polymers. *J. Macromol. Sci. Part C* **1989**, *29* (2–3), 201–317. https://doi.org/10.1080/07366578908055172.
- (2) Liu, W.; Rinaldi, P. L.; McIntosh, L. H.; Quirk, R. P. Poly(Ethylene-Co-1-Octene) Characterization by High-Temperature Multidimensional NMR at 750 MHz. *Macromolecules* **2001**, *34* (14), 4757–4767. https://doi.org/10.1021/ma001792k.
- (3) Wunderlich, B.; Czornyj, G. Macromolecules. *Macromolecules* **1977**, *10*, 906.
- (4) Mamun, A.; Chen, X.; Alamo, R. G. Interplay between a Strong Memory Effect of Crystallization and Liquid–Liquid Phase Separation in Melts of Broadly Distributed Ethylene–1-Alkene Copolymers. *Macromolecules* **2014**, *47* (22), 7958–7970. https://doi.org/10.1021/ma501937c.
- (5) Fillon, B.; Wittmann, J.; Lotz, B.; Thierry, A. J Polym Sci Pol Phys. *J. Polym. Sci. Part B Polym. Phys.* **1993**, *31*, 1383.
- (6) Michell, R. M.; Mugica, A.; Zubitur, M.; Müller, A. J. Self-nucleation of Crystalline Phases within Homopolymers, Polymer Blends, Copolymers, and Nanocomposites. In *Advances in Polymer Science*; 2015; Vol. 276, pp 215–256.
- (7) Müller, A. J.; Arnal, M. L. Thermal Fractionation of Polymers. *Prog. Polym. Sci.* **2005**, 30, 559–603.
- (8) Müller, A. J.; Hernández, Z. H.; Arnal, M. L.; Sánchez, J. J. Successive Self-Nucleation/Annealing (SSA): Novel Technique to Study Molecular Segregation during Crystallization. *Polym. Bull.* **1997**, *39*, 465–472.
- (9) Müller, A. J.; Michell, R. M.; Pérez, R. A.; Lorenzo, A. T. Successive Self-Nucleation and Annealing.
- (10) Liu, W.; Kim, S.; López, J.; Hsiao, B.; Keating, M. Y.; Lee, I. H. *J. Therm. Anal. Calorim.* **2000**, *59*, 245.
- (11) Lorenzo, A. T.; Arnal, M. L.; Müller, A. J.; Lin, M. C.; Chen, H. L. *Macromol. Chem. Phys.* **2011**, *212*, 2009.
- (12) Crist, B. Yet Another Visit to the Melting of Polyethylene Crystals. *J. Polym. Sci. Part B Polym. Phys.* **2007**, *45*, 3231–3236.

Chapter III

Characterization of commercial PE grades

3.1. Microstructural characterization

A full investigation about structure-property relationships in PE materials, as a function of processing conditions, requires establishing a clear correlation between the chain microstructure, the crystalline microstructure, and the final properties. Such a comprehensive study must start with the characterization of the samples, to identify their microstructural, structural, and morphological features, aiming to correlate them with the exhibited thermal and mechanical properties. Based on the available PE grades, the preliminary characterization could be of some help in the selection of which grade is most suitable for the biaxial stretching process, potentially utilizing the blending of different PEs. The goal is to identify which factors may influence stretchability and adaptability to the tentering process. The PE grades provided by industrial partners are one HDPE and three LLDPEs, which differ in microstructural features as molecular mass and distribution, branch type and branching concentration and distribution. In particular, the HDPE is produced by Borealis under the trade name BOR PURE MB5568 and has a very low content (0.5%mol) of 1-butene units. Borealis provided also the LLDPE grade FX1003 which contains 0.5%mol of 1-butene and 1.2%mol of 1-hexene. LLDPE that contains 2.6%mol of 1-octene as comonomer is the INNATE TF80 produced by Dow and the one with 3.1%mol of 1-hexene is produced by SABIC with the trade name SUPEER VM006. The difference in comonomer content is reflected in the density values of the samples, that decrease as the comonomer content increases. In Table 1 the molecular characteristics of the samples under study are summarized. To ensure a smoother discussion and

avoid confusion between samples, the table also defines the code names of the samples, specifying the type of polyethylene and the type of comonomer present.

Table 1 Density, Number (M_n) and Mass (M_w) average molecular mass, dispersity index D, Comonomer type and content and Code name of the samples.

| PE Grade | Density ^a (g/cm ³) | $M_{\rm n}$ $({ m g/mol})^b$ | $M_{ m w}$ $({ m g/mol})^{ m b}$ | Ð | Comonomer type ^a and content (mol%) ^c | Code name |
|-------------|---|------------------------------|----------------------------------|------|---|-----------|
| HDPE | 0.956 | 10000 | 137000 | 14.3 | Butene (0.5) | H-C4 |
| LLDPE | 0.941 | 9000 | 185000 | 19.5 | Butene (0.5) Hexene (1.2) | L-C4,C6 |
| LLDPE | 0.926 | 26000 | 105000 | 4.1 | Octene (2.6) | L-C8 |
| LLDPE | 0.920 | 44000 | 118000 | 2.7 | Hexene (3.1) | L-C6 |

^aValue extracted from technical datasheet. ^bValues measured from GPC analysis. ^cValues obtained from ¹³C-NMR analysis.

H-C4 and L-C4,C6 show a broader molecular mass distribution (Figure 1) compared to the other two LLDPEs, as indicated by the higher values of dispersity index *D*.

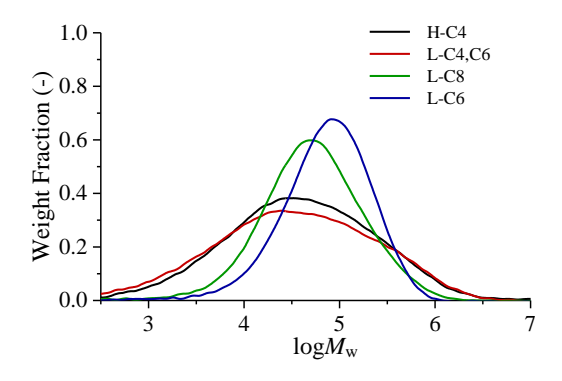


Figure 1 Molecular mass distribution via GPC of the PE samples under study.

3.2. Thermal and Structural characterization

DSC and WAXS analysis

In Figure 2, the DSC scans of the samples in the form of pellets are shown. The values of the temperatures of first and second melting ($T_{\rm m1}$, $T_{\rm m2}$, respectively), crystallization ($T_{\rm c}$) and corresponding enthalpies ($\Delta H_{\rm m1}$, $\Delta H_{\rm m2}$, $\Delta H_{\rm c}$) are listed in Table 2. All the samples show sharp melting and crystallization peaks, the position of which reflect the comonomer content (Figure 3). Looking at the second melting, less dependent from thermal and mechanical history of pellets, the HDPE sample H-4 with less comonomer content exhibits the highest $T_{\rm m2}$ of 132.0°C, followed by the sample L-C4.C6 ($T_{\rm m2}$ =130.4°C), L-C8 ($T_{\rm m2}$ =128.0°C) and L-C6 ($T_{\rm m2}$ =123.1°C), with the highest content of comonomer units. The values of the crystallinity index, evaluated by the ratio between the melting enthalpy $\Delta H_{\rm m2}$ and the melting enthalpy of a 100% crystalline PE (see Chapter 2) follow the same trend (Table2).

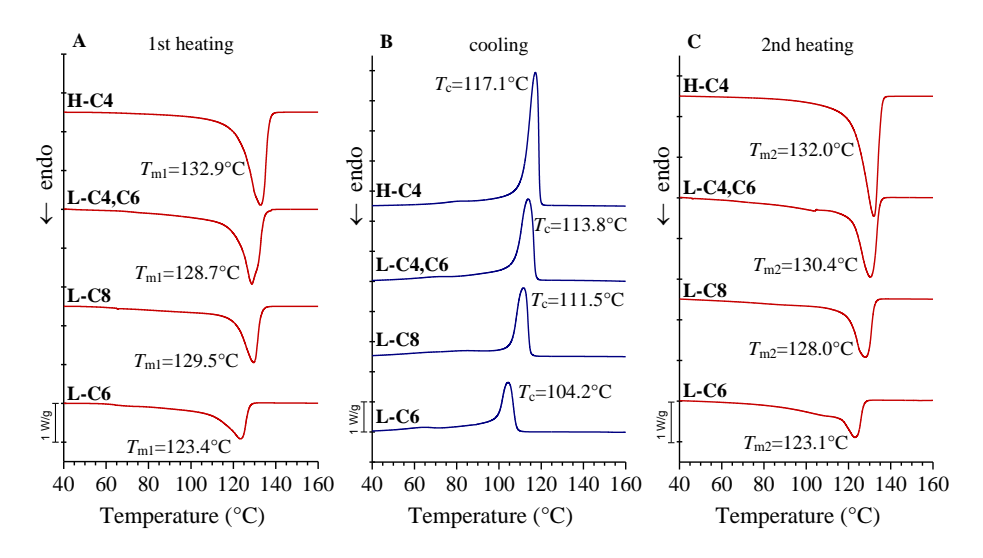


Figure 2 DSC scans recorded during the 1st (A) and 2nd (B) heating and the intermediate cooling (B) scans, at 10°C/min of PE samples. The values of T_{m1} , T_c and T_{m2} are indicated.

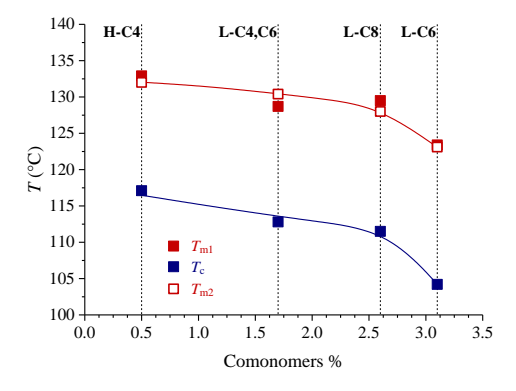


Figure 3 Values of T_{ml} , T_c , T_{m2} extracted from the DSC scans of Figure 2, as a function of total comonomer content.

Table 2 First (T_{ml}) and second melting temperatures (T_{m2}) , crystallization temperatures (T_c) , corresponding enthalpies $(\Delta H_{ml}, \Delta H_{m2}, \text{ and } \Delta H_c)$ and crystallinity index evaluated from DSC and WAXS data of the samples in the form of pellets

| Sample | T_{m1} | $T_{\rm c}$ | $T_{ m m2}$ | ΔH_{m1} | ΔH_c | ΔH_{m2} | x_c DSC | x_c WAXS |
|---------|-------------------|-------------|-------------|-----------------|--------------|-----------------|-----------|------------|
| | (°C) | (°C) | (°C) | (J/G) | (J/G) | (J/G) | (%) | (%) |
| H-C4 | 132.9 | 117.1 | 132.0 | -186.2 | 214.7 | -207.2 | 70 | 71 |
| L-C4,C6 | 128.7 | 113.8 | 130.4 | -173.7 | 188.1 | -188.9 | 63 | 66 |
| L-C8 | 129.5 | 111.5 | 128.0 | -123.4 | 144.8 | -129.9 | 44 | 61 |
| L-C6 | 123.4 | 104.2 | 123.1 | -103.2 | 120.3 | -109.1 | 37 | 45 |

The WAXS profiles of the pellets and compression molded films of PE samples are reported in Figure 4. Compression molded films were prepared by heating the melt to $T_{\rm max}=200~{\rm ^{\circ}C}$ between the plates of a press and after an isotherm at $T_{\rm max}$ for 10 min, by slow cooling the melt to 25 °C (average cooling rate 20 °C/min). All the samples show the 110 and 200 reflection at $2\theta\approx21^{\circ}$ and $2\theta\approx24^{\circ}$, of the orthorhombic form of PE. A hump at $2\theta\approx13^{\circ}$ is visible in the WAXS profiles of the pellets, due to the presence of calcium stearate, generally used as lubricant for processing.

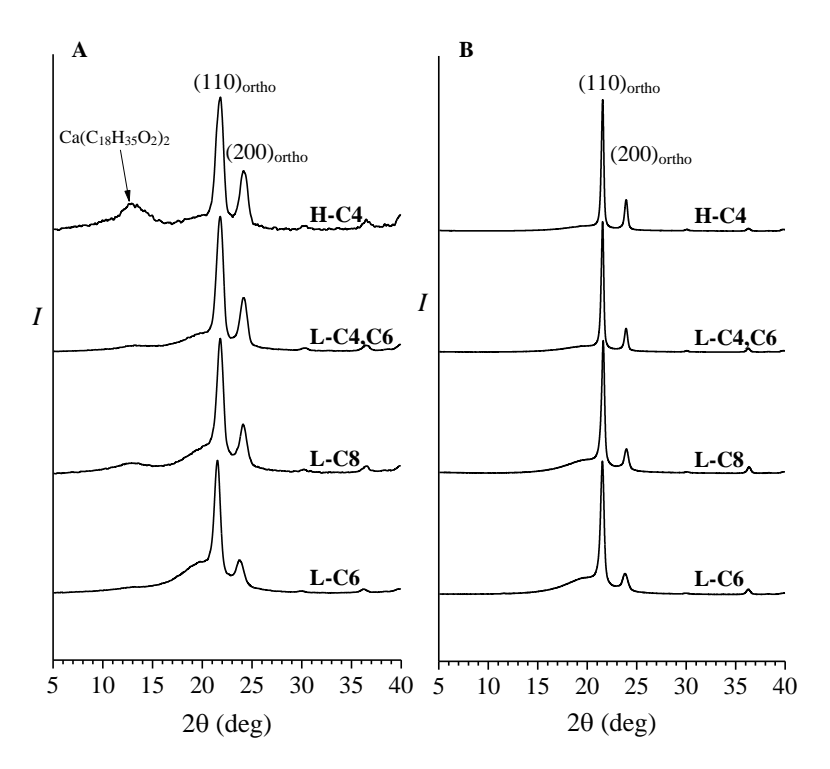


Figure 4 X-ray powder diffraction profiles of pellets (A) and compression-molded films (B) of the PE samples.

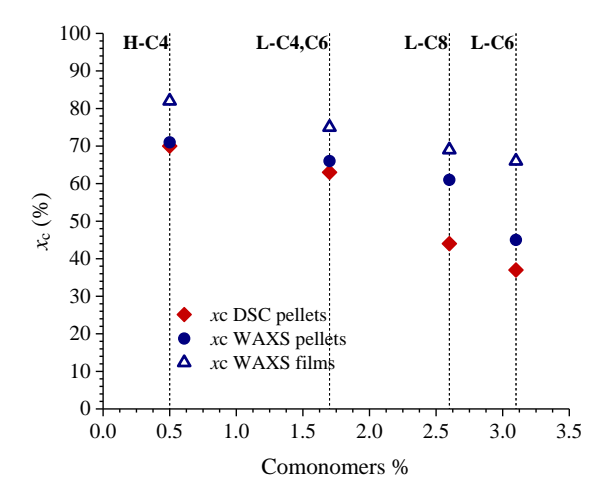


Figure 5 Crystallinity index evaluated from DSC (diamonds) and WAXS (circles and triangles) of PE samples. The circles and triangles are relative to pellets and compression molded films, respectively.

The values of the crystallinity index evaluated from the DSC curves and the WAXS profiles (Figure 5) decrease as the comonomer content increases. The values extracted from the WAXS profiles are greater than those extracted from DSC curves, especially for the LLDPE sample with high comonomer content. These differences are due to the fact that the WAXS crystalline index takes into account also the contribution from defective crystals, the latent heat of melting of which is lower than that of crystals with major perfection. Furthermore, compression molded films show the highest values of crystallinity index.

SAXS analysis

The SAXS profiles, before and after correction for the Lorentz factor, relative to the compression-molded films of the PE samples are shown in Figure 6. The films were prepared in between press plates by slow cooling the melt from $T_{\rm max} = 200$ °C, and annealing at $T_{\rm max}$ for $t_{\rm max} = 10$ min. All the samples show a SAXS profile (Figure 6B) with a well-defined main correlation peak, indicating the presence of a-well organized stacks of crystalline lamellae separated by amorphous layers. The samples H-C4 and L-C4,C6 show a narrow correlation

peak centered at q_1 =0.254 nm⁻¹, corresponding to a value of the characteristic correlation distance (long spacing) L_1 =2 $\pi/q_1 \approx 24.7$ nm. The presence of a second maximum at $q_2 \approx 2$ q_1 , corresponding to the second order of diffraction, confirms the quasi-ideal arrangement of crystallites in stacks of parallel lamellae nearly equidistant with average periodicity L_1 . For the samples L-C8 and L-C6, the main correlation peak shift to greater values, q_1 =0.294 nm⁻¹ and q_1 =0.38 nm⁻¹ respectively, corresponding to an average long spacing of L_1 =21.4 nm and L_1 =16.5 nm. Moreover, the main peaks of L-C8 and L-C6 are broader than the peaks observed for H-C4 and L-C4,C6, indicating greater variation in lamellar parameters. The second order of diffraction peak is broad and weak for the sample L-C8, and barely visible for the sample the sample L-C6, suggesting that the degree of disorder in the lamellar stacking increases as the comonomer conte increase.

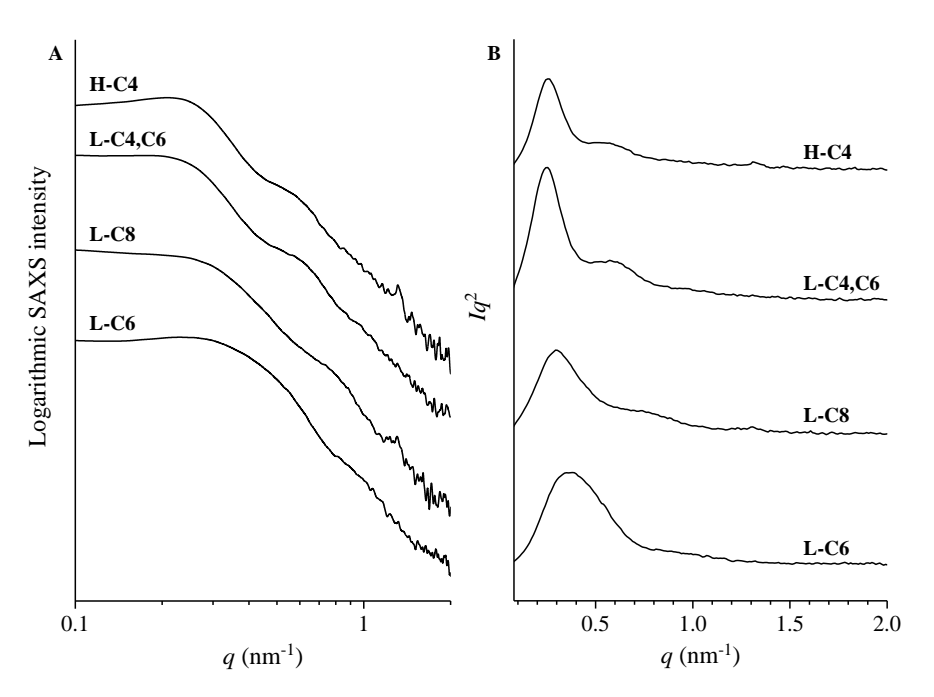


Figure 6 SAXS profiles before (A) and after (B) Lorentz's correction of intensity, for the compression-molded films of the samples, recorded at room temperature.

The position of the observed correlation peaks q_1 and q_2 in Figure 6 and the values of the corresponding values of L_1 and L_2 are reported in Table 3. The values of the thickness of the lamellar l_c and amorphous layers l_a are also reported in Table 3. They have been calculated as: as:

$$l_c = L_1 \Phi_c \tag{1}$$

and

$$l_a = L_1 - l_c \tag{2}$$

where Φ_c is the volume fraction of the crystalline phase, approximately calculated from the values of the crystallinity index x_c extracted from WAXS analysis, according to the following equation:

$$\Phi_{\rm c} = \frac{\frac{x_{\rm c}}{\rho_{\rm c}}}{\frac{x_{\rm c}}{\rho_{\rm c}} + \frac{(1 - x_{\rm c})}{\rho_{\rm a}}} \tag{3}$$

where ρ_c =1 g/cm³ and ρ_a =0.855 g/cm³ are the densities of crystalline and amorphous PE, respectively¹.

Table 3 Values of the position of the first and second order of the correlation peaks (q_1 and q_2) and corresponding characteristic correlation distances (L_1 and L_2 , derived using the Bragg's Law) observed in the Lorentz corrected SAXS profiles of the compression-molded films. From L_1 , the values of the lamellar crystal and amorphous layer thickness have been obtained.

| Sample | q ₁ (nm ⁻¹) | <i>L</i> ₁ (nm) | q ₂ (nm ⁻¹) | L ₂ (nm) | x _c (WAXS) | Φ _c (%) | l _c (nm) | la (nm) |
|---------|------------------------------------|----------------------------|------------------------------------|---------------------|-----------------------|-----------------------|------------------------|------------|
| H-C4 | 0.254 | 24.7 | 0.503 | 24.9 | 0.82 | 0.79 | 19.6 | 5.1 |
| L-C4,C6 | 0.254 | 24.7 | 0.572 | 21.9 | 0.75 | 0.72 | 17.8 | 6.9 |
| L-C8 | 0.294 | 21.4 | 0.741 | 16.9 | 0.69 | 0.65 | 14.0 | 7.4 |
| L-C6 | 0.38 | 16.5 | / | / | 0.66 | 0.62 | 10.3 | 6.2 |

The values of the lamellar parameters have been also calculated from SAXS data through the evaluation of the mono-dimensional self-correlation function of electron density fluctuations^{2,3} (correlation function, CF) and the interface distribution function⁴ (IDF), reported in Figure 7.

The correlation function relative to an ideal biphasic lamellar morphology characterized by sharp interfaces at the boundary between the lamellar crystals and the amorphous layers, is calculated by Equation 4:

$$\rho(r) = \frac{\int_0^\infty q^2 I_c(q) \cos(qr) dq}{\int_0^\infty q^2 I_c(q) dq}$$
(4)

With $I_c=I(q)-I_{bk}$ and I_{bk} is the background intensity, approximated by a straight line.

The interface distribution function has been calculated with Equation 5:

$$IDF(z) = K \int_0^\infty [K_p - q^4(I(q) - I_{bk})] \exp(-\sigma^2 q^2) \cos(qz) dq$$
 (5)

where K_p is the Porod constant.

Using the CF curves, the values of the lamellar parameters are evaluated from the position of the second maximum and by building the first correlation triangle as outlined in Figure 7A, whereas using the IDF curves, the values of the lamellar parameters are evaluated from the position of the maxima and the first minimum as outlined in Figure 7B.

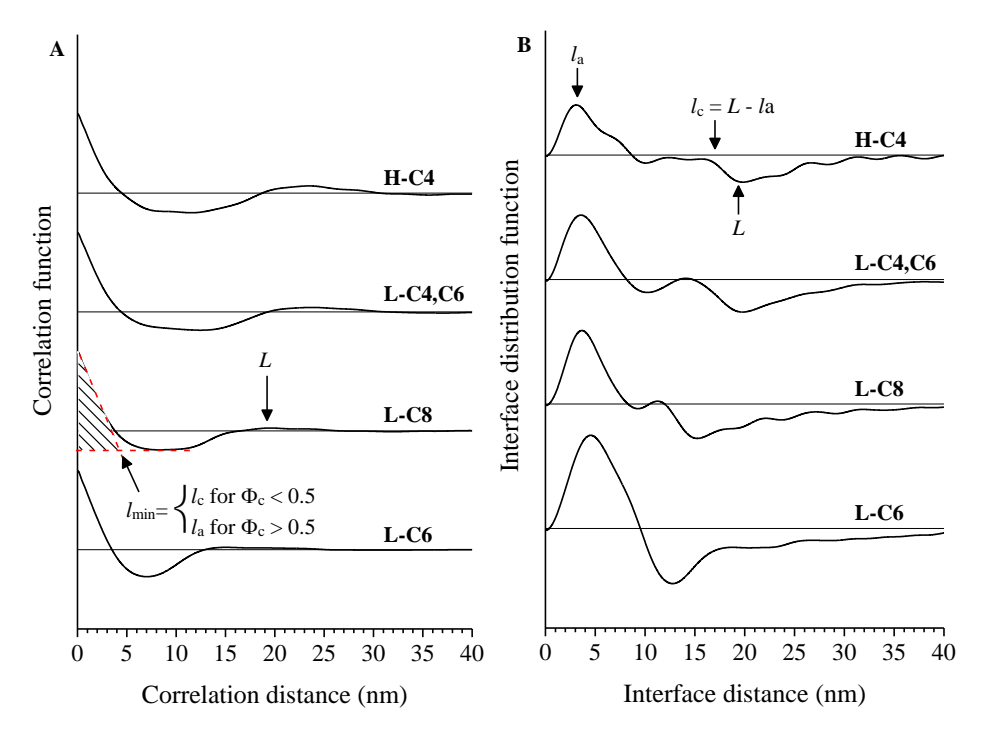


Figure 7 (A) Mono-dimensional self-correlation function of electronic densities fluctuation (Correlation function, CF) and (B) interface distribution function (IDF) calculated from SAXS data (Figure 6) of compression-molded films of the PE samples. The values of the lamellar parameters are evaluated as indicated in A and B. The values of l_{min} in A are in all cases coincident with l_c , as the volume fraction of the crystalline phase Φ_c is always greater than 0.5.

The values of the lamellar parameter extracted from the Bragg's law and the values of crystallinity index estimated through a different technique (BL), CF and IDF are reported in Figure 8 as a function of defect content in the PE samples. In all cases the values of the average long period L and lamellar thickness l_c decrease as the defect content increases. The decrease in l_c is in agreement with the diminution of the melting temperature (see Table 2). The values of the thickness of the amorphous layers l_a , instead are almost constant or exhibit a slight increase as the comonomer content increases. In general, the IDF and BL lamellar parameters are slightly smaller and greater, respectively, than those calculated from CF curves. Finally, the values of linear crystallinity, evaluated by the ratio

 l_c/L , are systematically greater than the crystalline volume fraction Φ_c evaluated from the WAXS crystallinity index, as the presence of the extra-lamellar amorphous phase is completely neglected in the elaboration of SAXS data for the evaluation of the lamellar parameters. These discrepancies reflect deviations of the lamellar stacks from the ideal model, characterized by regular and periodic repetition of the lamellar crystals and amorphous layer along the normal to the basal planes of the crystals, formation of stacks of infinite length and infinite lateral size, uniform thickness of the crystalline and amorphous layers, sharp interfaces at the interlayer boundaries and absence of extra-lamellar amorphous phase, i.e. the amorphous phase is 100% included into the intra-lamellar layers. Deviation from the ideal model reflect the presence of branches, especially for the LLDPE samples, the dispersity of molecular mass, especially for the H-C4 and L-C4,C6 samples (see Table 1) and the crystallization of the samples in noncontrolled (isothermal) conditions.

Table 4 Values of the lamellar periodicity (L) and thickness of amorphous (l_a) and crystalline (l_c) layers of PE samples, deduced from SAXS data (Figure 6) through the calculation of the mono-dimensional self-correlation function of electron density fluctuations CF (Figure 7A) and the interface distribution function IDF (Figure 7B).

| | | (| CF | | IDF | | | |
|---------|--------|---------------------|---------------------|-------------|--------|---------------------|---------------------|----------------------------|
| Sample | L (nm) | l _c (nm) | l _a (nm) | lc/L (-) | L (nm) | l _c (nm) | l _a (nm) | <i>l_c/L</i> (-) |
| Н-С4 | 23.5 | 18.9 | 4.6 | 0.81 | 19.8 | 16.7 | 3.1 | 0.84 |
| L-C4,C6 | 23.9 | 19.3 | 4.6 | 0.81 | 19.8 | 16.2 | 3.6 | 0.82 |
| L-C8 | 19.6 | 15.4 | 4.2 | 0.79 | 15.2 | 11.6 | 3.6 | 0.76 |
| L-C6 | 15.2 | 10.8 | 4.4 | 0.71 | 12.8 | 8.2 | 4.6 | 0.64 |

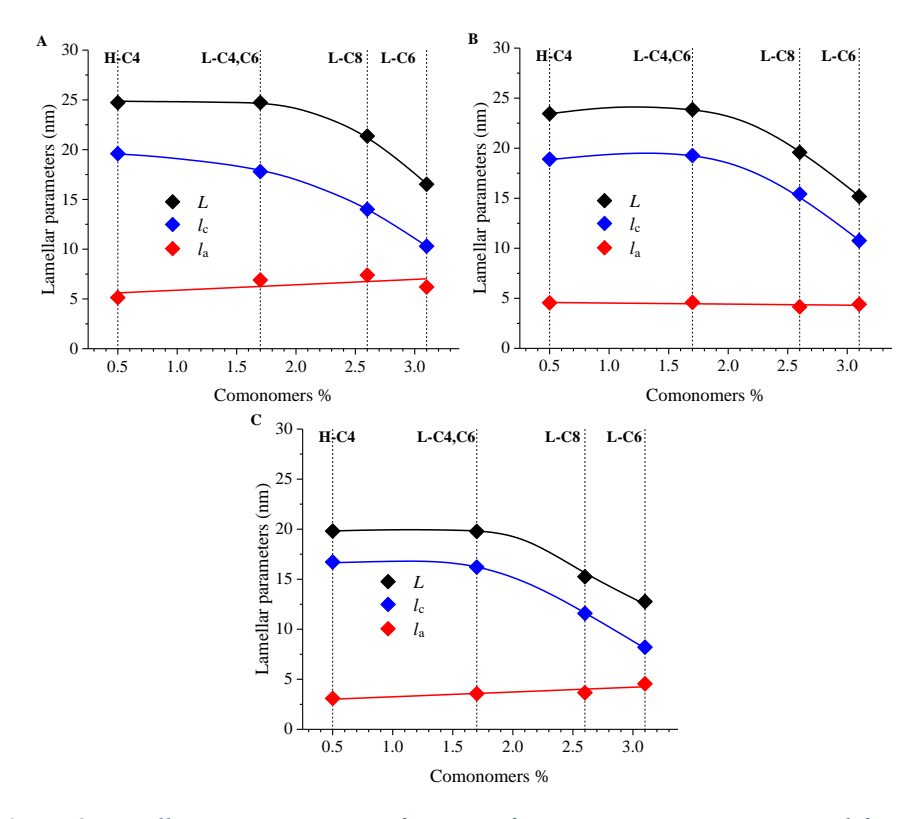


Figure 8 Lamellar parameters, as a function of comonomer content, extracted from A) Direct application of Bragg's law on Lorentz corrected SAXS intensity BL, B) Self-correlation function CF C) Interface distribution function IDF for compression-molded films of the samples. Black diamonds refer to lamellar periodicity L, blue diamonds refer to crystal thickness l_c , and red diamonds refer to the thickness of the amorphous layers l_a .

3.3. Melt memory effect

The results of melt memory effect experiments seem to confirm the differences in structural organization of the samples. The melt memory effect in polymers, occurs when aggregates of polymer segments in the melt retain a more ordered conformation than the conformation achieved in a fully equilibrated random coil state at that temperature. These clusters act as self-seeds, which reduce the free energy barrier for nucleation, thus enhancing the overall crystallization rate upon subsequent cooling. Self-seeds can originate from residual crystalline fragments due to incomplete melting, oriented molecular

segments in melts that did not fully relax, chains with different entangled topologies compared to the equilibrated random coil or crystalline sequences that remain near to each other in random copolymers containing non-crystallizable comonomers^{5–8}. For homopolymers, the melt memory effect is typically observed only at temperatures well below the equilibrium melting temperature $(T_{\rm m}^{~0})^9$, while when the melt is kept at temperatures above (T_m^0) for an adequate time, the subsequent crystallization kinetic become reproducible¹⁰. Conversely, random ethylene–1-butene copolymers exhibit a strong melt memory even at temperatures above their equilibrium melting point. For these copolymers, the crystallization temperature (T_c) increases as the initial melt temperature decreases, by the effect of on an enhanced homogeneous nucleation density¹¹. This phenomenon is attributable to the self-nucleation effect, where the self-nuclei are clusters of ethylene sequence that remain in neat to each other in the melt as a memory of the initial crystallizable sequence partitioning. This behaviour is attributed to the copolymer melt topology formed during crystallization or a weakly segregated melt state. The entangled structure that develops creates topological constraints 12 (e.g., ties, loops, knots) in the regions between crystals, which hinder the rapid homogenization of crystalline sequences in the melt.

As an example, the results of melt memory experiments, conducted following the procedure described in Chapter 2 for the least and most defective PE samples, i.e. H-C4 and L-C6, are presented in Figure 9. The maximum temperature reached in the melt $T_{\rm max}$ is plotted against the crystallization temperature $T_{\rm c}$ recorded from the subsequent cooling exotherm peak.

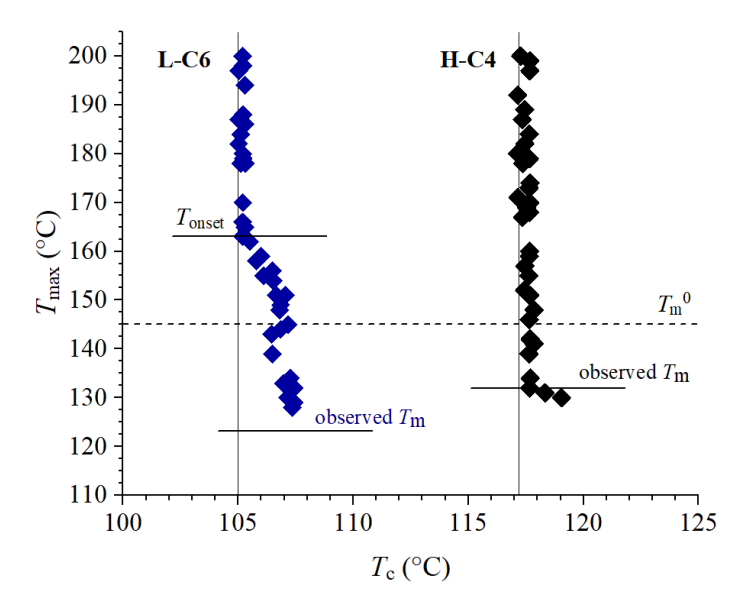


Figure 9 Maximum temperature reached in the melt (T_{max}) vs. crystallization temperature (T_c) for the samples H-C4 and L-C6. The dashed line corresponds to the equilibrium melting point of PE T_m^0 =145°C. The melting temperature of the samples measured in a standard DSC scan (Figure 2C) are indicated. T_{onset} corresponds to the maximum temperature achieved in the melt marking the onset of the T_c shift toward high temperatures.

The sample H-C4 does not show any melt memory effect within the selected conditions of the adopted thermal protocol, in which the permanence time at each $T_{\rm max}$ is fixed to 5 min (see Chapter 2). This is indicated by the independence of the measured $T_{\rm c}$ from the initial melt temperature ($T_{\rm max}$). $T_{\rm c}$ start to shift only when $T_{\rm max}$ is below the melting point $T_{\rm m}$ of the sample. Instead, for the sample L-C6 a distinct shift of $T_{\rm c}$ toward high temperatures for $T_{\rm max}$ lower than 163°C occur. The value of $T_{\rm max}$ marking the onset of the $T_{\rm c}$ shift, defined as $T_{\rm onset}$, occurs well above the equilibrium melting temperature $T_{\rm m}{}^0$ (=145 °C) of PE, that is at a temperature 18 °C (= $T_{\rm onset}{}^ T_{\rm m}{}^0$) above $T_{\rm m}{}^0$. The maximum shift of $T_{\rm c}$ for $T_{\rm max}$ < $T_{\rm onset}$ is ~2°C. Mamun et al¹³ have investigated melt memory effect for metallocene-made random ethylene–1-hexene copolymers with monomodal molecular mass distribution. They found that samples with 1-hexene units content comprised in

between 1.2 and 2.5 mol% show clear melt memory effect at temperatures above $T_{\rm m}^0$. They suggest that some crystalline sequences are unable to diffuse back to the initial randomized copolymer melt, even at temperature well above $T_{\rm m}^0$, due to a constrained chain topology in the intercrystalline region. This is the case of the sample L-C6, for which the branches not only hinder the formation of a regular crystalline structure during cooling but also act as constraints that remain even after melting. Comonomeric units help in creating a constrained conformation that guides the reorganization of the chains during cooling. On the contrary, the sample H-C4 show high crystallinity and thick lamellae, and no melt memory effect due to its highly linear structure and low branching (comonomer content < 1 mol%). When H-C4 is melted above its melting temperature, all the polymer chains can fully reach random coil conformations close to an equilibrium, as there are no branches or other residual structures acting as constraints.

Analysis of the melt memory effect for the samples L-C4,C6 and L-C8 indicate that they do not show any melt memory effect, even at temperatures below the equilibrium melting point $T_{\rm m}^{0}$ (see Appendix A1).

3.4. Mechanical, structural and morphological characterization as a function of cooling conditions

To investigate the effect of different cooling conditions on morphology at lamellar and micrometric scale and on mechanical properties, compression-molded films of the samples have been prepared by cooling the melt in six different ways:

- a) slow cooling (about 20 degrees per minute) from $T_{\text{max}} = 200^{\circ}\text{C}$, after an isotherm of the melt at T_{max} for $t_{\text{max}} = 10$ min;
- b) slow cooling (about 20 degrees per minute) from $T_{\text{max}} = 200^{\circ}\text{C}$, after an isotherm of the melt at T_{max} for $t_{\text{max}} = 30$ min;

- c) fast cooling (quenching) from 200°C, after an isotherm of the melt at T_{max} for $t_{\text{max}} = 10$ min;
- d) fast cooling (quenching) from 200°C, after an isotherm of the melt at T_{max} for $t_{\text{max}} = 30$ min;
- e) fast cooling (quenching) from 150 °C, after an isotherm of the melt at T_{max} for $t_{\text{max}} = 10$ min;
- f) fast cooling (quenching) from 150 °C, after an isotherm of the melt at T_{max} for $t_{\text{max}} = 30$ min.

The so obtained samples were subject to mechanical, structural and morphological characterization.

Analysis of mechanical properties

The engineering stress-strain curves of the PE films are reported in Figure A1 and A2 of Appendix A2. The values of the mechanical parameters, that is of Young's Modulus (E), strain (ε_y) and stress (σ_y) at yielding, and strain (ε_b) and stress (σ_y) at break are reported as a function of defect content in Figure 10 and A3 of Appendix A2, and in Table A1 – A8 of Appendix A2.

All samples show yielding behaviour, high ductility, strain hardening at high deformations and values of stress at any strain that decrease as the comonomer content, and hence the crystallinity degree, decreases, regardless of preparation conditions of the films.

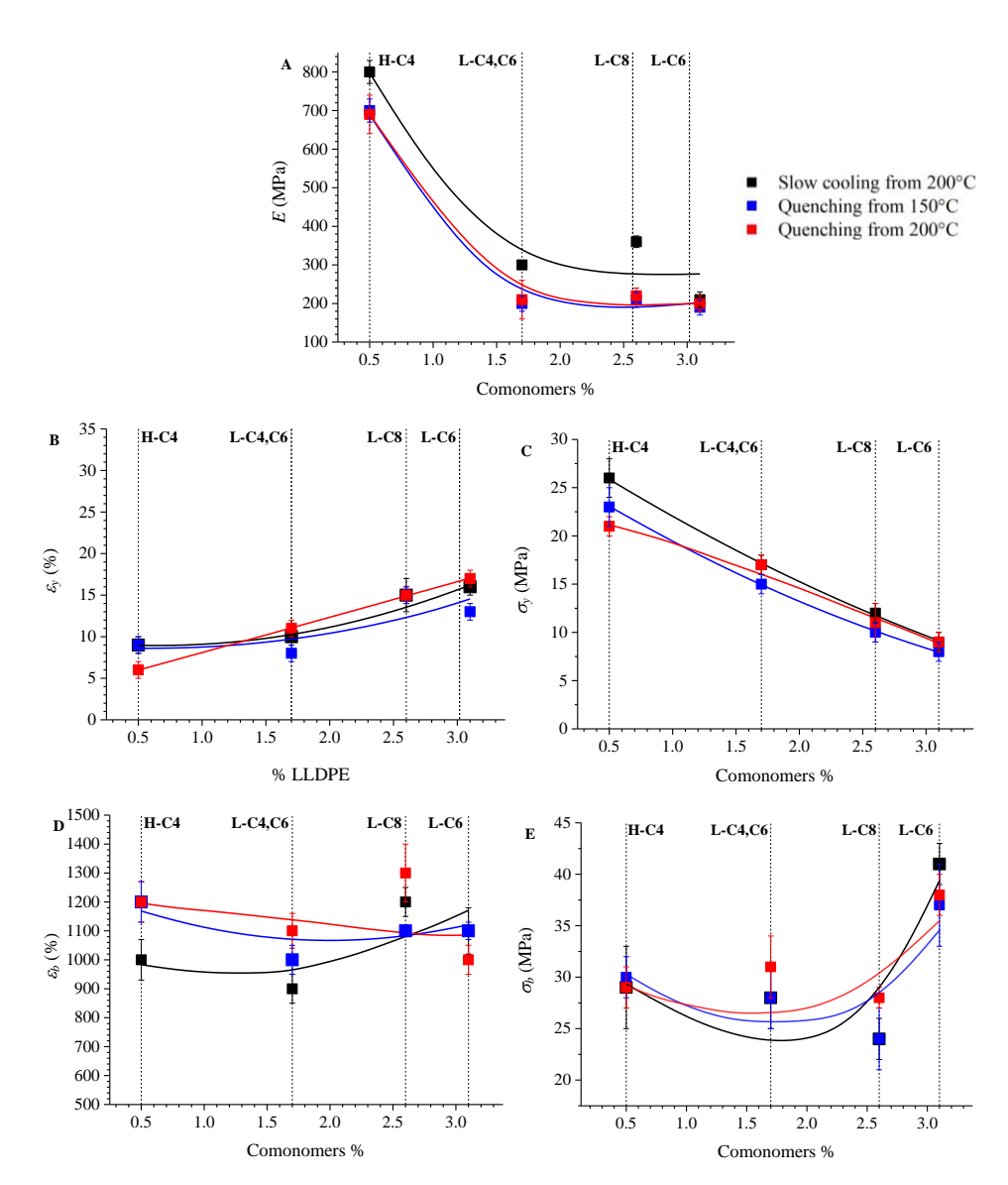


Figure 10 Values of the mechanical parameters as a function of comonomer content extracted from stress-strain curves of compression-molded films of the samples obtained through slow cooling from 200°C (black squares), quenching from 150°C (blue squares) and quenching from 200°C (red squares), after 10 min isotherm at the indicated temperatures. Young's Modulus (E, A), strain (ε_y, B) and stress (σ_y, C) at yielding, strain (ε_b, D) and stress (σ_b, E) at break.

For all the samples, the Young's modulus values of the compression-molded films obtained by slow cooling the melt are greater than those of the quenched film, due to the more ordered and more crystalline structures that result from slow cooling. Cooling conditions have only a minor effect on the values of stress and strain at yielding. Generally, the values of σ_v (Figure 10C) tend to decrease, while the values of ε_v (Figure 10B) tend to increase, as the comonomer content increases, in agreement with the parallel decrease of crystallinity. These trends can be interpreted by considering that at the yield point, the effect of the physical constraints provided by the crystalline regions prevail over other contributions, so that, as the degree of crystallinity decreases, the mechanical resistance to plastic deformation decreases and the deformation at yield point shifts toward higher deformation values. As already stated, all the samples show high ductility, with values of deformation at break comprised in between 900% and 1300% (Figure A1, A2, and A3D, Table A1-A8 of Appendix A2, and Figure 10D) and high values of stress at break due to strain hardening at high deformations. The less defective samples H-C4 and L-C4,C6, present values of deformation at break spanning a wide range, whereas the defective samples L-C6 and L-C8 show almost similar mechanical behaviour, regardless of the conditions adopted for preparation of the films.

The differences in the mechanical behaviour of PE samples are attributable to their chain microstructure, specifically to the complex balance between molecular weight distribution, dispersity, and comonomer content. The comonomer content, in turn, is linked to crystallinity, and to the morphology that develops upon cooling. Differences in the preparation of the films have minor effect. In particular, the low defective sample H-C4 shows the highest values of Young's modulus ($E \sim 700-800$ MPa), regardless of the adopted conditions for the preparation of the films, due to its higher crystallinity. As the comonomer content increases, the values of the Young's modulus E decrease (Figure 10A and A3 of Appendix A2).

Exception occurs for the sample L-C8 that, despite of his higher comonomer content and slightly lower crystallinity, shows an E modulus greater than that of the sample L-C4,C6. This can be related to microstructural differences (Table 1). The sample L-C8, indeed, is characterized by a molecular mass ($M_n \approx 26$ kDa), which is higher than that of the sample L-C4,C6 ($M_n \approx 9$ kDa), indicating that, on average, the chains are longer and thus experience a greater number of entanglements and/or tie chains connecting adjacent lamellar crystals, able of acting as physical cross-links of the amorphous network. The consequent increase of cross-link density/chain, in turn, induces an increase of rigidity. In addition, the sample L-C4,C6 exhibits higher dispersity ($\Theta \approx 19$) than that of the sample L-C8 $(\theta \approx 4)$, entailing that the presence of a non-negligible fraction of short chains results in an increase of the flexibility of the polymer chains due to dilution effect (see Figure 1). This means that the values of the Young's modulus depend not only on the degree of crystallinity, related to comonomer content, but also on other microstructural features such as the molecular mass, dispersity and entanglement density.

These results suggest that at the maximum temperature achieved in the melt, i.e. $T_{\rm max}=150~{\rm or}~200~{\rm °C}$, the annealing times $t_{\rm max}$ at $T_{\rm max}$ of 30 or even 10 min are sufficiently long to allow achieving a state of the melt that leads, upon cooling, to creation of an entangled network able to efficiently transmit the stress. In particular, for the sample L-C6, which shows melt memory effect for $T_{\rm max}$ below $163~{\rm °C}$ adopting an annealing time of 5 min at those temperatures, it is found that 10 min of annealing at $T_{\rm max}=150~{\rm °C}$ is good enough to bring the melt in a state which is equivalent to the state achieved by the sample when it is cooled form the melt after 30 min annealing at $T_{\rm max}=200~{\rm °C}$. The determination of the time scale of these re-arrangements is out of the scope of the present investigation, but the obtained results help to set up the basis for understanding the tendency of PE melts to rearrange on cooling after suitable heat treatments.

SAXS analysis

In this paragraph, the values of the lamellar parameters evaluated through SAXS analysis for compression molded films of the PE samples obtained from by slow cooling the melt from $T_{\rm max} = 200$ °C, and annealed at $T_{\rm max}$ for $t_{\rm max} = 10$ min already shown before, are compared with those relative to films prepared by quenching the melt from $T_{\rm max} = 200$ and 150 °C, after annealing the samples at $T_{\rm max}$ for $t_{\rm max} = 10$ min. These data are also compared with the lamellar parameters achieved by the PE in films prepared by cooling the melt at the same rates from $T_{\rm max} = 200$ and 150 °C, but heat treated at those $T_{\rm max}$ for $t_{\rm max} = 30$ min.

The SAXS profiles of the compression-molded films used for mechanical analysis of the PE samples are shown in Figure A1A,B-A4A,B of Appendix A3. The correlation function (CF) and the interface distribution function (IDF) curves are also shown in Figure A1C,D-A4C,D of Appendix A3. All the samples show a strong correlation peak at $q < 0.5 \text{ nm}^{-1}$. A faint second order correlation peak is also present at $q > 0.5 \text{ nm}^{-1}$, especially for the less defective samples H-C4 and L-C4,C6 (Figure A1A,B, A2A,B of Appending A3). The value of the lamellar parameters extracted from SAXS data are shown in Figure 11-13 and collected in Table 5-7, and A1-A4 of Appendix A3.

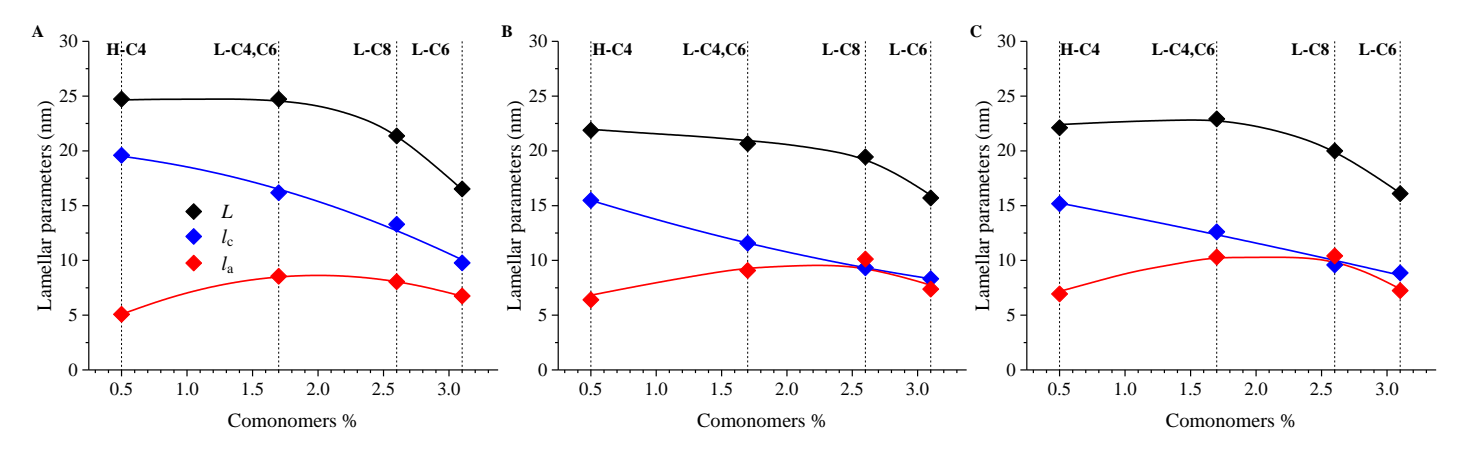


Figure 11 Lamellar parameters, as a function of comonomer content, deduced from direct application of Bragg's Law (BL) on Lorentz corrected SAXS intensity, for compression-molded films of the PE samples obtained by A) Slow cooling from $T_{max} = 200$ °C, B) Quenching from $T_{max} = 150$ °C, and C) Quenching from $T_{max} = 200$ °C, after heat treatment at T_{max} for $t_{max} = 10$ min. Black diamonds: lamellar periodicity L; blue diamonds: crystal thickness l_c ; red diamonds: thickness of amorphous layers l_a .

Table 5 Values of the lamellar periodicity (L) and thickness of amorphous (l_a) and crystalline (l_c) layers of lamellar stacks, deduced from SAXS data through direct application of Bragg's law (BL), for compression-molded films of the PE samples obtained by Slow cooling from $T_{max} = 200^{\circ}$ C and Quenching from $T_{max} = 150$ and 200° C, after heat treatment at T_{max} for $t_{max} = 10$ min.

| | Slow c | cooling from | 200°C | Que | nching from 1 | 50°C | Quench | ing from 2 | 200°C |
|---------|--------|----------------|-------|------|----------------|------------------|--------|------------|-----------------------|
| Sample | L | l _c | la | L | l _c | l_{a} | L | le | <i>l</i> _a |
| | (nm) | (nm) | (nm) | (nm) | (nm) | (nm) | (nm) | (nm) | (nm) |
| H-C4 | 24.7 | 19.6 | 5.1 | 21.9 | 15.5 | 6.4 | 22.1 | 15.2 | 6.9 |
| L-C4,C6 | 24.7 | 16.2 | 8.5 | 20.7 | 11.6 | 9.1 | 22.9 | 12.6 | 10.3 |
| L-C8 | 21.4 | 13.3 | 8.1 | 19.4 | 9.3 | 10.1 | 20.0 | 9.6 | 10.4 |
| L-C6 | 16.5 | 9.8 | 6.8 | 15.7 | 8.3 | 7.4 | 16.1 | 8.9 | 7.2 |

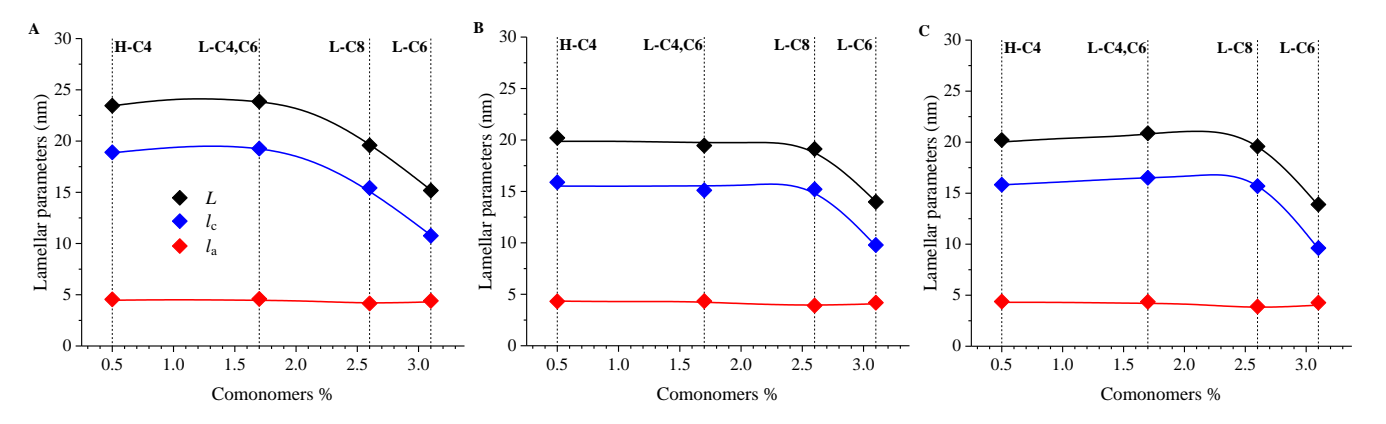


Figure 12 Lamellar parameters, as a function of comonomer content, deduced from SAXS data analysis through the calculation of the mono-dimensional self-correlation function of electron density fluctuations (correlation function, CF) for compression-molded films of the PE samples obtained by A) Slow cooling from $T_{max} = 200^{\circ}$ C, B) Quenching from $T_{max} = 150^{\circ}$ C, and C) Quenching from $T_{max} = 200^{\circ}$ C, after heat treatment at T_{max} for $t_{max} = 10$ min. Black diamonds: lamellar periodicity L; blue diamonds: crystal thickness l_c ; red diamonds: thickness of amorphous layers l_a .

Table 6 Values of the lamellar periodicity (L) and thickness of amorphous (l_a) and crystalline (l_c) layers of lamellar stacks, deduced from SAXS data through the calculation of the mono-dimensional self-correlation function of electron density fluctuations (correlation function, CF), for compression-molded films of the PE samples obtained by Slow cooling from $T_{max} = 200$ °C and Quenching from $T_{max} = 150$ and 200°C, after heat treatment at T_{max} for $t_{max} = 10$ min.

| Slow cooling from 200°C | | | Quenching from 150°C | | | Quenching from 200°C | | | |
|-------------------------|-------|----------------|----------------------|------|----------------|----------------------|------|----------------|-------------|
| Sample | L | l _c | $l_{\rm a}$ | L | l _c | l_{a} | L | l _c | $l_{\rm a}$ |
| | (nm) | (nm) | (nm) | (nm) | (nm) | (nm) | (nm) | (nm) | (nm) |
| H-C4 | 23.45 | 18.9 | 4.6 | 20.2 | 15.9 | 4.3 | 20.2 | 15.8 | 4.4 |
| L-C4,C6 | 23.86 | 19.27 | 4.6 | 19.5 | 15.1 | 4.3 | 20.9 | 16.5 | 4.4 |
| L-C8 | 19.58 | 15.43 | 4.1 | 19.1 | 15.2 | 3.9 | 19.8 | 15.7 | 3.9 |
| L-C6 | 15.17 | 10.76 | 4.4 | 14.0 | 9.8 | 4.2 | 13.9 | 9.6 | 4.3 |

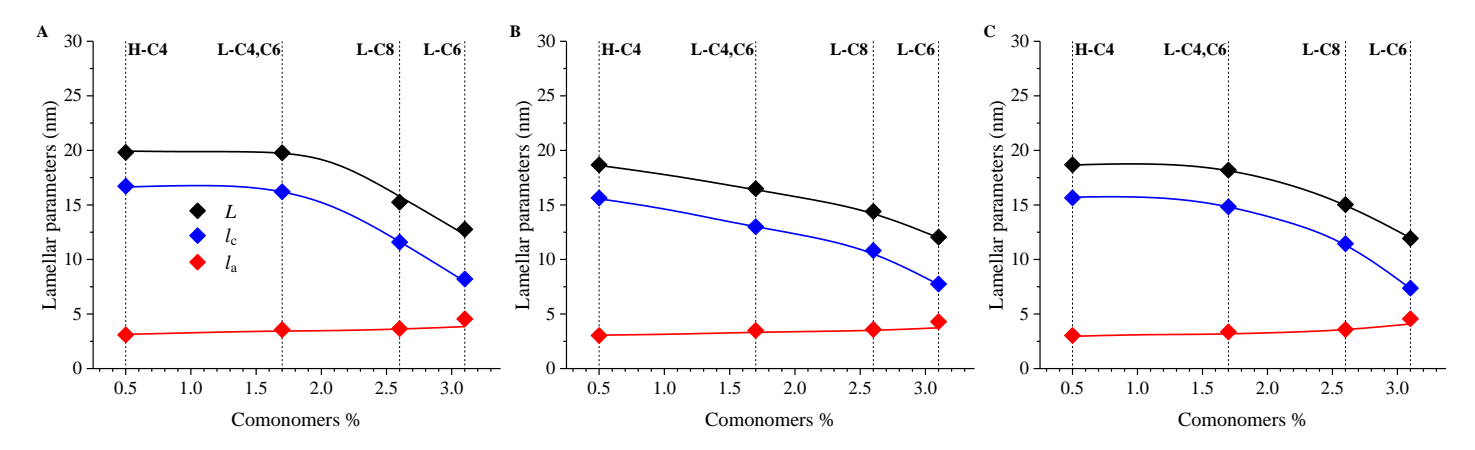


Figure 13 Lamellar parameters, as a function of comonomer content, deduced from SAXS data) through the calculation of the interface distribution function (IDF) for compression-molded of the PE samples obtained by A) Slow cooling from $T_{max} = 200$ °C, B) Quenching from $T_{max} = 150$ °C, and C) Quenching from $T_{max} = 200$ °C, after heat treatment at T_{max} for $t_{max} = 10$ min. Black diamonds: lamellar periodicity L; blue diamonds: crystal thickness l_c ; red diamonds: thickness of amorphous layers l_a .

Table 7 Values of the lamellar periodicity (L) and thickness of amorphous (l_a) and crystalline (l_c) layers of lamellar stacks, deduced from SAXS data through the calculation of interface distribution function IDF, for compression-molded films of the PE samples obtained by Slow cooling from $T_{max} = 200^{\circ}\text{C}$ and Quenching from $T_{max} = 150$ and 200°C , after heat treatment at T_{max} for $t_{max} = 10$ min.

| | Slow cooling from 200°C | | | Quenching from 150°C | | | Quenching from 200°C | | |
|---------|-------------------------|------------|------|----------------------|----------------|------------------|----------------------|-------|------|
| Sample | L | <i>l</i> c | la | L | l _c | l_{a} | L | lc | la |
| | (nm) | (nm) | (nm) | (nm) | (nm) | (nm) | (nm) | (nm) | (nm) |
| H-C4 | 19.81 | 16.72 | 3.09 | 18.67 | 15.64 | 3.03 | 18.68 | 15.65 | 3.03 |
| L-C4,C6 | 19.78 | 16.21 | 3.57 | 16.49 | 13 | 3.49 | 18.19 | 14.83 | 3.36 |
| L-C8 | 15.25 | 11.59 | 3.66 | 14.4 | 10.82 | 3.58 | 15.03 | 11.45 | 3.58 |
| L-C6 | 12.76 | 8.21 | 4.55 | 12.05 | 7.75 | 4.3 | 11.93 | 7.37 | 4.56 |

The values of the lamellar parameters calculated from the Bragg's law BL and the correlation function CF are similar, while those evaluated from the interface distribution function IDF are lower (Table 4,5,6, A1-A4 of Appendix A3). The low defective samples H-C4 and L-C4,C6 show the highest values of lamellar periodicity L, and l_c regardless of the adopted preparation conditions of the films. In particular, the values of L and l_c extracted from BL and CF analysis are about 23-25 and 19-20 nm, respectively, after slow cooling, while they decrease to 20-22 and 15-16 nm, respectively, by effect of quenching; similarly, those extracted from IDF analysis are ≈ 20 nm and 15-16 nm, respectively, after slow cooling, and 16-19 and 13-16 nm, respectively, by quenching. The decrease in L values by effect of fast cooling rate is essentially due to the decrease of lamellar thickness, as the thickness of the amorphous layers l_a are almost constant, regardless of the cooling rate. In particular, the values of l_a evaluated from CF and IDF analysis are around 3-5 nm, whereas those extracted from BL analysis are almost doubled. For the defective samples L-C8 and L-C6 the discrepancy among the values of the lamellar parameters evaluated through the different methods (BL, CF and IDF) is more pronounced, because of the major deviations of the lamellar stacks from the ideal model. In particular, regardless of preparation conditions of the films, for the sample L-C8 the values of long spacing evaluated from BL and CF analyses are around 20-21 nm, and decreases to 14-15 nm using the IDF analysis, whereas the values of l_c extracted from BL, CF and IDF analysis are 9-13, 15-16 and \approx 11 nm, respectively. As for the sample L-C6, the values of long spacing L and lamellar thickness l_c evaluated from BL are 16 and 8-9 nm, respectively, those evaluated from CF are 14-15 and 10-11 nm, respectively, while those evaluated from IDF are 12-13 and 7-8, respectively. Similar to the low defective samples H-C4 and L-C4,C6, also the defective samples L-C8 and L-C6 show values of the thickness of the amorphous layers evaluated from CF and IDF analysis around 4-5 nm, and values almost doubled when extracted from BL. In all cases, the values of linear

crystallinity l_c/L values result greater than the crystalline volume fraction Φ_c determined from the WAXS crystalline index.

In summary, the greatest values of lamellar thickness are achieved for the PE samples crystallized by slow cooling the melt from 200°C. For all samples, the melt kept at 200 °C reaches full relaxation already after $t_{\rm max}$ =10 min, as there are no significant differences with respect to the values of the lamellar parameter achieved in slow cooling conditions after $t_{\rm max}$ = 30 min. As for the films obtained by fast cooling (quenching) from the melt kept at 150 or 200 °C the values of lamellar parameters achieved after 10 or 30 min annealing are similar, but more scattered than those achieved by slow cooling.

Polarized optical microscopy (POM) analysis

The morphology achieved by the PE samples at micrometric length scale due to the different chain microstructure has been investigated using polarized light optical microscopy (POM) (Figure 14-17). The samples have been cooled from the melt under the same cooling conditions adopted for the preparation of the films subjected to mechanical testing and SAXS analysis, that is by slow and fast (quenching) cooling the melt from $T_{\text{max}} = 200$ or 150 °C after annealing at T_{max} for 10 min.

For the specimens slowly cooled from 200 °C (Figure 14A-17A), the low defective sample H-C4 exhibits a morphology composed of small spherulites (Figure 14A). The formation of small spherulites is generally indicative of a high nucleation density. The adopted cooling conditions, indeed, favour formation of numerous nuclei, preventing individual spherulites from growing to a large size. This results in a high density of lamellar aggregates covering the whole POM observation window. When spherulites are small, the lamellae within them have small lateral size and achieve a tight packing and good cohesion. The small lateral size of lamellar aggregates also induces an increase of the inner surface area at

amorphous/crystalline interfaces, creating a well-interconnected network. The formation of a well-interconnected and compact network, along with the high overall crystallinity value, contributes to the high rigidity and mechanical strength of the slowly cooled sample H-C4, and accounts for the high value of the Young's modulus. In contrast, in samples with large spherulites, the distance between lamellar stacks within each spherulite is often large and less uniform, resulting in decrease of structural cohesion. Larger spherulites also tend to have less defined boundaries, which can lead to the presence of extra-lamellar (inter and intraspherulites) amorphous regions and, as a consequence, to a decrease of mechanical strength. This is the case of the samples L-C4,C6 and L-C8, which form well-defined banded spherulites (Figure 15A,16A), and the sample L-C6 (Figure 17A), which instead forms non-banded spherulites. In particular, for the samples L-C8 and L-C6, the spherulites are separated by lamellar sheaves bridging adjacent spherulites, able to contribute to the good rigidity of these samples. This aspect can explain why, despite a higher comonomer content and a lower crystallinity, the sample L-C8 shows a higher Young's modulus compared the sample L-C4,C6, with a pure spherulitic morphology.

Quenching significantly affects the morphology of the samples as the reduced time available for crystallization leads to the formation of more disordered lamellar aggregates compared to slow cooling. For all the samples, upon quenching (Figure 14B,C, 15B,C, 16B,C and 17B,C) the spherulites superstructures are replaced by crossed lamellar sheaves, leading to a less crystalline but more uniform morphology.

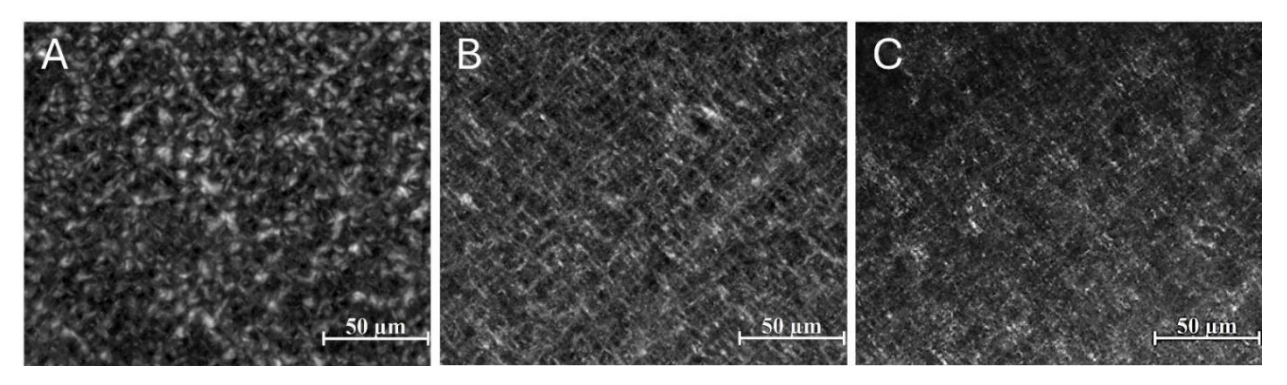


Figure 14 Polarized micrographs (magnification 40x) of the compression-molded films of sample H-C4, obtained in 3 different cooling conditions: A) Slow cooling from $T_{max} = 200$ °C; B) Quenching from $T_{max} = 150$ °C; C) Quenching from $T_{max} = 200$ °C. In all cases the cooling is carried out after annealing the samples at T_{max} for $t_{max} = 10$ min.

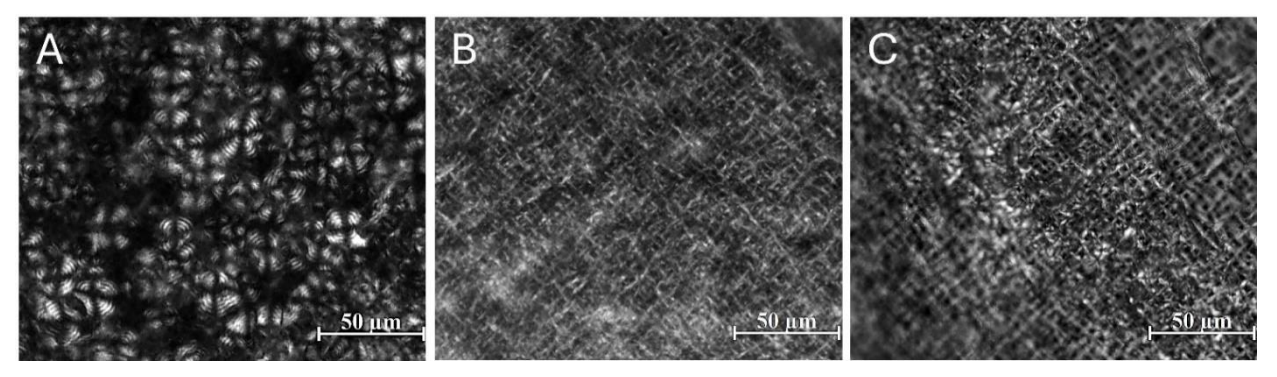


Figure 15 Polarized micrographs (magnification 40x) of the compression-molded films of sample L-C4,C6, obtained in 3 different cooling conditions: A) Slow cooling from $T_{max} = 200$ °C; B) Quenching from $T_{max} = 150$ °C; C) Quenching from $T_{max} = 200$ °C. In all cases the cooling is carried out after annealing the samples at T_{max} for $t_{max} = 10$ min.

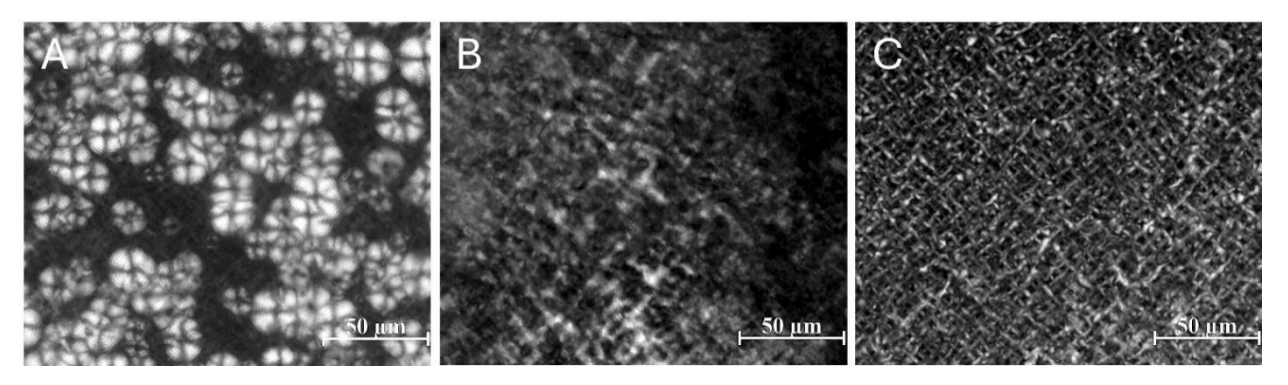


Figure 16 Polarized micrographs (magnification 40x) of the compression-molded films of sample L-C8, obtained in 3 different cooling conditions: A) Slow cooling from $T_{max} = 200$ °C; B) Quenching from $T_{max} = 150$ °C; C) Quenching from $T_{max} = 200$ °C. In all cases the cooling is carried out after annealing the samples at T_{max} for $t_{max} = 10$ min.

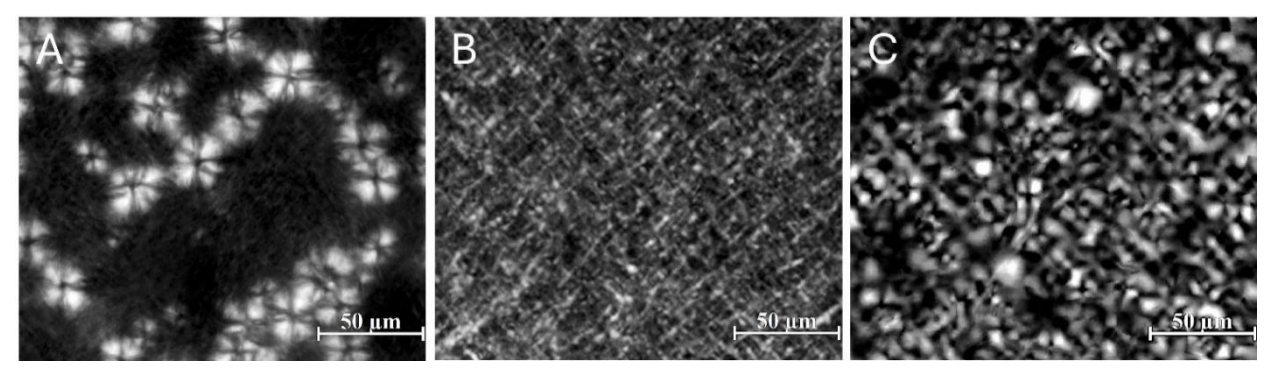


Figure 17 Polarized micrographs (magnification 40x) of the compression-molded films of sample L-C6, obtained in 3 different cooling conditions: A) Slow cooling from $T_{max} = 200$ °C; B) Quenching from $T_{max} = 150$ °C; C) Quenching from $T_{max} = 200$ °C. In all cases the cooling is carried out after annealing the samples at T_{max} for $t_{max} = 10$ min.

The spherulite radius distribution extracted from the POM images of the slowly cooled samples L-C4,C6, L-C8 and L-C6 of Figure 15A-17A, is shown in Figure 18. The size of spherulites, formed through heterogeneous nucleation in the melt, is quite similar for all the LLDPEs. The spherulite radius distribution is centred around 9 μ m for the samples L-C4,C6 and L-C8, and around 11 μ m for the sample L-C6.

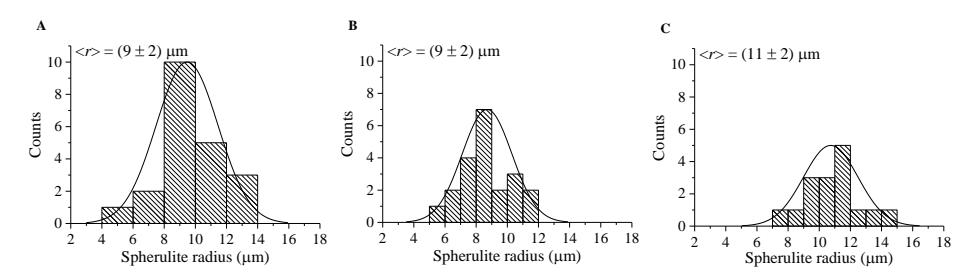


Figure 18 Average distribution of spherulite radii (Figure 15A, 16A, 17A) detected in polarized micrographs of compression-molded films obtained by slow cooling the melt from $T_{max} = 200$ °C, after annealing at T_{max} for $t_{max} = 10$ min, of the samples A) L-C4,C6 B) L-C8 C) L-C6.

3.5. Characterization of blends of selected grades

Samples H-C4 and L-C8 have been selected for blending, based on rheological measurements performed at UNISA. In practice the LLDPE sample selected for blending with the HDPE component were the grade with a low dispersity index Đ and melt viscosity that matches the melt viscosity of the sample H-C4 in a wide temperature range. Blends at 5 different compositions have been prepared, that is the LLDPE-HDPE blends with 20 (20L-80H), 40 (40L-60H), 50 (50L-50H), 60 (60L-40H) and 80 wt% (80L-20H) of LDPE. They have been prepared at UNISA by melt-extrusion, in the shape of pellets.

The DSC curves of the so-obtained pellets are compared with those of the pure components in Figure 19. The values of the temperatures of first melting $T_{\rm ml}$, crystallization $T_{\rm c}$ and second melting $T_{\rm m2}$ and corresponding enthalpies ($\Delta H_{\rm ml}$,

 ΔH_c , ΔH_{m2}) are collected in Table 8. The values of T_{m1} , T_c and T_{m2} are also reported in Figure 20 as a function of blend composition.

All blends show a single melting and crystallization peak, at temperatures comprised in between those of the pure components, equal to ≈ 133 °C for HDPE and ≈ 129 °C, for LLDPE. It is worth noting that, except for the blend 60L-40H crystallizing at ≈ 113 °C, the crystallization temperatures T_c of the blends are closer to that of neat H-C4 (≈ 117 °C) rather than to that of neat L-C8 (≈ 111 °C), regardless of composition (Figure 20). This suggests that the presence of H-C4, with less defective and hence more linear chains, induces an acceleration of the crystallization kinetics of the L-C8 component.

The X-ray powder diffraction profiles of the pellets of the blends and of neat components LLDPE and HDPE are reported in Figure 21A. All the samples crystallize in the orthorhombic form of PE as indicated by the presence of 110 and 200 reflections at $2\theta \approx 21$ and 24° , typical of this form.

The values of the crystallinity index of the blends evaluated from DSC scans x_c (DSC) and WAXS profiles x_c (WAXS) are compared in Figure 21B. They are in all cases greater than 44%, and increase as the HDPE content increases, the values of x_c (WAXS) being systematically greater than the values of x_c (DSC).

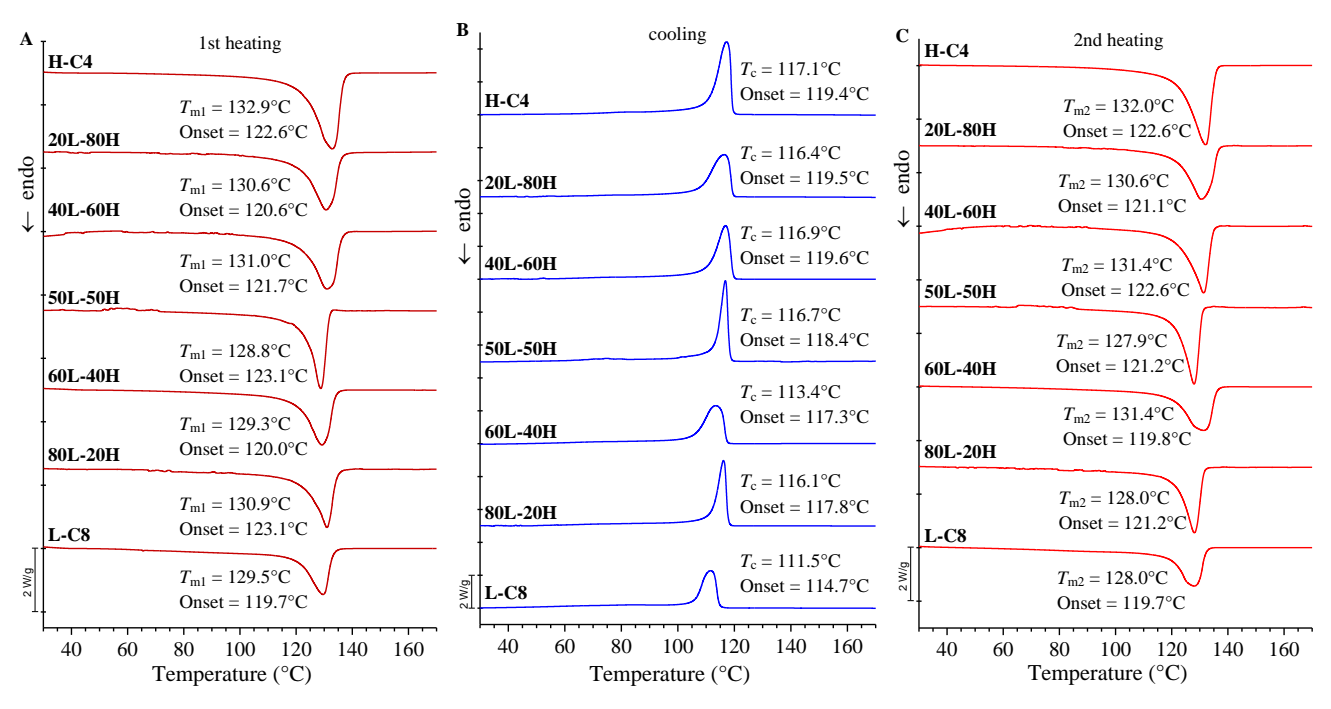


Figure 19 DSC scans recorded during the 1^{st} heating (A), cooling (B) and 2^{nd} heating (C) scans, at 10° C/min for of pellets of the LLDPE-HDPE blends at the indicated compositions, and of neat components. The values of T_{ml} , T_c and T_{m2} and relative onset temperatures are indicated.

Table 8 First (T_{m1}) and second melting temperatures (T_{m2}) , crystallization temperatures (T_c) , corresponding enthalpies $(\Delta H_{m1}, \Delta H_{m2}, \text{ and } \Delta H_c)$ and crystallinity index evaluated from DSC scans and WAXS profiles of pellets of the LLDPE-HDPE blends.

| Sample | <i>T</i> _{m1} (°C) | <i>T</i> _c (°C) | <i>T</i> _{m2} (°C) | ΔH_{m1} (J/G) | ΔH_c (J/G) | ΔH_{m2} (J/G) | <i>x_c</i> DSC (%) | x _c WAXS (%) |
|---------|-----------------------------|----------------------------|-----------------------------|-----------------------|--------------------|-----------------------|------------------------------|-------------------------|
| Н-С4 | 132.9 | 117.1 | 132.0 | -186.2 | 214.7 | -207.2 | 70 | 71 |
| 20L-80H | 130.6 | 116.4 | 130.6 | -146.9 | 166.4 | -165.6 | 56 | 66 |
| 40L-60H | 131.0 | 116.9 | 131.4 | -151.0 | 169.8 | -161.4 | 55 | 65 |
| 50L-50H | 128.8 | 116.7 | 127.9 | -139.8 | 162.9 | -162.1 | 55 | 61 |
| 60L-40H | 129.3 | 113.4 | 131.3 | -138.3 | 154.6 | -156.7 | 53 | 59 |
| 80L-20H | 130.9 | 116.1 | 128.0 | -136.2 | 147.4 | -154.3 | 52 | 57 |
| L-C8 | 129.5 | 111.5 | 128.0 | -123.4 | 144.8 | -129.9 | 44 | 61 |

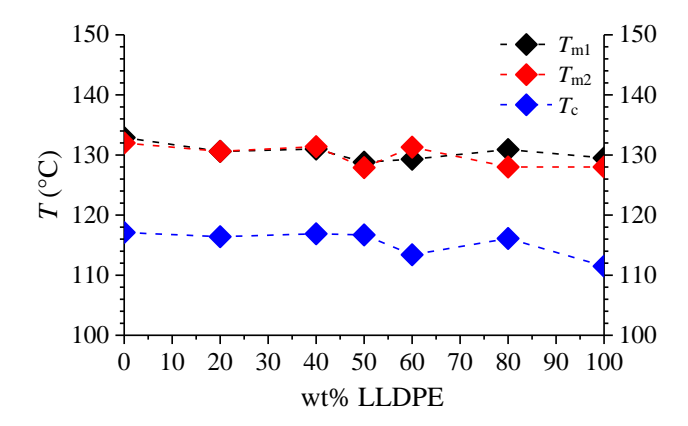


Figure 20 Thermal parameters T_{m1} , T_c and T_{m2} of blends and pure components, as a function of LLDPE content.

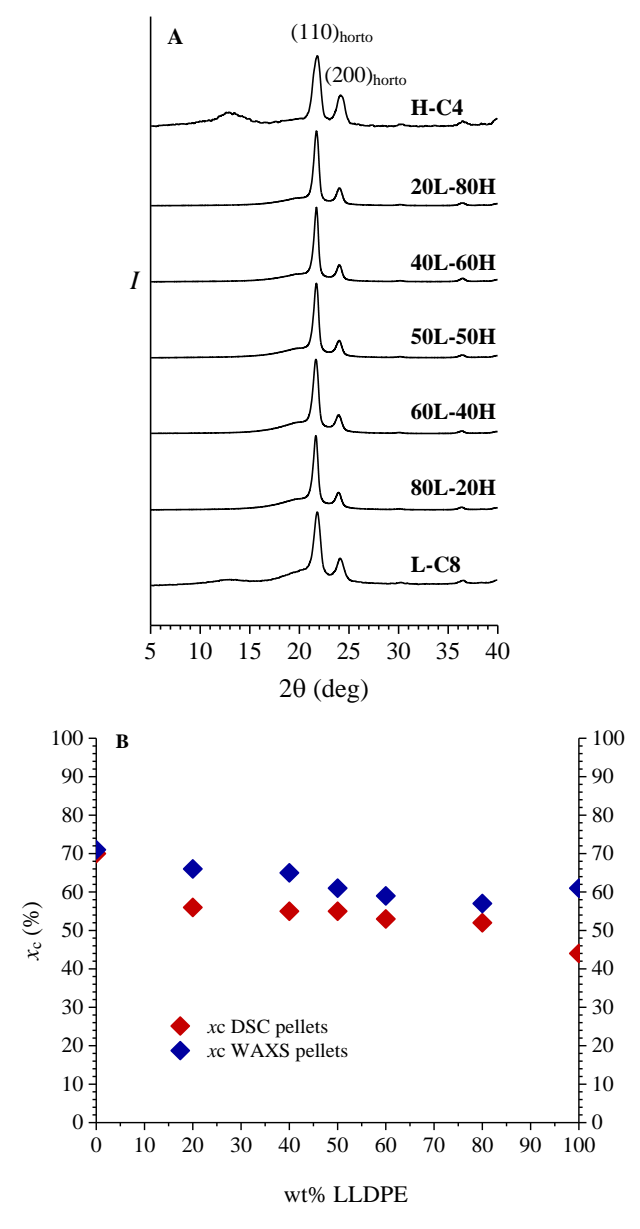


Figure 21 X-ray powder diffraction profiles of pellets of the LLDPE-HDPE blends and of the pure components (A) and corresponding values of the crystallinity index (B) evaluated from DSC (red diamond) and WAXS (blue diamond) as a function of LLDPE content.

The stress-strain curves relative to compression-molded films of LLDPE-HDPE blends are reported in Figure A1, A2 of Appendix A4. The films have been prepared in six different ways (the same as those used for the pure components): slow cooling (about 20 °C/min) from $T_{\rm max}$ =200°C and quenching from for $T_{\rm max}$ = 200 and 150°C, after annealing the melt at for $T_{\rm max}$ for $t_{\rm max}$ =10 and 30 min. The mechanical parameters extracted from stress-strain curves of Figure A1 and A2 of Appendix A4 are reported in Figure 22 and A3 of Appendix A4, as a function of LLDPE content.

The blends show, regardless of composition and cooling mode, high ductility, with value of deformation at break exceeding 1000%, pronounced yield and strain hardening at high deformations. The values of Young's modulus decrease as the LLDPE content increases, and are the highest for the slowly cooled samples, regardless of the annealing time at $T_{\rm max}$. For the fast cooled (quenched) samples the values of Young's modulus are nearly coincident regardless of preparation conditions.

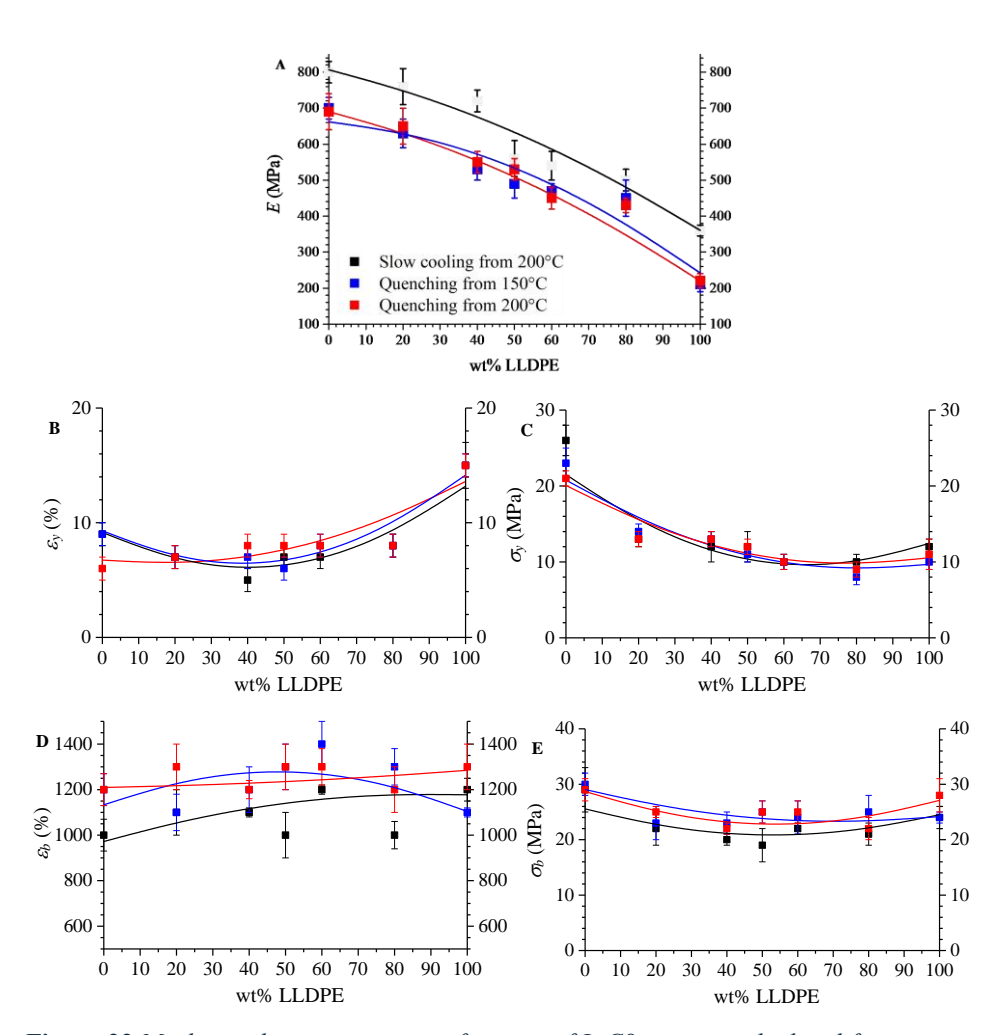


Figure 22 Mechanical parameters as a function of L-C8 content calculated from stress-strain curves of compression-molded films of the samples obtained through slow cooling from 200°C (black squares), quenching from 150°C (blue squares) and quenching from 200°C (red squares) after an equilibration time at the indicated temperature of 10 minutes. Mechanical parameters are Young's Modulus (A), strain (B) and stress (C) at yielding, strain (D) and stress (E) at break.

The values of stress (σ_y) at yield tend to decrease and those of strain (ε_y) at yield tend to increase as the LLDPE content increases. Both parameters are scarcely dependent on the preparation conditions of the films (Figure 22B,C and A3B,C of Appendix 4). Finally, the values of stress (σ_b) and strain (ε_b) at break of the blends

span a relatively narrow range comprised 20 and 30 MPa and 1000-1400%, respectively, regardless of preparation conditions of the films (Figure 22D,E and A3D,E of Appendix 4).

The mechanical properties of LLDPE-HDPE blends, clearly show a good degree of miscibility of the two components H-C4 and LC8, due to the formation of a well interconnected network of crystalline and amorphous regions, able to transmit the stress up to high deformations.

3.6. Thermal fractionation of selected samples

To further investigate the complex microstructure of the pure grades and relative blends, three LLDPE-HDPE mixtures have been selected and subjected to thermal fractionation, following the protocol of successive self-nucleation and annealing (SSA protocol) described in Chapter 2. The SSA technique has been designed to resolve the complex wide melting endotherms of polymers including defects that interrupt the regular sequences of the crystallizable units along the chains, in terms of "elementary melting processes", at temperatures which reflect the distribution of lamellar crystals and thus the distribution of methylene sequence length (MSL). In the present context, the aim is to highlight the possible occurrence of co-crystallization of ethylene sequences belonging to the two components in the HDPE-LLDPE blends, as a result of a good miscibility in the melt and amorphous state of ethylene sequences of similar length of the two components, able to oppose to molecular segregation. It has been shown, indeed, that application of an SSA protocol to blends of branched and linear PEs, may allow to study the occurrence of miscibility and segregation phenomena in these mixtures, highlighting that only those PE fractions that have similar microstructure of the chains in terms of length of ethylene sequences are able to reach a good miscibility in the melt and hence produce co-crystals, upon cooling¹⁴.

Results of SNA experiments

To correctly design an SSA fractionation protocol, is crucial to identify for each sample the ideal self-nucleation temperature $T_{\rm s\,ideal}$, corresponding to the temperature at which the maximum concentration of self-nuclei survives, without occurrence of annealing. Hence, prior to SSA fractionation, experiments of self-nucleation and annealing (SNA) have been carried out. This analysis allows to investigate self-nucleation behaviour of the samples, identifying the range of seeding temperatures $T_{\rm s}$ marking the complete destruction of self-nuclei (Domain I), the survival of self-nuclei (Domain II) and survival of self-nuclei coupled with annealing due to incomplete melting of the crystals (Domain III). In a view of understanding the early stages of tentering process, SNA analysis can help to determine the state of the melt as a function of the selected tentering temperature in the steps before the stretching. SNA protocol is described in Chapter 2.

As an example, the DSC curves recorded during the SNA protocol applied to H-C4 sample are reported in Figure 23. In particular, the DSC curves recorded by cooling the sample from the different T_s temperatures to 25 °C are reported in Figure 23A (step 4 in SNA protocol), whereas the subsequent heating scans recorded from 25 °C until 200 °C are reported in Figure 23B (step 5 in SNA protocol. The set of DSC curves recorded during the SNA protocol on LLDPE-HDPE blends and corresponding pure components are shown in Figure A1-A7 of Appendix A5.

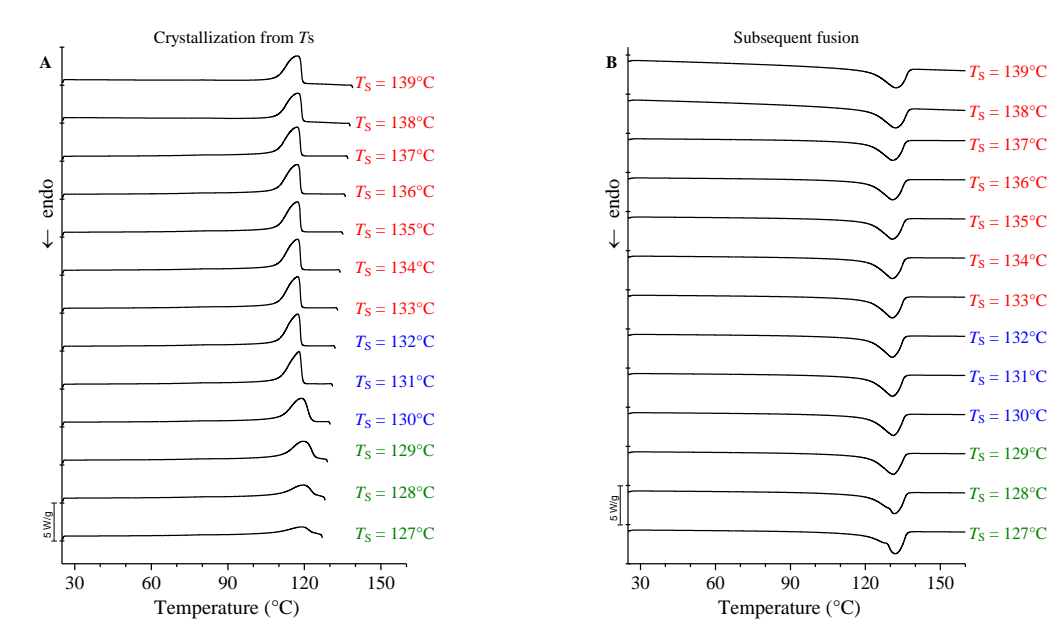
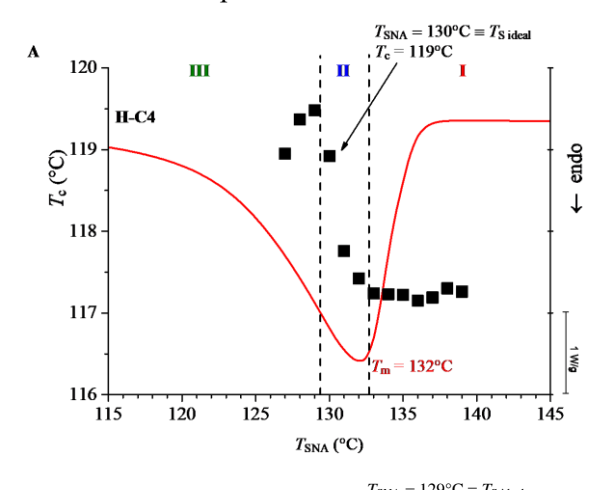
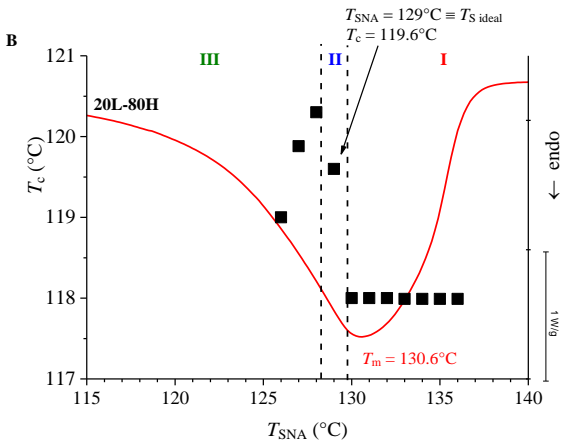
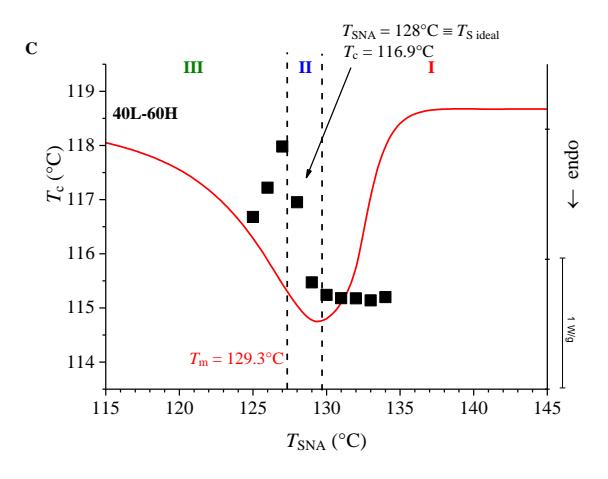


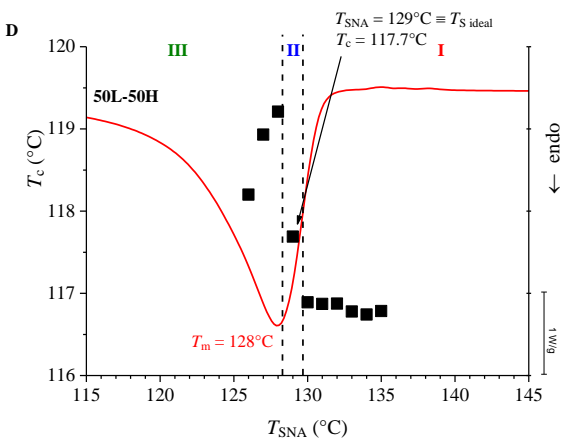
Figure 23 (A) DSC scans recorded in the cooling steps after 5 minutes at the indicated T_s (step 4 of SNA protocol) and (B) subsequent heating scans (step 5 of SNA protocol), for sample H-C4. The scanning rate is 10 °C/min. The colour used to indicate the seeding temperatures reflects the achieved nucleation regime: red for regime I, blue for regime II, green for regime III.

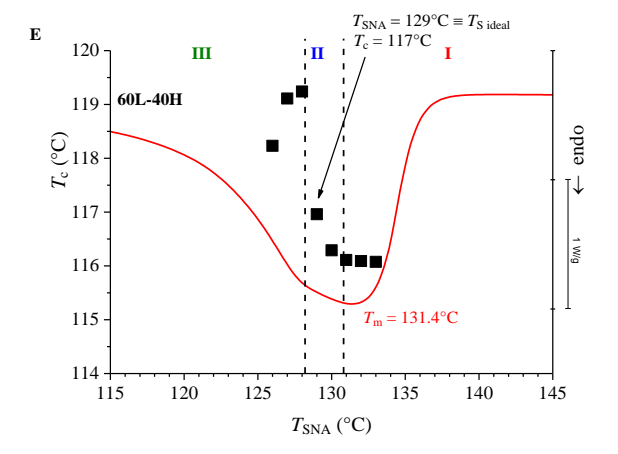
The crystallization temperatures T_c extracted from the DSC scans of Figures 23A are reported in figure 24A as a function of the seeding temperature T_s . In Figure 24B-G, the results of the SNA protocol applied on the neat sample L-C8 and the LLDPE-HDPE blends are also reported. For











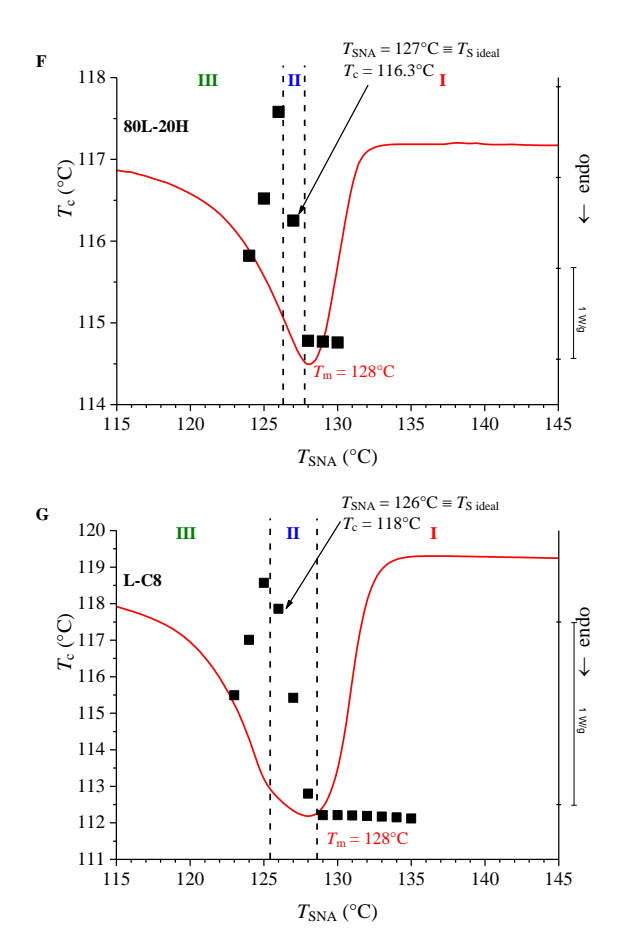


Figure 24 Crystallization temperatures T_c as a function of the seeding temperatures T_s , extracted from the SNA cooling scans (step 4, see chapter 2), for the LLDPE-HDPE blends with the indicated compositions, and the corresponding neat components, H-C4 and L-C8. The (T_s, T_c) diagram defining the domains I-III overlies the DSC melting curve recorded in the second heating scan at 10 °C/min of the melt crystallized sample (red line). The boundary lines separating Domains I, II and III are indicated. The values of T_s ideal and the corresponding values of T_c , along with the melting temperatures T_m obtained from the DSC scans are also indicated.

For the sample H-C4, the Domain I (Figure 24A) occurs for $T_s \ge 133$ °C, as indicated by the constat values of T_c as a function of T_s around 117.2°C. This means that no self-nuclei survive for $T_s \ge 133$ °C and that crystallization takes place starting from an "isotropic melt" in which only temperature-resistant heterogeneous nuclei of unknown nature survive. As stated before, (see Chapter

2, section 2.3.2) the term "isotropic" is not related to any concept of orientation, but it is used to describe a fully relaxed melt. Domain II is roughly located in the T_s range between 130 and 132°C. In this T_s range, T_c increases steeply as T_s decreases, till the value of 119 °C. This increase is due to the survival of self-nuclei, the concentration of which increases as T_s decreases. Domain III starts at $T_s = 129$ °C, as confirmed by the decrease of ΔH_m values measured in the DSC heating scans (step 5 of SNA protocol, see Chapter 2) recorded after the cooling step from T_s . This indicates that for $T_s \leq 129$ °C not all the crystals undergo melting, but part of them survive and experience annealing. The evidence of this phenomenon can be traced back in the appearance of a small hump in the DSC curves of Figure 23B, at T close to previous seeding temperature. According to Müller et al. 16,17 the optimum self-nucleation temperature or T_s ideal is defined as the minimum temperature within Domain II of nucleation and corresponds to the temperature at which the number of self-nuclei in the melt is maximum. The value of T_s ideal for HDPE is 130°C.

For the sample L-C8 the boundaries between Domain I-II and Domain II-III result shifted to lower values of T. An "isotropic melt" occurs for $T_s \ge 129^{\circ}\text{C}$, while Domain II is reached for $T_s < 129^{\circ}\text{C}$. Here the effect of self-nucleation arises as indicated by the increase of T_c recorded in the cooling step from T_s , as T_s decreases (Figure 24G). For $T_s \le 125^{\circ}\text{C}$, partial melting occurs within the Domain III, as indicated by the appearance of a well-defined annealing peak in the heating curves (step 5 of SNA protocol, see Chapter 2) recorded after the cooling step from T_s . The value of T_s ideal for LLDPE is 126°C. The values of T_s defining the boundaries between the SNA domains ($T_s^{\text{I-II}}$ and $T_s^{\text{II-III}}$) are reported as function LLDPE content in Figure 25 and Table 9. It is apparent that for the blends the Domain II of self-nucleation occurs in a T_s range which is narrower than that of pure components. It is also apparent that the values of T_s ideal, reported in Table 9, fall in between the values of T_s ideal of the pure components H-C4 and L-C8.

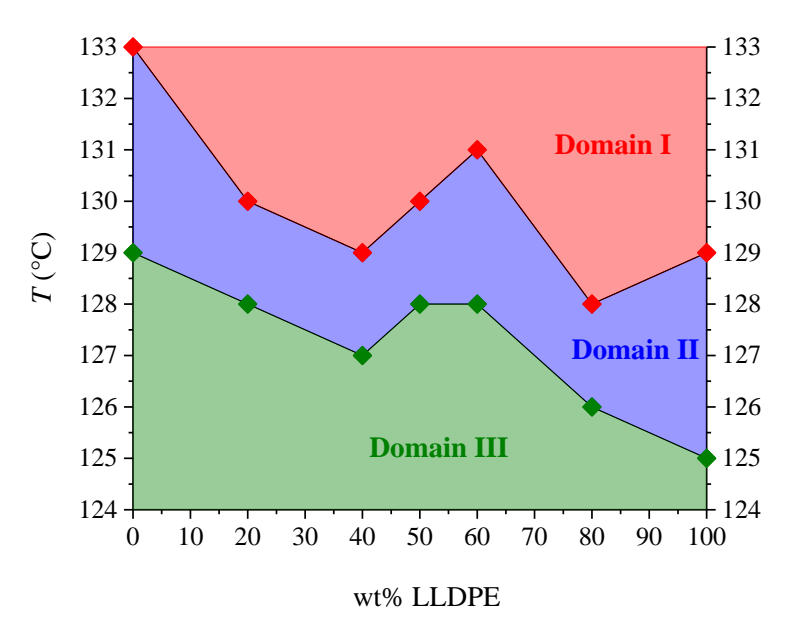


Figure 25 Values of the seeding temperature T_s marking the boundaries between Domain I and II, and Domain II and III of LLDPE-HDPE blends and neat components H-C4 and L-C8, as a function of LLDPE content.

Table 9 Values of the temperatures that define the boundaries of existence of Domain I, II, and III for LLDPE-HDPE blends and neat components H-C4 and L-C8, and values of $T_{s\,ideal}$

| Sample | Domain III | Domain II | Domain I | T _{s ideal} |
|---------|------------------|---|------------------|----------------------|
| Н-С4 | <i>T</i> ≤ 129°C | 129°C < T < 133°C | <i>T</i> ≥ 133°C | 130°C |
| 20L-80H | <i>T</i> ≤ 128°C | $128^{\circ}\text{C} < T < 130^{\circ}\text{C}$ | $T \ge 130$ °C | 129°C |
| 40L-60H | <i>T</i> ≤ 127°C | $127^{\circ}\text{C} < T < 129^{\circ}\text{C}$ | $T \ge 129$ °C | 128°C |
| 50L-50H | <i>T</i> ≤ 128°C | $128^{\circ}\text{C} < T < 130^{\circ}\text{C}$ | $T \ge 130$ °C | 129°C |
| 60L-40H | <i>T</i> ≤ 128°C | $128^{\circ}\text{C} < T < 131^{\circ}\text{C}$ | $T \ge 131$ °C | 129°C |
| 80L-20H | <i>T</i> ≤ 126°C | $126^{\circ}\text{C} < T < 128^{\circ}\text{C}$ | $T \ge 128$ °C | 127°C |
| L-C8 | <i>T</i> ≤ 125°C | $125^{\circ}\text{C} < T < 129^{\circ}\text{C}$ | $T \ge 129$ °C | 126°C |

The observed narrowing of the self-nucleation Domain II is due to the simultaneous decrease of the $T_s^{\text{I-II}}$ and $T_s^{\text{II-III}}$ of the blends with respect to those neat HDPE. The decrease of $T_s^{\text{I-II}}$ may be explained in terms of dilution effect

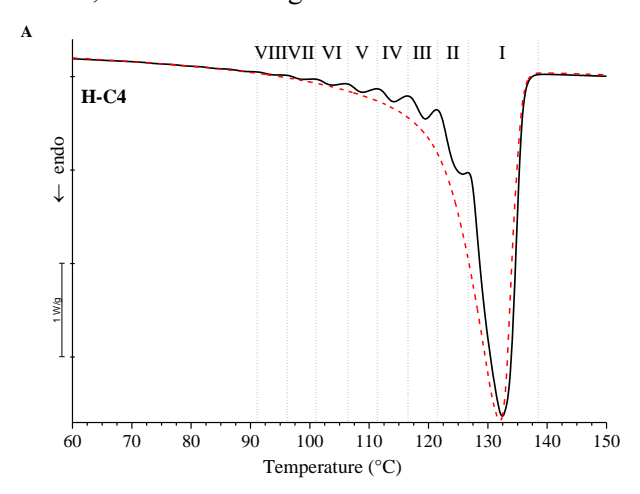
exerted by LLDPE, that suppresses, at least in part, the tendency of HDPE to form self-nuclei at higher temperatures, whereas the decrease of $T_s^{\text{II-III}}$ reflects the fact that the survival of crystalline fragments of the LLDPE components requires lower temperatures than HDPE.

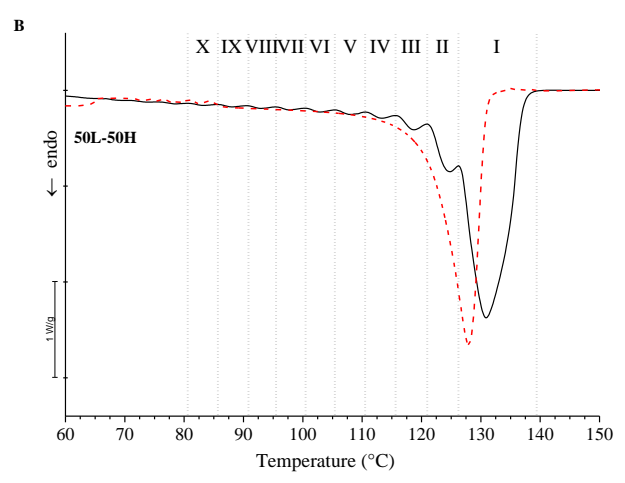
Results of SSA experiments

As outlined in Chapter 2, the tendency of regular sequences of monomers with different lengths to crystallize separately is exploited in a SSA protocol, through a sequence of thermal cycles. The first step is to create a standard crystalline state, by cooling the sample from the melt after an isotherm of 5 minutes at temperature (T = 200°C) high enough to erase all previous thermal and mechanical history. Subsequently, heating steps to a designated self-seeding temperature (T_s) , with a brief (5 min) isotherm at T_s , followed by cooling to room temperature, are repeated a number of times, while gradually decreasing values of T_s , in steps of $\Delta T_s = 5$ °C. A scanning rate of 10°C/min is used in both the cooling and heating steps (see Chapter 2). For each sample, the final melting endotherm shows the effect of accumulation of several self-nucleation and annealing step, using decreasing T_s values from the $T_{s \text{ ideal}}$ (i.e. $T_{s \text{ ideal}}$, $T_{s \text{ ideal}}$ - ΔT_s ; $T_{s \text{ ideal}}$ - $2\Delta T_s$) until covering the entire melting range. The value of ΔT_s defines the fractionation windows and the number of SSA cycles to be repeated to cover the whole melting range. The number of peaks corresponds to the number of T_s employed minus one: in the first step T_{s ideal} (in Domain II of nucleation, Table 9) causes only selfseeding and only the successive steps, with T_s that fall in Domain III, involves annealing. In each case the observed distributions of melting peaks are unimodal and reflects a random distribution of defects, i.e. the branches distribution along the PE backbone.

The results of SSA experiments carried out on the pure components (H-C4 and L-C8) and the corresponding 50L-50H blend are illustrated below. The DSC scans

recorded during the SSA protocol for pure grades and 50L-50H blend are reported in the Appendix A6. The final SSA DSC melting curves, compared with the corresponding standard non-isothermal heating scan, recorded in the second melting at 10 °C/min, are shown in Figure 26.





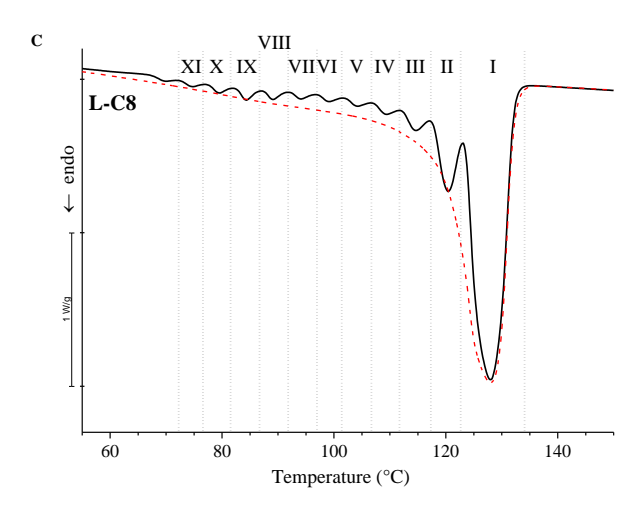


Figure 26 DSC heating scans recorded at the end of the SSA protocol (black curves) relative to H-C4 (A), 50L-50H blend (B) and L-C8 (C). They overlay the DSC melting curve recorded in the second heating scan of the melt-crystallized samples (red dashed lines). For each sample, the identified fractions are indicated by roman numbers.

The final melting endotherm of the sample H-C4 (Figure 26A) shows a relevant sharp peak at $T_{\rm ml} \approx 132$ °C (relative area $A_{\rm I} \approx 49\%$) and a not completely resolved peak at $T_{\rm mlI} \approx 127$ °C (relative area $A_{\rm I} \approx 31\%$). These two fractions are the most abundant in this sample. Six additional fractions for a total of 8 fractions are detected, with melting peak centred at values of $T_{\rm mi} < T_{\rm mll}$. In the evaluation of the relative area of the peaks centred at each $T_{\rm mi}$, $A(T_{\rm mi})$, the possible presence of humps spanning the temperature range below the $T_{\rm mi}$ of the last peak has been neglected. These subsidiary endotherms, indeed, correspond to the melting of crystals formed during cooling from the lowest $T_{\rm s}$, and do not correspond to crystals really formed in the SSA protocol. In all cases the relative amount of these subsidiary crystals is less than 10%.

Similar considerations have been applied to the other samples. In particular, for LLDPE (Figure 26C) the detectable SSA fractions are eleven. Fraction I ($T_{\rm ml} \approx 128~^{\circ}\text{C}$) alone accounts for about 60% of the total, while for the II endothermic peak at $T_{\rm mII} \approx 120~^{\circ}\text{C}$, the relative area $A(T_{\rm mII})$ is about 11%. Finally, for the blend

50L/50H SSA fractionation puts in evidence a first relevant melting peak at $T_{\rm ml} \approx 131^{\circ}$ C (relative area $A_{\rm I} \approx 50\%$) followed by nine less intense peaks.

The fractionation peaks appearing in the DSC heating scans recorded at the end of the SSA protocol reflect the distribution of methylene sequence length (MSLi), that is, the distribution of consecutive methylene units comprised in between two branching points able to crystallize. For each fraction, the greater the MSL value the thicker are the lamellar crystals, the higher the corresponding melting temperature $T_{\rm mi}^{18,19}$. Moreover, depending on MSL value, both chain folded and chain unfolded lamellar crystals can be formed. Previous studies^{20,21} indicate that, for PE, lamellar crystals including stems of length lower than 150 methylene units are expected to be unfolded.

For each melting peak centred at $T_{\rm mi}$ (relative area $A(T_{\rm mi})$), the corresponding value of the MSLi is calculated using the Gibbs–Thomson approach²² (see Chapter 2), and Zhang ²³ and Keating²⁴ equations (Table 10, 11, 12). According to Zhang²³ and Keating²⁴ approach, the relationship between the melting temperature $T_{\rm mi}$ of each fraction detected in the final SSA melting curve and the corresponding MSLi value can be evaluated through Equations 3 and 4, respectively:

$$ln(X_i) = 0.3451 - \frac{142.2}{T_{mi}(MSLi)} \quad (3)^{22}$$

$$ln(X_i) = 0.331 - \frac{135.5}{T_{mi}(MSLi)}$$
 (4)²³

with X_i defined as the mole fraction of carbon atoms in a methylene sequence that melts at $T_{\rm mi}$. These equations were found by the fit of suitable calibration curves, built up based on SSA in Ref.²² and stepwise crystallization in Ref.²³ experiments, respectively, on linear hydrocarbons of known MSL value. The relationship between X_i and the MSLi value, in turn, is given by Equation 5:

$$MSL = \frac{2X}{1-X}$$
 (5)²³

The melting temperature and relative area of the SSA fractions of HDPE, LLDPE and the blend H50H-50L are given in Table 10-12. The MSLi values calculated through the Gibbs–Thomson²², Zhang ²³ and Keating²⁴ approaches are also collected in Table 10-12. The values of l_c calculated through the Gibbs-Thomson approach are also reported in Table 10-12. The values l_c of the most abundant fractions are in a good agreement with the l_c values extracted from the SAXS data of the samples.

The three approaches used for the calculation of the MSLi values lead to results that follow similar trends. This is shown in Figure 27A-29A, in which the fractional amounts of crystals of a given lamellar thickness melting at a given $T_{\rm mi}$ $(A(T_{\rm mi}))$ are reported as a function of the corresponding MSLi values, calculated according to the different approaches. For each sample, also the cumulative distributions of MSLs are reported in Figure 27B-29B. It is apparent that the relative amount of methylene sequences of a given length tends to increase as their length increases. The sample H-C4 presents a rather broad distribution of MSL values, in agreement with the high dispersity of molecular mass. Based on the Gibbs-Thomson approach, two main thermal fractions corresponding to MSL values of about 219 and 142 units are present. These MSL values correspond to lamellar thickness of ≈28 nm and 18 nm, and account for 49% and 31% of the total MSLs, respectively. Due to the high molecular mass and the low comonomer content, the sample H-C4 shows higher lamellar thickness and MSL values than the sample L-C8 and the blend. Indeed, the fraction of MSL having length greater than 100 units is around 80% for HDPE, 61% for LLDPE and 56% for the blend 50L-50H.

The distributions of MSL values for the sample L-C4 and the blend 50L-50H present similar shapes, with the relative amount of MSLs that increases smoothly for MSL values lower than a threshold, corresponding to 100 units for the sample L-C8 and to 120 units for the blend 50L-50H, and then rapidly increases.

Compared with the MSL distribution of the sample H-C4, the main difference consists in the fact that the sample L-C8 and the blend 50L-50H show a single main fraction of methylene sequences of high length, that, according to the Gibbs-Thomson approach corresponds to ≈ 150 and 200 units, respectively, whereas the relative amount of each fraction with lower MSL values is less than 11%.

Comparing the positions and the relative underneath area of the main fractionation peaks in the blends and neat components, it appears that the fractionation peaks at \approx 132 and 1127 °C (relative area of \approx 50 and 30%, respectively) for HDPE, and at \approx 125 °C (relative area of \approx 60 %) for LLDPE, are replaced by a fractionation peak at 131 °C (area ≈50%) for the blend 50L-50H. Hence, the main peak of the fractionated blend occurs at a temperature (≈131 °C) close to the temperature of the main peak of fractionated HDPE (\approx 132 °C), with the same relative intensity. However, this does not mean that the main fractionation peak in the blend corresponds to crystals that are merely formed by the HDPE chains. In fact, the final DSC curve of the SSA protocol for the blend is not coincident with the DSC scan calculated by performing a weighted average of the final DSC scans of the SSA protocol for the neat components, but it is quite similar to that of the neat HDPE, and different from that of neat LLDPE. In addition, even the cumulative MSLs distributions of the blend 50L-50H are more similar to those of the neat HDPE component, rather than to those of the LLDPE component. This suggests that HDPE and LLDPE chains are probably miscible in the melt and form stable co-crystals in the blend, during the SSA protocol.

Table 10 Values of the seeding temperatures used in the SSA protocol, melting temperature T_{mi} and percentage area A(Tmi) of the melting peaks detected in the SSA final DSC heating scan, and corresponding values of methylene sequence lengths (MSLi) calculated according three different approaches, for the sample H-C4.

| | | | | Gibbs-Thomson | | | | Keating |
|---------------------|-------------------------|-----------------------|------------------|------------------|------------------|------------------------------------|------|---------|
| | | | _ | σe (90 mJ/m²) | | σe (44 mJ/m ²) | | |
| T _s (°C) | T _{mi} (°C) | A(T _{mi}) % | <i>l</i> ci (nm) | MSLi | <i>l</i> ci (nm) | MSLi | MSLi | MSLi |
| 90 | 92.9 | 1.3 | 5.4 | 43 | 2.7 | 21 | 45 | 50 |
| 95 | 98.2 | 1.9 | 6.1 | 48 | 3.0 | 23 | 52 | 58 |
| 100 | 104.1 | 3.8 | 7.1 | 56 | 3.4 | 27 | 62 | 70 |
| 105 | 108.9 | 2.2 | 8.1 | 64 | 4.0 | 31 | 73 | 83 |
| 110 | 114.4 | 5.9 | 9.7 | 76 | 4.7 | 37 | 91 | 106 |
| 115 | 119.2 | 2.8 | 11.8 | 93 | 5.7 | 45 | 114 | 138 |
| 120 | 127.0 | 31.0 | 18.0 | 142 | 8.8 | 69 | 194 | 262 |
| 125 | 132.3 | 49.0 | 27.8 | 219 | 13.6 | 107 | 353 | 618 |

Table 11 Values of the seeding temperatures used in the SSA protocol, melting temperature T_{mi} and percentage area A(Tmi) of the melting peaks detected in the SSA final DSC heating scan, and corresponding values of methylene sequence lengths (MSLi) calculated according three different approaches, for the blend 50L-50H.

| | | | | Gibbs-Thomson | | | | Keating |
|----------------|----------------------|---------------------|----------------------------------|---------------|----------------------------------|------|------|---------|
| | | | | re 1/2) | σe (44 mJ/m²) | | | |
| T _s | T _{mi} (°C) | A(T _{mi}) | (90 m l _{ci} (nm) | J/m²) MSLi | (44 m l _{ci} (nm) | MSLi | MSLi | MSLi |
| 79 | 83.6 | 2.8 | 4.6 | 36 | 2.2 | 18 | 36 | 40 |
| 84 | 88.6 | 2.6 | 5.0 | 39 | 2.4 | 19 | 41 | 45 |
| 89 | 93.3 | 2.9 | 5.5 | 43 | 2.7 | 21 | 46 | 51 |
| 94 | 98.0 | 3.1 | 6.1 | 48 | 3.0 | 23 | 52 | 58 |
| 99 | 102.7 | 3.2 | 6.8 | 54 | 3.3 | 26 | 59 | 67 |
| 104 | 108.4 | 5.3 | 8.0 | 63 | 3.9 | 31 | 71 | 82 |
| 109 | 113.3 | 2.5 | 9.3 | 73 | 4.6 | 36 | 86 | 101 |
| 114 | 119.0 | 8. | 11.7 | 92 | 5.7 | 45 | 113 | 136 |
| 119 | 124.0 | 5.5 | 15.0 | 118 | 7.3 | 58 | 154 | 196 |
| 124 | 131.3 | 50.2 | 25.2 | 199 | 12.3 | 97 | 306 | 493 |

Table 12 Values of the seeding temperatures used in the SSA protocol, melting temperature Tmi and percentage area A(Tmi) of the melting peaks detected in the SSA final DSC heating scan, and corresponding values of methylene sequence lengths (MSLi) calculated according three different approaches, for the sample L-C8.

| | | | Gibbs-T | Gibbs-Thomson | | | | Keating |
|-------------|-------------|-------------|-------------|---------------|-------------|-------|-------|---------|
| | | | _ | e | | re | | |
| | | | (90 m | J/m²) | (44 m | J/m²) | | |
| $T_{\rm s}$ | $T_{ m mi}$ | $A(T_{mi})$ | $l_{ m ci}$ | MSLi | $l_{ m ci}$ | MSLi | MSLi | MSLi |
| (°C) | (°C) | % | (nm) | WISLI | (nm) | WISLI | WISLI | WISLI |
| 71 | 74.8 | 1.1 | 4.0 | 31 | 1.9 | 15 | 30 | 33 |
| 76 | 79.7 | 1.7 | 4.3 | 34 | 2.1 | 17 | 34 | 37 |
| 81 | 84.4 | 2.2 | 4.6 | 37 | 2.3 | 18 | 37 | 41 |
| 86 | 89.1 | 2.2 | 5.1 | 40 | 2.5 | 19 | 41 | 46 |
| 91 | 94.2 | 2.5 | 5.6 | 44 | 2.7 | 22 | 47 | 52 |
| 96 | 99.1 | 2.2 | 6.2 | 49 | 3.1 | 24 | 53 | 60 |
| 101 | 104.5 | 4.1 | 7.1 | 56 | 3.5 | 27 | 63 | 71 |
| 106 | 109.3 | 3.0 | 8.2 | 65 | 4.0 | 33 | 74 | 85 |
| 111 | 114.9 | 8.8 | 9.9 | 78 | 4.8 | 38 | 93 | 109 |
| 116 | 120.3 | 11.1 | 12.4 | 98 | 6.1 | 48 | 122 | 149 |
| 121 | 127.6 | 60.8 | 18.8 | 148 | 9.1 | 72 | 205 | 282 |

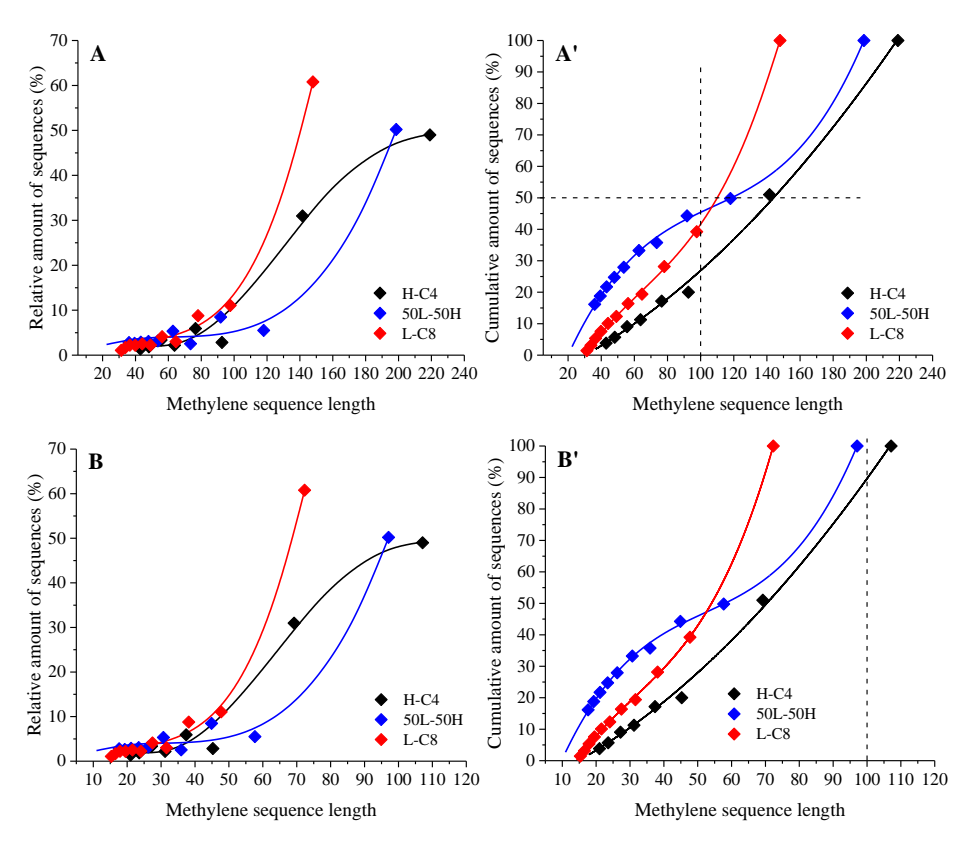


Figure 27 Relative (A,B) and cumulative (A',B') distributions of methylene sequence lengths (MSLs) for the samples H-C4, L-C8 and the corresponding blend 50L-50H. The MSL values are calculated following the Gibbs-Thomson approach, using two different values for the fold surface energy σ_e (see Equation 2 of Chapter 2): 90 mJ/m² (A,A'), which is valid for extended chain crystals of PE, and 44 mJ/m² (B,B'), valid for folded chain crystals of PE.²¹

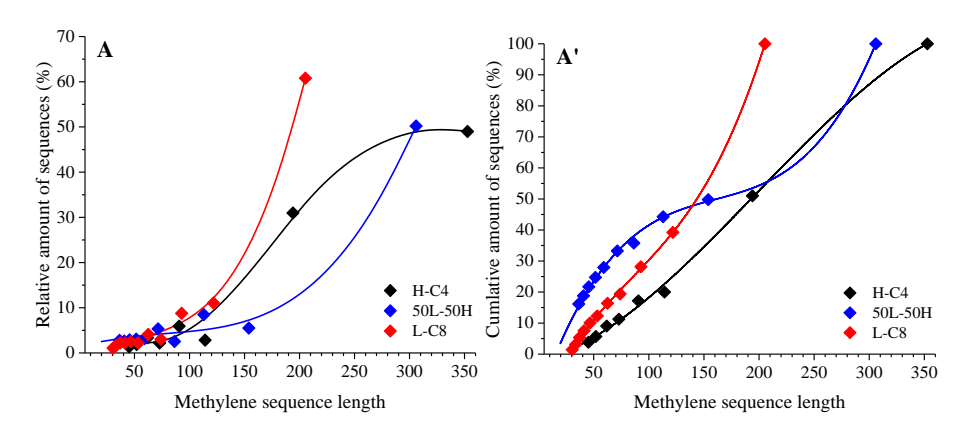


Figure 28 Relative (A) and cumulative (A') distributions of methylene sequence lengths (MSLs) for the samples H-C4, L-C8 and the corresponding blend 50L-50H. The MSL values are calculated following the Zhang approach.²²

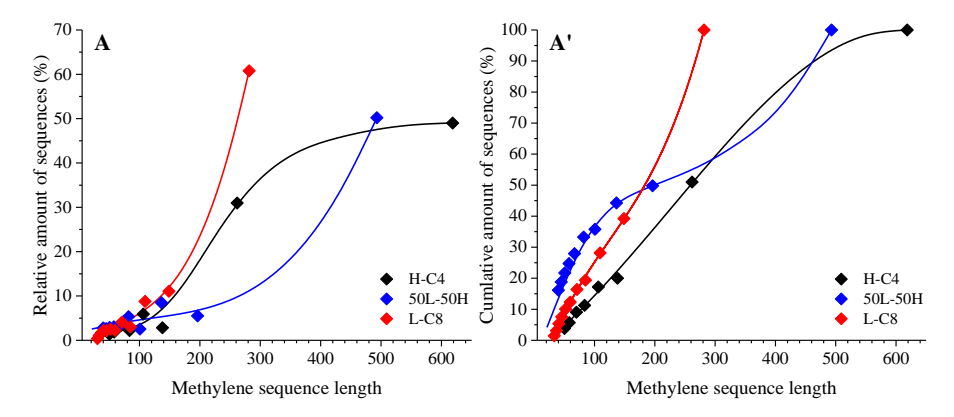


Figure 29 Relative (A) and cumulative (A') distributions of methylene sequence lengths (MSLs) for the samples H-C4, L-C8 and the corresponding blend 50L-50H. The MSL values are calculated following the Keating approach.²³

3.7. Conclusion

Several techniques and analytical methods have been employed to gain a detailed characterization of the commercial PE grades and blends of selected samples, focusing on basic microstructural characterization, structural and morphological analysis at nanometric and micrometric length scales, and characterization of thermal and mechanical properties. Moreover, to better understand the structural features of the samples, the effect of different cooling conditions has been investigated in the preparation of compression molded films. Finally, nucleation behaviour and thermal fractionation on designated samples have been studied.

The pure grades differ in molecular mass, molecular mass distribution and comonomer content. All of them approach a nearly random branching distribution. These microstructural differences underlie the various properties observed in the different samples and provide a key framework for interpreting the results achieved in subsequent analyses presented in Chapter 4. The samples H-C4 (M_w = 137 kDa) and L-C4,C6 (M_w = 185 kDa) produced by Borealis show broad molecular mass distributions, with dispersity index D = 14.3 and 19.5, respectively. The sample H-C4 has a low content (0.5%mol) of 1-butene units while the sample L-C4,C6 contains 0.5%mol of 1-butene and 1.2%mol of 1-hexene units. The sample L-C8 (M_w = 105 kDa) provided by Dow, with D = 4.1, contains 2.6%mol of 1-octene units. The sample L-C6 (M_w = 118 kDa) with 3.1%mol of 1-hexene, produced by SABIC, presents molecular mass distribution with D = 2.7.

The values of crystallinity index, melting and crystallization temperatures evaluated from DSC and/or WAXS analysis, decrease as the total comonomer content increase, and hence as the density decreases.

The SAXS profiles reveal a well-defined main correlation peak for all the samples, indicating that the lamellar crystals are stacked along the direction normal to the

basal planes, separated by amorphous layers. The samples H-C4 and L-C4,C6 exhibit a narrow correlation peak at $q \approx 0.254$ nm⁻¹, corresponding to a long spacing of \approx 24.7 nm, while the samples L-C8 and L-C6 show a broad correlation peak at $q \approx 0.294$ and 0.38 nm⁻¹, respectively, corresponding to long spacings of \approx 21.4 and 16.5 nm, respectively. SAXS data analysis indicates disorder in lamellar stacking, due to non-uniform thickness of the lamellar crystals and amorphous layers, especially for the defective samples L-C8 and L-C6. The low defective samples H-C4 and L-C4,C6, with a broad molecular mass distribution, form thick lamellae that are arranged in less disordered stacks. Conversely, the defective samples L-C8 and L-C6, form thin lamellae that are more disorderedly arranged in stacks.

DSC experiments aimed to analyse melt memory effect show that for the samples H-C4 L-C4,C6 and L-C8, an annealing time of 5 min at different values of the maximum temperature reached in the melt $T_{\rm max}$, are enough to remove any melt memory, as the crystallization temperatures $T_{\rm c}$ determined as a function of $T_{\rm max}$ remains constant. The sample L-C6, instead, shows a distinct shift in $T_{\rm c}$, by about 2 °C, toward higher temperature, starting from $T_{\rm max} = 163$ °C ($T_{\rm onset}$), that is at temperatures well above, by ≈ 18 °C, the thermodynamic melting temperature $T_{\rm m0}$ (=145 °C) of PE. This effect indicates that the sample L-C6 retain constrained crystalline sequences even above $T_{\rm m0}$. In L-C6, branches hinder regular crystalline formation during cooling and act as constraints after melting, maintaining a conformation that directs reorganization upon cooling.

The analysis of the mechanical properties indicates that the most relevant differences in mechanical behaviour of the PE grades stem from the chain microstructure, that is the balance between molecular mass, molecular mass distribution, comonomer content, and the resulting crystallinity and morphology achieved after cooling, and are less dependent on the specific thermal protocol adopted for preparation of compression molded films utilized for mechanical

testing. All the samples show yielding behaviour, high ductility and strain hardening at high deformations. The highly crystalline sample H-C4 exhibits the highest values of the Young's modulus E (700-800 MPa). As the comonomer content increases, the values of the Young's modulus decrease. Exception occurs for the sample L-C8, which, in spite of the higher comonomer content and lower crystallinity, shows a greater value of the Young's modulus compared with the sample L-C4,C6. It has been argued that this behaviour is due to microstructural differences. Effects due to differences in molecular mass and molecular mass distribution have been considered as responsible for an increase/decrease of the rigidity besides the main effect caused by branch content on the crystallinity. On one hand the presence of a non-negligible faction of chains with high molecular mass for the sample L-C8, able to establish a large number of entanglements acting as physical cross-links of the amorphous network, induce an increase of rigidity. On the other hand, the presence of a relevant fraction of chain with low molecular mass acting as a diluent for the sample L-C4,C6, induces an increase of flexibility. For the sample L-C6, with the highest molecular mass ($M_n = 44 \text{ kDa}$), the benefit of the presence of long chains on the Young's modulus value is counterbalanced by the lower level of crystallinity achieved, owing to the presence of the highest concentration of branches. Slowly cooled, compression-molded films show higher Young's modulus values than the films obtained by fast cooling (quenching), due to more ordered, crystals formed under slow cooling. Cooling conditions slightly affect yield stress (σ_v) and strain (ε_v). In particular, the values of σ_y decrease while those of ε_y increase as the comonomer content increases. Stress and strain at break vary slightly among samples. The most defective sample L-C6 exhibits the highest values of strain at break, which can be attributed to the high molecular mass. Adopting preparation conditions of the compression molded film that include an annealing step at the maximum temperature achieved in the melt T_{max} of $t_{\text{max}} = 10$ or 30 min, no significant differences arise in mechanical

properties, suggesting that the structural organization achieved by the samples affecting the tensile properties after 10 min are equivalent to those achieved for longer annealing times (30 min). This indicates that under the adopted processing condition the morphology achieved in the solid state depends primarily on the cooling rate. Notably, the sample L-C6, which exhibits melt memory effect by bringing the melt to T_{max} below 163°C adopting an annealing time of 5 min at T_{max} , returns to equivalent states after 10 or 30 min annealing at $T_{\text{max}} = 150$ or even 200 °C. This suggests that the relevant chain dynamics of this sample controlling its properties involves collective movements with characteristic times on the order of 5-10 min.

SAXS analysis of the compression molded films subjected to mechanical testing indicates that the low defective samples H-C4 and L-C4,C6 display long spacing values of 24-25 nm, and 20-22 nm for the films obtained by slow and fast cooling, respectively due to the formation of lamellar crystals of different thickness, as the thickness of the amorphous layers remains nearly constant. The lamellar parameters of the defective samples L-C8 and L-C6, instead, are similar, regardless of the conditions adopted for the preparation of the compression molded films.

Optical microscopy shows that the low defective sample H-C4 forms, by slow cooling the melt, small spherulites with high nucleation density, resulting in the formation of a well interconnected, interpenetrated network of the amorphous and crystalline phases, in agreement with the high values of the Young's modulus. The samples L-C4,C6, L-C8, and L-C6 form by slow cooling the melt, large and well defined spherulites. The sample L-C8, in particular, gives rise to a mixed morphology with lamellar sheaves located in between adjacent spherulites. The samples obtained by fast cooling the melt (quenching) exhibit disordered superstructures, in which crossed lamellar sheaves replace the spherulitic structure, filling the space with a uniform morphology. These morphological

features, along with the decrease of crystallinity as the comonomer content increases, help explaining the unique mechanical properties of the PE samples under study.

The samples H-C4 and L-C8 have been selected for blending and LLDPE-HDPE blends at five different compositions have been prepared, that is blends with 20 (20L-80H), 40 (40L-60H), 50 (50L-50H), 60 (60L-40H) and 80 wt% (80L-20H) of LDPE.

All blends display a single melting and crystallization peak at temperatures in between those of the pure components. The crystallization temperatures of the blends are close to that of the sample H-C4, suggesting that the presence of less defective, linear HDPE chains accelerates the crystallization of the L-C8 component.

The mechanical characterization of the blends has been performed, for the preparation of compression molded films, selecting the same conditions adopted for the pure grades. Similar to the neat components, all the blends show high ductility, marked yielding behaviour and strain hardening at high deformations. The values of the Young's modulus decrease as the LLDPE content increases. Also the values of stress at yield σ_y tend to decrease as the LLDPE content increases, while the values of strain at yield tend to increase. The values of stress and strain at break are less sensitive to the blend composition, as they remain almost constant within the experimental error, regardless of the preparation condition of the compression molded specimens.

In a view of understanding the early stages of the tentering process, SNA analysis has been performed to determine the state of the melt as a function of the possible tentering temperature, in the step immediately preceding biaxial stretching. The temperature ranges defining Domains I, II and III of the PE samples have been determined. It has been found that the temperature range of the self-nucleation Domain II for LLDPE-HDPE blends is narrower than that of the neat components.

This narrowing is due to the simultaneous decrease of the seeding temperature marking the boundary between Domains I and II ($T_s^{\text{II-III}}$) and between Domains II and III ($T_s^{\text{II-III}}$). It has been argued that the decrease of the values of $T_s^{\text{II-III}}$ may be due to the dilution effect exerted by the LLDPE component, that reduces the tendency of HDPE to form self-nuclei at high temperatures. The decrease of $T_s^{\text{II-III}}$, instead, has been ascribed to the fact that the survival of crystalline fragments of the LLDPE components requires lower temperatures than HDPE. From SNA experiments, the values of T_s ideal have been determined, that is the seeding temperature of Domain II at which the maximum concentration of self-nuclei is achieved. This temperature is 130°C for HDPE, 126 °C for LLDPE and 129 °C for the blend 50L-50H.

To further investigate the complex microstructure of the pure grades H-C4 and L-C8 and 50/50 blend thermal fractionation via successive self-nucleation and annealing (SSA) has been performed.

The final melting endotherm of the SSA protocol shows, for all the samples, the presence of multiple peaks due to fractionation of crystals with different lamellar thickness, that arise from the tendency of regular sequences of monomers with different lengths to crystallize separately. From this analysis, the distributions of methylene sequence length (MSL) have been determined. It emerges that the final DSC scan of the SSA protocol for the blend 50L-50H is more similar to that of the pure HDPE component rather than to that of neat LLDPE. This result has been deemed as a clue of the tendency of HDPE and LLDPE components to form cocrystals in the blend 50L-50H.

The analyses conducted have been essential for understanding the structural differences among the samples and their influence on the material properties. The gathered information will also be valuable for interpreting the outcomes of annealing and in-situ stretching experiments, offering deeper insight into how

these structural variations influence the behaviour of PE under different processing conditions.

Bibliography of chapter III

- (1) Brandrup, J.; Immergut, E. H.; Grulke, E. A. *Polymer Handbook*; 4th ed., Ed.; John Wiley & Sons, Inc.: New York, 1999.
- (2) Vonk, C. G. [Article Title Not Provided]. J. Appl. Crystallogr. 1975, 8, 340.
- (3) Strobl, G. R.; Schnieder, M. J. [Article Title Not Provided]. *J. Polym. Sci. Polym. Phys. Ed.* **1980**, *18*, 1343.
- (4) Ruland, W. The Evaluation of the Small-Angle Scattering of Lamellar Two-Phase Systems by Means of Interface Distribution Functions. *Colloid Polym. Sci.* **1977**, *255* (5), 417–427. https://doi.org/10.1007/BF01536457.
- (5) Fillon, B.; Wittmann, J.; Lotz, B.; Thierry, A. J Polym Sci Pol Phys. *J. Polym. Sci. Part B Polym. Phys.* **1993**, *31*, 1383.
- (6) Wunderlich, B. *Macromolecular Physics*; Academic Press: New York, 1976; Vol. 2.
- (7) Reid, B. O.; Vadlamudi, M.; Mamun, A.; Janani, H.; Gao, H.; Hu, W.; Alamo, R. G. [Title Not Provided]. *Macromolecules* **2013**, *46*, 6485–6497.
- (8) Lorenzo, A. T.; Arnal, M. L.; Sánchez, J. J.; Müller, A. J. [Title Not Provided]. *J. Polym. Sci. Polym. Phys. Ed.* **2006**, *44*, 1738–1750.
- (9) Supaphol, P.; Spruiell, J. E. [Title Not Provided]. *J. Appl. Polym. Sci.* **2000**, *75*, 337–346.
- (10) Ren, M.; Tang, Y.; Gao, D.; Ren, Y.; Yao, X.; Shi, H.; Zhang, T.; Wu, C. Recrystallization of Biaxially Oriented Polyethylene Film from Partially Melted State within Crystallite Networks. *Polymer* **2020**, *191*, 122291. https://doi.org/10.1016/j.polymer.2020.122291.
- (11) Liu, X.; Wang, Y.; Wang, Z.; Cavallo, D.; Müller, A. J.; Zhu, P.; Zhao, Y.; Dong, X.; Wang, D. The Origin of Memory Effects in the Crystallization of Polyamides: Role of Hydrogen Bonding. *Polymer* **2020**, *188*, 122117. https://doi.org/10.1016/j.polymer.2019.122117.
- (12) Luo, C.; Sommer, J.-U. Frozen Topology: Entanglements Control Nucleation and Crystallization in Polymers. *Phys. Rev. Lett.* **2014**, *112* (19), 195702.
- (13) Mamun, A.; Chen, X.; Alamo, R. G. Interplay between a Strong Memory Effect of Crystallization and Liquid–Liquid Phase Separation in Melts of Broadly Distributed Ethylene–1-Alkene Copolymers. *Macromolecules* **2014**, *47* (22), 7958–7970. https://doi.org/10.1021/ma501937c.

- (14) Arnal, M. L.; Sánchez, J. J.; Müller, A. J. Miscibility of Linear and Branched Polyethylene Blends by Thermal Fractionation: Use of the Successive Self-Nucleation and Annealing (SSA) Technique. *Polymer* **2001**, *42*, 6877–6890. https://doi.org/10.1016/S0032-3861(01)00177-.
- (15) Sangroniz, L.; Cavallo, D.; Müller, A. J. [Title Not Provided]. *Macromolecules* **2020**, *53*, 4581–4604.
- (16) Müller, A. J.; Michell, R. M.; Pérez, R. A.; Lorenzo, A. T. Successive Self-Nucleation and Annealing. **2005**.
- (17) Müller, A. J.; Arnal, M. L. Thermal Fractionation of Polymers. *Prog. Polym. Sci.* **2005**, *30*, 559–603.
- (18) Mirabella, F. M. Correlation of the Melting Behaviour and Copolymer Composition Distribution of Ziegler–Natta-Catalyst and Single-Site-Catalyst Polyethylene Copolymers. *J. Polym. Sci. Part B Polym. Phys.* **2001**, *39* (22), 2800–2818. https://doi.org/10.1002/POLB.10040.
- (19) Mandelkern, L.; Stack, G. M. Equilibrium Melting Temperature of Long-Chain Molecules. *Macromolecules* **1984**, *17* (4), 871–878. https://doi.org/10.1021/MA00134A057.
- (20) Ungar, G.; Keller, A. Inversion of the Temperature Dependence of Crystallization Rates Due to Onset of Chain Folding. *Polymer* **1987**, *28* (11), 1899–1907. https://doi.org/10.1016/0032-3861(87)90298-9.
- (21) Stack, G. M.; Mandelkern, L. On the Crystallization of High Molecular Weight Normal Hydrocarbons. *Macromolecules* **1988**, *21* (2), 510–514. https://doi.org/10.1021/MA00180A038.
- (22) Crist, B. Yet Another Visit to the Melting of Polyethylene Crystals. *J. Polym. Sci. Part B Polym. Phys.* **2007**, *45*, 3231–3236.
- (23) Zhang, M.; Wanke, S. E. Quantitative Determination of Short-Chain Branching Content and Distribution in Commercial Polyethylenes by Thermally Fractionated Differential Scanning Calorimetry. *Polym. Eng. Sci.* **2003**, *43* (12), 1878–1888. https://doi.org/10.1002/PEN.10159.
- (24) Keating, M.; Lee, I. H.; Wong, C. S. Thermal Fractionation of Ethylene Polymers in Packaging Applications. *Thermochim. Acta* **1996**, *284* (1), 47–56. https://doi.org/10.1016/0040-6031(96)02891-2.

Chapter IV

Thermal protocol

As described in Chapter 1, tentering process involves the biaxially stretching of the material by securing the edges of the material on a framework, known as a tenter frame. The actual stretching step is preceded by the heating of the material, in order to reach a semi-solid state. The semi-solid state of a polymer refers to an intermediate condition between solid and liquid, where the material exhibits both elastic and viscous characteristics. In this state, part of the polymer retains an ordered, crystalline structure, while the remaining part is amorphous and mobile. The semi-solid polymer can deform under stress without fully flowing like a liquid. This state is typically achieved by heating the polymer to a temperature above the glass transition (T_g) but below the end melting temperature (T_m), allowing an increase in molecular mobility without a total destruction of the pristine "crystalline scaffold". For polyethylene, suitable temperatures for tentering are those behind the melting endotherm recorded in a standard DSC scan. In particular, a good processing window at an industrial level is approached at temperatures comprised in between 110 and 130°C.

Since heating the polymer to temperatures close to its melting point can alter the crystalline structure, due to effects such as nucleation, annealing, secondary crystallization, and melting-recrystallization processes, selecting the proper temperature in the step prior to stretching is crucial to the effectiveness of the tentering process itself. To examine the phenomena occurring in samples selected for in situ biaxial stretching tests (Chapter 7), a thermal protocol has been designed to investigate the effects of thermal pre-treatments as a function of temperature ($T_{\text{treatment}}$) and the treatment time ($t_{\text{treatment}}$).

The analysis has been carried out on the samples H-C4 and L-C8, and on the corresponding blend 50L-50H. The adopted thermal protocol is described in Chapter 2. The samples have been initially kept at T=200 °C for 10 min and then cooled to room temperature at 40 °C/min, in order to create a standard crystalline state. The DSC scans and the X-ray diffraction profiles of the so obtained samples are collected in Figure 1 and 2. The results of the DSC thermal analysis are summarized in Table 1. The samples crystallize in the orthorhombic form of PE (Figure 2) and show a single melting and crystallization temperature at 125-129 °C, and 112-118 °C, respectively.

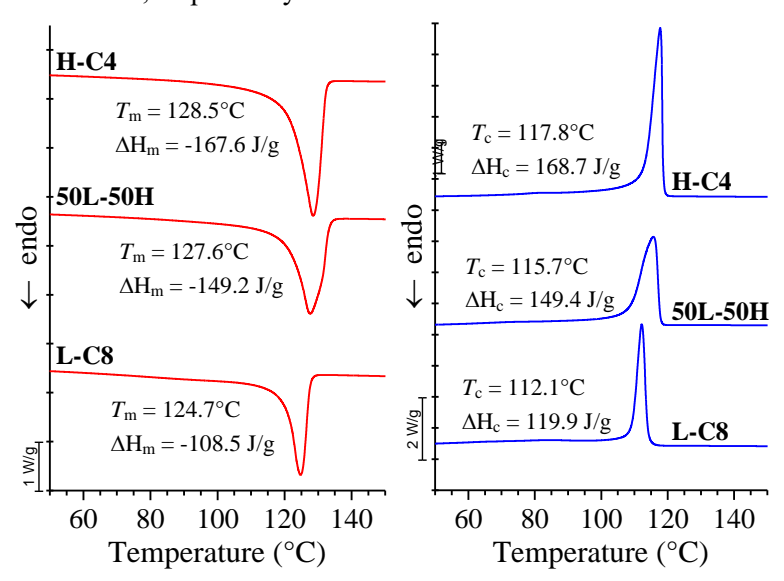


Figure 1 DSC scans of PE samples prepared in a standard crystalline state, recorded in heating (A) and successive cooling (B) runs, at scanning rate of 40°C/min.

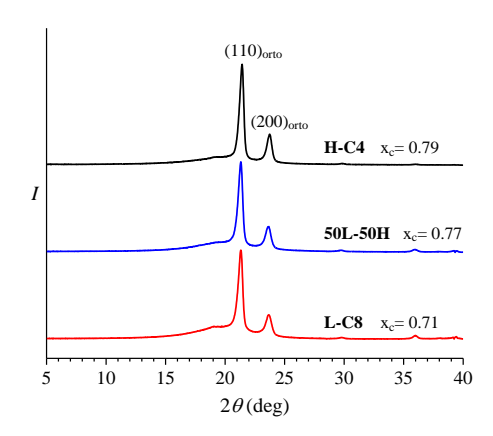


Figure 2 X-ray powder diffraction profiles of PE samples prepared in a standard crystalline state. The values of crystallinity index x_c are indicated.

Table 1 Values of the melting (T_m) , and crystallization temperatures (T_c) , corresponding enthalpies $(\Delta H_m, \Delta H_c)$ and crystallinity index evaluated from DSC and WAXS data of the PE samples prepared in a standard crystalline state.

| Comple | $T_{ m m}$ | $T_{\rm c}$ | ΔH_m | ΔH_c | x_c DSC | x_c WAXS |
|---------|------------|-------------|--------------|--------------|-----------|------------|
| Sample | (°C) | (°C) | (J/G) | (J/G) | (%) | (%) |
| H-C4 | 128.5 | 117.8 | -167.6 | 168.7 | 57 | 79 |
| 50L-50H | 127.6 | 115.7 | -149.2 | 149.4 | 51 | 77 |
| L-C8 | 124.7 | 112.1 | -108.5 | 119.9 | 41 | 71 |

The selected temperatures adopted for the thermal treatment of the PE samples initially prepared in a standard crystalline state $T_{\text{treatment}}$ are 125, 130 and 135°C. Their positions with respect to the DSC melting curves of the samples prepared in the standard crystalline state are highlighted in Figure 3.

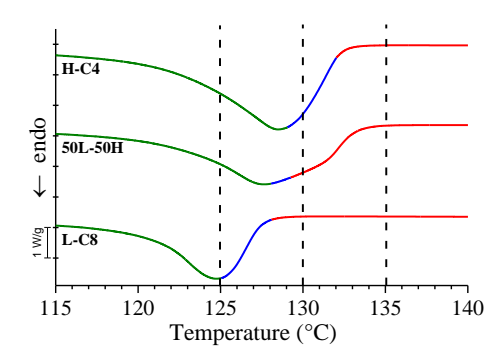


Figure 3 DSC heating scans of the PE samples prepared in a standard crystalline state, with indication of the SNA Domains I (red), II (blue) and III (green). The vertical dashed lines indicate the selected values $T_{treatment}$

From figure 3 it is apparent that at $T_{\text{treatment}} = 125$ °C the sample H-C4 and the blend 50L-50H are in domain III whereas the sample L-C8 is close to the boundary between Domains II and III; at $T_{\text{treatment}} = 130$ °C, the sample H-C4 is in Domain II, whereas the blend 50L-50H and the sample L-C8 are in Domain I; at $T_{\text{treatment}} = 135$ °C, all the samples are in Domains I. The SNA domains corresponding to the different $T_{\text{treatment}}$ values for each sample are summarized in Table 2.

Table 2 Domains of nucleation of the PE samples at the selected values of $T_{treatment}$.

| Selected T _{treatment} (°C) | H-C4 | 50L-50H | L-C8 |
|--------------------------------------|------------|------------|------------|
| 135 | Domain I | Domain I | Domain I |
| 130 | Domain II | Domain I | Domain I |
| 125 | Domain III | Domain III | Domain III |
| | | | |

Samples prepared in the standard crystalline state defined above will be used to carry out heat treatments at the selected values of $T_{\text{treatment}}$ for different amounts of time $t_{\text{treatment}}$.

4.1. Effect of thermal treatment on the sample H-C4

Effect of long treatment time

The wide-angle X-ray diffraction (WAXS) profiles of the sample H-C4 collected at the temperature $T_{\rm treatment}$ = 125, 130 and 135 °C and of the sample heat treated at $T_{\rm treatment}$ = 125, 130, 135 °C for 10 min and then fast cooled (40°C/min) at room temperature are reported in Figure 4. They are compared with the WAXS profile collected at 25°C of the sample in the standard crystalline state initially used for their preparation.

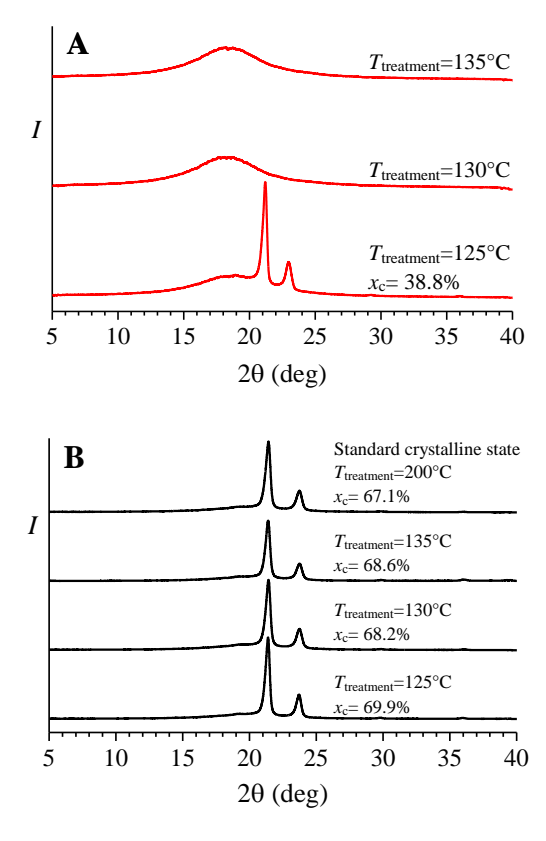


Figure 4 WAXS profiles of specimens of the sample H-C4 recorded at the indicated values of the temperature $T_{treatment}$ (A, red lines) and at 25 °C after heat-treatment at the indicated temperatures for 10 min, obtained by fast cooling (40 °C/min) to room temperature (B, black lines).

It is evident that at $T_{\text{treatment}}$ =135 and 130°C the samples are in the melt state. The WAXS profiles collected at $T_{\text{treatment}}$ =125°C, instead, shows crystalline peaks meaning that HDPE is only partially melt (Figure 4A). The heat-treated samples at $T_{\text{treatment}}$ = 125, 130, 135 and 200 (pristine sample) °C for 10 min, crystallize in the orthorhombic form of PE, upon cooling (Figure 4B). The values of crystallinity index are greater than 65% and increase only slightly as the maximum temperature achieved in the melt decreases.

The SAXS intensity profiles, recorded simultaneously with WAXS profiles, are shown in Figure A1A, A2A of Appendix 7. The Lorentz corrected SAXS intensity collected at high temperatures confirm the absence of any short- and long-range order at $T_{\text{treatment}}$ =135°C and 130°C (Figure 5A), since all the material is in melt state. The SAXS data collected at $T_{\text{treatment}}$ =125°C, instead, shows a main correlation peak, centred around $q_1 = 0.164 \text{ Å}^{-1}$ (long spacing, L = 38.3 nm), confirming that the sample is only partially melted.

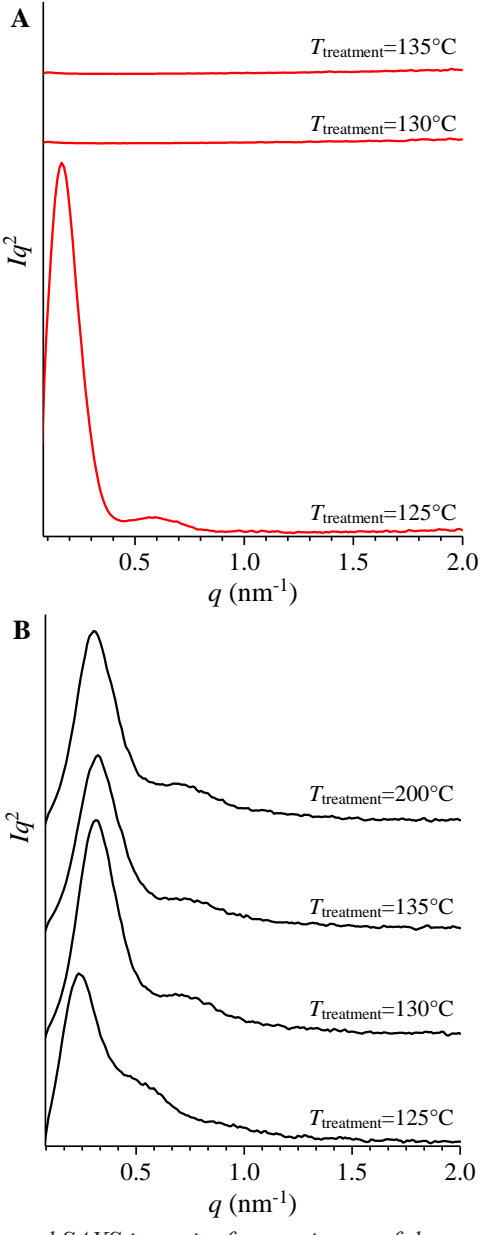


Figure 5 Lorentz corrected SAXS intensity for specimens of the sample H-C4 recorded at the indicated values of the temperature $T_{treatment}$ (A, red lines) and collected at 25 °C, for specimens subjected to heat-treatment at the indicated temperatures for $t_{treatment} = 10$ min and quickly cooled (40 °C/min) from $T_{treatment}$ to room temperature (B, black lines).

The Lorentz corrected SAXS intensity profiles collected at room temperature for the sample H-C4 heat-treated for 10 min at $T_{\text{treatment}}$ =125, 130, 135 and 200 (pristine sample) °C (Figure 5B), show well-defined correlation peaks at q comprised in between 0.2 and 0.3 nm⁻¹, typical of the organization of the lamellar crystals in stacks with a well-defined average periodicity.

The calculated correlation function CF and interface distribution function IDF are reported in the Appendix A7 (Figure A1B, A2B,C). The position of the correlation peaks q_1 and q_2 shown by the Lorentz corrected SAXS intensity profiles (Figure 5), the values of the lamellar parameters (long spacing L and thickness of the amorphous and crystalline layers l_a and l_c respectively), calculated by direct application of Bragg's law, CF and IDF are reported in Table 3-5. The values of the lamellar parameters extracted through the different methods are not significantly different. For this reason, without loss of generality, here in the following the discussion of the results is based on the results extracted from CF.

Table 3 Values of the position of the I and II order correlation peaks (q_1 and q_2) and corresponding characteristic correlation distances (L_1 and L_2 , derived using the Bragg's Law) observed in the Lorentz corrected SAXS intensity profiles of the sample H-C4, crystallized by fast cooling (40 °C/min) after isothermal treatment for 10 min at the indicated values of $T_{treatment}$. The values of the thickness of the lamellar crystals l_c and amorphous layers l_a have been evaluated as $l_c = L_1 \Phi_c$ and $l_a = L_1 \Phi_c$, where Φ_c is the volume fraction of the crystalline phase (see Chapter 3).

| Ttreatment | q ₁ (nm ⁻¹) | <i>L</i> ₁ (nm) | q_2 (nm^{-1}) | L ₂ (nm) | x _c (WAXS) | Φ _c (%) | l _c (nm) | la (nm) |
|------------|------------------------------------|----------------------------|-------------------|---------------------|--------------------------|-----------------------|------------------------|------------|
| 200°C | 0.304 | 20.7 | 0.691 | 18.2 | 0.67 | 0.63 | 13.1 | 7.6 |
| 135°C | 0.324 | 19.4 | 0.731 | 17.2 | 0.69 | 0.65 | 12.6 | 6.7 |
| 130°C | 0.314 | 20.0 | 0.711 | 17.7 | 0.68 | 0.65 | 12.9 | 7.1 |
| 125°C | 0.234 | 26.8 | 0.542 | 23.2 | 0.73 | 0.70 | 17.8 | 9.0 |

Table 4 Values of the lamellar periodicity (L) and thickness of amorphous (l_a) and crystalline (l_c) layers, relative to the sample H-C4, crystallized by fast cooling (40 °C/min) after isothermal treatment for 10 min at the indicated values of $T_{treatment}$. They are deduced from SAXS data through the calculation of the mono-dimensional self-correlation function of electron density fluctuations (correlation function, CF) and the interface distribution function IDF. The heat-treated samples at 125, 130 and 135 °C are prepared from the samples heat treated at 200 °C representing the standard crystalline state.

| | CF | | | | | | IDF | |
|--------|--------|---------------------|------------|--------------------------|--------|---------------------|------------|----------------------------|
| Sample | L (nm) | l _c (nm) | la (nm) | l _c /L (-) | L (nm) | l _c (nm) | la (nm) | <i>l_c/L</i> (-) |
| 200°C | 18.9 | 14.6 | 4.3 | 0.77 | 16.7 | 13.7 | 3.0 | 0.82 |
| 135°C | 18.2 | 13.8 | 4.3 | 0.76 | 16.0 | 13.6 | 2.4 | 0.75 |
| 130°C | 18.4 | 14.1 | 4.4 | 0.76 | 16.2 | 13.4 | 2.7 | 0.83 |
| 125°C | 25.2 | 21.0 | 4.3 | 0.83 | 21.5 | 18.9 | 2.6 | 0.88 |

Table 5 Values of the Lamellar parameters extracted from SAXS data collected at $T_{treatment}$ =125°C using the Bragg's Law and CF for the sample H-C4.

| | Bragg | CF |
|-----------------------|-------|------|
| L (nm) | 38.3 | 39.2 |
| $l_{\rm c}({ m nm})$ | 24.8 | 26.7 |
| $l_{\rm a}({\rm nm})$ | 13.5 | 12.5 |
| <i>lc/L(-)</i> | 0.65 | 0.68 |

For the heat-treated samples at 130, 135 and 200 (pristine sample) °C, the values of the lamellar parameters measured at 25°C are not substantially different ($L\approx18$ nm, $l_c\approx14$ nm and $l_a\approx4$ nm) (Table 4). In contrast, the sample heat treated at 125°C for 10 min exhibits at 25 °C different values of the lamellar parameter L, l_c and l_a , equal to ≈25 , 21 and 4 nm, respectively. Hence, as shown in Figure 6, the lamellar thickness achieved by cooling at 40 °C/min the sample in the semi-solid state from 125 °C, is greater than that achieved by cooling the melt at the same rate from 130, 135 and 200°C. On the other hand, during the heat treatment at 125°C, that is when the sample is in the semi-solid state, (Figure 5A and 6) the initial lamellar thickness l_c equal to ≈14 nm increases to about 27 nm while the values of long

spacing L and of the thickness of the amorphous layers l_a becomes on the order of 39 and 12 nm, respectively. The remarkable increase of L and l_c during the treatment at 125 °C is due to the survival of the thickest and more perfect crystals, as the less thick crystals of minor perfection melt. This means that the thickening of the crystals observed in the successive cooling step after 10 min at $T_{\text{treatment}}$ is due to the survival of the thickest crystals during the heat treatment at 125 °C.

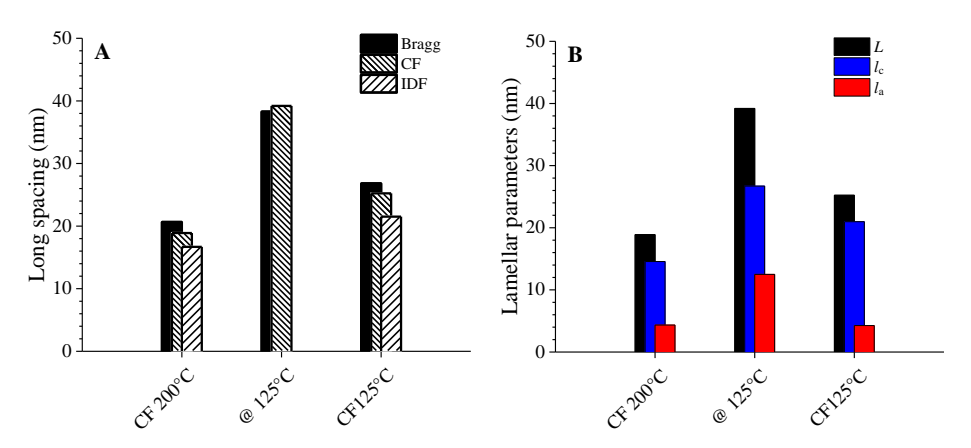


Figure 6 Values of the long spacing L(A,) and thickness of amorphous l_a and crystalline l_c layers (B) evaluated from SAXS data collected at: $25^{\circ}C$ for the sample H-C4 in the standard crystalline state, obtained by fast cooling (40 °C/min) to $25^{\circ}C$ after 10 min at $200^{\circ}C$ (CF $200^{\circ}C$); at $125^{\circ}C$ for the sample H-C4 in the initial standard crystalline state, subjected to heating to $125^{\circ}C$ (@ $125^{\circ}C$); at $25^{\circ}C$ for the sample H-C4 in the initially standard crystalline state, subjected to fast cooling (40 °C/min) to $25^{\circ}C$, after 10 min at $125^{\circ}C$ (CF $125^{\circ}C$). In A the values of L have been calculated by using the Bragg's law, the monodimensional self-correlation function of electron density fluctuations (CF) and the Interface distribution function (IDF). The lamellar parameters in B are obtained from CF.

Effect of short treatment times

The structural changes induced at the selected $T_{\rm treatment}$ temperatures for short $t_{\rm treatment}$ time are also studied. The DSC heating scans of the sample H-C4 in the initial standard crystalline state, subjected to thermal treatments at 125, 130 and 135 °C for different amounts of time $t_{\rm treatment}$ and then cooled to 25 °C at 40

°C/min, are shown in Figure 7. The melting curve of the sample in the initial standard crystalline state, and the corresponding melting temperature, equal to 128.6 °C are also indicated.

The melting scans recorded after thermal treatment at 135° C (Figure 7A) do not change with the time that the sample is kept at this temperature before cooling and match the DSC heating curves of the sample in the standard crystalline state. Regardless of the heat treatment time $t_{\text{treatment}}$ at 135° C, indeed, the sample is characterized by the same T_{m} and the same ΔH_{m} . It means that at this temperature no crystals survive, and the melt reaches an "isotropic state" (SNA Domain I), able to reproduce, after cooling, the standard crystalline state. The invariance of the melting temperature with the treatment time at 135° C is in agreement with the SAXS results, that show that the lamellar parameters of the sample H-C4 in the initial standard crystalline state do not change significantly after heat treatment at 135° C, even for prolonged time (Table A1 of Appendix A7).

For $T_{\text{treatment}}$ =130°C, it should be noted that the selected temperature corresponds to the $T_{\text{s ideal}}$ of the sample. This temperature is close to that of the melting peak of the sample in the standard crystalline state (128.6 °C) and, as shown in the preceding paragraph (Figure 4A), complete melting is achieved for prolonged treatment times at 130 °C. The DSC scans (Figure 7B) recorded for $t_{\text{treatment}}$ <10 s show splitting of the endothermic peaks. The new peaks are centred at $T_{\text{m1}}\approx$ 129 and $T_{\text{m2}}\approx$ 131 °C. The first temperature is close to the melting temperature of the sample in the standard crystalline state, while the second temperature is 1 °C above the selected $T_{\text{treatment}}$ value. Increasing the treatment time from 1 to 10 s, the relative area of the peaks changes. In particular, the peak at T_{m2} decreases in intensity, after10 s of heat treatment appears as a shoulder of the first peak, and disappears completely for $t_{\text{treatment}} \geq$ 20 s. Further increase of the thermal treatment time results in endotherms with a single peak, centred at the temperature of 129.3 °C, which is 0.7 °C above the melting temperature of the sample in the standard

crystalline state (128.6 °C). These results suggest the occurrence of strong changes in the melt in the early 20 s of the heat treatment at $T_{\text{treatment}}$ =130 °C, because of incomplete melting. The survived crystals in the early 20 s of heat treatment experience annealing and give rise to the high temperature melting peak at $T_{\rm m2}$. The relative area of this peak decreases, because the relative amount of survived crystal decreases as $t_{\text{treatment}}$ increases and, after $t_{\text{treatment}}$ of 20 s, disappear completely. In other terms, for $t_{\text{treatment}} > 20 \text{ s}$ the sample achieves complete melting at 130 °C. The crystals that form by cooling the melt from $T_{\text{treatment}} = 130$ °C, instead, give rise to crystals that melt at $T_{\rm ml} \approx 129$ °C already for low permanence time at this temperature. Since the sample at 130 °C is the SNA Domain II, close to the boundary with the Domain III, the concentration of self-nuclei is very high, so that the crystallization of this new crystals during the cooling step as well as the annealing process that the survived crystals are subjected to are very fast. Hence, the effect of the thermal treatment at 130 °C for different amounts of time $t_{\text{treatment}}$ results, already for short treatment time (1 s), in the formation of slightly thicker crystals upon cooling, than those of the initial sample crystallized in the standard crystalline state. The constant melting temperature suggests that the lamellar thickness of these new crystals does not change by prolonging $t_{\text{treatment}}$ till to 300 s. This is confirmed by the results of SAXS data analysis in Figure 8. The SAXS data are collected at room temperature, for the sample H-C4 in the initial standard crystalline state, subjected to heat treatment at 130 °C for different amounts of time (Figure A8 of Appendix A7). It is apparent that after 10 s of thermal treatment at 130 °C, the value of the lamellar parameters L and l_c increase from 22.7 and 18.3 nm, respectively, for the sample in the standard crystalline state, to 24.7 and 20.4 nm, respectively for the heat-treated sample. After 300 s at 130°C, the lamellar crystals undergo further thickening, reaching l_c value of 21 nm. The values of the thickness of the amorphous layers, instead, remain almost constant and close to 4 nm.

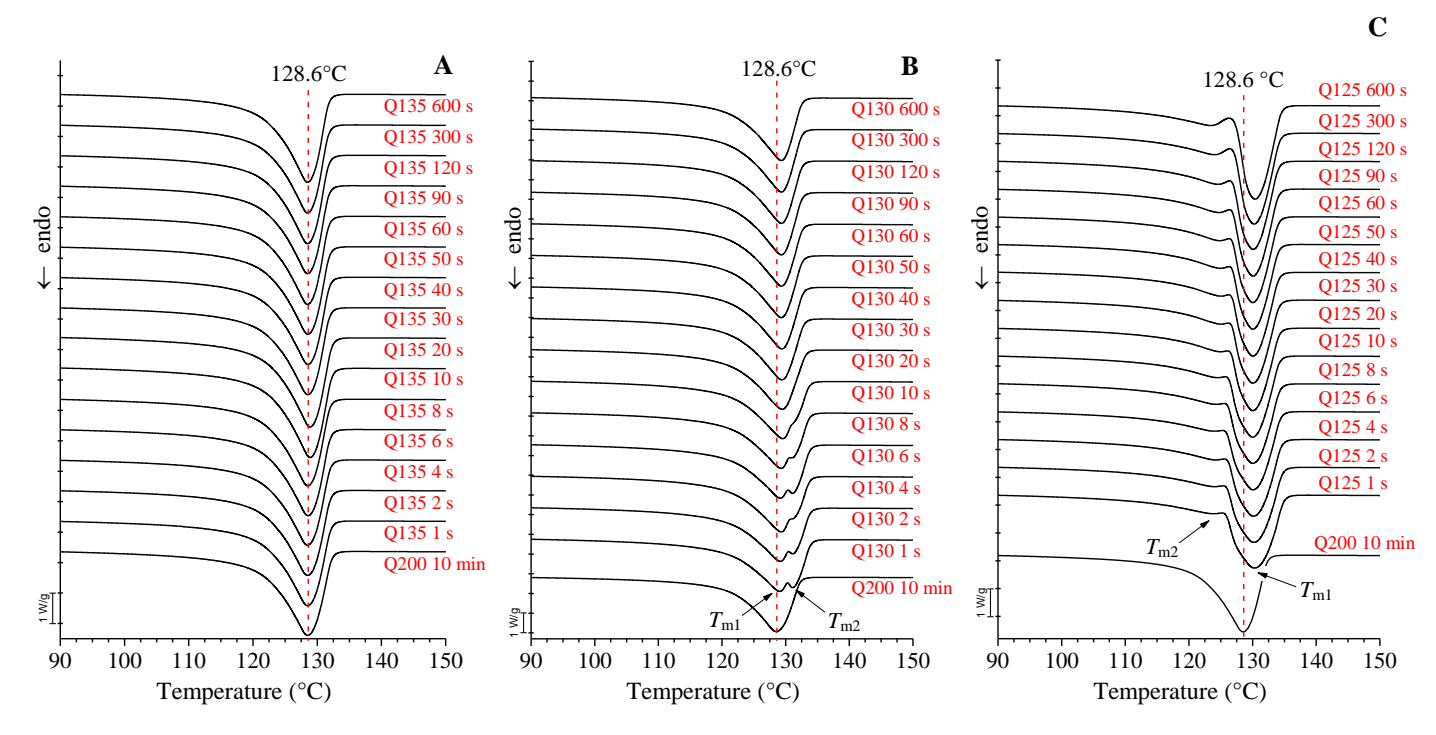


Figure 7 DSC heating scans of the sample H-C4 in the initial standard crystalline state (Q200 10 min), subjected to thermal treatments at $T_{treatment}$ = 135 (A), 130 (B) and 125 (C) °C, for the indicated amounts of time $t_{treatment}$. The melting temperature of the sample in the standard crystalline state equal to 126.8 °C is indicated.

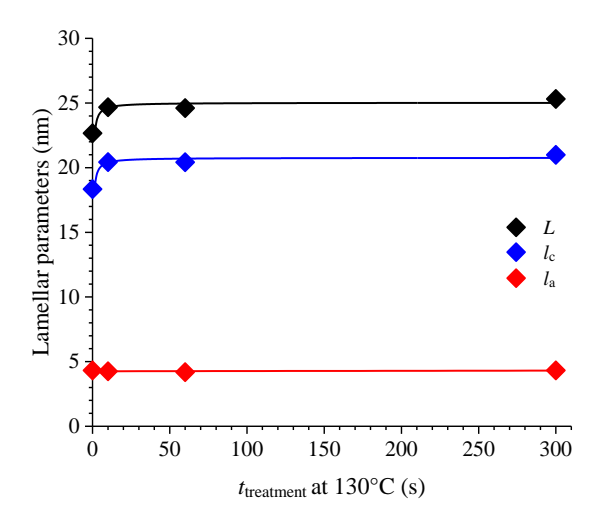


Figure 8 Values of the lamellar parameters of the sample H-C4 obtained from the monodimensional self-correlation function of electron density fluctuations (CF), extracted from SAXS data of the sample H-C4 in the initial standard crystalline state (Q200 10 min), subjected to thermal treatment at $T_{treatment} = 130$ °C, for different amounts of time $t_{treatment}$. The data at $t_{treatment} = 0$ s are relative to the sample in the standard crystalline state (non-heat treated).

The DSC scans of Figure 7C show the effect of thermal treatment at $T_{\text{treatment}} = 125^{\circ}\text{C}$, corresponding to Domain III, of self-nucleation and annealing of the sample H-C4 (Table 2). The DSC curves of the sample H-C4 show a main melting peak at $T_{\text{ml}} \approx 130$ °C which is slightly greater than the melting temperature of the sample in the initial standard crystalline state ($T_{\text{m}} = 128.6$ °C). Moreover, after just 1 s of thermal treatment at 125 °C, a small endothermic hump appears at $T_{\text{m2}} \approx 124$ °C, immediately below the selected value of $T_{\text{treatment}}$. The area subtending this peak tends to increase with time, while the peak at T_{m1} becomes narrower. As observed in the WAXS profiles collected at high temperatures (Figure 4A), 10 min of thermal treatment at 125°C induces partial melting. The relative amount of pristine crystals that melt during the isothermal treatment at 125°C increases as the treatment time increases. The endothermic peak centred at T_{m1} greater than the melting temperature of the pristine sample is due to the melting of the surviving crystals that experience structural rearrangements by effect of annealing. The

broad hump at low temperature $T_{\rm m2}$, instead, is due to the melting of the crystals that are formed during fast cooling from 125 to 25°C, starting from the residual melt. As the treatment time at 125 °C increases, the melt fraction increases, and the area subtending the hump at $T_{\rm m2}$, increases. As pointed out by Bassett¹, polymer chains may easily experience molecular fractionation during crystallization, due to the tendency of chain segments with different defect content to crystallize separately, even if the resultant crystals melt under a single endothermic peak. In our case, the heat treatment at 125 °C induces the melting of the most defective crystals, whereas the less defective crystals survive, and undergo annealing. In the successive cooling step, the defective chain segments rejected in the melt crystallize at lower temperatures. During the final heating scan, also melting occurs separately as, compared with the melting temperature of the pristine crystals, the annealed crystals melt at greater temperature while the crystals formed upon cooling melt at lower temperature.

Figure 9 shows the values of the melting temperatures $T_{\rm m1}$ and $T_{\rm m2}$ as a function of the treatment time at 125 °C. The melting temperature $T_{\rm m2}$ relative to the crystals formed during the cooling step increases in the first 20 s and then becomes approximately constant until 60 s (~125°C). Further increase of $t_{\rm treatment}$ induces a decrease in $T_{\rm m2}$, till approaching a value of 123.5 °C for $t_{\rm annealing} = 600$ s. This decrease is probably due to the fact that, as the treatment time at 125 °C increases, the crystals that form during the successive cooling step tend to include a major number of defects, giving rise to crystals that melt at progressively lower temperatures. The main melting peak at $T_{\rm m1}$, instead, is constant in the first 120 s of $t_{\rm annealing}$, then tends to shift to higher temperatures (from 129.8°C to 130.5 °C for $t_{\rm annealing} = 600$ s), due to the progressive "perfectioning" of the residual crystals at 125 °C.

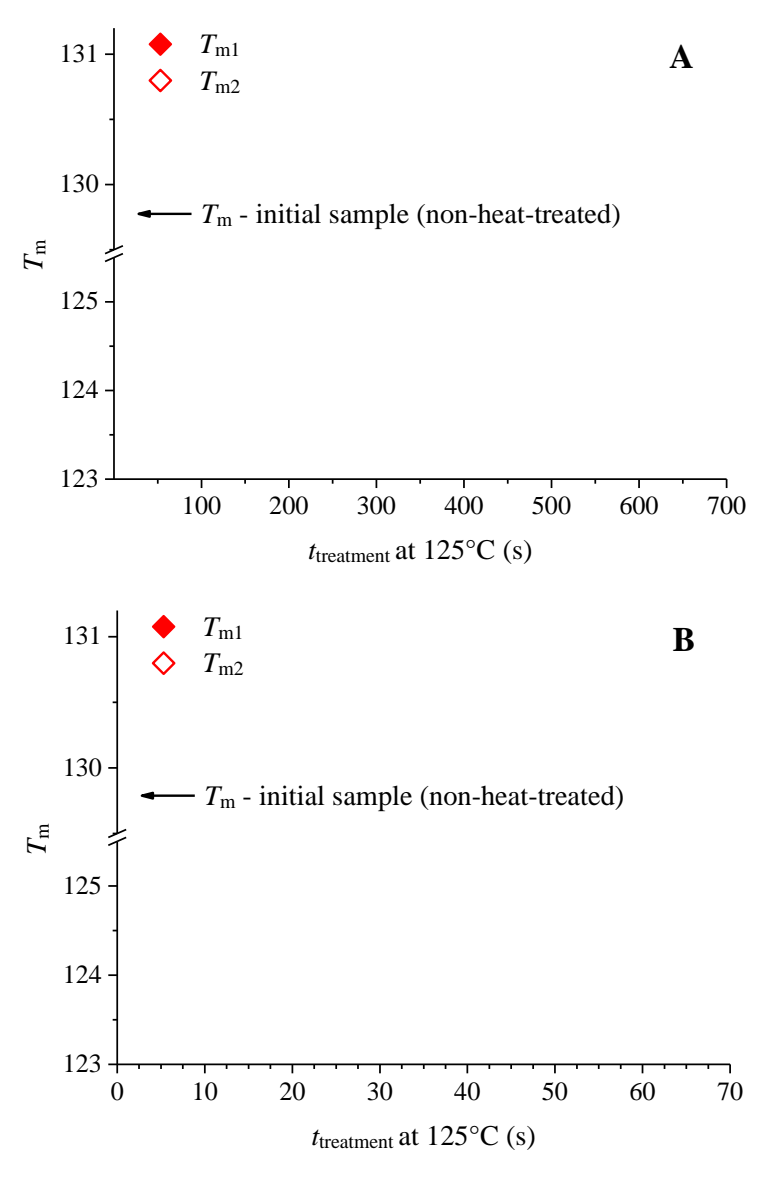


Figure 9 Temperatures of the 1° (T_{m1}) and 2° (T_{m2} , hump) melting peaks of the sample H-C4 in the initial standard crystalline state, heat-treated at $T_{treatment}$ =125°C as a function of time $t_{treatment}$ in the first 600 (A) and 60 s (B).

The SAXS data collected at room temperature, for the sample H-C4 heat treated at 125 °C for 10, 60 and 300 s are illustrated in Figure A9 of Appendix 7. The

values of the lamellar parameters extracted using the Bragg's law, CF and IDF methods are reported in Table A1 of Appendix A7. In particular, the values of the lamellar parameters extracted from CF calculations are reported in Figure 10 as a function of the treatment time $t_{\text{treatment}}$ at 125 °C. Compared with the lamellar parameters of the sample in the pristine standard crystalline state, similar to the heat treatment at 130 °C, also the heat treatment at 125 °C induces an increase of long spacing and lamellar thickness already in the early 10 s. After 10 s the long spacing reaches the value of 24.1 nm and after 300 s increases to 24.6 nm, corresponding to values of crystal thickness of 19.7 nm and 20 nm, respectively. The thickness of the amorphous layers, instead, remains constant, around 4.5 nm.

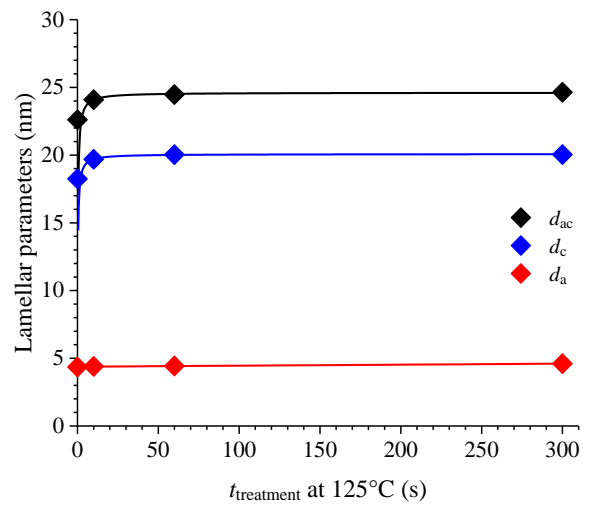


Figure 10 Values of the lamellar parameters of the sample H-C4 obtained from the monodimensional self-correlation function of electron density fluctuations (CF), extracted from SAXS data of the sample in the initial standard crystalline state, subjected to thermal treatment at $T_{treatment} = 125$ °C, for different amounts of time $t_{treatment}$. The data at $t_{treatment} = 0$ s are relative to the sample in the standard crystalline state (non-heat treated).

The POM images recorded for the sample H-C4 in the standard crystalline state and after heat treatment at $T_{\rm treatment} = 125$ °C for $t_{\rm treatment} = 10$ min and successive cooling from 125 to 25 °C at 40 °C/min (Figure 11) do not show substantial differences. In all cases the morphology is characterized by the presence of small

birefringent entities (small lamellar aggregates) covering uniformly the observation field, with no substantial differences. The same results have been obtained for the other samples at each investigated $T_{\rm treatment}$ and $t_{\rm treatment}$, indicating that the effect of thermal treatment should be sought at smaller length scale.

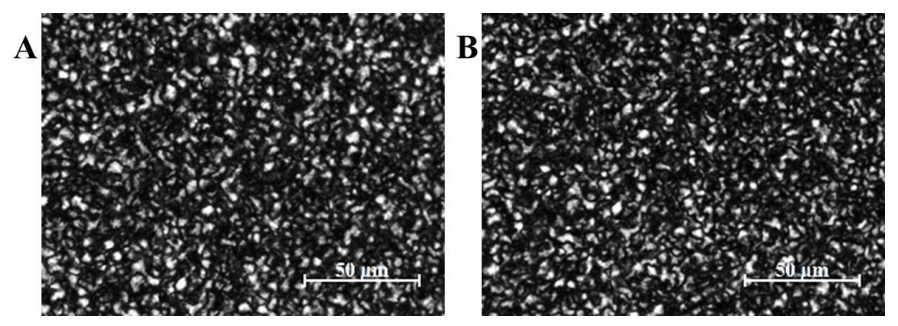


Figure 11 Polarized light microscopy images of the H-C4 sample: A) in the standard crystalline state; B) after heat treatment at $T_{treatment}$ =125°C for $t_{treatment}$ = 10 min and successive cooling from 125 to 25 °C at 40 °C/min.

4.2. Effect of thermal treatments on the sample L-C8

Effect of long treatment time

The sample L-C8 has been subjected to heat treatment at selected temperatures equal to 125, 130 and 135°C. The SNA results (Figure 3) indicate that the sample L-C8 is in Domain I of nucleation for $T_{\rm treatment}$ =135 and 130°C, and in Domain III, close to the boundary with Domain II for $T_{\rm treatment}$ =125°C.

WAXS data collected at high temperatures (Figure 12A) indicate complete melting at 130 and 135°C, while only partial melting at $T_{\rm treatment}$ =125°C occurs. The WAXS profile collected at 25 °C for the heat-treated samples at $T_{\rm treatment}$ are shown in Figure 12B. All the samples crystallize in the orthorhombic form of PE, and the crystallinity index increases as the treatment temperature decreases (Figure 12 B).

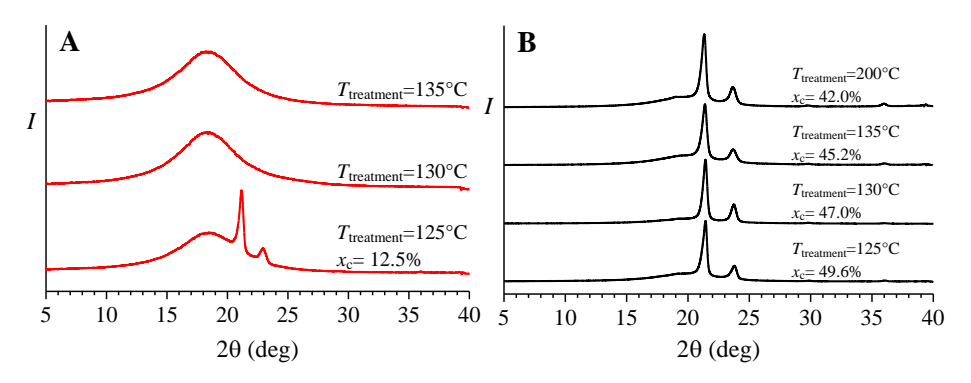


Figure 12 WAXS profiles of specimens of the sample L-C8 recorded at the indicated values of the temperature $T_{treatment}$ (A, red lines) and at 25 °C, after heat-treatment at the indicated temperatures for 10 min, obtained by fast cooling (40 °C/min) to room temperature (B, black lines).

The SAXS intensity profiles, before and after correction for the Lorentz factor, recorded simultaneously with WAXS profiles, are shown in Figure A3-A4 of Appendix 7 and Figure 13, respectively. The Lorentz corrected SAXS intensity collected at 130 and 135 °C are featureless, confirming that the sample L-C8 is in

the melt state at these temperatures (Figure 13A). The SAXS data collected at $T_{\text{treatment}}$ =125°C, instead, show a well-defined correlation peak (Figure 13A) after correction for the Lorentz factor, centred at $q_1 = 0.125 \text{ Å}^{-1}$ (L = 50.2 nm), confirming that the sample is partially melted.

The Lorentz's corrected SAXS profile (Figure 13B) collected at room temperature for the sample L-C8 heat treated at 125, 130 and 135 °C show a well-pronounced first order correlation peak at q = 0.2-0.3 nm⁻¹ followed by a faint second order peak at q_2 = 0.5-0.7 nm⁻¹ (see Table 6). The values of the lamellar parameter extracted from SAXS data of Figure 13 through application of Bragg's law, and the calculation of CF and IDF are shown in Table 6-8.

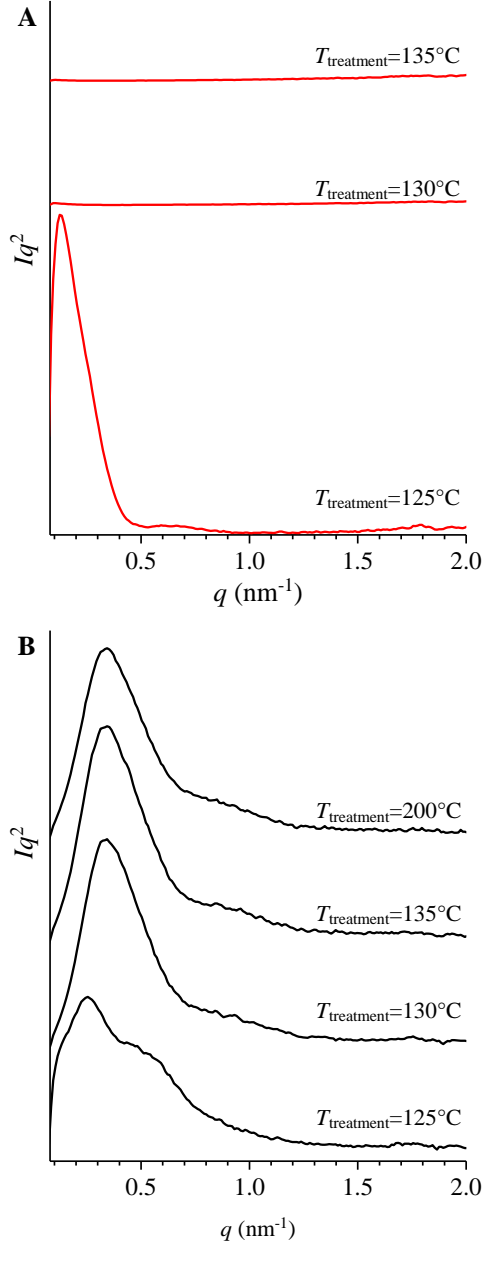


Figure 13 SAXS Lorentz corrected SAXS intensity for specimens of the sample L-C8 recorded at the indicated values of the temperature $T_{treatment}$ (A, red lines) and collected at 25 °C, for specimens subjected to heat-treatment at the indicated temperatures for $t_{treatment}$ = 10 min and quickly cooled (40 °C/min) from $T_{treatment}$ to room temperature (B, black lines).

Table 6 Values of the position of the I and II order correlation peaks $(q_1 \text{ and } q_2)$ and corresponding characteristic correlation distances $(L_1 \text{ and } L_2, \text{ derived using the Bragg's } Law)$ observed in the Lorentz corrected SAXS profiles of the sample L-C8, crystallized by fast cooling $(40 \, ^{\circ}\text{C/min})$ after isothermal treatment for 10 min at the indicated values of $T_{treatment}$. The values of the thickness of the lamellar crystals l_c and amorphous layers l_a have been evaluated as $l_c = L_1 \, \Phi_c$ and $l_a = L$ - l_c , where Φ_c is the volume fraction of the crystalline phase (see Chapter 3).

| Ttreatment | q ₁ (nm ⁻¹) | <i>L</i> ₁ (nm) | q ₂ (nm ⁻¹) | L ₂ (nm) | x _c (WAXS) | Φ _c (%) | l _c (nm) | la (nm) |
|------------|------------------------------------|----------------------------|------------------------------------|---------------------|-----------------------|-----------------------|------------------------|------------|
| 200°C | 0.343 | 18.3 | / | / | 0.42 | 0.38 | 7.0 | 11.3 |
| 135°C | 0.343 | 18.3 | / | / | 0.45 | 0.41 | 7.7 | 10.6 |
| 130°C | 0.343 | 18.3 | / | / | 0.47 | 0.43 | 7.9 | 10.4 |
| 125°C | 0.254 | 24.7 | / | / | 0.50 | 0.46 | 11.4 | 13.3 |

Table 7 Values of the lamellar periodicity (L) and thickness of amorphous (l_a) and crystalline (l_c) layers, relative to the sample L-C8, crystallized by fast cooling (40 °C/min) after isothermal treatment for 10 min at the indicated values of $T_{treatment}$. They are deduced from SAXS data through the calculation of the mono-dimensional self-correlation function of electron density fluctuations (correlation function, CF) and the interface distribution function IDF.

| Cr | | | | | | J | IDF | |
|--------|--------|---------------------|------------|-------------|--------|---------------------|---------|----------------------------|
| Sample | L (nm) | l _c (nm) | la (nm) | lc/L (-) | L (nm) | l _c (nm) | la (nm) | <i>l_c/L</i> (-) |
| 200°C | 17.7 | 13.5 | 4.2 | 0.77 | 13.8 | 9.7 | 4.1 | 0.70 |
| 135°C | 18.4 | 14.1 | 4.3 | 0.77 | 13.4 | 9.3 | 4.1 | 0.69 |
| 130°C | 17.2 | 12.8 | 4.4 | 0.75 | 13.7 | 9.4 | 4.3 | 0.69 |
| 125°C | 27.9 | 23.8 | 4.1 | 0.85 | 21.6 | 17.3 | 4.3 | 0.89 |

Table 8 Values of the Lamellar parameters extracted from SAXS data collected at $T_{treatment}$ =125°C using the Bragg's Law and CF for the sample L-C8.

| | Bragg | CF |
|----------------------|-------|------|
| L (nm) | 50.2 | 49.7 |
| $l_{\rm c}({ m nm})$ | 44.8 | 38.8 |
| l _a (nm) | 5.4 | 10.9 |
| $l_{ m c}/L$ (-) | 0.89 | 0.78 |

Thermal treatments at 135°C and 130°C do not bring significant effects on the values of the lamellar parameters compared to those of the initial standard crystalline state. In particular, with reference to the values of the parameters extracted from CF, the values of long spacing, thickness of the amorphous and crystalline layers (L, l_a and l_c) are \approx 17-18, 4 and 13-14 nm, respectively. When the sample L-C8 in the initial standard crystalline state is heat-treated at 125°C, a substantial increase in long spacing and lamellar thickness value is observed, with $L \approx 28$ nm, $l_c \approx 24$ nm. The thickness of the amorphous layers, instead, l_a remains almost constant and equal to \approx 4 nm. These changes are summarized in Figure 14. Finally, the lamellar parameters calculated for the sample L-C8 in the semi-solid state at 125 °C, Table 8, reveal that at this temperature only a small fraction of thick crystals survive, with thickness around 39 nm. The long spacing L and the thickness of amorphous layers l_a reach the values of \approx 50 and 11 nm, respectively. The large thickness of the surviving crystals accounts for the large value of the lamellar thickness achieved by the sample by fast cooling from 125 °C to 25 °C.

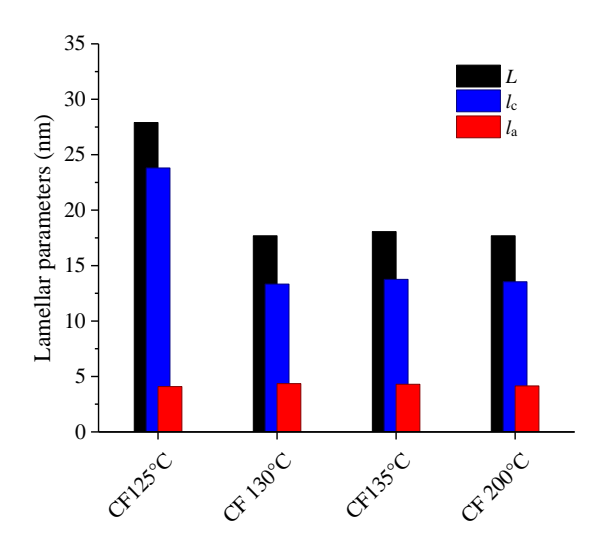


Figure 14 Values of the long spacing L and thickness of amorphous l_a and crystalline l_c layers evaluated from SAXS data collected at 25°C for the sample L-C8 in the standard crystalline state (CF 200°C), successively subjected to fast cooling (40 °C/min) to 25 °C, after 10 min at 125 °C (CF 125°C), at 130 °C (CF 130°C) and at 135 °C (CF 135°C). The lamellar parameters are obtained from CF.

Effect of short treatment times

The effect of short treatment times at $T_{\text{treatment}} = 125$, 130, 135 °C for the sample L-C8 has been studied with different techniques.

The DSC heating scans recorded for the sample L-C8 in the initial standard crystalline state, subjected to heat treatments at 125, 130 and 135 °C for different amounts of time $t_{\text{treatment}}$ and then cooled to 25 °C at 40 °C/min are shown in Figure 15.

The DSC heating curves recorded for the heat-treated sample at 130 and 135 °C (Figure 15A,B) do no show significant changes, and are similar to the DSC curve of the sample in the initial standard crystalline state. At these temperatures, indeed, the sample L-C8 is in Domain I (Table 2) that is, the treatment temperatures of 130 and 135 °C are high enough to melt all the crystallizable material and to erase any melt memory.

In parallel experiments, the heat-treated sample L-C8 at 130 and 135 °C for different amounts of time, have been analysed also by collecting SAXS data at room temperature (Figure A10 and A11 and Table A2 of Appendix A7). The values of the lamellar parameters extracted from the SAXS data through CF calculations are reported in Figure 16 as a function of the treatment time. It is apparent that when the selected $T_{\text{treatment}}$ is 135°C (Figure 16A), the values of lamellar parameter are identical to those of the sample in the initial standard crystalline state, regardless of the value of treatment time. This result agrees well with the fact that the melting temperature of the sample L-C8 heat treated at 135 °C does not change with the treatment time (Figure 15A). However, by effect of the thermal treatment at 130 °C (Figure 16B), the values of long spacing and lamellar thickness increase from ≈15 and 20 nm, respectively, to ≈18 and 22 nm, respectively, already after 10 s of treatment time. The thickness of the amorphous layers, instead, remain constant at ≈5 nm. The increase of lamellar thickness is in contrast with the invariance of the melting temperature observed in the DSC scans of the sample L-C8 heat treated at 130 °C (Figure 15B). This increase is probably due to the fact that the lamellar stacks namely contributing to SAXS intensity (i.e. characterized by a major contrast) after heat treatment at 130 °C are essentially the thickest crystals.

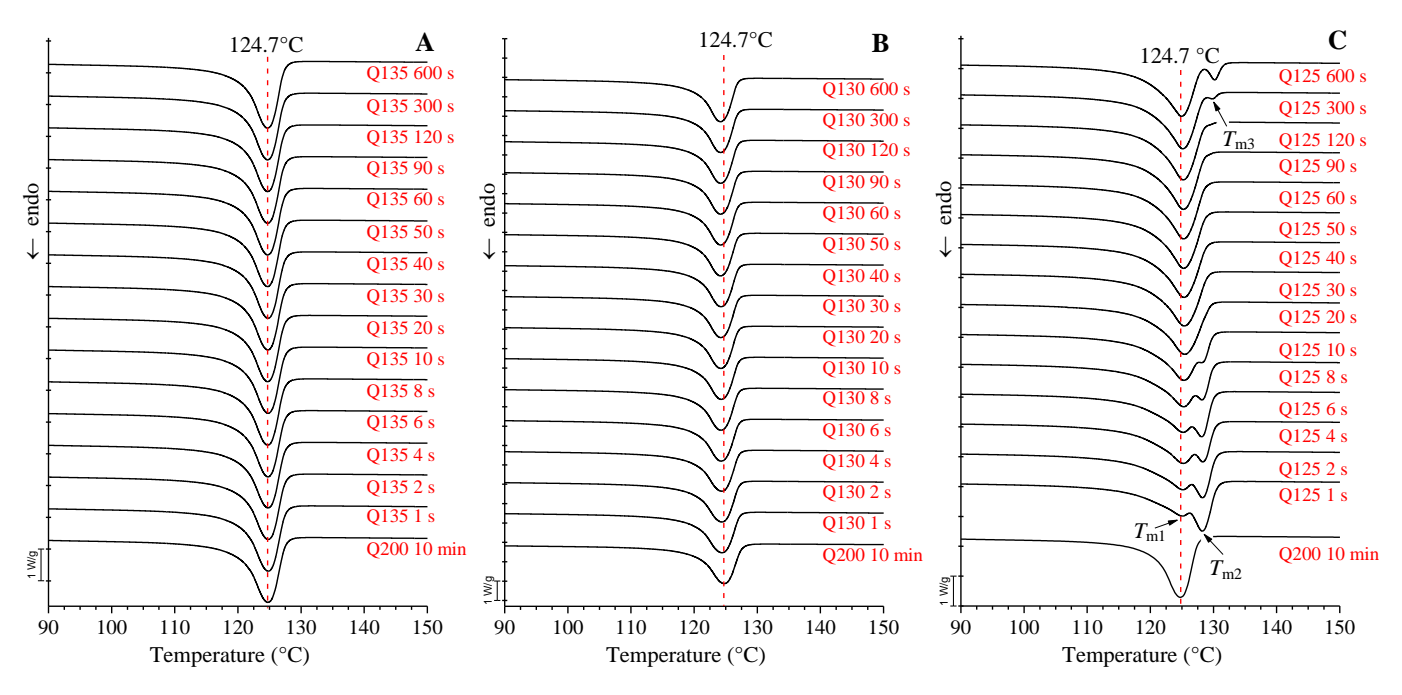


Figure 15 DSC heating scans of the sample L-C8 in the initial standard crystalline state (Q200 10 min), subjected to thermal treatments at $T_{treatment} = 135$ (A), 130 (B) and 125 (C) °C, for the indicated amounts of time $t_{treatment}$. The melting temperature of the sample in the standard crystalline state equal to 124.7 °C is indicated.

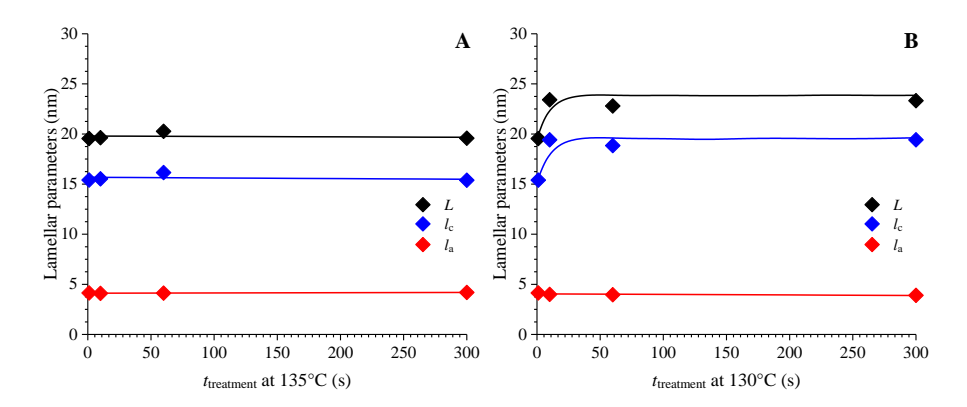


Figure 16 Values of the lamellar parameters of the sample L-C8 obtained from the monodimensional self-correlation function of electron density fluctuations (CF), extracted from SAXS data of the sample in the initial standard crystalline state (Q200 10 min), subjected to thermal treatment at $T_{treatment} = 135$ (A) and 130 (B) °C, for different amounts of time $t_{treatment}$. The data at $t_{treatment} = 0$ are relative to the sample in the standard crystalline state (non-heat treated).

The DSC heating curves recorded for the heat-treated sample L-C8 at 125 °C (Figure 15C) show that a permanence time of 1s at this temperature (Figure 15C), induces a splitting of the melting peak. The first peak is centred at temperature $T_{\rm ml}$ of 125.1°C that is close to the melting temperature of the sample in the initial standard crystalline state (124.7 °C), while the second peak is centred at $T_{\rm m2}$ = 128.2°C (Figure 15C). For $t_{\text{treatment}} \leq 20 \text{ s}$, as the treatment time increases, the intensity of the first melting peak increases, while the intensity of the second peak, decreases up to disappear. For t_{treatment} comprised between 20 and 300 s only a single melting peak at $T_{\rm ml}$ is present For $t_{\rm treatment} \ge 300$ s, a third melting peak appears, at temperatures $T_{\rm m3}$ greater than 125 °C. The position of $T_{\rm m1}$, $T_{\rm m2}$, and $T_{\rm m3}$ as a function of the annealing time are shown in Figure 17. Considering that the sample L-C8 is in Domain III, close to boundary with Domain II at 125 °C, the results of DSC analysis suggest that the changes occurring in the melt in the early 20 s of the heat treatment at $T_{\text{treatment}}$ =125 °C are due to incomplete melting. As already described for the sample H-C4 heat treated at 130°C, the fraction of crystals that survive in the early 20 s of heat treatment experience annealing,

giving rise to the high melting temperature peak at $T_{\rm m2}$. The intensity of this peak decreases as the annealing time increases, because the relative amount of the surviving crystals decreases. The low melting temperature peak at $T_{\rm m1}$, instead, is due to the melting of the crystals that form during cooling. The relative area of this peak increases, because the relative amount of pristine crystals that undergo melting increases. For $t_{\rm treatment} > 20$ s the sample achieves complete melting at 125 °C, and the DSC curves show the presence of single melting peak at $T_{\rm m1}$. However, prolonging the heat treatment at 125 °C for $t_{\rm treatment} \ge 300$ s, part of the crystals that melt at $T_{\rm m1}$ undergo fast re-crystallization during the DSC scan, giving rise to a small high temperature melting peak at a $T_{\rm m3}$. Re-crystallization probably occurs because the prolonged treatment of the melt in a region in between Domain II and III leads to a remarkable increase of self-nuclei, able to accelerate the formation of these new crystals.

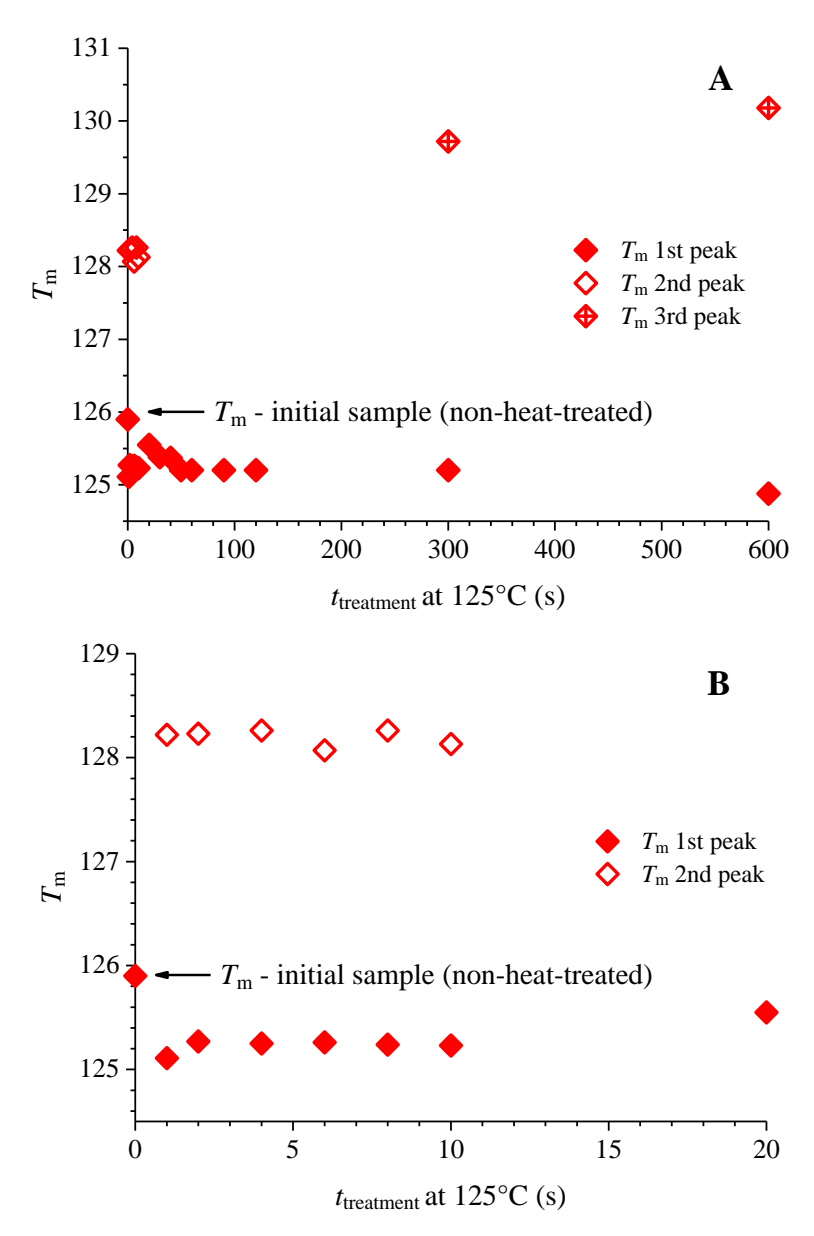


Figure 17 Melting temperature of the $1^{\circ}(T_{ml})$, $2^{\circ}(T_{ml})$ and $3^{\circ}(T_{m3})$ melting peaks of the sample L-C8 in the initial standard crystalline state, heat-treated at $T_{treatment}$ =125°C as a function of time $t_{treatment}$ in the first 600 (A) and 60 s (B).

The SAXS data collected at room temperature, for the sample L-C8 heat treated at 125 °C for 10, 60 and 300 s are collected in Figure A12 of Appendix 7. The values of the lamellar parameters extracted using the Bragg's law, CF and IDF methods are reported in Table A2 of Appendix A7. In particular, the values of the lamellar parameters extracted from CF calculations are reported in Figure 18 as a function of the treatment time $t_{\text{treatment}}$ at 125 °C. Compared with the lamellar parameters of the initial sample in the standard crystalline state, also for the sample L-C8 the heat treatment at 125 °C induce a sudden increase of long spacing and lamellar thickness already in the early 10 s. In particular, after 10 s, the values of long spacing and lamellar thickness increase from \approx 20 and 15 nm, respectively, to the values of \approx 24 and 19 nm, respectively, while the thickness of the amorphous layers remains constant, around \approx 4 nm.

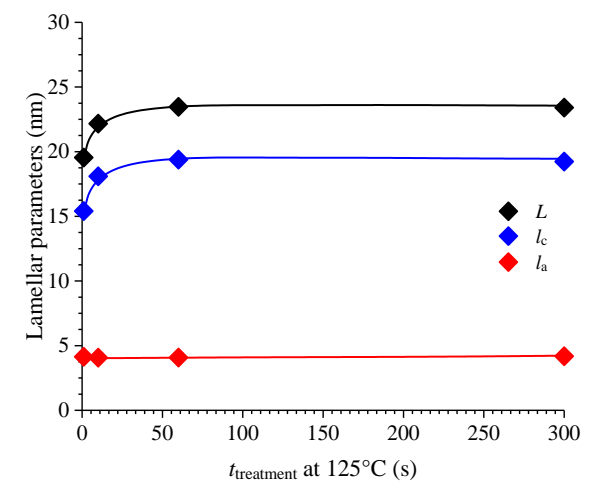


Figure 18 Values of the lamellar parameters of the sample L-C8 obtained from the monodimensional self-correlation function of electron density fluctuations (CF), extracted from SAXS data of the sample in the initial standard crystalline state, subjected to thermal treatment at $T_{treatment} = 125$ °C, for different amounts of time $t_{treatment}$. The data at $t_{treatment} = 0$ are relative to the sample in the standard crystalline state (non-heat treated).

4.3. Effect of heat treatments on the blend 50L-50H

Effect of long treatment time

Heat treatments have been applied also to the LLDPE-HDPE blend 50L-50H, starting from the standard crystalline state. As shown in Table 2 and Figure 3, the blend 50L-50H is in the SNA Domain I at the temperature of heat treatment $T_{\text{treatment}} = 130^{\circ}\text{C}$ and 135°C , and in the SNA Domain III at $T_{\text{treatment}} = 125^{\circ}\text{C}$.

The WAXS profiles collected at 125, 130 and 135 °C are shown in Figure 19A. Similar to the neat components H-C4 and L-C8, also the blend 50L-50H results in the melt state at 130 ad 135 °C, and is only partially melted at 125 °C (crystallinity index $x_c \approx 29$ %). The WAXS profile collected at 25 °C for the sample in the standard crystalline state before and after heat-treatment at 125, 130 and 135 °C are shown in Figure 19B. All the samples crystallize in the orthorhombic form of PE, and the crystallinity index increases as the treatment temperature decreases from 135 to 125 °C (Figure 12B).

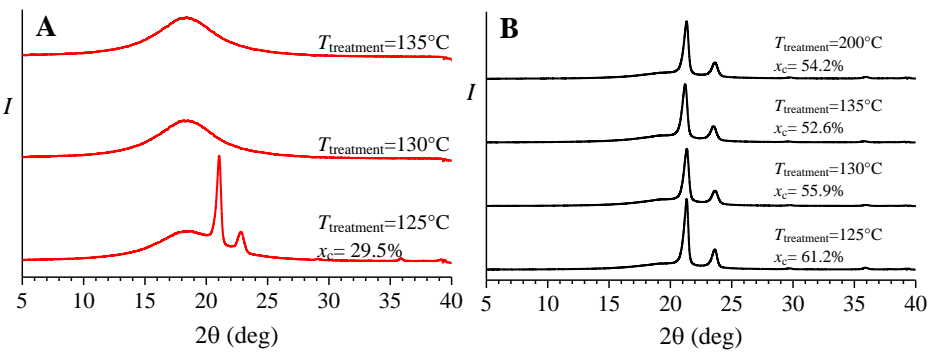


Figure 19 WAXS profiles of specimens of the blend 50L-50H recorded at the indicated values of the temperature $T_{treatment}$ (A, red lines) and at 25 °C, after heat-treatment at the indicated temperatures for 10 min, obtained by fast cooling (40 °C/min) to room temperature (B, black lines).

The SAXS intensity profiles, before and after correction for the Lorentz factor, recorded simultaneously with WAXS profiles, are shown in Figure A5A, A6A of Appendix 7 and 20, respectively. The Lorentz corrected SAXS intensity profiles,

collected in parallel with WAXS data are shown in Figure 20. The SAXS data collected at the 130 and 135 °C are featureless, because the sample is in the melt state. For the data collected at 125 °C, a correlation peak centred at $q_1 = 0.154$ Å⁻¹ (L = 40.8 nm) is present, indicating that the residual crystals are organized in stacks. The values of lamellar parameters evaluated from Bragg approach, CF and IDF are listed in Table 9-11.

Similar to the neat components, also for the 50L-50H blend the heat treatments at 135° C and 130° C do not bring significant effects on the values of the lamellar parameters measured at 25° C compared to those of the initial standard crystalline state. In particular, with reference to the values of the parameters extracted from CF, the values of long spacing, thickness of the amorphous and crystalline layers $(L, l_a \text{ and } l_c)$ are $\approx 8\text{-}19$, 4 and 13-14 nm, respectively. Finally, compared with the sample in the standard crystalline state, also for the blend 50L-50H, a remarkable increase in the values of L and L after heat treatment at 125° C occurs, from 18 and 14 nm, respectively, to 28 and 25 nm, respectively. This increase is due to the remarkable increase of these parameters to \approx 43 and 32, nm respectively, during the permanence of the sample at 125° C (Table 11). At 125° C, indeed, the sample is partially in the melt state, and only a small fraction of crystals with high thickness survives, accounting for the large value of the lamellar thickness achieved by fast cooling the sample from 125 to 25° C.

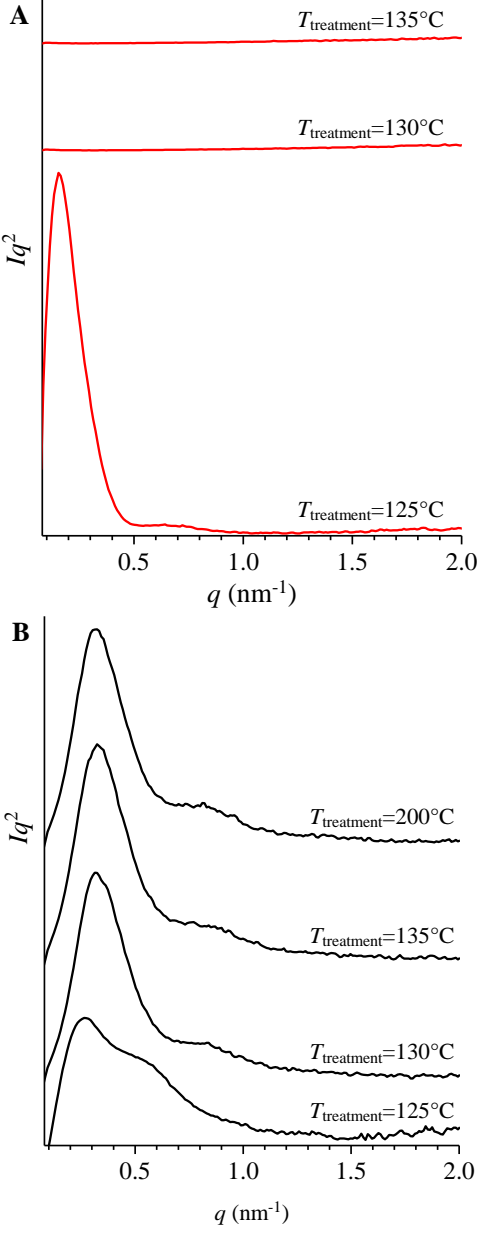


Figure 20 Lorentz corrected SAXS intensity for specimens of the blend 50L-50H recorded at the indicated values of the temperature $T_{treatment}$ (A, red lines) and collected at 25 °C, for specimens subjected to heat-treatment at the indicated temperatures for $t_{treatment} = 10$ min and quickly cooled (40 °C/min) from $T_{treatment}$ to room temperature (B, black lines).

Table 9 Values of the position of the I and II order correlation peaks (q_1 and q_2) and corresponding characteristic correlation distances (L_1 and L_2 , derived using the Bragg's Law) observed in the Lorentz corrected SAXS intensity profiles of the blend 50L-50H, crystallized by fast cooling (40 °C/min) after isothermal treatment for 10 min at the indicated values of $T_{treatment}$. The values of the thickness of the lamellar crystals l_c and amorphous layers l_a have been evaluated as $l_c = L_1$ Φ_c and $l_a = L_1$, where Φ_c is the volume fraction of the crystalline phase (see Chapter 3). The heat-treated samples at 125, 130 and 135 °C are prepared from the samples heat treated at 200 °C representing the standard crystalline state.

| Ttreatment | q ₁ (nm ⁻¹) | <i>L</i> ₁ (nm) | q ₂ (nm ⁻¹) | L ₂ (nm) | xc (WAXS) | Φ _c (%) | lc (nm) | la (nm) |
|------------|------------------------------------|----------------------------|------------------------------------|---------------------|--------------|-----------------------|------------|------------|
| 200°C | 0.325 | 19.3 | 0.81 | 15.5 | 0.54 | 0.50 | 9.7 | 9.6 |
| 135°C | 0.323 | 19.4 | 0.84 | 14.9 | 0.53 | 0.49 | 9.4 | 10.0 |
| 130°C | 0.323 | 19.4 | 0.83 | 15.1 | 0.56 | 0.52 | 10.1 | 9.3 |
| 125°C | 0.264 | 23.8 | / | / | 0.61 | 0.57 | 13.6 | 10.2 |

Table 10 Values of the lamellar periodicity (L) and thickness of amorphous (l_a) and crystalline (l_c) layers, relative to the blend 50L-50H, crystallized by fast cooling (40 °C/min) after isothermal treatment for 10 min at the indicated values of $T_{treatment}$. They are deduced from SAXS data through the calculation of the mono-dimensional self-correlation function of electron density fluctuations (correlation function, CF) and the interface distribution function IDF. The heat-treated samples at 125, 130 and 135 °C are prepared from the samples heat treated at 200 °C representing the standard crystalline state.

| | | (| CF | | IDF | | | | | | |
|--------|--------|---------------------|------------|-------------|--------|---------------------|------------|----------------------------|--|--|--|
| Sample | L (nm) | l _c (nm) | la (nm) | lc/L (-) | L (nm) | l _c (nm) | la (nm) | <i>l_c/L</i> (-) | | | |
| 200°C | 17.8 | 13.6 | 4.2 | 0.76 | 14.6 | 11.5 | 3.0 | 0.79 | | | |
| 135°C | 17.7 | 13.5 | 4.2 | 0.76 | 14.4 | 11.3 | 3.1 | 0.78 | | | |
| 130°C | 17.7 | 13.5 | 4.2 | 0.76 | 14.7 | 11.4 | 3.3 | 0.77 | | | |
| 125°C | 28.3 | 25.5 | 2.8 | 0.90 | 19.5 | 17.6 | 1.9 | 0.90 | | | |

Table 11 Values of the Lamellar parameters extracted from SAXS data collected at $T_{treatment}$ =125°C using the Bragg's Law and CF for the blend 50L-50H.

| | Bragg | CF |
|---------------------------|-------|------|
| L (nm) | 40.8 | 42.8 |
| $l_{\rm c}({\rm nm})$ | 30.1 | 32.1 |
| la (nm) | 10.7 | 10.7 |
| <i>l_c/L(-)</i> | 0.74 | 0.75 |

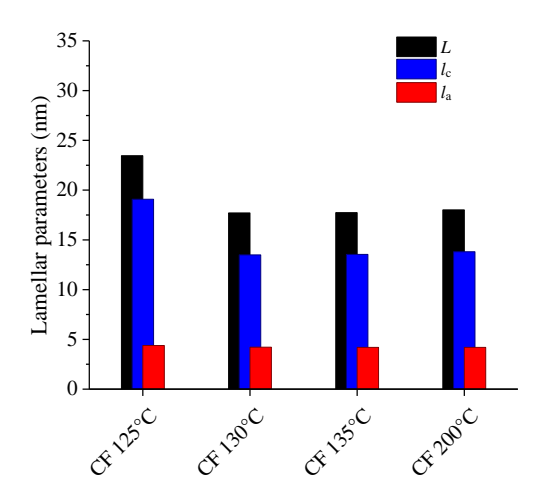


Figure 21 Values of the long spacing L and thickness of amorphous l_a and crystalline l_c layers evaluated from SAXS data collected at 25°C for the blend 50L-50H in the standard crystalline state (CF 200°C), successively subjected to fast cooling (40 °C/min) to 25 °C, after 10 min at 125 °C (CF 125°C), at 130 °C (CF 130°C) and at 135 °C (CF 135°C). The lamellar parameters are obtained from CF.

Effect of short treatment times

The effect of application of the heat treatments at $T_{\text{treatment}}$ =125, 130 and 135 °C for short time on the blend 50L-50H is studied, resorting to different techniques.

The DSC heating scans recorded for the blend 50L-50H in the initial standard crystalline state, subjected to heat treatments at 125, 130 and 135 °C for different amounts of time $t_{\text{treatment}}$ and then cooled to 25 °C at 40 °C/min are shown in Figure 22.

The DSC heating scans relative to the blend heat treated at 130 and 135°C do not show substantial differences, at any investigated values of $t_{\text{treatment}}$, in agreement with the fact that the sample is the SNA Domain I (Figure 22A,B). For heat treatments at 125 °C, instead, the DSC heating curves undergo changes as the treatment time increases (Figure 22C). In particular, at 125 °C, the evolution of the DSC signal with time (Figure 22C) for the blend is similar to that observed for the pure component H-C4 (Figure 7C) and L-C8 (Figure 15C), as all the samples are in the SNA Domain III at this temperature. It is apparent, in fact, that that the main endothermic peak of the heat-treated blend 50L-50H shifts toward higher temperatures ($T_{\rm ml} = 129.1^{\circ}$ C) compared with the melting temperature of the sample in the initial, standard crystalline state (127.6°C). This shift is due to the annealing experienced by the crystals surviving at 125 °C. The fraction of crystals that instead melt at this temperature, crystallize during the successive cooling to 25°C, giving rise to a melting hump at lower temperature ($T_{\rm m2} \approx 124^{\circ}$), the intensity of which tends to increase with $t_{\text{treatment}}$. As shown in Figure 23, the value of $T_{\rm m2}$ increases in the first 20 s and then becomes approximately constant until 60 s. For $t_{\text{treatment}} \ge 90$ s, T_{m2} tends to decrease, reaching the value of 123.3°C after 600 s. The main melting peak at $T_{\rm ml}$, instead, tends to shift to higher temperatures as the treatment time at 125 °C increases, indicating a progressive annealing of the residual crystals.

Further evidence of occurrence annealing process during the heat treatment at 125 $^{\circ}$ C derive from the results of SAXS data analysis (Figure 24), that show a sudden increase of the long period and lamellar thickness with respect to the initial standard crystalline state, already after 10 s of treatment time at 125 $^{\circ}$ C, from 22 and 18 nm, respectively, to 23-27 and 18-19 nm, respectively, while the thickness of the amorphous layers remains constant at \approx 4 nm.

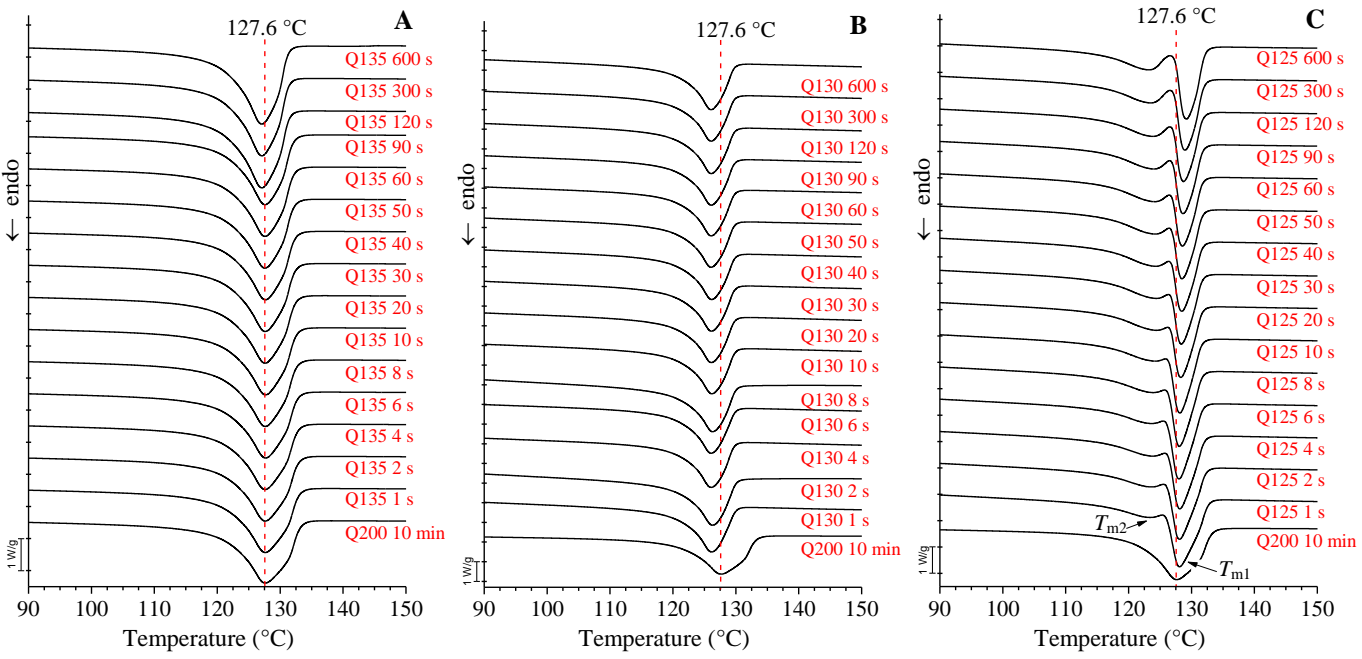
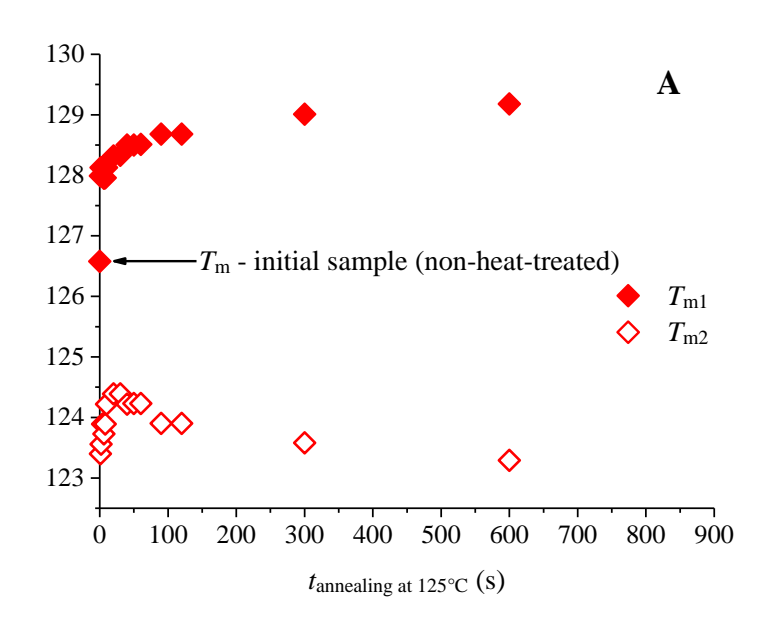


Figure 22 DSC heating scans of the blend 50L-50H in the initial standard crystalline state (Q200 10 min), subjected to thermal treatments at $T_{treatment} = 135$ (A), 130 (B) and 125 (C) °C, for the indicated amounts of time $t_{treatment}$. The melting temperature of the blend in the standard crystalline state equal to 127.6 °C is indicated.



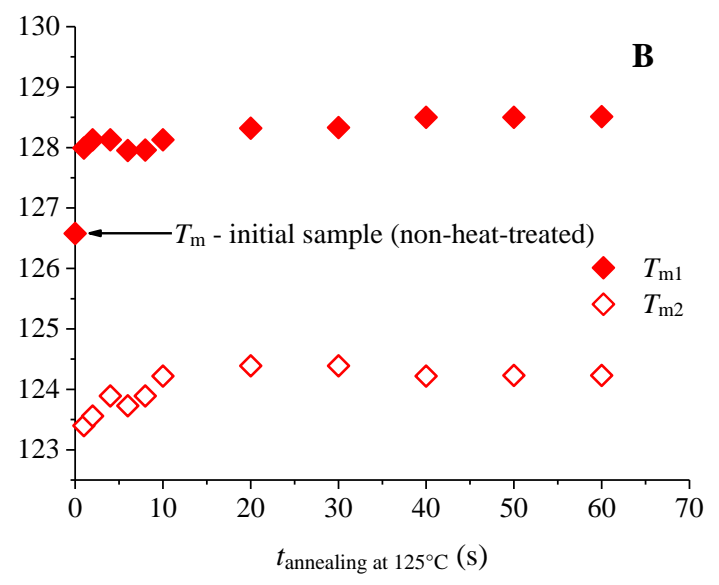


Figure 23 Temperatures of the 1° (T_{ml}) and 2° (T_{m2} , hump) melting peaks of the sample 50L-50H in the initial standard crystalline state, heat-treated at $T_{treatment}$ =125°C as a function of time $t_{treatment}$ in the first 600 (A) and 60 s (B).

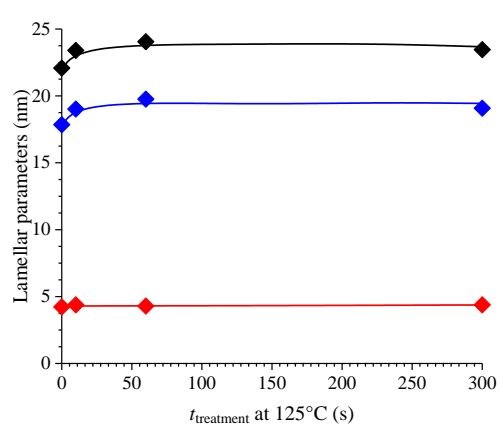


Figure 24 Values of the lamellar parameters of the blend 50L-50H obtained from the mono-dimensional self-correlation function of electron density fluctuations (CF), extracted from SAXS data of the sample in the initial standard crystalline state, subjected to thermal treatment at $T_{treatment} = 125$ °C, for different amounts of time $t_{treatment}$. The data at $t_{treatment} = 0$ are relative to the sample in the standard crystalline state (non-heat treated).

4.4. Conclusion

In this chapter the effect of thermal treatments at selected temperatures ($T_{\text{treatment}} = 125$, 130 and 135 °C) on the structural rearrangement occurring for the HDPE sample H-C4, the LLDPE sample L-C8 and the corresponding blend at 50-50 wt%/wt% composition is analysed. The analysis is carried out on samples initially prepared in a standard crystalline state, and successively heat treated at the selected temperatures for different amounts of time, and then rapidly cooled to room temperature.

The involved structural transformations depend on the SNA domain in which the sample are located at the selected temperatures for the heat treatment $T_{\text{treatment}}$. In particular, the sample H-C4 falls in the SNA Domains I, II and III at $T_{\text{treatment}} = 135$, 130 and 125 °C, respectively, whereas the sample L-C8 and the blend 50L-50H fall in the SNA Domain I at 130 and 135 °C, and Domain III at 125 °C.

It is shown that heat treatments carried out in Domain I do not bring significant

structural re-arrangements, and complete melting of the pristine crystals is achieved very rapidly. The heat-treated samples show structures and melting behavior similar to those of the pristine samples in the standard crystalline state. For heat treatments carried out in Domain II, instead, the melting process is not complete in the first 10-20 s, and the survived crystals undergo annealing. However, prolonging the treatment time above a threshold, all the pristine crystals melt, and the samples tend to show a single melting endotherm.

Heat treatments carried out in Domain III induce annealing of the more regular crystals that survive at those temperatures and melting of the most irregular crystals. The defective chains previously belonging to these irregular crystals, in turn, upon cooling form defective crystals that melt at lower temperatures than the original crystals. The melting temperature and the lamellar thickness achieved by the annealed crystals, instead, are greater than those of the original crystals in the sample in the pristine state.

The achieved results demonstrate that the adopted thermal protocol represents a valuable method to monitor the effect of treatment time at temperatures behind the melting endotherm at different length scales, from lamellar to micrometric one. By employing this kind of protocol, various phenomena can be detected and analysed, leading to a better understanding of the changes experienced by the sample upon heat-treatments. Evaluating the output of the protocol by integrating the results of other analyses such as SNA and SSA can provide detailed information on the behaviour of the material, in its melt or semi-solid state, at different temperatures. This integrated approach can allow to identify optimal conditions of industrial processes based on thermal pre-treatments of a material, like tentering.

Bibliography of chapter IV

(1) Bassett, D. C. *Principles of Polymer Morphology*; Cambridge University Press: Cambridge, England, 1981.

Chapter V

Annealing in-situ analysis

As demonstrated in Chapter IV, PE samples subjected to thermal treatments in the semi-solid state undergo structural rearrangements of the crystalline and amorphous phases. The enhanced mobility of chains at temperatures behind the melting peak, indeed, leads to partial melting, consequent reorganization of crystalline and amorphous phases, changes in the thickness of crystalline and amorphous layers, annealing of surviving crystals, melting/recrystallization processes and lamellar thickening, in a very short time. As biaxial stretching involves a step of thermal conditioning at the tentering temperature before initiating the actual biaxial stretching, elucidating these transformations occurring by effect of temperature during the conditioning time, can help in identifying the state of the melt in the early stages of the tentering process. The state of the melt, in turn, has great influence on the response to mechanical stresses and successive evolution upon cooling of a material. Although the room temperature SAXS measurements presented in Chapter IV provide valuable information, they do not adequately reveal the relevant transformations occurring during the high temperature treatment, because the information collected at room temperature namely reflect the structural organization achieved by the sample upon cooling, by effect of crystallization. The experiments presented in this Chapter are aimed at studying in situ the structural changes occurring in the initial stages of the tentering process. This study has been carried out during the six months stage at University KU Leuven in the research unit Polymer Chemistry and Materials (PCM) of Prof. Bart Goderis.

5.1. Experimental

Time resolving WAXS/SAXS measurements have been performed at selected temperatures ($T_{\rm treatment}$) on PE samples in the semi-solid state, using the high flux of X-ray radiation produced at synchrotron light sources. The aim is to follow the evolution of the lamellar parameters and crystallinity in PE samples at selected temperatures as a function of time. Experiments have been carried out following the scheme illustrated in Figure 1. In-situ SAXS/WAXS measurements are coupled with ex-situ DSC analysis on independent specimens prepared with the same protocol adopted for time-resolving WAXS/SAXS experiments. In practice, the samples have been heated to the selected $T_{\rm treatment}$ at 40°C/min, and kept at this temperature for 10 min. Then the samples have been fast cooled to room temperature at 40°C/min to enable complete crystallization. Finally, melting curves of samples subjected to the same thermal treatment applied during the insitu experiment have been recorded at 10°C/min using DSC.

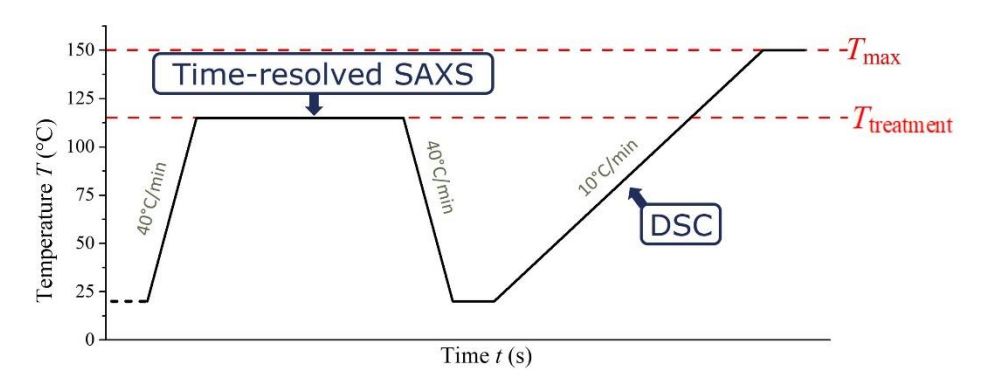


Figure 1 Scheme of the in-situ/ex-situ experiments.

SAXS/WAXS in-situ measurements have been performed at Beamline BM26B at the European Synchrotron Radiation Facility (ESRF, Grenoble, FR). Experiments were conducted using an X-ray with a wavelength of 1.033 Å and a beam diameter of $\approx 300 \ \mu m$. SAXS data have been collected with a Pilatus 1M detector (981 x

1043 pixels of 172 μm x 172 μm) located at 3 m from the sample while the WAXS 300K-W linear Pilatus detector (254mm x 33.5mm active area) has been placed at a distance of 30 cm from the sample. The distances and tilt angle have been calibrated using silver behenate (AgC₂₂H₄₃O₂) (for SAXS) and aluminium oxide (Al₂O₃) (for WAXS) as standard. A Linkam Single Cell Calorimetry (Optical DSC600) has been used in the heating/cooling step and during the isothermal analysis at T_{treatment} of the samples. Differently from ex-situ protocol described in Chapter IV, the here used thermal protocol does not include the creation of a standard crystalline state by heating the sample to 200°C and fast cooling (40°C/min) to room temperature after 10 min of conditioning. For these experiments, indeed, cast films (thickness ~700 µm) of the PE samples, produced at Karo Bruckner facility, have been used. Since the in-situ analysis of the samples by biaxial stretching (Chapter VI) has been carried out on cross-shaped samples obtained from cast films (vide infra), the objective of this Chapter has been to examine temperature-induced phenomena while preserving an initial state aligned with the conditions used in the biaxial stretching tests. X-ray images have been corrected for background scattering and the empty Linkam cell. Scattering data have been then corrected for the transmission factor, measured using a photodiode positioned on the beamstop. SAXS profiles often presented a correlation hump around 1.5 nm⁻¹, due to crystalline calcium stearate present in the sample. The contribution of this additive to SAXS intensity has been fitted with a gaussian function and subtracted. WAXS/SAXS data have been collected during the isotherm at T_{treatment}. With a time of acquisition of 4.65 s/frame and a dead time of 1.35 s, a frame was collected every 6 seconds.

The mono-dimensional self-correlation function of electron density fluctuations (correlation function) was evaluated as detailed in Chapter 2.

DSC analysis has been carried out with a TA Instruments Q2000 DSC apparatus. The scans have been recorded in flowing nitrogen atmosphere at a scan rate of 10 °C/min.

5.2. Results and discussion

Characterization of cast films

The DSC curves and the WAXS profiles of cast films of the PE samples H-C4, L-C8 and the corresponding blend 50L-50H are shown in Figure 2. The melting and crystallization temperatures are close to those of the pellets. The WAXS profile of the cast films are shown in Figure 2. They show that all the samples crystallize in the orthorhombic form of PE, achieving values of the crystallinity index of about 46% for the LLDPE sample, \approx 66% for the HDPE sample, and \approx 53% for the blend 50L-50H. Table 1 summarizes the properties of the cast films of the PE samples deducted from DSC and WAXS analysis of Figure 2 and 3.

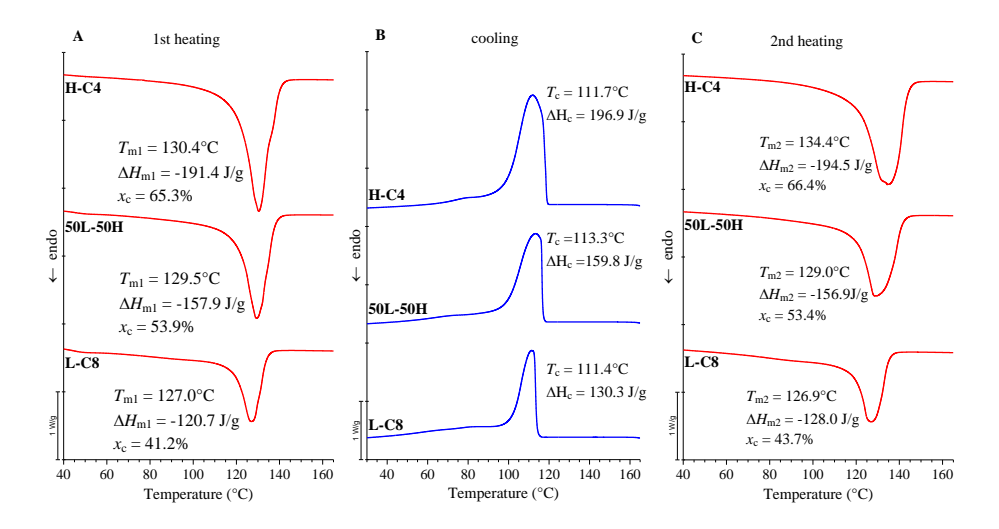


Figure 2 DSC scans recorded during the 1st heating (A), cooling (B) and 2nd heating (C) scans, at 10°C/min for the cast films of the PE samples. The values of T_{m1} , T_c and T_{m2} , corresponding enthalpy, and crystallinity degree $x_c(DSC)$ are indicated.

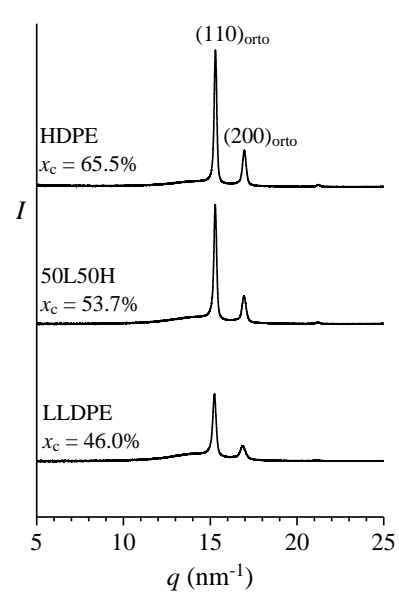


Figure 3 X-ray powder diffraction profiles of cast films of the PE samples. The values of crystallinity index $x_c(WAXS)$ are indicated.

Table 1 First (T_{m1}) and second melting temperatures (T_{m2}) , crystallization temperatures (T_c) , corresponding enthalpies $(\Delta H_{m1}, \Delta H_{m2}, \text{ and } \Delta H_c)$ and crystallinity index evaluated from DSC and WAXS analysis of the cast films of samples.

| Sample | | | | | | | | x_c WAXS |
|---------|-------|-------|-------|--------|-------|--------|------|------------|
| | | | | | | | (%) | |
| H-C4 | 130.4 | 111.7 | 134.4 | -191.4 | 196.9 | -194.5 | 65.3 | 65.5 |
| 50L-50H | 129.5 | 113.3 | 129.0 | -157.9 | 159.8 | -156.9 | 53.9 | 53.7 |
| L-C8 | 127.0 | 111.4 | 126.9 | -127.0 | 130.3 | -128.0 | 41.2 | 46.0 |

In situ WAXS/SAXS analysis

The results obtained operating at $T_{treatment}$ of 120 and 125°C are here illustrated as an example. All the samples, at these temperatures, fall into the SNA Domain III, in which surviving crystals dive in a highly nucleated melt and experience annealing.

To determine the initial structure of the cast films of the PE samples, i.e. before the heat treatment, SAXS data have been first collected at room temperature. The values of the lamellar parameters calculated from the CF are reported in Figure 4 and Table 2. The results of Table 2 indicate that the lamellar parameters of cast films are similar to those of the samples in the standard crystalline state.

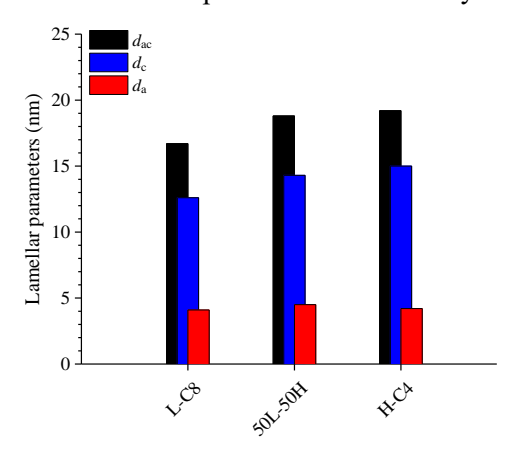


Figure 4 Values of long period L, thickness of crystalline l_c and amorphous l_a layers, evaluated from SAXS data analysis through calculation of the Correlation Function CF, for cast films of the samples L-C8, H-C4 and the blend 50L-50H. SAXS data have been collected at room temperature.

Table 2 Values of the lamellar periodicity (L) and thickness of amorphous (l_a) and crystalline (l_c) layers calculated from the CF, for cast films of the PE samples.

| Sample | L (nm) | $l_{\rm c}({\rm nm})$ | l _a (nm) | <i>l_c/L (-)</i> |
|---------|--------|-----------------------|---------------------|----------------------------|
| L-C8 | 16.7 | 12.6 | 4.1 | 0.75 |
| 50L-50H | 18.8 | 14.3 | 4.5 | 0.76 |
| H-C4 | 19.2 | 15.0 | 4.2 | 0.78 |

Heat treatment at 120 °C

The WAXS and SAXS intensity profiles collected during heat treatment at 120 °C are shown in Figure A1A,D, A3A,D and A5A,D of the Appendix A8. The SAXS curves obtained after correction for the Lorentz's factor are also reported (Figure A1B, A3B and A5B of Appendix A8).

The WAXS profiles show, in all cases, the 110 and 200 reflections of PE (Figure A1D, A3D and A5D of Appendix A8). The Lorentz's corrected SAXS intensity

profiles show a well-defined correlation peak at values of $q \approx 0.2 \text{ nm}^{-1}$ (Figure A1B, A3B and A5B of Appendix A8).

The values of the lamellar parameters (L, l_c and l_a) calculated from the CF (Figure A1C, A3C and A5C of Appendix A8) during the 10 min isothermal treatment at $T_{treatment} = 120^{\circ}$ C are reported in Figure 5 as a function of time. These data are also collected in Table 3. The corresponding values of the crystallinity index evaluated from WAXS collected simultaneously with SAXS data are reported in Figure 6.

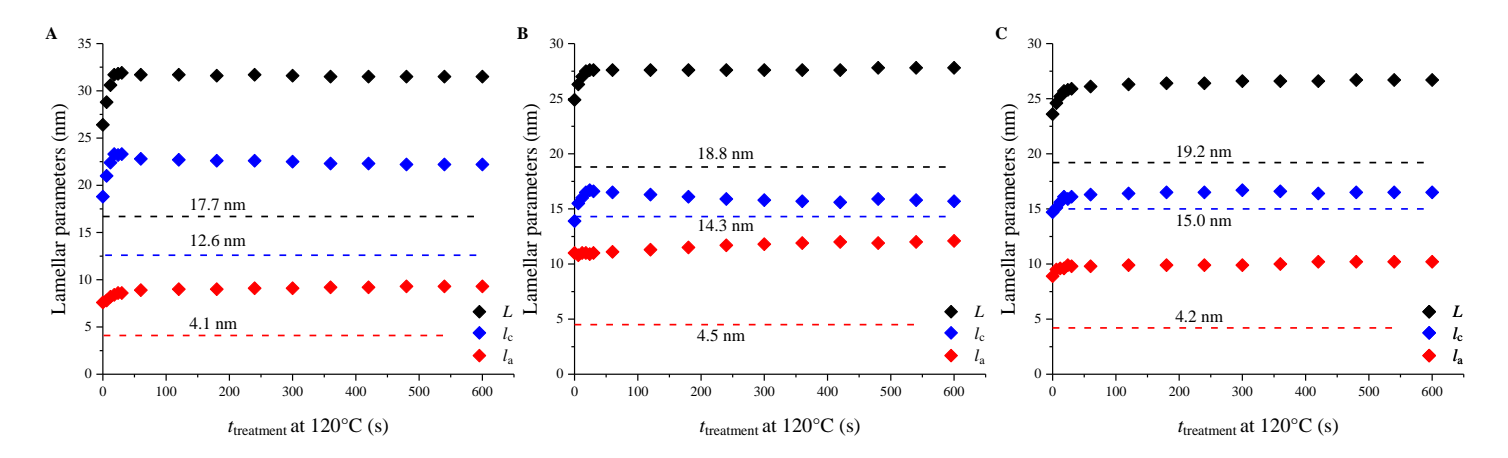


Figure 5 Values of the lamellar parameters (L, l_c and l_a) vs. the treatment time $t_{treatment}$ of the PE samples at 120 °C, extracted from the mono-dimensional self-correlation function of electron density fluctuations (correlation function, CF) for cast films of the samples A) L-C8; B)50L-50H; and C) H-C4. Lamellar periodicity L: black diamonds; Crystal thickness l_c : red diamonds; thickness of the amorphous layers l_a : blue diamonds. The values of the lamellar parameters of cast films measured at 25 °C are indicated by the dashed horizontal line.

Table 3 Values of lamellar parameters L, l_c and l_a (expressed in nm) extracted from CF of each sample for different $t_{treatment}$ times at the selected $T_{treatment}=120$ °C.

| | | 0s | 6s | 12s | 18s | 24s | 30s | 60s | 120s | 180s | 240s | 300s | 360s | 420s | 480s | 540s | 600s |
|---------|----------------|------|------|------|------|------|------|------|------|------|------|------|------|------|------|------|------|
| L-C8 | L | 26.4 | 29.0 | 30.6 | 31.7 | 31.8 | 31.9 | 31.7 | 31.7 | 31.6 | 31.7 | 31.6 | 31.5 | 31.5 | 31.5 | 31.5 | 31.5 |
| | la | 7.6 | 7.8 | 8.2 | 8.4 | 8.6 | 8.6 | 8.9 | 9.0 | 9.0 | 9.1 | 9.1 | 9.2 | 9.2 | 9.3 | 9.3 | 9.3 |
| | l _c | 18.8 | 21.0 | 22.4 | 23.3 | 23.2 | 23.3 | 22.8 | 22.7 | 22.6 | 22.6 | 22.5 | 22.3 | 22.3 | 22.2 | 22.2 | 22.2 |
| | L | 24.9 | 26.0 | 27.0 | 27.5 | 27.6 | 27.6 | 27.6 | 27.6 | 27.6 | 27.6 | 27.6 | 27.6 | 27.6 | 27.8 | 27.8 | 27.8 |
| 50L-50H | la | 11.0 | 11.0 | 11.0 | 11.0 | 10.9 | 11.0 | 11.1 | 11.3 | 11.5 | 11.7 | 11.8 | 11.9 | 12.0 | 11.9 | 12.0 | 12.1 |
| | l _c | 13.9 | 16.0 | 16.0 | 16.5 | 16.7 | 16.6 | 16.5 | 16.3 | 16.1 | 15.9 | 15.8 | 15.7 | 15.6 | 15.9 | 15.8 | 15.7 |
| | L | 23.6 | 25.0 | 25.2 | 25.7 | 25.8 | 25.9 | 26.1 | 26.3 | 26.4 | 26.4 | 26.6 | 26.6 | 26.6 | 26.7 | 26.7 | 26.7 |
| H-C8 | la | 8.9 | 9.5 | 9.6 | 9.6 | 9.9 | 9.8 | 9.8 | 9.9 | 9.9 | 9.9 | 9.9 | 10.0 | 10.2 | 10.2 | 10.2 | 10.2 |
| | $l_{\rm c}$ | 14.7 | 15.0 | 15.6 | 16.1 | 15.9 | 16.1 | 16.3 | 16.4 | 16.5 | 16.5 | 16.7 | 16.6 | 16.4 | 16.5 | 16.5 | 16.5 |

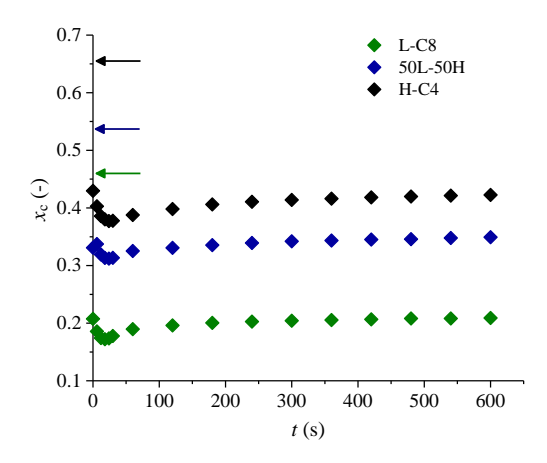


Figure 6 Values of crystallinity index evaluated from WAXS data as a function of time during the isotherm of 10 min at the selected $T_{treatment}$ =120°C. The values of the initial crystallinity index of cast films measured at 25 °C from WAXS, of 0.655, 0.46 and 0.537 for the samples H-C4, L-C8 and blend L50-H50, respectively (Table 1), are indicated by the arrows.

It is apparent that all the samples experience a sudden decrease of the crystallinity index by heating from 25 to 120 °C (Figure 6), from \approx 66 to 40% for the sample H-C4, from \approx 54 to 33% for the blend 50L-50H, and from \approx 46 to 20% for the sample L-C8. This decrease is due to the melting of the most defective crystals, characterized by low lamellar thickness, as indicated by the increase of the thickness of the amorphous layers l_a by a factor greater than two, from \approx 4-5 to 9-11 nm, and the simultaneous increase of lamellar thickness l_c . In particular, at 120 °C, only the crystals with lamellar thickness l_c greater than a threshold are able to survive, but whereas for the sample H-C4 and the blend 50L-50H, the average values of l_c of the surviving crystals increase just a little, from \approx 14-15 to \approx 16-17 nm, for the LDPE samples, the l_c values increase by a factor of about 2, i.e. from \approx 13 to \approx 22-23. These large differences are due to differences in the chain microstructure. The sample H-C4 from Ziegler-Natta heterogeneous catalysis, indeed, is characterized by a low concentration of comonomers (1-butene content = 0.5 mol%) and an uneven distribution of defects at inter- and intra-chain level.

More than 50 % of regular ethylene sequences are present that are able to form crystals of thickness large enough to be stable at 120 °C (Figure 6). The distribution of these sequences is non-uniform, so that the distribution of crystals thickness achieved at 120 °C is expected to be rather broad. For the LLDPE sample L-C8, obtained from metallocene catalysis, the concentration of comonomers is greater than in HDPE (1-octene content = 2.6%) and the distribution of these defects is uniform. As a consequence, the fraction of long ethylene sequences able to form thick crystals stable at 120 °C is only 20%. These crystals are thicker than those achieved at 120 °C for HDPE, as the distribution of lamellar thickness at 120 °C is expected to be narrower than that achieved by HDPE at the same temperature. The 50L-50H blend shows a stability behaviour at 120 °C similar to that of HDPE, as the contribution to long ethylene sequences stable at 120 °C from the LLDPE component reduces to only 10 %, and also because of the possible occurrence of co-crystallization of the two components. The change of lamellar parameters (Figure 5) as a function of time during the isotherm at 120 °C include a steep increase in the early 30 s, followed by reaching of a quasi-plateau after the first 60 min. Simultaneously, the values of crystallinity index (Figure 6) decrease slightly in the first 30 s and successively increase, achieving a quasi-plateau after 60 s, recovering the same level of crystallinity achieved by the samples at the beginning of the heat treatment. In all cases, the most significant changes occur in the first 60 s. The initial decrease of crystallinity level corresponds to small adjustments of the initial crystalline/amorphous scaffold, associated with an increase of lamellar thickness because of the melting of a residual fraction of crystals of small thickness that are not thermally stable at 120 °C. This step is followed by fast re-crystallization, with formation of lamellae of the same thickness. Re-crystallization is fast, due to the presence of a high concentration of self-nuclei in the melt.

Comparing the values of the lamellar parameters at the beginning and at the end of the heat treatment at 120 °C, the sample L-C8 shows the largest increase in long spacing and lamellar thickness, from ≈26 and 19 nm, respectively, to ≈31 and 22 nm, respectively. This is due to the presence of a high proportion of amorphous regions (80%) and to the high mobility of the chains, that makes the sample highly responsive to temperature changes (Figure 5A and Table 3). The blend 50L-50H and the sample H-C8, instead, show a less marked increase in the values of long spacing and lamellar thickness by effect of the heat treatment, from ≈11 and 25 nm, respectively, to ≈ 12 and 29 nm for the blend, and from ≈ 15 and 24 nm, respectively, to ≈ 16 and 28 nm, respectively, for the H-C4 neat component. Finally, the thickness of the amorphous layers is subject to less remarkable changes, from ≈8 to 9 for the sample L-C8, from ≈11 to 12 nm for the blend H50-L50, and from ≈9 to 19 nm for the sample H-C4. This suggests that the increase of lamellar thickness during isothermal treatments is also due to thickening processes taking place at high temperature, according to a reversible mechanism of melting/recrystallization taking place at the surface of the lamellar crystals, underlying secondary crystallization¹. According to this mechanism, a change of temperature is accompanied by a continuous shift of the interface, on cooling towards the amorphous regions and on heating towards the crystallites, resulting in a decrease or increase of lamellar thickness, respectively. The "surface crystallization and melting" mechanism requires a high mobility of the chains not only in the amorphous layers but also in the crystals. This mechanism becomes active in PE, in correspondence of the α-relaxation. It allows for a reversible exchange of segments located at the interfaces, between the two phases.

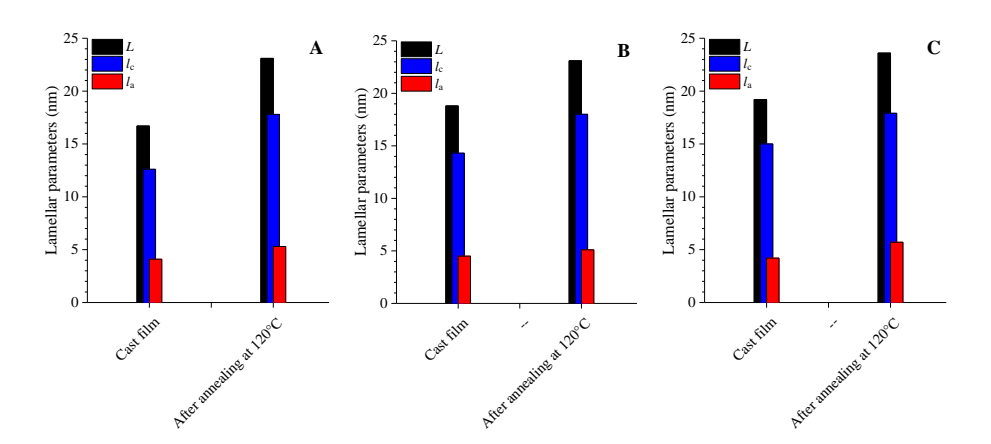


Figure 7. Values of the lamellar parameters (L, l_c , l_a), extracted from the SAXS profiles collected at 25 °C, for the PE samples before and after thermal treatment at 120°C. A): sample L-C8; B): blend 50L-50H; C): sample H-C4.

The values of the lamellar parameter of the PE samples determined at room temperature for the cast films before and after the heat treatment at 120 °C are shown in Figure 7. It is apparent that the changes occurring at lamellar length scale by effect of heat treatment at 120 °C and successive cooling induce a remarkable increase in the values of long spacing L and lamellar thickness l_c , especially for the sample L-C8. The values of the thickness of the amorphous layers, instead, increase only slightly. In particular, the values of L, l_c and l_a before and after the heat treatment increase from \approx 19, 14 and 4 nm to 24, 18 and 6 nm, respectively, for the sample H-C4, from \approx 17, 13 and 4 nm to 23, 18 and 5 nm, respectively, for the sample L-C8, and from \approx 19, 14 and 4 nm to 23, 18 and 5 nm, respectively, for the blend 50L-50H. In other terms, the new values of the lamellar parameters L and L_c are close to those achieved at 120 °C, at the end of the heat treatment, and only the values of L_a decrease, due to insertion of new crystals (of lower thickness) in the intra-lamellar amorphous regions during cooling.

The WAXS profiles collected at room temperature for the samples before and after the heat treatment at 120 °C (Figure 8) reveal a small but significant increase of the crystallinity index, especially for the blend 50L-50H.

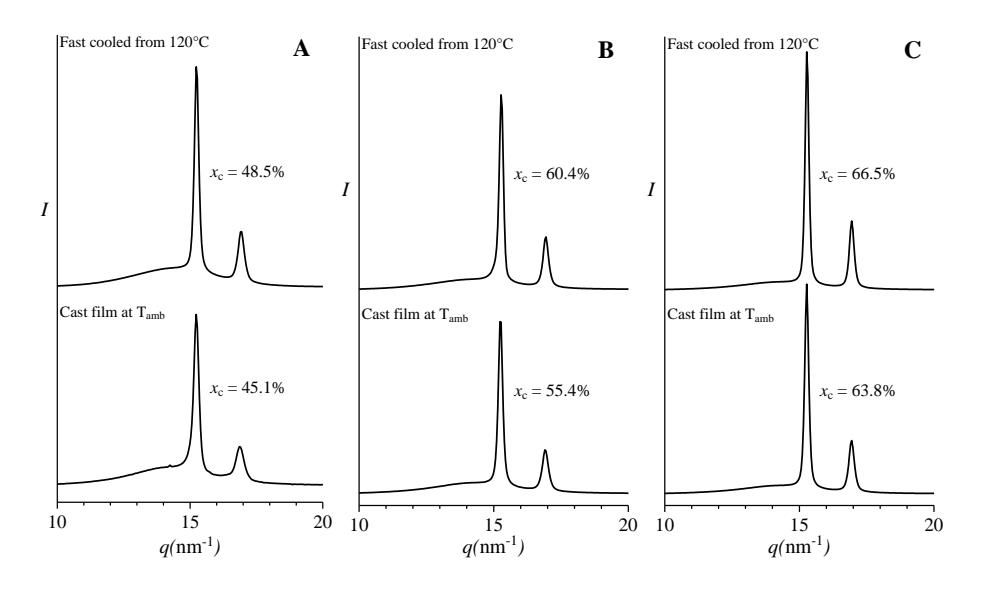


Figure 8 WAXS profiles collected at 25 °C before and after thermal treatment at 120°C for the samples A): L-C8; B): 50L-50H; C) H-C4.

Heat treatment at 125 °C

The WAXS and SAXS intensity profiles collected during heat treatment at 125 °C are shown in Figure A2A,D, A4A,D and A6A,D of the Appendix A8. The SAXS curves obtained after correction for the Lorentz's factor are also reported (Figure A2B, A4B and A6B of Appendix A8).

Also in this case, the WAXS profiles collected at 125 °C show the 110 and 200 reflections of PE (Figure A2D, A4D and A6D of Appendix A8), indicating that the samples are not completely melted. The Lorentz's corrected SAXS intensity profiles show a strong correlation peak at values of q that are lower than those observed in the Lorentz's corrected SAXS intensity profiles collected at $T_{\text{treatment}}$

= 120 °C, due the increase of the long period (Figure A2B, A4B and A6B of Appendix A8).

The values of the lamellar parameters (L, l_c and l_a) calculated from the CF (Figure A2C, A4C and A6C of Appendix A8) during the 10 min isothermal treatment at $T_{treatment} = 125$ °C are reported in Figure 9 as a function of time. These data are also collected in Table 4. The corresponding values of the crystallinity index evaluated from WAXS collected simultaneously with SAXS data are reported in Figure 10.

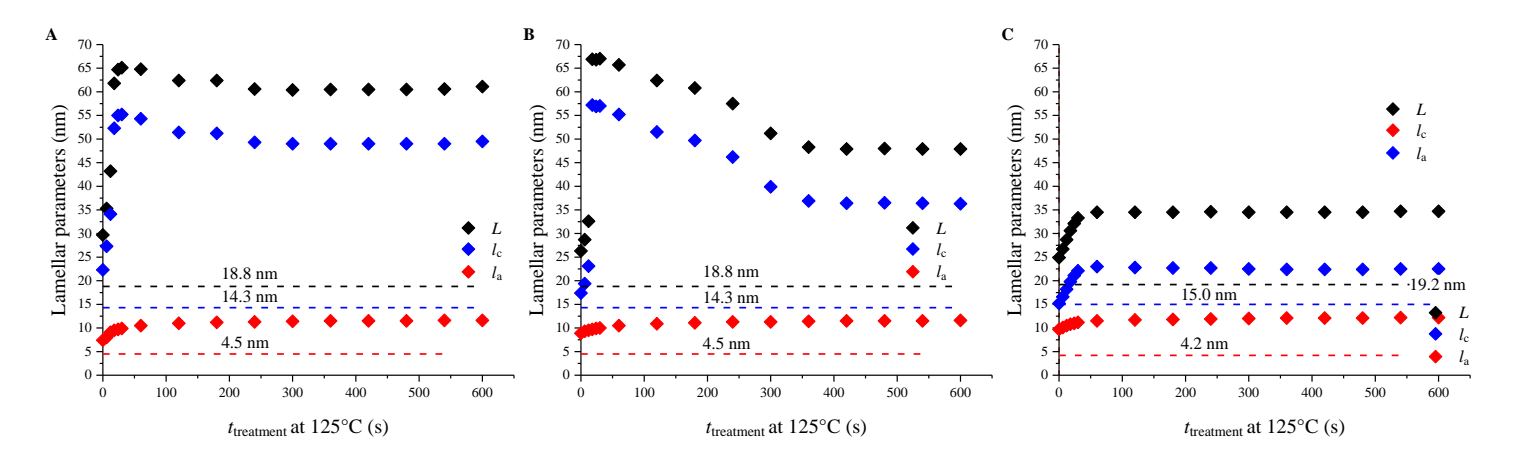


Figure 9 Values of the lamellar parameters (L, l_c and l_a) vs. the treatment time $t_{treatment}$ of the PE samples at 125 °C, extracted from the mono-dimensional self-correlation function of electron density fluctuations (correlation function, CF) for cast films of the samples A) L-C8; B)50L-50H; and C) H-C4. Lamellar periodicity L: black diamonds; Crystal thickness l_c : red diamonds; thickness of the amorphous layers l_a : blue diamonds. The values of the lamellar parameters of cast films measured at 25 °C are indicated by the dashed horizontal line.

Table 4 Values of lamellar parameters L, l_c and l_a (expressed in nm) extracted from CF of each sample for different $t_{treatment}$ times at the selected $T_{treatment}$ =125°C.

| | | 0s | 6s | 12s | 18s | 24s | 30s | 60s | 120s | 180s | 240s | 300s | 360s | 420s | 480s | 540s | 600s |
|---------|------------------|------|------|------|------|------|------|------|------|------|------|------|------|------|------|------|------|
| L-C8 | L | 29.7 | 35.3 | 43.2 | 61.8 | 64.7 | 65.1 | 64.8 | 62.4 | 62.4 | 60.6 | 60.4 | 60.5 | 60.5 | 60.5 | 60.6 | 61.1 |
| | $l_{\rm a}$ | 7.4 | 8.0 | 9.1 | 9.5 | 9.7 | 9.9 | 10.5 | 11.0 | 11.2 | 11.3 | 11.4 | 11.5 | 11.5 | 11.5 | 11.6 | 11.6 |
| | le | 22.3 | 27.3 | 34.1 | 52.3 | 55.0 | 55.2 | 54.3 | 51.4 | 51.2 | 49.3 | 49.0 | 49.0 | 49.0 | 49.0 | 49.0 | 49.5 |
| 50L-50H | \boldsymbol{L} | 26.3 | 28.7 | 32.6 | 66.9 | 66.8 | 67.0 | 65.7 | 62.4 | 60.8 | 57.5 | 51.2 | 48.3 | 47.9 | 48 | 47.9 | 47.9 |
| | la | 8.9 | 9.3 | 9.5 | 9.7 | 9.9 | 10.0 | 10.5 | 10.9 | 11.1 | 11.3 | 11.3 | 11.4 | 11.5 | 11.5 | 11.5 | 11.6 |
| | l _c | 17.4 | 19.4 | 23.1 | 57.2 | 56.9 | 57.0 | 55.2 | 51.5 | 49.7 | 46.2 | 39.9 | 36.9 | 36.4 | 36.5 | 36.4 | 36.3 |
| Н-С8 | \boldsymbol{L} | 24.9 | 26.7 | 28.7 | 30.6 | 32.1 | 33.3 | 34.5 | 34.5 | 34.5 | 34.6 | 34.5 | 34.5 | 34.5 | 34.5 | 34.7 | 34.7 |
| | la | 9.7 | 10.1 | 10.5 | 10.8 | 11.0 | 11.2 | 11.5 | 11.7 | 11.8 | 11.9 | 12 | 12.1 | 12.1 | 12.1 | 12.2 | 12.2 |
| | l _c | 15.2 | 16.6 | 18.2 | 19.8 | 21.1 | 22.1 | 23.0 | 22.8 | 22.7 | 22.7 | 22.5 | 22.4 | 22.4 | 22.4 | 22.5 | 22.5 |

Similar to the heating from 25 °C to 120 °C (Figure 5 and Table 3), the heating to 125 °C induces a sudden increase of the lamellar parameter, but this increase is more pronounced, due to the increase of the melt fraction (Figure 9 and Table 4). In fact, the values of the crystallinity index (Figure 10) are generally lower compared to those calculated during the isotherm at 120°C (Figure 6), and show a more pronounced decrease in the first 60 seconds of treatment, before of showing a slight upturn for $t_{\rm treatment} > 60$ s. In particular, compared with the values of the crystallinity index achieved by the samples H-C4 and L-C8 and the blend 50L-50H at the end of the heat treatment at 120 °C equal to \approx 0.4, 0.2 and 0.35, respectively, those achieved at the end of the heat treatment at 125 °C are 0.3, 0.1 and 0.2, respectively.

As for the evolution of the lamellar parameter L, l_c and l_a during the isothermal treatment at 125 °C, the sample H-C4 shows changes in lamellar parameters as a function of time (Figure 9C) similar to those occurring during the hat treatment at 120 °C (Figure 5C). In particular, after a first increase of the lamellar parameter values in the first 30 s, a plateau value is approached corresponding to \approx 35, 22 and 12 nm for L, l_c and l_a , respectively (Table 4). These values, especially for the values of l_c , are greater than those achieved for $t_{\text{treatment}} > 60$ at $T_{\text{treatment}} = 120$ °C, corresponding to 20, 16 and 10 nm, for L, l_c and l_a , respectively (Table 3). For the samples L-C8 and the blend 50L-50H (Figure 9A, B), instead, the values of L and l_c change at 125 °C according to a completely different way with respect to changes occurring at 120 °C. In particular, at 125 °C, after a steep increase in the first 30 s, the values of L and l_c decrease according to a monotonic trend in the first 300 s, and then approach a quasi-plateau value equal to ≈ 60 and 50 nm, respectively, for the sample L-C8, and ≈ 50 and 35 nm, respectively for the blend 50L-50H. The values of l_a , instead, after a slight increase in the first 30 s, approach a quasi-plateau value of \approx 12 nm, for both samples. Therefore, also for the sample L-C8 and the blend 50L-50H, the values of the lamellar parameters L, l_c and l_a , achieved at the end of the heat treatment at 125 °C are greater than those achieved at the end of the treatment at 120 °C, equal to \approx 31, 20 and 9, respectively, for the sample L-C8 and 29, 16 and 12 nm, respectively, for the blend 50L-50H. These results indicate that the treatment temperature of 125 °C selects lamellar crystals with thicknesses which are almost two times greater than those selected at 120 °C, while the thickness of the amorphous layer increases only slightly. The oscillating behaviour of L and L observed for the sample L-C8 and the blend 50L-50H, reflect an initial fast melting of thin crystals and consequent survival of the most thick and perfect crystals, followed by a gradual re-crystallization of the sequences of medium length able to form stable crystals at 125 °C and consequent decrease of L and L, and then the final approach to an average thickness value of quasi-plateau in the last stage of the heat treatment.

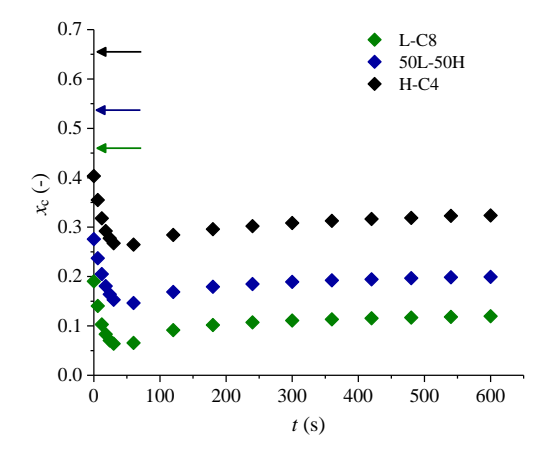


Figure 10 Values of crystallinity index evaluated from WAXS data as a function of time during the isotherm of 10 min at the selected $T_{treatment}$ =125°C. The values of the initial crystallinity index of cast films measured at 25 °C from WAXS of 0.655, 0.46 and 0.537 for the samples H-C4, L-C8 and blend L50-H50, respectively (Table 1), are indicated by the arrows.

The values of the lamellar parameter of the PE samples determined at room temperature for the cast films before and after the heat treatment at 125 °C are shown in Figure 11. Also in this case, the heat treatment at 125 °C and successive cooling induce a remarkable increase in the values of long spacing L and lamellar thickness l_c , especially for the sample L-C8, while the increase in the values of the thickness of the amorphous layers is less marked. In particular, the values of L, l_c and l_a before and after the heat treatment at 125 °C increase from ≈19, 14 and 4 nm to 26, 20 and 5 nm, respectively, for the sample H-C4, from \approx 17, 13 and 4 nm to 24, 18 and 5 nm, respectively, for the sample L-C8, and from \approx 19, 14 and 4 nm to 25, 20 and 5 nm, respectively, for the blend 50L-50H. These values of the lamellar parameters are close to those achieved at 120 °C, and indicate that isothermal treatments of PE samples in the semi-solid state, induce a neat increase of the average lamellar parameter L and l_c , and only minor changes in the values of l_a . The nature of these changes is further investigated in the next paragraph, through DSC analysis.

Finally, similar to the heat treatment at 120 °C, also the heat treatment at 125 °C induce an increase in the crystallinity index with respect to the pristine cast films, as indicated by the analysis of the WAXS profiles collected at room temperature for the samples before and after the heat treatment at 125 °C (Figure 12).

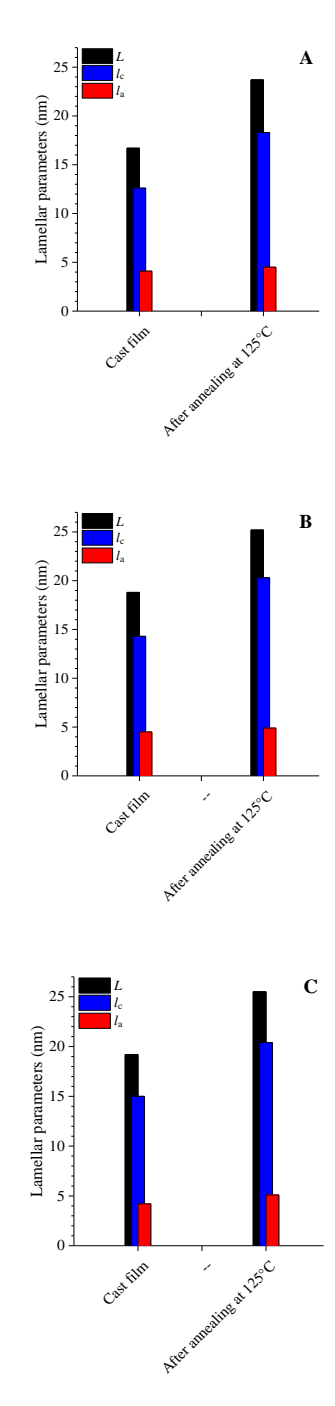


Figure 11 Values of the lamellar parameters (L, l_c , l_a), extracted from the SAXS profiles collected at 25 °C, for the PE samples before and after thermal treatment at 125 °C. A): sample L-C8; B): blend 50L-50H; C): sample H-C4.

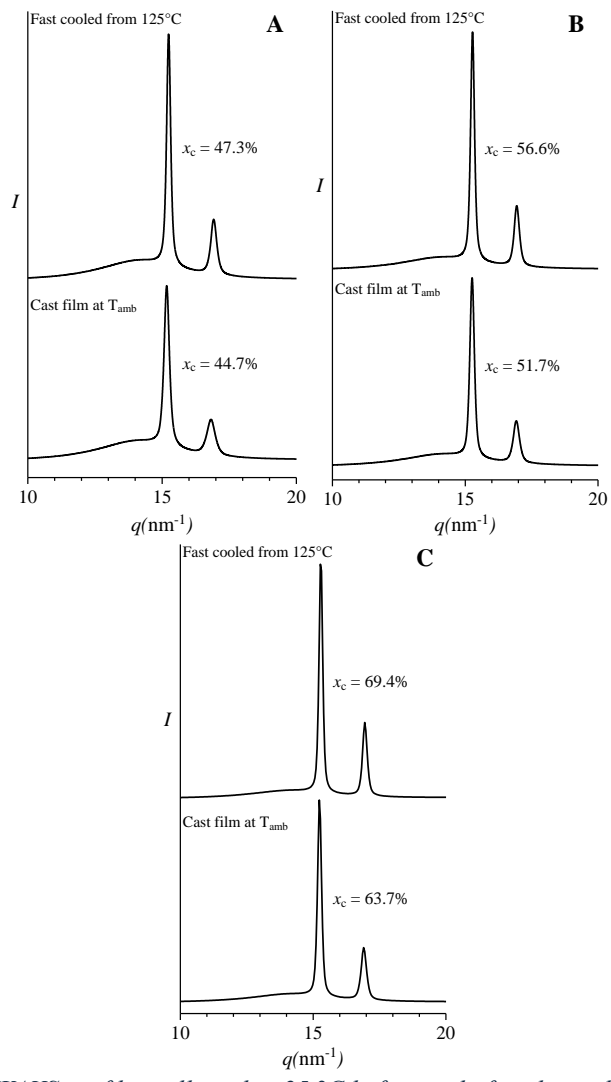


Figure 12 WAXS profiles collected at 25 °C before and after thermal treatment at 125 °C for the samples A): L-C8; B): 50L-50H; C): H-C4.

Ex-situ analysis of the heat-treated PE samples, after cooling to 25 °C

The samples subjected to the heat treatments at 120 and 125 °C, and successively cooled to room temperature, have been subjected to DSC analysis. The DSC curves of the so-obtained samples are compared with those of the pristine sample, i.e. cast films not subjected to heat treatment. It is evident that the single (broad) melting peak of the pristine samples, is replaced by a narrow, primary peak centred at temperatures $T_{\rm ml}$ that are slightly greater than the melting temperatures of the non-heat-treated sample, flanked by a comparatively broader peak centred at temperatures $T_{\rm m2}$ lower than $T_{\rm m1}$. This secondary peak at $T_{\rm m2}$ appears as a hump of small area, for the samples heat treated at 120 °C, and as a tailed peak of greater area for the samples heat treated at 125 °C. The peak at $T_{\rm m2}$ is clearly due to the melting of the crystals that are formed by cooling the sample from 120 or 125 °C to room temperature. These crystals are indeed formed by short ethylene sequences comprised in between consecutive defects, which are not able to form crystals at the temperatures of the heat treatment. The so-formed crystals are less thermally stable than the crystals subjected to annealing at 120 and 125 °C, and thus melt at lower temperatures. The area behind the peaks at $T_{\rm m2}$ for the samples heat treated at 125 °C are greater than the corresponding area shown by the samples heat treated at 120 °C, in agreement with the major fraction of pristine crystals that melt at 125 °C.

The values of the melting temperatures $T_{\rm m1}$ and $T_{\rm m2}$ determined in the DSC scans of Figure 13 for the PE samples heat treated at 120 and 125 °C are reported in Figure 14, as a function of $T_{\rm treatment}$. It is apparent that the greater the treatment temperature $T_{\rm treatment}$, the greater the values of $T_{\rm m1}$ and $T_{\rm m2}$. Hence, the treatment temperature not only influences the melting temperature of the annealed crystals but also the melting temperatures of the crystals that form during cooling.

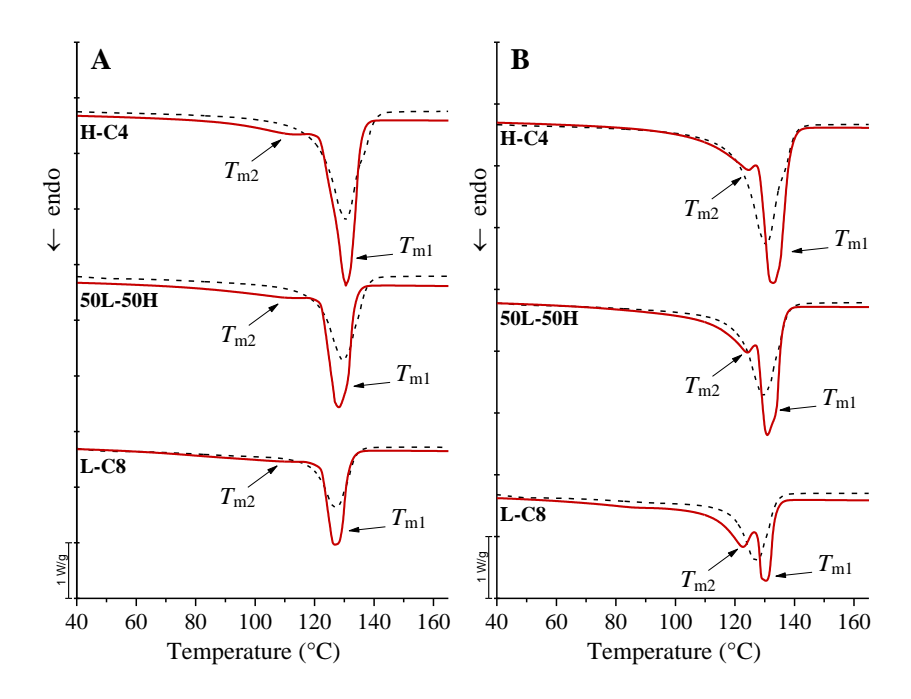


Figure 13 DSC heating scans of the samples L-C8, 50L-50H and H-C4 subjected to the same heating treatment at 120 (A) and 125 (B) °C (red curves) that have been successively cooled to room temperature. They overlay the DSC melting curve recorded in the first heating scan of cast films of the PE samples (black dashed lines). Heating rate is 10°C/min.

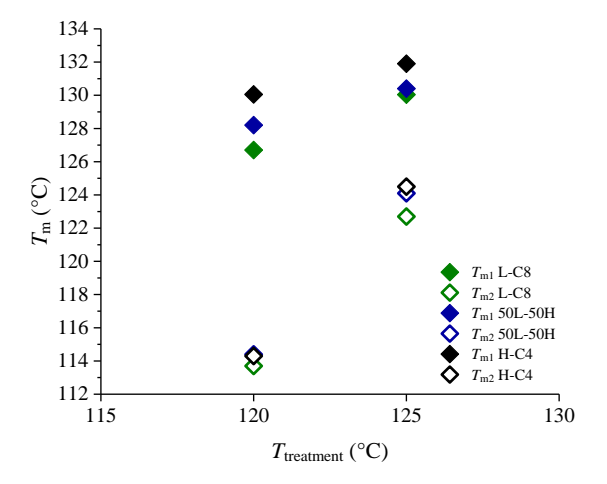


Figure 14 Temperatures of 1° and 2° melting peaks observed in the DSC heating scans of the heat-treated PE samples at $T_{treatment}$ =120°C and $T_{treatment}$ =125°C.

Finally, it is worth to compare the melting behaviour of samples obtained after heat treatment for 10 min at 125 °C and successive cooling to room temperature, starting from the standard crystalline state (HT-FCS, Chapter IV) and from cast films (HT-CF, this Chapter). As an example, the DSC heating curves of the sample L-C8, heat treated for 10 min at 125 °C, and successively cooled at 40 °C/min to room temperature, starting from the different initial states are shown in Figure 15. Both samples show two melting peaks. It is apparent that the peak related to the melting of the annealed crystals occur at the same temperature $T_{\rm ml}~(\approx 130~{\rm ^{\circ}C})$ but the area behind this peak for the HT-FCS sample is lower than that occurring for the HT-CF sample. The peak related to the non-annealed crystals, instead, occurs at two different temperatures $T_{\rm m2}$. In particular, the values of $T_{\rm m2}$ for the HT-SCS sample (\approx 125 °C) is higher than the $T_{\rm m2}$ value observed for the HT-CF sample (\approx 123 °C). Furthermore, the width of and the area behind the peak at $T_{\rm m2}$ are lower and greater, respectively, for of the former sample than the width and area of the same peak in the latter samples. These remarkable differences suggest that the fraction of crystals participating in the annealing process is substantially different in the two initial samples. The adopted conditions to obtain the standard crystalline state induce the formation of crystals with a narrow distribution of lamellar thickness, and only a small fraction of them is able to survive at 125 °C. The majority of the crystals melt at 125 °C, and give rise to a large fraction of crystals upon cooling that melt at $T_{\rm m2} \approx 125$ °C, in a narrow temperature range. For the cast film, instead, the distribution of lamellar thickness is wide. In this case, the majority of crystals survive at 125 °C, and only a minor fraction melt, giving rise to highly defective crystals upon cooling, that, in the successive heating step, melt at $T_{\rm m2} \approx 123$ °C, in a rather broad temperature range.

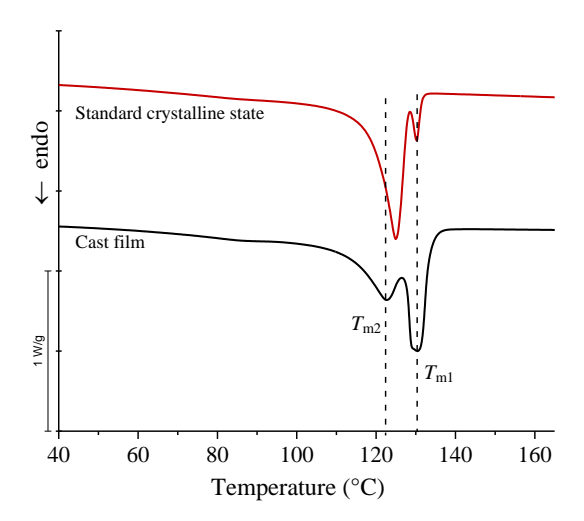


Figure 15 Melting endotherms of sample L-C8 recorded after thermal treatment at 125°C for 10 min, starting from the sample in standard crystalline state (red line) and the cast film (black line).

5.3. Conclusion

The in-situ annealing analyses carried out in this chapter on PE samples at different temperatures have been useful in understanding how in the semi-solid thermal treatments state impact can crystalline/amorphous scaffold of PE. These analyses reveal important details about the values of the lamellar parameter, and the degree of structural disorder that develops in the samples during suitable heat treatments. All these features are strictly related to the chain microstructure, the selected $T_{\text{treatment}}$ and the original semicrystalline state of the sample subjected to the heat treatment.

In all the examined cases, the adopted heat treatment promotes the formation of larger, more perfect lamellae and a modest increase in overall crystallinity. However, it also introduces greater structural disorder and heterogeneity within the samples, generating also fractions of less perfect crystals melting at lower temperature than those in the initial state. The extent of these rearrangements and their impact on the final structure are closely linked to the mobility of macromolecular chains and, more broadly, to the compactness of the semicrystalline structure at the treatment temperature. Indeed, at the same temperature, a less dense structure with higher chain mobility is more sensitive to refinement processes, compared to more ordered and packed structures. This is evident in the study of the structural changes occurring during the heat treatments at 120 and 125°C, where the LLDPE sample demonstrates greater responsiveness to the heat treatments than HDPE. Phenomena such partial melting, annealing of surviving crystals, changes in lamellar parameters and crystallinity have been outlined as function of time at selected treatment temperatures.

The comparison with the results obtained in this Chapter with those obtained in Chapter 4, on samples treated at 125°C for 10 min and then cooled to room temperature, starting from a different initial state has

evidenced the significant impact of the starting structural organization at lamellar length scale on the successive transformations. A narrow lamellar thickness distribution combined with variable long spacings disrupts the ideal conditions for annealing by limiting cooperative chain movement, creating uneven energy landscapes, and preventing uniform crystal growth, all of which reduce the effectiveness of the annealing process.

These observations provide valuable insights into the annealing behaviour of polyethylene in conditions that match with those experienced by the samples in the early stages of the tentering process. The effectiveness of biaxial stretching is closely linked to the structural changes induced by the temperature. Therefore, these findings can help in interpreting the mechanical behaviour of PE samples in the semi-solid state and in identifying optimal processing conditions for tentering.

Chapter VI

Biaxial stretching in-situ analysis

In this chapter, the results of structural analyses carried out by performing in situ Wide Angle X-ray (WAXS) and Small Angle X-ray (SAXS) Scattering experiments during the biaxial stretching process of selected PE samples are reported. The designed in-situ WAXS/SAXS experiments allow for monitoring, structural changes occurring to polyethylene cast films during biaxial stretching. This approach is essential to establish precise correlations between chain microstructure and the crystallization behaviour of the selected samples with the structural transformations occurring at the molecular level induced by stretching, as far as crystallinity, orientation, and morphology are concerned.

Experiments have been carried using the high flux of X-ray radiation available at ESRF in Grenoble and ALBA in Barcelona, employing a biaxial stretching device (tentering frame) built at the Department of Engineering at the University of Salerno, a project partner. To precisely and independently define the effective stretching temperature, calibration methods based on the measure of long period via SAXS or diffraction peak positions via WAXS have been developed.

6.1. Biaxial stretching device

The device is a custom-built apparatus for in situ SAXS/WAXS analysis, specifically engineered to perform real-time structural measurements during the biaxial stretching of polymer films (Figure 1). It consists of a precise, computer-controlled stretching stage that allows simultaneous extension of the sample along two perpendicular axes, simulating industrial tentering processes. To ensure compatibility of the

device with the experimental setups available at synchrotron beamlines, several design guidelines has been followed. In particular, the device has a compact size (35x40x15 cm) and is designed to be compatible with a wide range of uniaxial testing machines, allowing for versatile integration into existing experimental setups. This adaptability ensures that the device can be used in various testing configurations, extending its functionality for both biaxial and uniaxial stretching analyses in synchrotron environments.

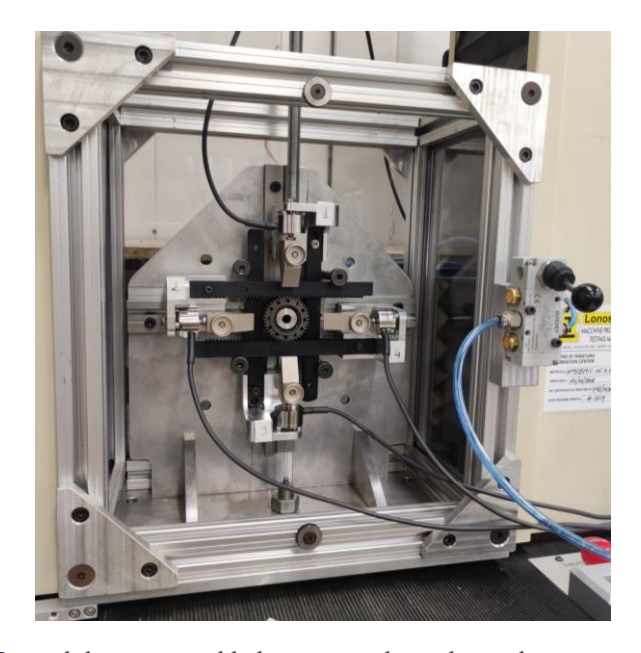


Figure 1 Biaxial device assembled on uniaxial tensile machine

The device consists of several key systems, each designed to optimize testing conditions and ensure precise, reliable results during in situ SAXS/WAXS analysis of biaxial stretching. The main components include:

Moving system

The device operates without an external motor, instead utilizing the crosshead movement of a tensile testing machine, which powers a rack-and-pinion mechanism (Figure 2). Clamps are attached to four

moving blocks, each mounted on individual gear racks. The upper block is linked to the moving crosshead of the tensile testing machine. As the crosshead rises, it causes the two pinions to rotate, driving the other racks and allowing simultaneous stretching of the sample both vertically and horizontally, while keeping the center of the sample stationary for optimal in situ analysis. As visible in Figure 2, the central gear is designed with a hole that enables X-ray beam to pass directly through the sample.

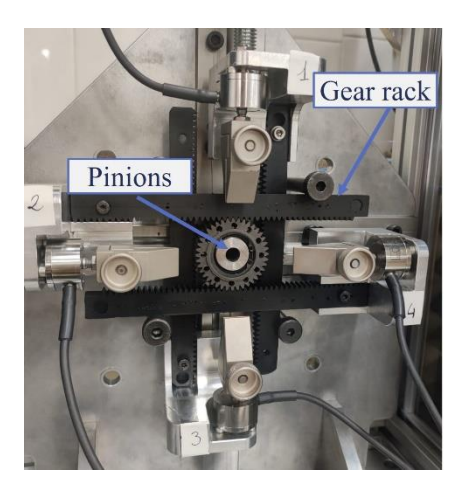


Figure 2 Rack-and-pinion system of the device

Heating system

The device is designed to facilitate biaxial testing at a range of stretching temperatures, from room temperature up to 140°C. This temperature control is essential, as the biaxial stretching process of polyethylene occurs in a semi-solid state, within a temperature range between the onset and peak of its melting endotherm. Heating of the sample is achieved through convection: compressed air is preheated by two coil heating elements housed in ceramic tubes (Figure 3). These heating elements are mounted on adjustable holders, allowing precise adjustment of their position and distance from the sample to optimize

temperature distribution homogeneity. The air pressure and flow rate are controlled using rotameters and pressure regulators. Generally, the air pressure is set to 1.5 bar, resulting in an airflow of 10⁻³ standard m³/s through each heating element. Air temperature is measured by two thermocouples positioned 10 cm from each heating element outlet, approximately 1 cm from the sample, and managed via two OMRON E5CB temperature controllers. To ensure accurate temperature application during stretching, a calibration protocol is employed, allowing precise control of the temperature experienced by the material. To track structural evolution during crystallization upon sample cooling, the system can deactivate the heating elements and instead circulate room-temperature compressed air, facilitating controlled cooling conditions.

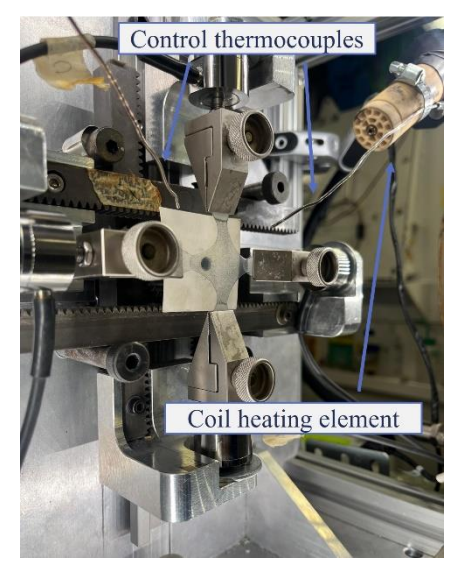


Figure 3 Heating system consisting in two heating coil elements (only one is visible in the picture, the other one is located in a symmetric position with respect to the sample) connected to compressed air and controlled using two thermocouples close to the sample.

Monitoring system

The device includes a comprehensive monitoring system that tracks force and deformation throughout the stretching process. This setup enables assessment of deformation uniformity and potential detection of sample damage, such as crack formation. Force measurements are obtained on each clamp via four HBM K_U9C load cells, with a maximum load capacity of 100N and an operating temperature range up to 140°C (Figure 3). The data are captured using an HBM acquisition system, which features a universal signal amplifier (MX840-PAKEASY) and CATMAN-EASY software for data processing and analysis.

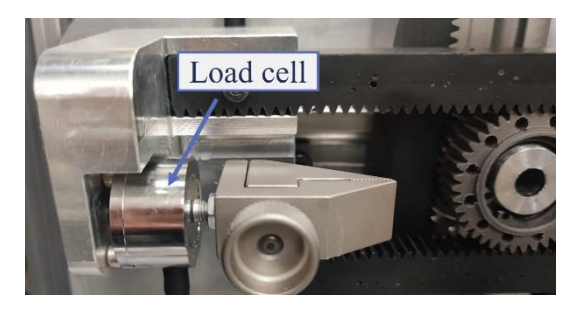


Figure 4 Load cell (the cylinder on which the clamps are screwed) and clamp mounted in the moving block.

To evaluate material deformation behaviour, the system employs Digital Image Correlation (DIC), a non-contact, image-based technique. DIC uses image registration algorithms to track relative displacements of points on the material surface by comparing a reference image (of the undeformed samples) with subsequent images (at different deformation degree), providing detailed deformation data. Therefore, the samples used in these analyses were pre-coated with a heat-resistant spray paint to create a point pattern (Figure 5). The open-source DIC software Ncorr was used for this analysis, enabling precise

and efficient tracking of deformation patterns at the centre of the sample.

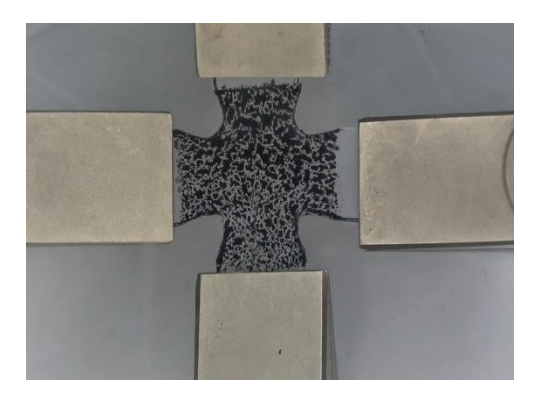


Figure 5 Biaxial sample covered by a random speckle pattern.

Once the reference image and the image to analyse have been selected, a Region of Interest (ROI) and the parameters for the analysis must be defined. The main parameters are subset radius and subset spacing: they establish how large is the subsets and the spacing between the tracked points. The spacing component is solely intended to reduce computational load, while the subset radius strongly impacts the evaluation. For this application, the optimum was found to be with a subset radius of around 20 pixels and spacing of 2 pixels. To allow the evaluation in case of materials undergoing large deformation, Ncorr algorithm enables a discontinuous analysis whereas the ROI and reference image are updated during the analysis, changing frame by frame. Biaxial stretching experiments have been recorded using a commercial camera (CMOS image sensor). Subsequently, 25 frames for each second are extracted from the video and used for the DIC analysis. The algorithm estimates the four displacement gradients (horizontal and vertical displacement with respect to defined x and y directions) and calculates Green-Lagrangian strains as follows (Eq. 1):

$$E_{xx} = \frac{1}{2} \left(2 \frac{\partial u}{\partial x} + \left(\frac{\partial u}{\partial x} \right)^2 + \left(\frac{\partial v}{\partial x} \right)^2 \right)$$

$$E_{yy} = \frac{1}{2} \left(2 \frac{\partial v}{\partial y} + \left(\frac{\partial u}{\partial y} \right)^2 + \left(\frac{\partial v}{\partial y} \right)^2 \right)$$

$$E_{xy} = \frac{1}{2} \left(\frac{\partial u}{\partial y} + \frac{\partial v}{\partial x} + \frac{\partial u}{\partial x} \frac{\partial u}{\partial y} + \frac{\partial v}{\partial x} \frac{\partial v}{\partial y} \right)$$
(1)

Where u and v are horizontal and vertical displacements respectively. The deformation field can be expressed as a deformation tensor of the calculated strain (Eq. 2). To obtain a global description of deformation that does not consider the strain directionality, the second invariant of strain tensor was evaluated as shown in Equation 3 and one half of the second invariant was considered.

$$A = \begin{bmatrix} E_{xx} & E_{xy} \\ E_{xy} & E_{yy} \end{bmatrix}$$

$$E = \frac{1}{2} I_{II} = \frac{1}{2} \sqrt{E_{xx}^2 + E_{yy}^2 + 2E_{xy}^2}$$
(3)

The second invariant of the deformation tensor provides also an effective measure of the average deformation state throughout the test. For this reason it results particularly useful evaluating SAXS results as a function of strain rather than time of experiments, enabling comparisons between samples that differs in deformation behaviors.

To calculate the engineering stress an estimation of the true cross-section of samples is needed. While for uniaxial stretching rectangular specimens it is generally easier to consider the initial length L_0 and thickness, for cruciform specimens used in biaxial stretching tests, the unique shape complicates the calculation. Therefore, a nominal cross-section has been calculated, considering the vertical and horizontal initial lengths (indicated as L_0^{vertical} and $L_0^{\text{horizontal}}$ respectively) of 7 mm, determined based on sample

geometry (Figure 6) and sample thickness of 0.7 mm. The engineering stresses were calculated using the following relation:

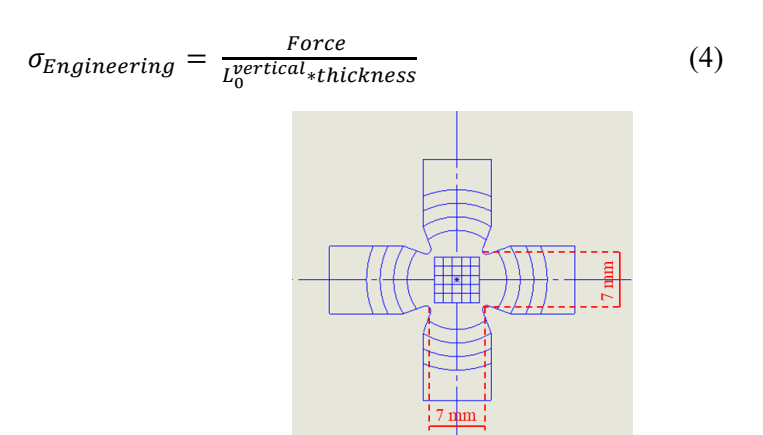


Figure 6 Cruciform shape of samples designed to ensure a more homogenous deformation during biaxial stretching. The indicated lengths of 7 mms are the selected L_0 in the horizontal (x) and vertical (y) directions, for determining engineering stresses.

6.2 Experimental

In this Chapter the results obtained for biaxial stretching of the samples L-C8 at selected $T_{\rm tentering}$ =117, 114, 118 °C are illustrated, as an example. In each run performed in different synchrotrons experiments, the samples used are pre-casted sheets (mentioned as cast films in Chapter V) produced at Karo Bruckner facility, with an average thickness of 0.7 mm. These sheets have been cut in a cross shape, kept at $T_{\rm tentering}$ for a certain amount of time (~5 min) grafted to the clamps and then biaxially stretched at 7 mm/s at target temperatures, corresponding to 200%/s, which is an industrial-relevant condition for tentering. The selected $T_{\rm tentering}$ temperature falls under the melting endotherm of the sample, ensuring that the stretching is performed in the semi-solid state. The cast films are basically isotropic, but there is a slight orientation in one direction,

hereafter MD, due to the extrusion process adopted for preparation. The transversal directions is instead addressed as TD. For this reason, although the stretching is biaxial, both directions are specified in the 2D WAXS and SAXS patterns.

6.3. 2D-SAXS/1D-WAXS analysis on samples stretched until breakage

The first set of experiments involves in-situ SAXS/WAXS structural analysis of samples biaxially stretched until failure. The results obtained for sample L-C8 are presented below, along with a comparison between the results of biaxial and uniaxial stretching experiments. Biaxial sample geometry was selected as described previously (Figure 6), while a rectangular-shaped sample was used for uniaxial testing (width 15 mm and length 30 mm). Uniaxial sample dimensions were selected to ensure that the beam would pass through the sample during the stretching process, even though the necking phenomenon would result in a reduction of the surface area perpendicular to the beam. In the context of the in-situ measurements, the tensile machine was provided by Beamline BM26B at the European Synchrotron Radiation Facility (ESRF, Grenoble, FR), where analysis have been carried out. Experiments have been conducted using an X-ray source with a 1.033 Å and a beam diameter of 300 µm All SAXS patterns were collected using a Pilatus 1M detector (981 x 1043 pixels of 172 μm x 172 μm placed at a distance of 2.98 m). All WAXS patterns were instead collected using a 300K-W linear Pilatus detector (254mm x 33.5mm active area) placed at distance of \sim 30 cm from the sample. The sample-to-detector distance and the detector tilt angle were calibrated using silver behenate (AgC₂₂H₄₃O₂) as a standard.

All X-ray images were corrected for the background scattering and normalized for synchrotron beam fluctuations using an ionization chamber placed before the sample and for the transmission of the film using a photodiode placed on the beamstop. Biaxial stretching experiments, conducted at a strain rate of about 150% s⁻¹, are completed in about 8 seconds. To accurately capture the process without introducing noise, an exposure time of 0.1 seconds was used for real-time monitoring of structural changes. In this set of experiments the samples have been stretched up to failure.

A photograph illustrating the experimental setup for carrying out biaxial stretching while simultaneously collecting SAXS and WAXS data is shown in Figure 7, while a schematic representation of the entire setup is reported in Figure 8.

The camera for DIC analysis was positioned close to the WAXS detector, this resulted in a slight parallax angle, which was subsequently corrected through the implementation of a camera calibration protocol. The vacuum tube connected to the SAXS chamber was kept as close as possible to the sample to minimize the air gap during measurements. Data acquisition was triggered by directing a LED light source toward a photodiode and using an ad-hoc LabVIEW software developed by the research team in Salerno. LED light was fixed to the crosshead, while a photodiode was hung on the column of the tensile machine (7): when the crosshead arose, the LED light left the photodiode, which registered a change in tension (from 0V to 5V); the analogical signal was converted into a digital signal by a multifunction DAQ device (NI USB-6210) and elaborated by the LabVIEW software, which enabled the X-ray measurement to be triggered.

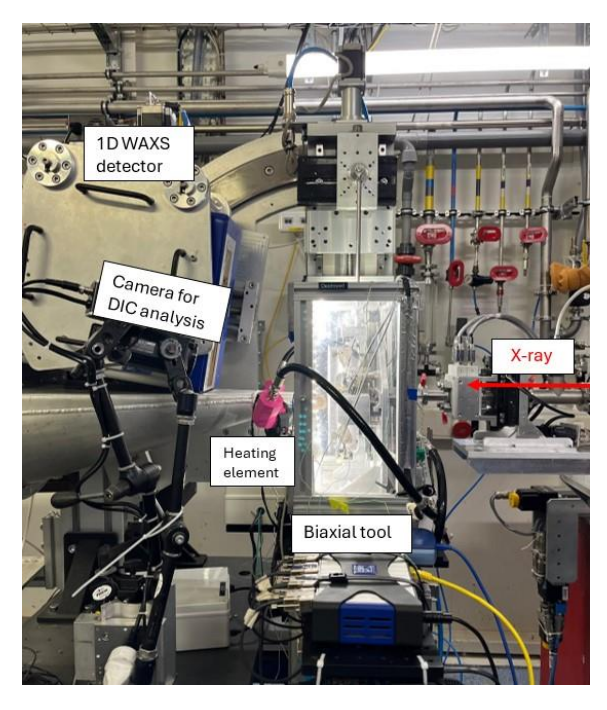


Figure 7 Biaxial tool coupled with X-ray setup in experimental hutch of the European Synchrotron Radiation Facility (ESRF).

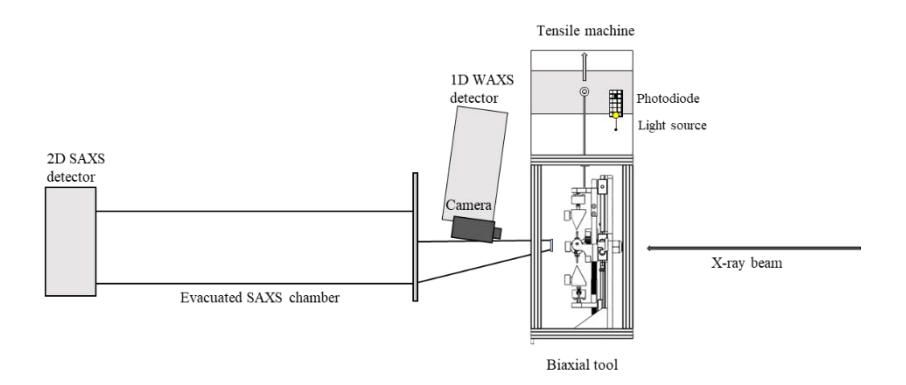


Figure 8 Schematic representation of biaxial tool combined with X-ray setup at ESRF.

Temperature calibration

To determine the sample temperature of the tests, a temperature calibration procedure has been performed, measuring Small Angle X-Ray Scattering (SAXS) data on cast films of the sample L-C8, at 115, 120 and 125°C, at ESRF facility. The sample has been heated using a Linkam HFS91 cell. From structural analysis conducted on cast films subjected to thermal treatment at 120 and 125 °C in Chapter V, it has been observed that the values of long spacing L tend to steady around a constant values after ~ 5 min at these temperatures (Figure 5 and 9 of Chapter V). The same happens for $T_{\text{treatment}} = 115$ °C too. As shown in Figure 8, the correlation peak of the Lorentz's corrected SAXS intensity profiles measured after 10 min at 115, 120 and 125 °C shifts to lower q values, as the temperature increases. The linear fit of the position of the maximum of the correlation peaks (q_{peak}) versus the temperature gives the calibration plot of Figure 9.

After mounting the sample in the tentering frame, before starting biaxial stretching, the sample has been kept at the selected tentering temperatures for at least 5 min. Hence, a SAXS pattern of the cast film has been collected, and the q_{peak} value in the Lorentz's corrected intensity SAXS profile has been determined. The tentering temperature has been hence identified as the temperature in the calibration plot that corresponds to the so-determined value of q_{peak} .

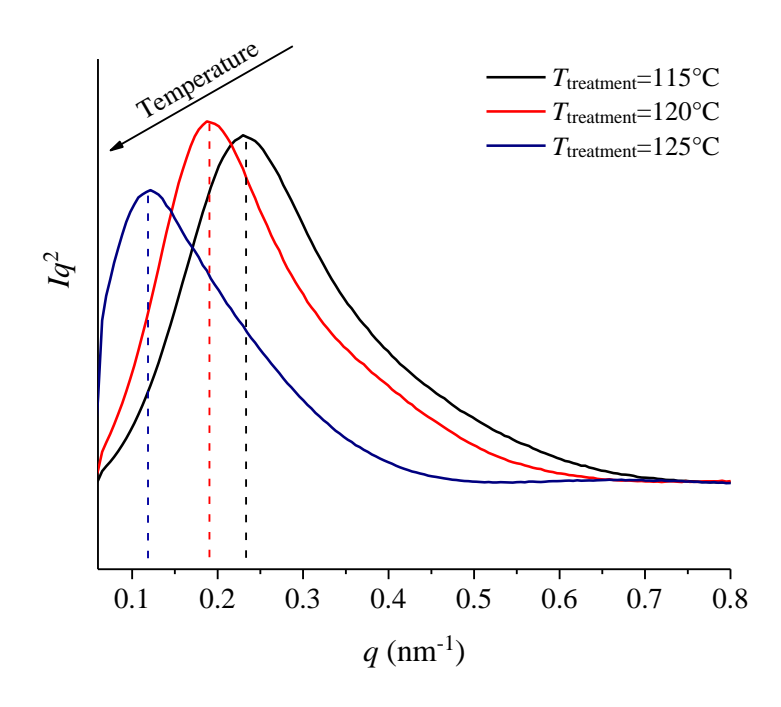


Figure 8 Lorentz's corrected SAXS intensity profiles collected after 10 min at the indicated temperatures. The dashed vertical lines at the peak maximum (q_{peak}) are indicated.

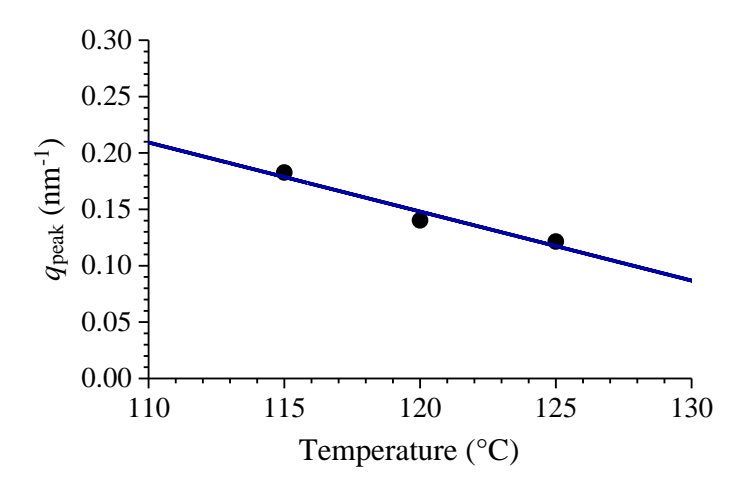


Figure 9 Calibration plot obtained by the linear fit of the position of correlation peak q_{peak} of Figure 8 vs. the temperature.

The obtained calibration curve is expressed by Equation 5:

$$q_{peak} = 0.88281 - 0.00612 T \tag{5}$$

According to equation 5, the peak position at $q_{\rm peak}$ =0.165 nm⁻¹ measured for the cast films of the sample L-C8 before uniaxial and biaxial deformation corresponds to a stretching temperature of 117°C.

Stretching experiments - Uniaxial test

To perform the uniaxial stretching test, the rectangular sample was secured to the device using only the horizontal clamps, with the machine direction (MD) of the original cast film aligned to the stretching direction. The whole experiment lasted a total of 5.6 seconds, before the sample reached its breaking point and ruptured under the applied stress. Figure 10 shows the force measured by the load cells as a function of time.

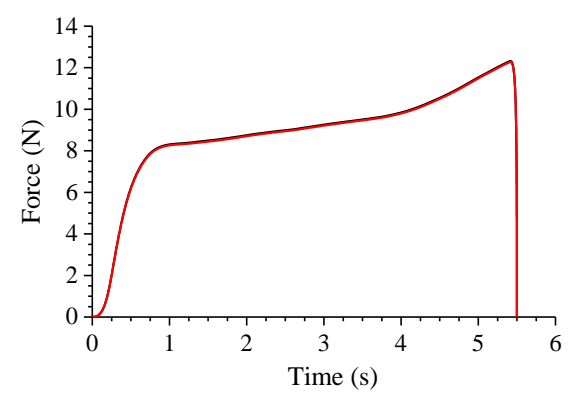


Figure 10 Force vs time measured by the load cells during uniaxial stretching of L-C8 sample.

The strain distribution upon uniaxial stretching, measured by using Digital Image Correlation (DIC) technique, reached before failure is shown in Figure 11. Although the stretching was uniaxial, low strains were also observed in the transverse direction (TD) of the sample, corresponding to the reference direction y, due to the insurgence of necking during the stretching. In Figure 12 the evolution of strain with time is illustrated. It is apparent that the sample L-C8 subjected to monoaxial stretching, achieves a remarkable high draw ratio (DR) at rupture, equal to 15. The

corresponding stress-strain curve is shown in Figure 13. The sample exhibits flat yielding behaviour and strain hardening at high deformations, due to the increase in orientation during stretching.

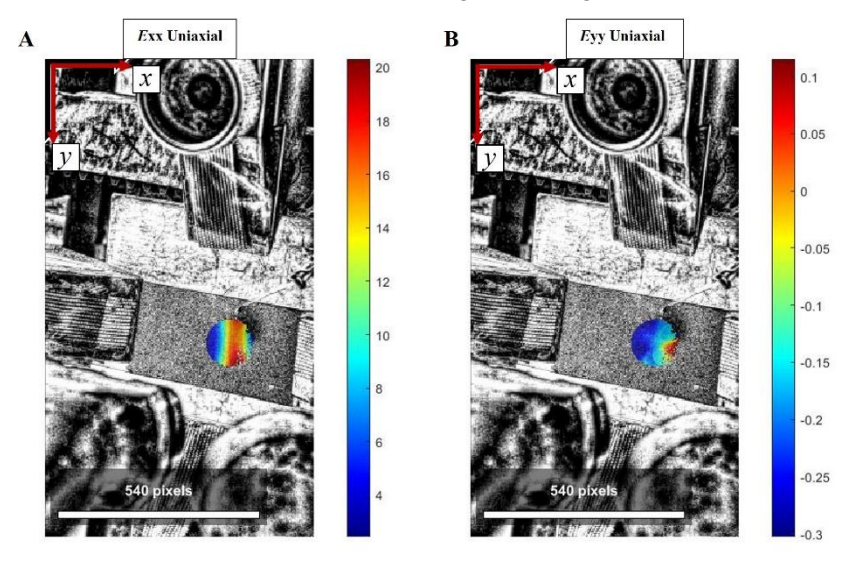


Figure 11 (A) Horizontal and (B) Vertical strain distribution upon uniaxial stretching test, measured by DIC technique, before failure of the L-C8 sample. Failure occurred after 5.6 s. The red arrows indicate the directions x and y along which the displacement gradients have been calculated.

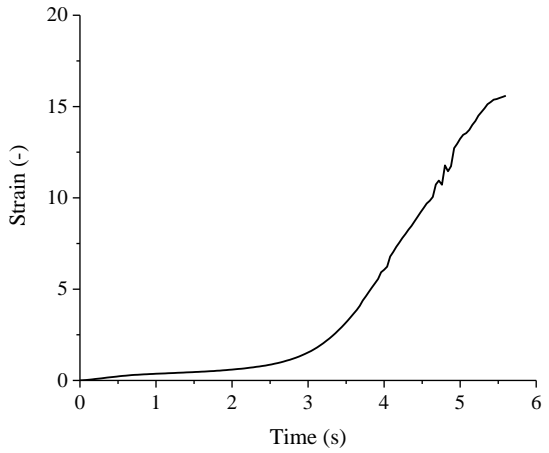


Figure 12 Evolution of strain with time during uniaxial stretching of L-C8 sample.

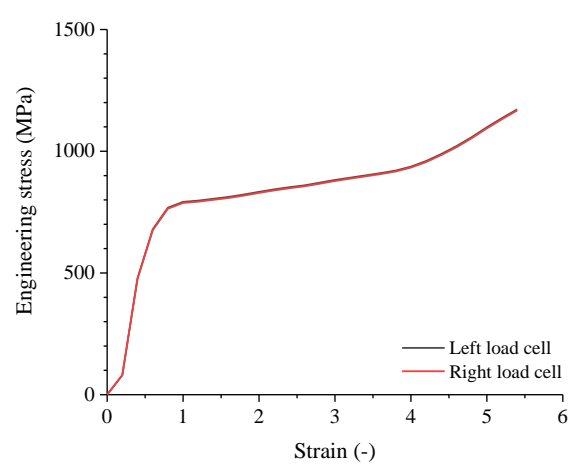


Figure 13 Stress-strain curve for uniaxial stretching of sample L-C8

In Figure 14, representative 2D-SAXS patterns acquired during uniaxial stretching at different values of draw ratio (*DR*) are reported, along with the corresponding photographs of the sample captured during the test. In the uniaxial stretching test, the vertical and horizontal directions of the bidimensional (2D) patterns are parallel to the transverse (TD) and machine (MD) directions of the cast film, respectively.

At the beginning of the stretching (t=0 s, DR=0) the SAXS pattern appears as a circle with uniform intensity distribution, indicating that the undeformed cast film is characterized by an isotropic lamellar stacks network. As the sample is stretched along the MD direction (t=1.6 s, DR=0.5), the SAXS intensity distribution becomes elliptical with long and short axes directed along the vertical (parallel to TD), and horizontal directions (parallel to MD), respectively. This indicates that the lamellar crystals tend to become oriented along the direction parallel to the stretching direction. As the draw ratio increases ($t \ge 3.2$ s, $DR \ge 2$) and the necking region enters into the beam, two signals of significant intensity $^{1-3}$ emerge and become increasingly more pronounced, consisting in a narrow streak across the beamstop along the vertical direction (parallel to TD), and two lobes along the horizontal direction (parallel to MD). The two lobes

patterns and the equatorial streak are the hallmark of the formation welloriented fibrillar entities along the MD, around which lamellar crystals grow with the normal to the basal planes parallel to the fibrillar entities, giving rise to shish-kebab-like morphologies.

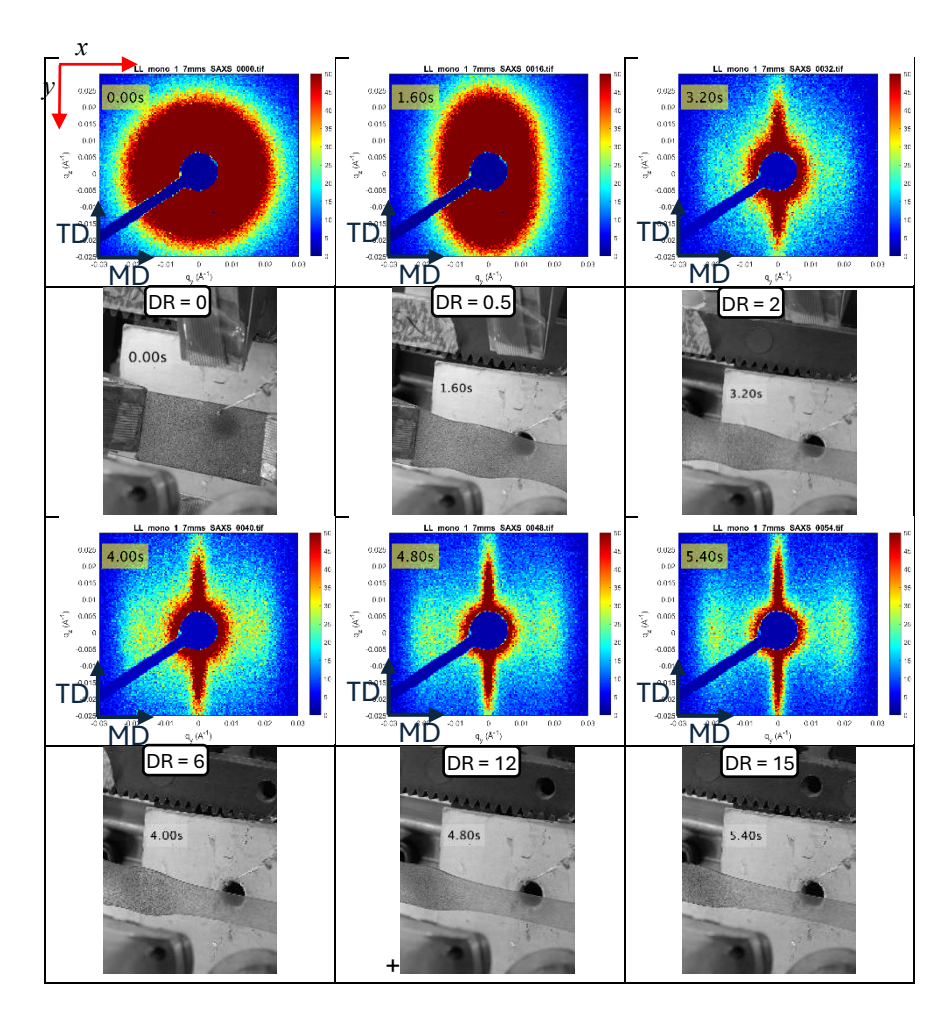


Figure 14 2D-SAXS patterns and related photographs capturing the deformation state that the sample is subjected during the uniaxial elongation test. The stretching direction is horizontal.

Stretching experiments - Biaxial test

Biaxial stretching of sample L-C8 has been performed mounting the specimen with the MD direction of the cast film aligned vertically. This direction is indicated with y in Figure 15, where the strain distribution upon biaxial stretching in the horizontal (x) and vertical (y) directions of the unstretched sample are indicated.

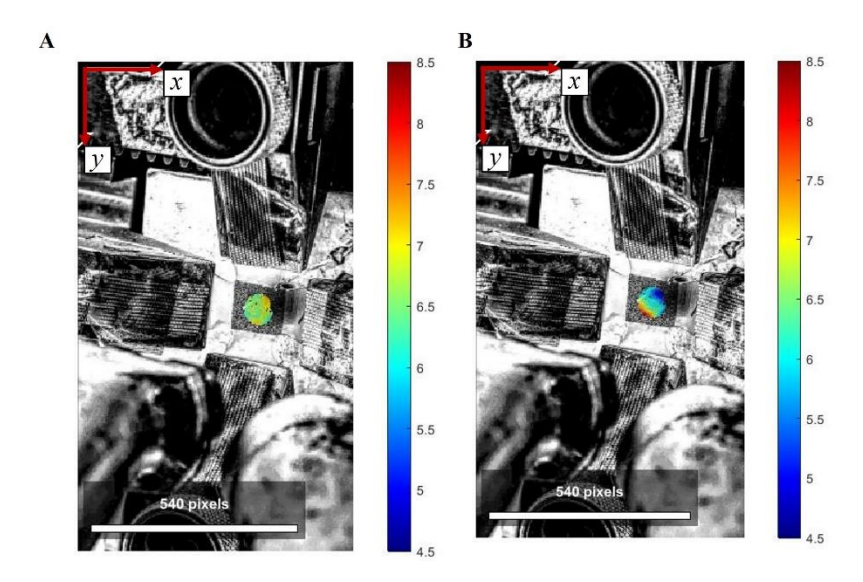


Figure 15 Horizontal(A) and Vertical (B) strain distributions of the unstretched cast film, measured by DIC technique, for the sample L-C8. Upon biaxial stretching failure occurred in 4 s. The red arrows indicate the directions x and y along which the displacement gradients have been calculated.

The forces measured by the four load cells as a function of time are shown in Figure 16. The forces measured by the bottom and top load cells in the y-direction are lower and greater, respectively, than those measured by the couple of cells in the x-direction. The values of strain experienced by the sample in the x and y directions as a function of time (Figure 17) increase with time according to similar, but not coincident trends, indicating that the deformation is slight inhomogeneous. In particular, in first 3 s of biaxial stretching, the values of E_{yy} are greater than those of E_{xx} and only after 3 s they become more similar. At failure, occurring after 4 s, the sample

reaches a draw ratio of ≈ 6 in both direction ($\approx 6x6$ strain). The corresponding stress-strain curves are shown in Figure 18. Similar to uniaxial test (Figure 13), the stress-strain curve measured at the four load cells show non pronounced yielding, and only a slight strain-hardening (if any) at high deformations.

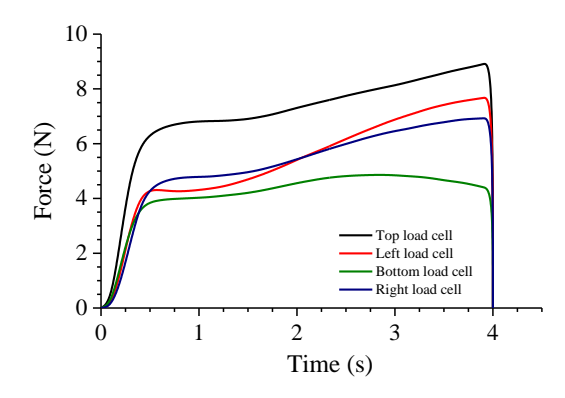


Figure 16 Force vs time measured by the 4 load cells during biaxial stretching of the sample L-C8.

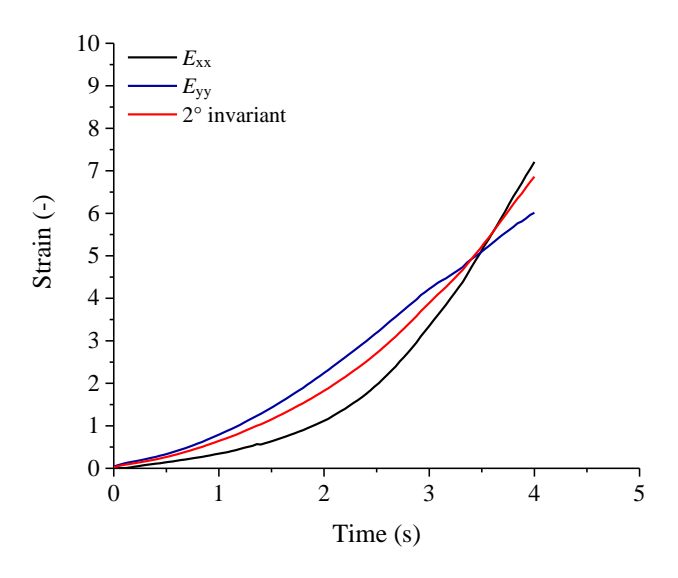


Figure 17 Evolution of strain (DR) along x and y direction and calculated 2° invariant with time during biaxial stretching of the sample L-C8.

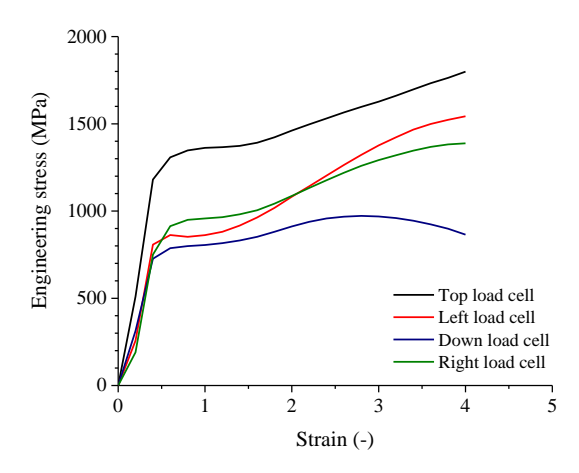


Figure 18 Stress-strain (DR) curves collected during biaxial stretching of the sample L-C8.

Representative 2D-SAXS images collected during biaxial stretching are shown in Figure 19. For each frame, the photograph of the specimen stretched at the indicated DR are also reported. At variance with uniaxial stretching test, in the biaxial stretching test, the vertical and horizontal directions of the bi-dimensional (2D) patterns are parallel to the machine (MD) and transverse (TD) directions of the cast film, respectively.

The undeformed sample (t=0, DR=0x0) shows a 2D-SAXS image characterized by a uniform radial intensity distribution due to isotropic orientation of lamellar stacks. As the deformation increases, the radial intensity distribution becomes less uniform, approaching an elliptical shape until a draw ration DR of 2.5x2.5 is reached (t = 2.4 s). At variance with the uniaxial stretching (Figure 14), for biaxial stretching the long and short axes of the ellipse are directed along the horizontal (parallel to TD), and vertical (parallel to MD) directions, respectively. This is due to unbalanced deformation experienced the sample, in agreement with the results of Figure 17 that show $E_{yy} \ge E_{xx}$, and indicate that the lamellar crystals tend to become oriented along the direction parallel to MD. As the biaxial deformation increases, the elliptical pattern changes back to a

circular shape, indicating that deformation tend to become more balanced. It is worth noting that the intensity of scattering decreases substantially during stretching due to the significant thinning of the sample. The final shape of the 2D-SAXS pattern at DR=6x6 and t = 3.6 s, suggests a uniform in plane orientational distribution of the crystals.

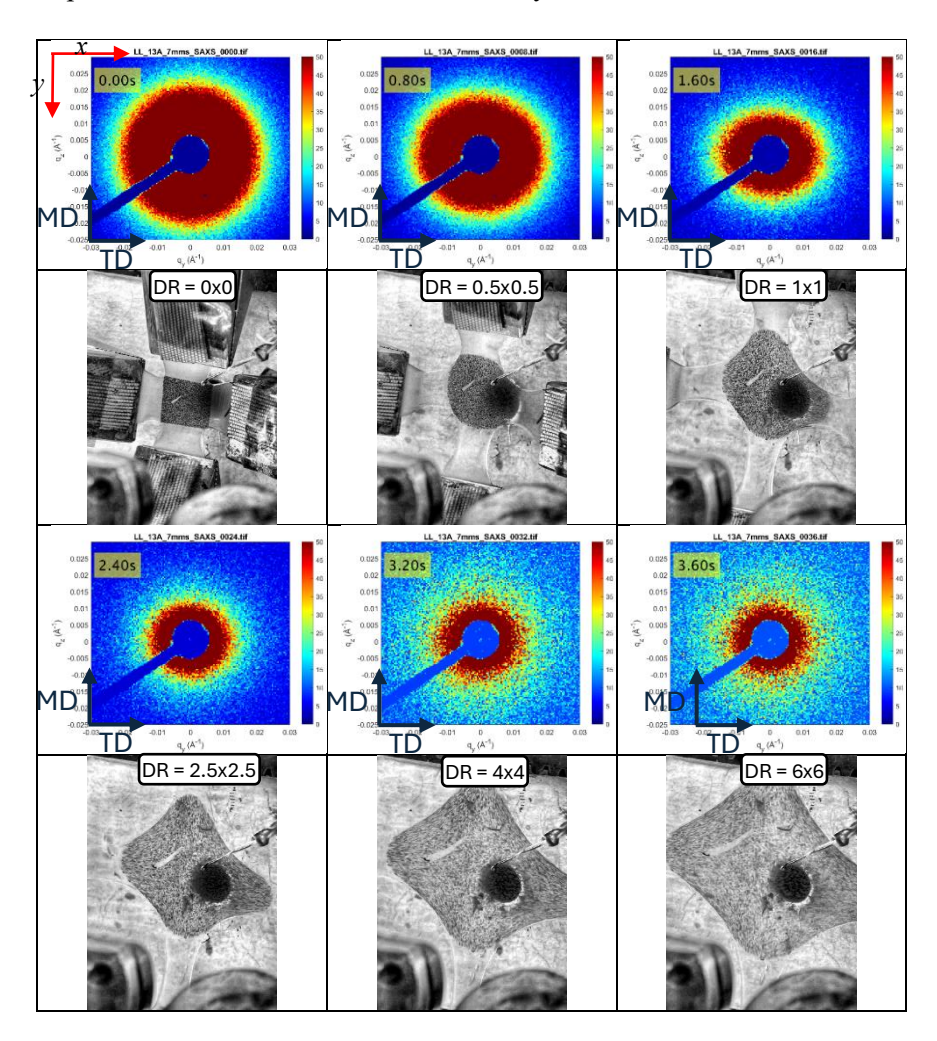


Figure 19 2D-SAXS patterns and related photographs capturing the deformation state that the sample is subjected during the biaxial stretching test.

By azimuthally averaging the 2D-SAXS patterns, monodimensional SAXS profiles of the sample L-C8 during biaxial stretching have been extracted

as a function of q, with $q = 4\pi \text{sen}\theta/\lambda$ and θ half the scattering angle. They are reported in Figure A1 of Appendix A9. The monodimensional self-correlation function of electron density fluctuations (correlation function CF), extracted from SAXS data, are reported in Figure A2A of Appendix A9, while the values long period L extracted from CF are reported in Figure 20A as a function of time. The 1D-WAXS profiles collected simultaneously with the SAXS data are instead reported in Figure A2B of Appendix A9. The values of the apparent crystallinity index extracted from WAXS data are reported in Figure 20B as function of time. The so-obtained values of crystallinity index are only "apparent", as they represent a qualitative parameter, due to anisotropic orientational distribution achieved by the crystals during stretching.

During biaxial stretching, the values of long spacing (Figure 20A) first increase from ≈41 nm at the beginning, to a maximum equal to ≈48 nm after 1.6 s, then decrease to a minimum of ≈28 nm after≈3.5 s, and finally increase again approaching the value of ≈32 nm at failure, after 4s. This oscillating behaviour suggests the emergence of at least two phenomena. During stretching, at the beginning of the biorientation process, the applied mechanical stress field induces an increase of the average interlamellar distances (long spacing) because of the stretching of the chains in the intralamellar amorphous layers. This initial stage eventually induces lamellar breaking and increase of orientation of the amorphous and crystalline phases. Once a certain degree of orientation is achieved during stretching, part of the (oriented) amorphous chains start to crystallize, generating new lamellae in between the survived crystals. As a consequence, the values of L tend to decrease. With further increase of strain, the stretching of the amorphous chains in the intra-lamellar layers comes into play again, causing the last increase in lamellar periodicity, until the mechanical energy administered to the sample becomes high enough to finally break the sample. The values of the apparent crystallinity index (Figure 20B), instead, decrease monotonously as the time increases.

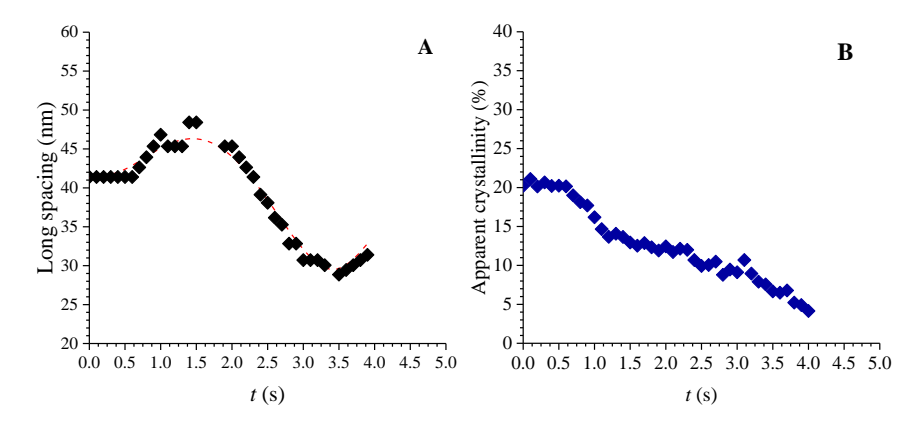


Figure 20 (A) Values of long spacing extracted from the Correlation Function and (B) Corresponding values of the apparent crystallinity index evaluated from WAXS profiles, relative to the sample L-C8 subjected to bi-axial stretching at 117 °C.

6.4 2D-SAXS/1D-WAXS analysis on samples stretched until a specific draw ratio and successive cooling

To monitor the structural development of the sample L-C8 during the biaxial stretching at a given draw ratio (DR) at a fixed temperature, and the successive cooling step, a specific experimental setup has been implemented, that allows the simultaneous and remote shutdown of the heating system, along with the stopping of the drawing process at the select values of DR. When the heating elements are turned off, they still insufflate compressed air at room temperature. Sample cooling is governed by transport phenomena equations and is influenced by the initial temperature of the sample. The team involved in this project of the Engineering Department at the University of Salerno (DIIn) has previously carried out analyses on polyethylene cast-films, in order to simulate the experiment carried out at synchrotron facility, and to estimate a temperature profile experienced by the sample during cooling. The resultant temperature

profile has allowed to establish precise correlations between the time lapsed during the in-situ collection of SAXS and WAXS data in the planned stretching experiments, with the temperature achieved by the sample during the cooling step.

Cooling process calibration

The cooling process has been calibrated by measuring the air temperature with the above-mentioned thermocouples (Figure 3) and mounting a third thermocouple sandwiched between two PE sheets, with an overall thickness of 0.7 mm. Sample cooling rate can be expressed as:

$$\frac{dT_s}{dt} = -a(T_s - T_a) \tag{6}$$

Where T_s is the temperature of the sample, T_a is the temperature of the external air blown by the heating guns and a is a coefficient that can be expressed as:

$$a = \frac{h}{\rho C_p \delta/2} \tag{7}$$

In Equation 7, h is the heat transfer coefficient, ρ and C_p are the density and the specific heat, respectively, and δ is the sample thickness.

During cooling, fresh air is blown by the heating elements and therefore the air temperature T_a can be expressed by an exponential law.

$$T_a = T_{a\infty} + (T_{a0} - T_{a\infty})e^{-bt}$$
 (8)

where b is a coefficient which was experimentally determined as $b = 0.051 \, s^{-1}$ by fitting the time evolution of the measured air temperature (Figure 21, black curve).

From Equation 6 and 8 it is possible to describe the temperature evolution of the sample during cooling, with the initial boundary condition:

$$T_s(t=0) = T_{s0} = T_{a0}$$
:

$$T_s = T_{a\infty} + (T_{s0} - T_{a\infty}) \left(e^{-at} + \frac{a}{a-b} \left(e^{-bt} - e^{-at} \right) \right)$$
 (9)

The parameter a was determined by fitting the sample temperature evolution (Figure 21, blue curve). Figure 21 shows a good agreement between temperature evolution experimentally observed and calculated through the transport phenomena equations.

The heat transfer coefficient h was determined from Equation 7 as 370 W/m²K. The dimensionless Biot number (Bi) has been calculated as follows:

$$Bi = \frac{h\delta/2}{k} \tag{10}$$

where h is the heat transfer coefficient, k is the thermal conductivity. When the sample is 0.7mm thick, as in the test adopted for calibration, the Biot number is of the order of 10^{-2} , which means that the temperature inside the sample is homogeneous. During the stretching experiments the sample thickness significantly decreases from the initial value, and when cooling starts the thickness δ corresponds to the final value, estimated to be 0.05 mm. In this case, the parameter a in Equation δ becomes so large (about 0.5/s) that the sample temperature essentially follows the air temperature history (black line in Figure 21). The cooling rate in this case becomes about 3° C/s. The dimensionless Biot number for the stretched samples becomes of the order 10^{-3} , hence the temperature field inside the sample can surely be considered homogeneous.

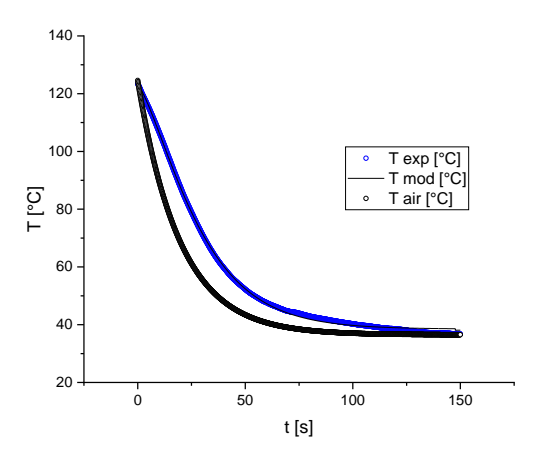


Figure 21 Sample temperature evolution during cooling. Blue circles correspond to experimental temperature measured with the thermocouple sandwiched between PE sheets, black circles correspond to experimental temperatures measured by thermocouples in air (\approx 10 cm from the heating elements), black line corresponds to the fit of experimental data (blue circles) with equation 9.

Biaxial test

SAXS data have been collected in situ on the sample L-C8 during bi-axial stretching and, after stopping the deformation at a selected time, during the successive cooling. A schematic representation of the adopted setup is shown in Figure 22. Measurements have been carried out at NCD-SWEET Beamline at ALBA synchrotron facility (Barcelona, Spain), using X-rays with a wavelength of 1.033 Å and a beam diameter of 300 μ m. The SAXS patterns have been collected using a Pilatus 1M detector (981 x 1043 pixels of 172 μ m x 172 μ m) placed at a sample-to-detector distance of 2.98 m. The sample-to-detector distance and tilt angle have been calibrated using silver behenate (AgC₂₂H₄₃O₂) as a standard. The obtained 2D-SAXS patterns have been subtracted for the contribution from the empty tentering cell and corrected for the transmission factor. The obtained patterns have been converted into 1D intensity profiles using the Python library PyFai. The pixel scale was converted into the q scale using the known peak positions from the standard silver behenate sample, where $q = 4\pi \sin\theta/\lambda$, λ

is the wavelength and θ is half of the scattering angle. The Lorentz's correction was also applied and the obtained profiles were fitted with a pseudo-Voigt function. SAXS data have been collected with an exposure time of 0.1 s.

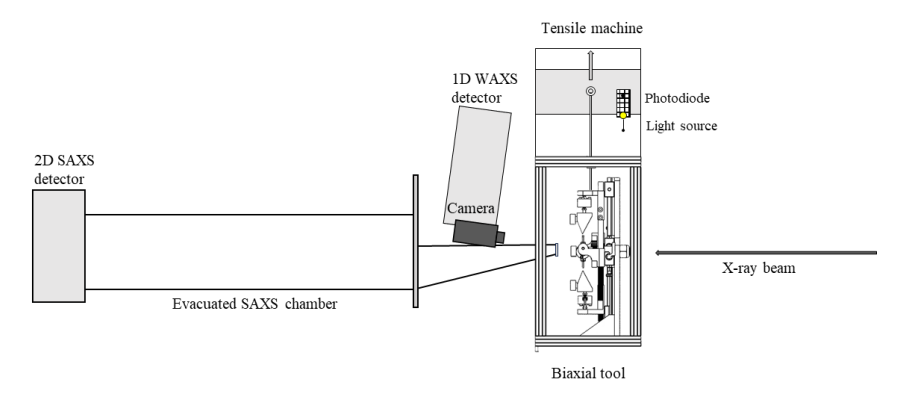


Figure 22 *Schematic representation of the tool for biaxial stretching combined with X-ray setup at ALBA.*

The experiment consists of a stretching phase in the first 2 s, immediately followed by a cooling step. The stretching rate has been adjusted in order reach a clamp displacement of approximately 8 cm in 2 s. Using the calibration curve of Figure 9, the adopted tentering temperature corresponds to 114 °C. Data have been collated for a total of 15 s.

The values of the force and strain achieved during this experiment are reported in Figure 23 as a function of time. In the first 2 s, the force shows a linear increase in the first 0.8 s, successive softening, followed by a new increase. At beginning of the cooling step, the force gradually decreases, by effect of relaxation of the material, up to reach a quasi-plateau. Moreover, at the end of the tentering step, the sample reaches a final strain equal to 2x2. The deformation appears slightly unbalanced, as the horizontal component E_{xx} is greater than the vertical component E_{yy} throughout the entire stretching phase, and also the force probed by left load cell is greater than the force probed by the other load cells.

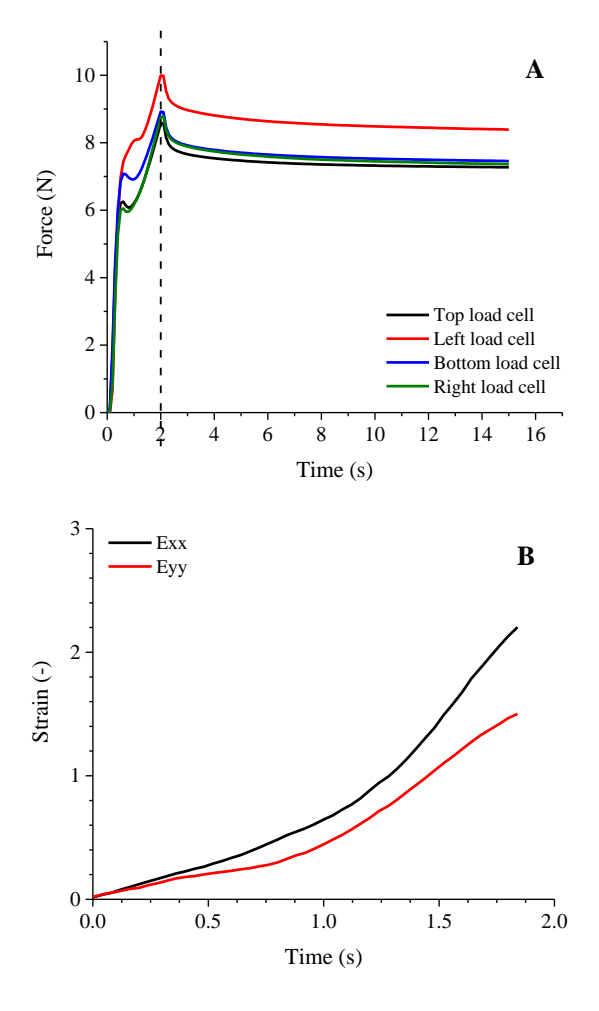


Figure 23 (A) Force vs time measured by the 4 load cells and (B) Evolution of strain along x and y direction with time during biaxial stretching of the sample L-C8.

Representative 2D SAXS images collected at different times are shown in Figure 24. The isotropic distribution of SAXS intensity, of circular shape, collected in the initial frame for the undeformed sample, is replaced by a less isotropic distribution of elliptical shape at the end of the tentering process (after 2 s). At the end of the cooling step an isotropic distribution of SAXS intensity is recovered, indicating that the lamellar orientation is isotropic in the deformed specimen (t=15s, DR=2x2).

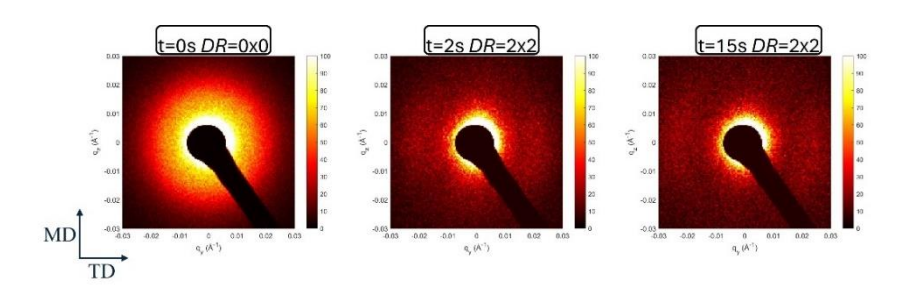


Figure 24 Selected 2D-SAXS patterns collected during biaxial stretching test of sample L-C8, consisting of 2 s stretching at 114 °C, followed by a cooling step, for a total of lapsed time of 15 s.

The 2D-SAXS images have been azimuthally averaged as a function of the radial coordinate, to obtain 1D-SAXS profiles as a function of q. The soobtained 1D-SAXS profiles, before and after correction for the Lorentz factor, are reported in Figure A3 and A4 of the Appendix A9. From the correlation peak of the Lorentz corrected SAXS intensity profiles, the values of long spacing L have been calculated using the Bragg's law. The so-obtained values of L are reported in Figure 25 as a function of time. It is apparent that the initial value of L is \approx 37 nm. After an overshoot occurring in the first 0.8 s, characterized by a maximum of ≈ 43 nm at 0.3 s lapsed time, the long period L value decreases to 27 nm at the end of the stretching step (2 s). In the cooling step the L values keep decreasing until reaching at the end of the experiment (15 s) the value of 22 nm. In the stretching step, the initial increase of long spacing is due to the elongation of the amorphous chains located in between adjacent lamellar crystals and/or partial melting of the surviving crystals at 114 °C, while the successive decrease of L may be ascribed to fast re-crystallization of the oriented amorphous chains within the intra-lamellar amorphous regions. In the cooling step the further decrease of L is still due to formation of new crystals, but because of relaxation phenomena and crowding caused by the already formed crystals, the rate of change in L values becomes less fast.

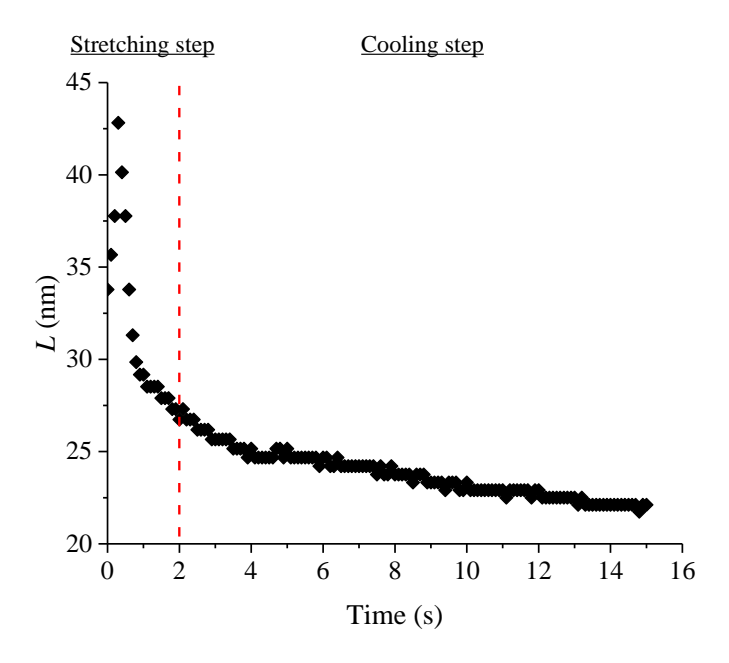


Figure 25 Values of long spacing L as a function of time, reached during the first 2 s of biaxial stretching, and the successive cooling, for a total of 15 s lapsed time. The vertical line, at 2 s, marks the boundary between the stretching the cooling steps.

6.5. 2D-WAXS analysis on samples stretched until a specific draw ratio

The last set of biaxial stretching tests is carried out to achieve indepth information about the structural transformations occurring in samples subjected to tentering, at unit cell length scale. To this end, the biaxial stretching apparatus has been integrated with a setup designed to collect two-dimensional WAXS patterns (Figure 26).

Measurements have been carried out at Beamline BM26B of the European Synchrotron Radiation Facility (ESRF, Grenoble, FR). Experiments have been conducted using X-rays with a wavelength of 1.033 Å and a beam diameter of 300 μ m. All WAXS patterns were collected using a Pilatus 1M detector (981 x 1043 pixels of 172 μ m x 172 μ m), and a sample-to-detector distance of 0.3 m. The sample-to-detector distance and tilt angle have been calibrated using silver behenate (AgC22H43O2) as a standard. The obtained 2D-WAXS patterns have been subtracted for the contribution from the empty tentering cell and corrected for the transmission factor. The obtained patterns have been then converted into 1D intensity profiles using the Python library PyFai. 2D-WAXS data have been collected with an exposure time of 0.15 s.

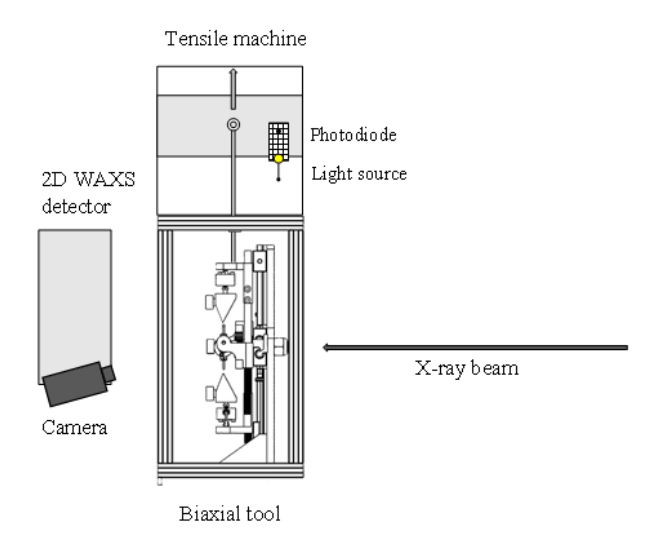


Figure 26 Schematic representation of the tool for biaxial stretching combined with X-ray setup at ESRF for collection of 2D-WAXS data.

Temperature calibration

Since the set-up adopted for the collection of 2D-WAXS data does not include a SAXS detector, for this experiment a different temperature calibration method is needed. Several studies^{4–6} have reported the variation of the orthorhombic unit cell parameters of PE as a function of the temperature. Thermal expansion of the crystal lattice causes shifts in the positions of diffraction peaks observed in WAXS patterns. The main diffraction peaks of PE correspond to the 110 and 200 reflections, and their positions, especially for the 200 diffraction peak, are particularly sensitive to temperature variations. As the temperature increases, the lattice parameters expand, leading to a decrease in the diffraction angles of these peaks.

In the present investigation, the temperature dependence of the a-axis dimension of the orthorhombic unit cell of PE has been modelled according to the polynomial Equation 11, proposed in Ref. ⁷:

$$a = 7.3681 + 0.1427(10^{-2})T + 0.0229(10^{-4})T^2 + 0.023(10^{-6})T^3 + 0.0103(10^{-8})T^4$$
 (11)

where T is expressed in °C. The values of the a-axis of the orthorhombic form of PE as a function of the temperature calculated with Equation 11 are reported in Figure 27. Hence, for the cast film of the sample L-C8, the value of a is calculated from the q position of the 200 reflection in the 2D-WAXS pattern collected at the beginning of the biaxial stretching test at the selected heating conditions. Comparing the calculated value of a with Equation 11, it has been possible to estimate that the adopted heating conditions correspond to a $T_{\text{tentering}}$ temperature of 118 °C.

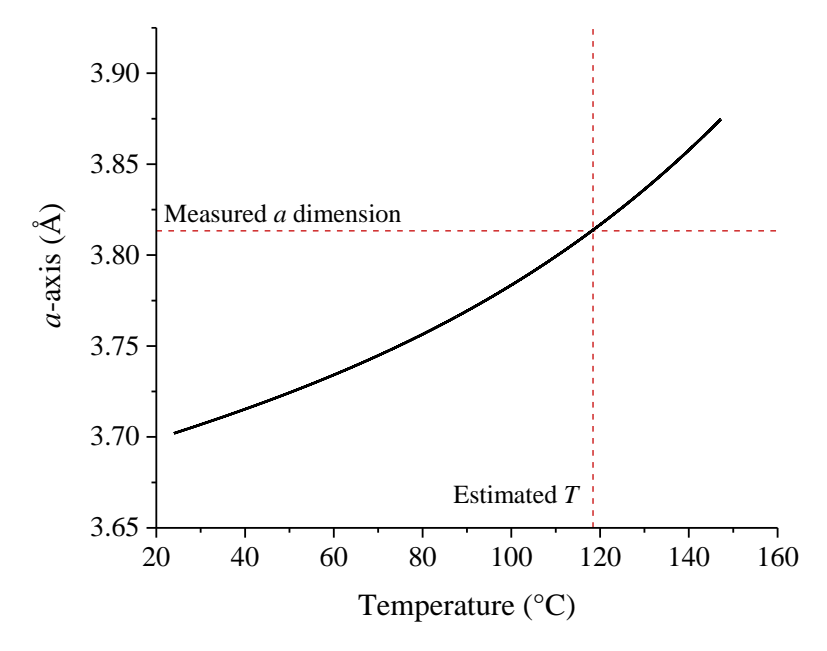


Figure 27 Temperature calibration plot based on thermal expansion of the a-axis (black line) according to Equation 11 proposed in Ref. ⁷.

Biaxial test

The experiment consists of a stretching phase in the first 2 s, immediately followed by a cooling step. The stretching test has been performed with an initial clamp separation of about 20 mm. Adopting

suitable deformation rates, in 2 s, the clamps of the tentering frame achieved a total displacement of 28 mm in both the horizontal and vertical directions. followed by the cooling step, the duration of which is ≈ 20 s.

The values of the force measured at the four clamps and of the strain, given by the second invariant of the deformation tensor (Equation 3) measured in the central region of the sample by DIC analysis, are reported in Figure 28 as a function of time. The values of force measured by the four load cells are similar (Figure 28A) and close to those measured in previous biaxial stretching tests (Figure 16 and 23A). This suggests that the values of the temperature evaluated using different calibration methods are well assessed. It is also evident that at the end of the biaxial stretching step (2 s), the value achieved by second invariant of the deformation tensor (Figure 28B) corresponds to a final *DR* of 6x6.

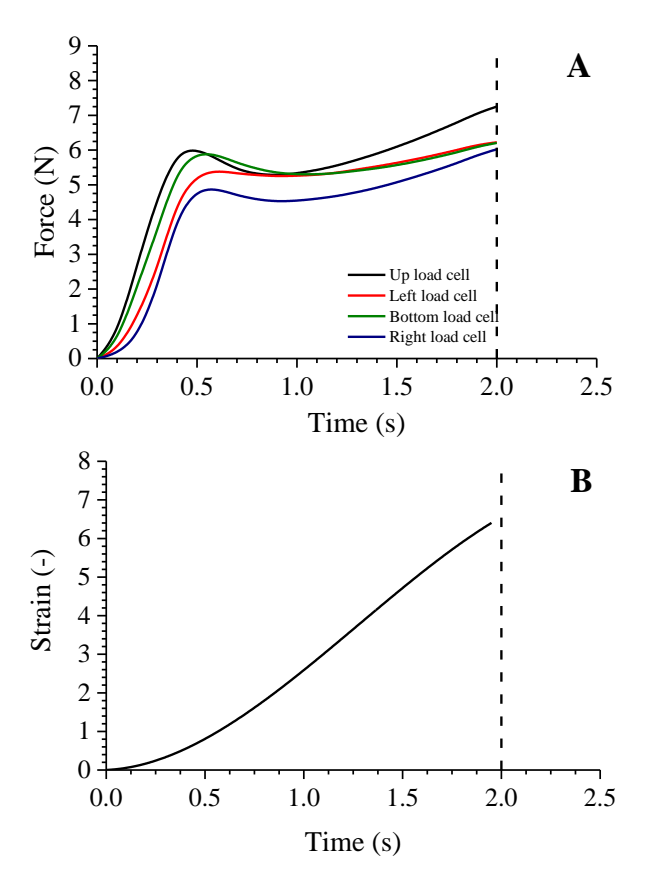


Figure 28 (A) Values of force measured by the 4 load cells and (B) of strain, expressed by the 2° invariant of the deformation tensor, as a function of time during biaxial stretching of the sample L-C8. The stretching time is of 2 s.

Representative 2D-WAXS patterns collected during the stretching and the successive cooling steps are shown in Figure 29 and 30, respectively. The undeformed cast film (t=0, DR=0x0) displays Debye-Scherrer rings for the 110 and 200 reflections and uniform intensity distribution of the amorphous halo, due to the isotropic orientation of the crystals and the amorphous chains. At low strain (t=1 s, DR=2.5x2.5), the 2D-WAXS patterns do not show significant changes, besides a global decrease of intensity, due to the decrease in thickness of the specimen. When the final strain of 6x6 is reached (t=2 s), the 200 reflection disappears, while the 110 reflection appears polarized in a reciprocal space region comprised in

between the meridian and the equator. The disappearance of the 200 reflection is due to preferred crystal orientation, with the 200 planes parallel to the film surface (uniplanar orientation). The off-equatorial and off-meridional polarization of 110 reflection, instead, is probable due to lamellar twisting.

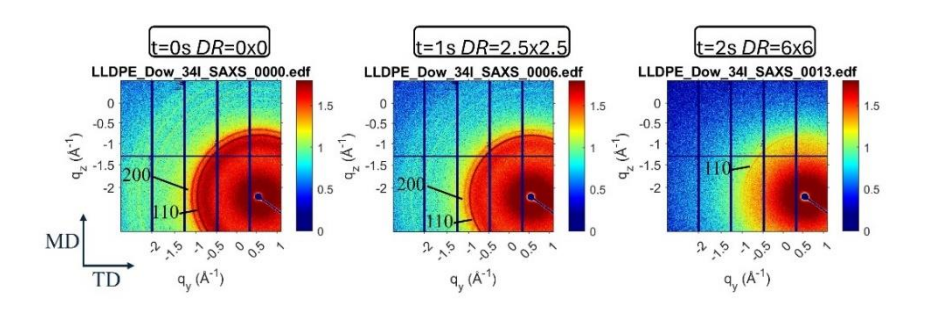


Figure 29 Selected 2D-WAXS patterns collected during the stretching at the DR =0x0, 2.5x2.5 and 6x6, for the sample L-C8 subjected for 2 s to biaxial stretching.

During cooling (Figure 30), the global diffraction intensity tends to increase due to crystallization. The polarization of the 110 reflection off the equator and off the meridian does not greatly change, and the 200 reflection remains absent.

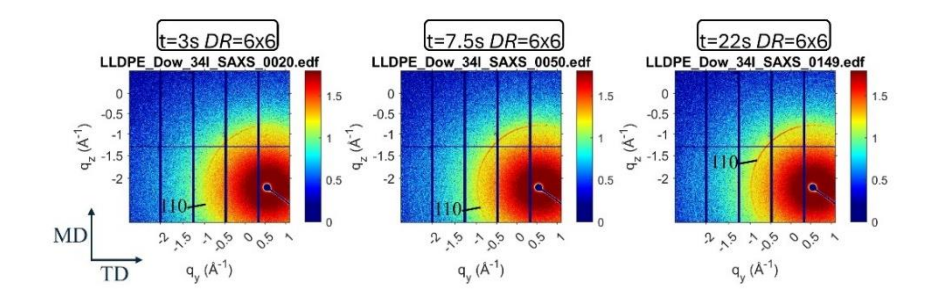


Figure 30 Selected 2D-WAXS patterns of the biaxially stretched sample L-C8 at DR 6x6, collected during cooling after a total amount of time of 6, 7.5 and 22 s. The sample has been early subjected to biaxial stretching at 118 °C for 2 s, and successively cooled.

Azimuthal integration of the 2D-WAXS patterns as a function of the radial coordinate has been carried out to obtain 1-D WAXS profiles as a function of q. The so-obtained 1D-WAXS profiles, collected during the biaxial stretching and successive cooling step of the sample L-C8, are collected in Figure A5 of Appendix A9, whereas selected profiles are shown in Figure 31. The curves obtained by the fit to the data through the sum of multiple Gaussian functions are also shown in Figure 31. These profiles have not been corrected for the decrease in thickness of the sample by effect of stretching. The values of the apparent crystallinity index, calculated from the curves obtained by the fit to the data, are also indicated in Figure 31. It is evident that, during stretching, the value of the apparent crystallinity index and the relative intensity of the 200 reflection decrease gradually since the beginning of the test. Due to the preferred orientation of the crystals, the 200 reflection disappears almost completely at the end of the stretching step (after 2 s). During the cooling step, the apparent crystallinity index increases and the 200 reflection gradually reappears, indicating that the formation of the new crystals occurs in a more random orientation. The values of the apparent crystallinity index are reported in Figure 32 as a function of time. During the first 2 s of the experiment, corresponding to the actual biaxial stretching step, the values of the apparent crystallinity index decrease and reaches a minimum value of ≈ 0.24 at ≈ 1.5 s. This observation is consistent with the decrease of the apparent crystallinity index observed for the sample stretched until rupture in Figure 20B. During

the cooling step, the value of the apparent crystallinity index increases,

reaching a plateau in ≈ 10 s. The final value of this parameter is ≈ 0.48 .

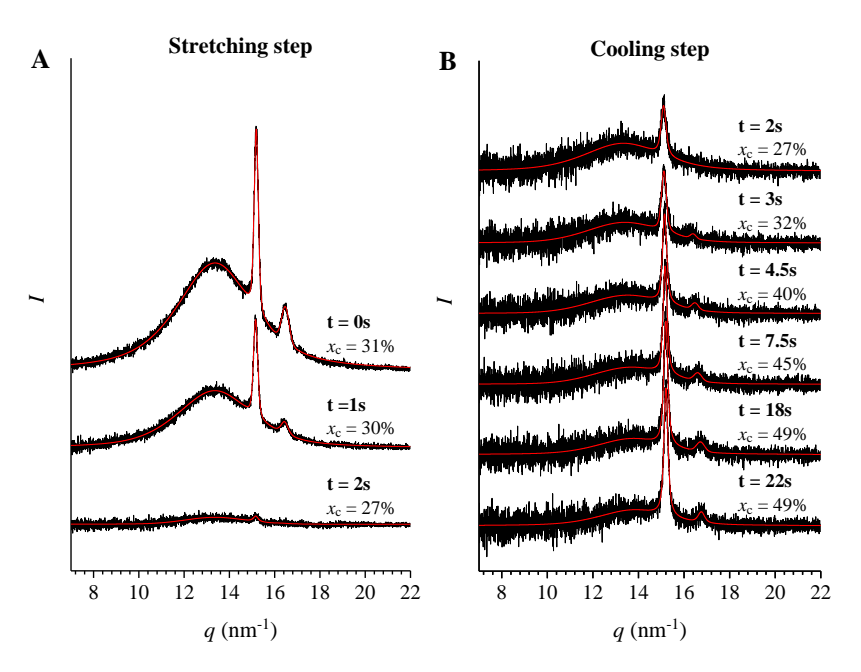


Figure 31 1D-WAXS profiles obtained by azimuthal integration of 2D-WAXS patterns as a function of the radial coordinate, collected during biaxial stretching (early 2 s, A) and successive cooling step (successive 20 s, B). Black curves: experimental data, red curves: fit to the data with the sum of multiple Gaussian functions.

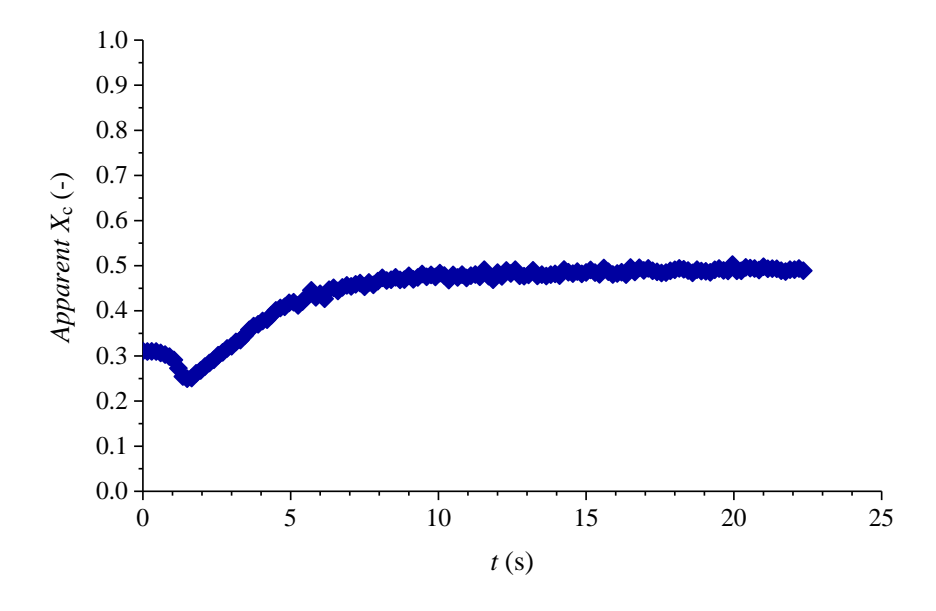


Figure 32 Values of the apparent crystallinity index calculated from the fit to 1-WAXS profiles with a sum of Gaussian functions as a function of time.

The results of Figure 32 confirm the hypothesis that during the stretching step the initial increase of long spacing is due to elongation of the amorphous chains located in between adjacent lamellar crystals coupled with a partial melting of the surviving crystals (Figure 25), as indicated by the initial decrease of the apparent crystallinity index. Furthermore, the successive decrease of long spacing (Figure 20), is in agreement with the simultaneous increase of the apparent crystallinity index (Figure 32), caused by formation of new crystals of low thickness in the intra-lamellar amorphous regions.

6.6. Conclusions

This chapter presents the results of time-resolved analyses conducted by collecting in situ WAXS and SAXS patterns at different Synchrotron light sources, during biaxial stretching of a LLDPE sample. The analysis has allowed following in real time the structural changes occurring in the sample mounted onto a tentering frame, in different experimental setups. This approach represents the pinnacle of the investigation on the tentering process. The extensive initial characterization, indeed, has been specifically designed to provide a basis for interpreting the findings from the biaxial stretching experiments.

The evolution of 2D-SAXS and WAXS patterns during biaxial stretching at high temperature suggest a change of the initial morphology of the cast film from an isotropic lamellar stacks network to a nearly uniplanar orientation of the lamellar crystals. From the Lorentz corrected SAXS intensity curve, the evolution of long spacing with time has been evaluated. The long period L first increases at the beginning of the stretching, then decreases to a value lower than the one initially recorded for the cast film at the selected tentering temperature. During the successive cooling, crystallization takes place while L keeps decreasing.

From WAXS analysis an apparent crystallinity index has been evaluated. During biaxial stretching (first 2s) the apparent crystallinity index shows a pronounced decrease, and then increases during the successive cooling. Looking at the evolution of intensity in the 2D-WAXS patterns, it is visible that the well-defined Debye-Scherrer rings relative to 110 and 200 reflections of PE initially present in the unstretched sample are replaced by a polarized 110 reflection and the gradual disappearance of the 200 reflection. This suggests that the fall in the apparent crystallinity index is also due, at least in part, to the orientation of 200 planes, parallel to the film surface. This orientation, indeed, prevents collecting quantitative

diffraction data in the adopted experimental setup for WAXS measurements. After cooling, the final value of crystallinity is higher than the original one of the cast film.

These results suggest that biaxial stretching promotes partial disruption of the original lamellar stacks present in the cast film, determining the breaking of part of the pristine crystals and the achievement of a uniplanar orientation of the lamellar crystals. Since the long period L achieves lower values during the crystallization occurring upon cooling, it is conceivable that the oriented amorphous chains crystallize during cooling, generating new thin crystals that are inserted in between the survived ones.

Bibliography of Chapter VI

- (1) Troisi, E. M.; Van Drongelen, M.; Caelers, H. J. M.; Portale, G.; Peters, G. W. M. Structure Evolution during Film Blowing: An Experimental Study Using in-Situ Small Angle X-Ray Scattering. *Eur. Polym. J.* **2016**, *74*, 190–208. https://doi.org/10.1016/j.eurpolymj.2015.11.022.
- (2) Chen, Q.; Chen, D.; Kang, J.; Cao, Y.; Chen, J. Structure Evolution of Polyethylene in Sequential Biaxial Stretching along the First Tensile Direction. *Ind. Eng. Chem. Res.* **2019**, *58* (27), 12419–12430. https://doi.org/10.1021/acs.iecr.9b01733.
- (3) Peterlin, A. Polymer Science Polymere Plastic Deformation of Polymers with Fibrous Structure. *Polym. Sci.* **1975**. https://doi.org/10.1007/BF01452401.
- (4) Bunn, C. W.; Alcock, T. C. [Title Not Provided]. *Trans. Faraday Soc.* **1945**, *41*, 317.
- (5) Miiller, A. [Title Not Provided]. *Proc. R. Soc. Lond.* **1932**, *A138*, 514.
- (6) Bunn CW. Trans. Faraday Soc. 1939, 35:428.
- (7) Swan, P. R. Polyethylene Unit Cell Variations with Temperature. *J. Polym. Sci.* **1962**, *56*, 403–407.

Chapter VII

Conclusions

The conclusions of this thesis emerge from a comprehensive investigation of the microstructural, thermal, structure and mechanical properties of various polyethylene (PE) grades and their blends, with a particular emphasis on the relevance that these aspects may have on the tentering process. Tentering, indeed, is a highly complex industrial process that requires precise control over temperature, orientation, and structural transformations to achieve desired material properties. Although this thesis addresses a vast and intricate subject, it offers preliminary yet valuable insights into optimizing this process. By investigating the structural evolution and performance of PE materials under conditions simulating tentering, it identifies potential pathways for improving the efficiency and output of industrial operations.

The study is methodically structured, beginning with general characterization to establish differences in molecular mass, branching content and related distribution, and crystallinity across PE grades and blends. The subsequent analyses have explored the thermal and mechanical responses of the samples under controlled conditions, particularly focusing on tentering-relevant scenarios such as the pre-stretching stage treatments at possible tentering temperature. These investigations have demonstrated how variations in cooling rates, annealing protocols, and structural transformations impact crystallinity, lamellar organization, and mechanical performance, offering actionable insights for refining processing techniques. The final phase of the work has directly addressed the structural changes induced by biaxial stretching, using a lab-scale tenter-frame device combined with time-resolved in-situ SAXS/WAXS analyses.

These advanced techniques have enabled real-time observation of the reorganization of crystalline and amorphous regions, shedding light on critical phenomena such as lamellar orientation, changes in crystallinity, and the setting in of new structural organizations at lamellar length scale. In particular, it has been found that all the samples present a characteristic organization of the crystals in stacks, consisting in layered arrangement of lamellar crystals along the direction normal to the basal plane, separated by amorphous layers. However, the regularity of the arrangement and the distribution of crystal and amorphous thickness is strictly related to microstructural features of the samples. Low-defective samples like the HDPE grade coded as H-C4, with a broad molecular mass distribution (D = 14.3) and low comonomer content (0.5 mol\% of 1-butene), exhibit thick lamellae, and regular lamellar stacks, as evidenced by the narrow correlation peaks observed in SAXS profiles. In contrast, the LLDPE sample coded as L-C6, with higher comonomer content (3.1 mol% 1hexene) and narrower molecular mass distribution (Đ=2.7Đ), demonstrate thinner lamellae and greater stacking disorder, with a broader SAXS peaks and shorter long spacing.

It has been also evidenced that microstructural differences may underpin the distinct thermal behaviour observed in the L-C6 sample, which, unlike the other samples, exhibits a distinct melt memory effect. It has been shown that a population of long crystallizable sequences remains entrapped in an ordered state in the melt even at $T_{\rm max}$ =163 °C, i.e. at a temperature significantly above the thermodynamic melting temperature of PE. This unique behaviour highlights the influence of the microstructure, particularly the presence of branching, in maintaining structural constraints that direct reorganization upon cooling.

The role of chain microstructure, cooling rate, preparation condition of the samples on the mechanical properties has been also highlighted. All the

samples show yielding behaviour, high ductility and strain hardening at high deformations. The Young's modulus is generally correlated with crystallinity. However, the mechanical behaviour of the LLDPE samples coded as L-C8 (M_n = 26000, Θ =4.1), containing 2.6%mol of 1-octene units, and L-C4,C6 ($M_n \approx 9$ kDa, $\oplus =19.5$), with 0.5 and 1.2 %mol of 1butene and 1-hexene, respectively, highlights that the presence of a significant fraction of high molecular mass chains in the former, and of a non-negligible fraction of chain with low molecular mass in the latter sample, play a role. Compared with the sample L-C4,C6, indeed, it has been observed that the presence of long chains, capable of forming a large number of entanglements, acting as physical cross-links within the amorphous network, account for the greater rigidity, despite the lower crystallinity, of the sample L-C8. It has been shown that the presence of long chains also influence deformation at break. This has been observed for the sample L-C6 ($M_n = 44000$), with the highest molecular mass, which shows also the highest ductility.

Slowly cooled compression-molded films exhibit higher Young's modulus compared to those obtained through fast cooling (quenching), attributed to the higher level of crystallinity achieved under slow cooling conditions. The mechanical properties of compression-molded films remain unchanged imposing a heat treatment of 10 or 30 min at $T_{\rm max}$ 150 °C or 200°C, indicating that the melt achieves a fully relaxed state already in the first 10 minutes at 150 °C. It has been evidenced that the solid-state morphology, and consequently the observed mechanical properties, are primarily influenced by the cooling rate, which governs the lamellar organization across different length scales. When the polymer chains have more time to organize and form crystals, the thickness of the lamellar crystals increases. However, the most significant change lies in the organization of the lamellae into superstructures, which defines the overall

morphology and properties of the materials. The low-defective HDPE sample H-C4, when slowly cooled from the melt, forms small spherulites with high nucleation density, resulting in a well-inter-connected and interpenetrated network of amorphous and crystalline phases, consistent with its high Young's modulus. In contrast, the defective LLDPE samples L-C4,C6, L-C8, and L-C6, under the same cooling conditions, develop large, well-defined spherulites. Notably, the sample L-C8 exhibits a mixed morphology, with lamellar sheaves situated in between adjacent spherulites. When the melt is rapidly cooled (quenched), all samples form disordered superstructures where crossed lamellar sheaves replace the spherulitic structure, leading to a more uniform morphology.

In the context of designing suitable PE microstructures for biaxial stretching, the potential of blending was also explored by selecting an HDPE (H-C4) and an LLDPE (L-C8) sample and preparing blends of these two components with different compositions. All blends exhibit a single melting and crystallization peak at intermediate temperatures between those of the pure components. Characterization of the mechanical properties reveals high ductility, marked yielding, and strain hardening across all blends, similar to the neat components. As LLDPE content increases, the Young's modulus and stress at yield σ_y decrease, while strain at yield ε_y increases, reflecting greater ductility. Stress and strain at break remain largely unaffected by blend composition, demonstrating consistent performance regardless of preparation conditions.

To better understand the early stages of the tentering process, SNA analysis has been performed to evaluate the melt state as a function of the potential tentering temperatures prior to biaxial stretching. Temperature ranges defining Domains I, II, and III have been identified for the PE samples, revealing that the self-nucleation Domain II for LLDPE-HDPE blends is narrower than that of the neat components. Compared with HDPE, this

narrowing is due to a decrease in the boundary temperatures $T_{\rm s}^{\rm I-II}$ and $T_{\rm s}^{\rm III}$. This decrease is caused by the dilution effect exerted by the LLDPE chains in reducing the self-nucleation tendency of HDPE at high temperatures, and to the fact that the survival of crystalline fragments of the LLDPE component requires lower temperatures compared to HDPE. The highest values of the seeding temperature in Domain II $T_{\rm s\ ideal}$, where the maximum concentration of self-nuclei occurs, has been found to be 130°C for HDPE, 126°C for LLDPE, and in between for the blends.

To further examine the microstructural complexity of the samples H-C4, L-C8, and the LLDPE-HDPE blend containing 50% of each component LC8 and H-C4 (50L-50H), thermal fractionation via SSA has been carried out. The final DSC curves reveal multiple melting peaks due to the fractionation of crystals with different lamellar thicknesses, driven by the crystallization of monomer sequences of varying lengths. Notably, the DSC curve of the 50L-50H blend closely resembles that of pure HDPE rather than to that of neat LLDPE, suggesting a tendency for HDPE and LLDPE components to form co-crystals in the blend.

These analyses have been crucial in elucidating structural differences among the samples and their impact on material properties.

The effects of thermal treatments at selected temperatures ($T_{\rm treatment} = 125$, 130 and 135 °C) on the structural rearrangements of the HDPE sample H-C4, the LLDPE sample L-C8, and their 50/50 blend have been investigated. Structural transformations have been found to depend on the SNA domain corresponding to $T_{\rm treatment}$: Domain I induces rapid and complete melting without significant structural rearrangements, resulting in a crystalline state similar to that found in the pristine sample; Domain II allows partial melting and annealing of the surviving crystals, but prolonged treatment leads to complete melting and uniform re-crystallization; Domain III promotes annealing of the most regular crystals and melting of defective

ones, with defective chains forming lower-melting crystals upon cooling, while the annealed crystals show increased melting temperatures and lamellar thickness compared to the original state.

To complement the findings of the ex-situ experiments, in-situ annealing analyses have been also carried out to provide a more comprehensive understanding of the structural changes occurring in polyethylene (PE) samples under thermal treatments for prolonged time. While the ex-situ experiments have provided valuable insights into the final structures and properties after cooling, the in-situ approach has allowed to monitor in realtime the transformations in the crystalline and amorphous phases during the heat treatments. In particular, in-situ annealing analyses have been carried out by recording WAXS and SAXS patterns as a function of time during 10 min of isothermal treatment at 120 and 125 °C. The analysed samples (H-C4, L-C8 and the corresponding 50-50 blend) are all in the SNA Domain III at these temperatures. It has been shown that these treatments induce increase of lamellar thickness of the surviving crystals, while the melt fraction gives rise to defective and less stable crystals during the successive cooling. The degree of structural rearrangement is closely related to the chain microstructure. In particular, it has been shown that LLDPE undergoes more significant structural re-arrangements than HDPE at these temperatures.

The final investigation has been focused on the effect of biaxial stretching tests on the LLDPE sample L-C8. To this purpose a home-made tentering frame has been used in experimental setups built at different synchrotron facilities. The sample has been biaxially stretched at temperatures around 115 °C while collecting in situ SAXS and/or WAXS data.

The analysis of the 2D SAXS and WAXS data collected during biaxial stretching has revealed that the initial cast film is subjected to structural rearrangements, leading from an isotropic lamellar stack network to a

nearly uniplanar orientation of lamellae. It has been shown that, during stretching, the long spacing L initially increases and, then decreases to a value lower than that of the original cast film, while during the successive cooling, the L value show further decrease. 2D-WAXS analysis has shown that, during stretching, the apparent crystallinity index first decreases than starts increasing, to reach in the successive cooling step a plateau value after about 10 s. Furthermore, the Debye-Scherrer rings of the 110 and 200 reflections of the cast film in the initial (undeformed) state, are replaced, by effect of stretching, by an arced 110 reflection located in an offequatorial and off-meridional region of reciprocal space, and the progressive decrease in intensity of the 200 reflection. This reflection eventually disappears almost completely at the end of the stretching step. In the successive cooling step, the 200 reflection reappears, and the 110 reflection becomes more intense.

These results suggest that during the 2 s of biaxial stretching, the crystalline/amorphous network originally present in the cast film kept at high temperatures is partially destroyed, even though, in the immediately successive instants re-crystallization of the oriented chains in new crystals occurs. These crystals are oriented with the 200 planes parallel to the surface of the film (uniplanar orientation). During the successive cooling, the crystallinity index increases, due to formation of new crystals in the amorphous regions placed in between the pre-existing lamellar crystals, stable at high temperatures. These crystals are less oriented than those that form in early 2 s during the stretching step, because the orientated state of the amorphous chains is lost due to chain relaxation.

In conclusion, in this thesis some relationships between fundamental knowledge and practical applications have been established in the realm of PE. It is shown how a detailed study of PE behaviour under various conditions can support the design of materials with specific properties. The

methodologies and results presented here provide a foundation for further research and for refining industrial processes, especially in applications requiring precise control of material structure and performance.

Appendix A1

Melt memory effect of commercial PE grades

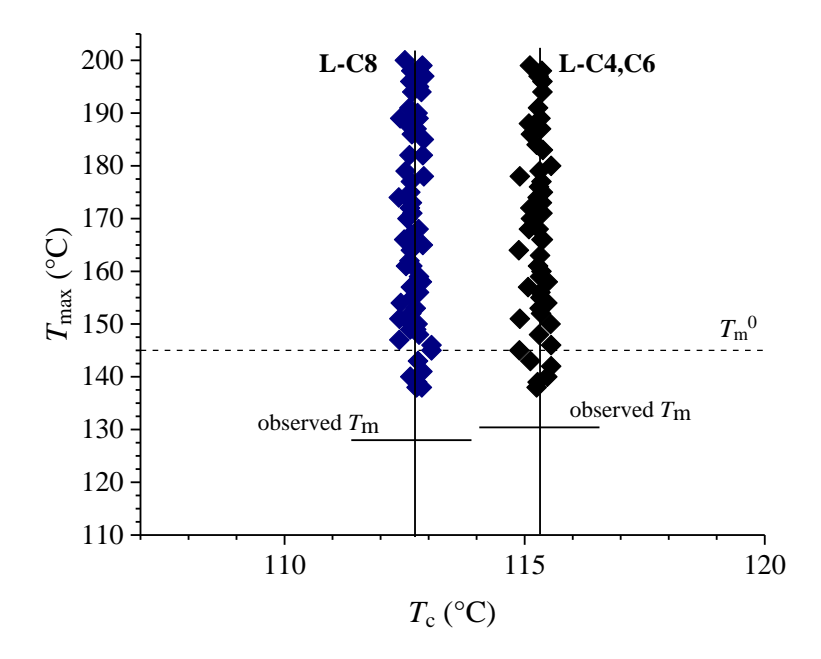


Figure A1 Maximum temperature reached in the melt (T_{max}) vs. crystallization temperature (T_c) for the samples L-C4,C6 and L-C8. The dashed line corresponds to the equilibrium melting temperature of PE T_m^0 =145°C. The melting temperatures of the samples measured in standard DSC scan (Figure 2C) are indicated.

Appendix A2

Mechanical properties of compression-molded films of the samples obtained in different cooling conditions.

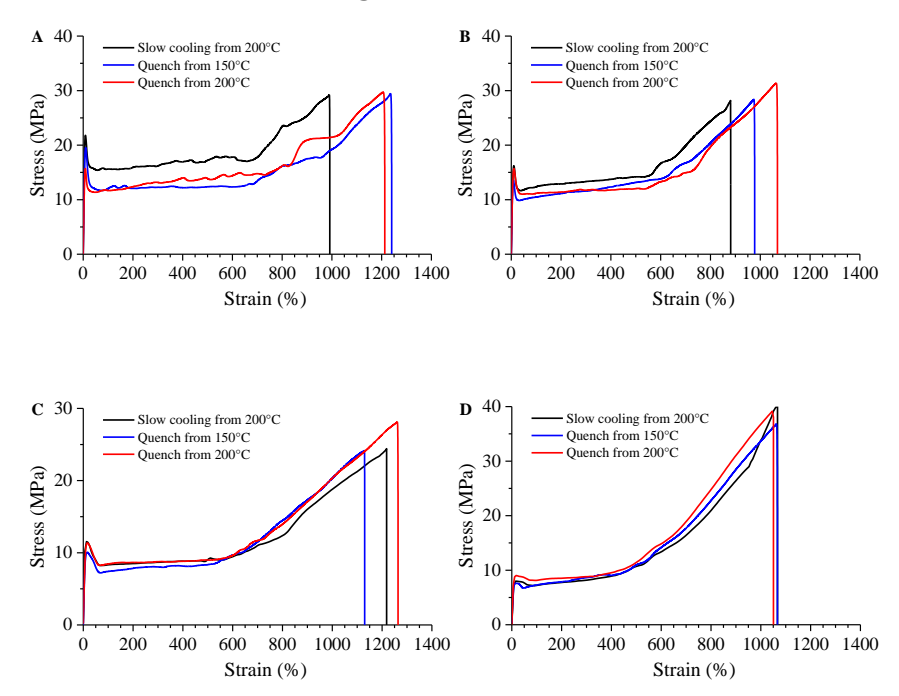


Figure A1 Stress-strain curve of compression-molded films of the samples H-C4 (A), L-C4,C6 (B), L-C8 (C) and L-C6 (D) obtained through slow cooling from 200°C (black curve) and quenching from 150 (blue curve) and 200°C (red curve) after 10 min isotherm at the indicated temperatures.

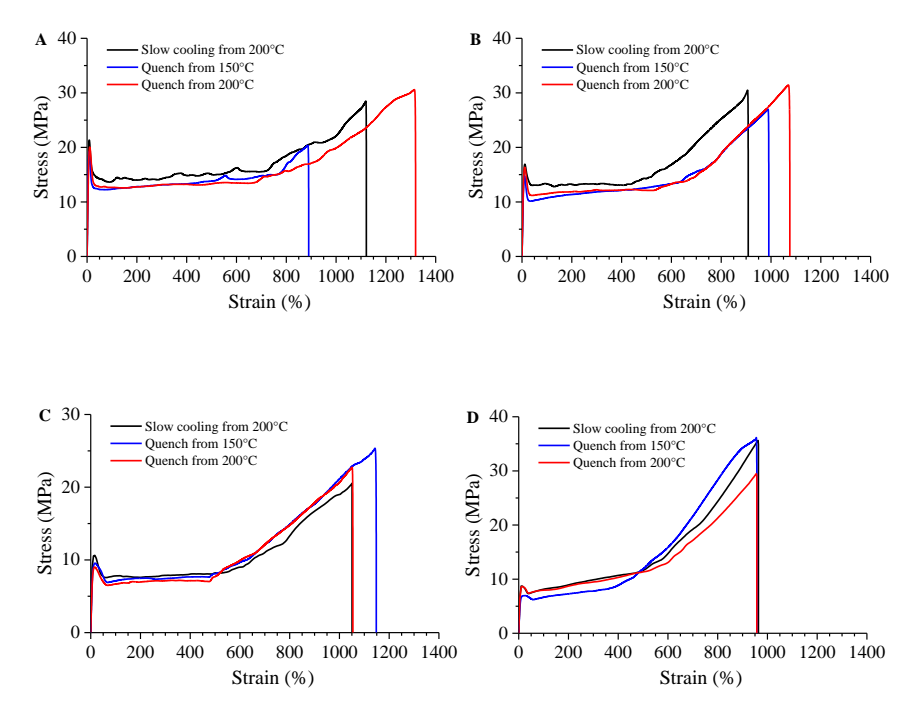


Figure A2 Stress-strain curve of compression-molded films of the samples H-C4 (A), L-C4,C6 (B), L-C8 (C) and L-C6 (D) obtained through slow cooling from 200°C (black curve) and quenching from 150 (blue curve) and 200°C (red curve) after 30 min isotherm at the indicated temperatures.

.

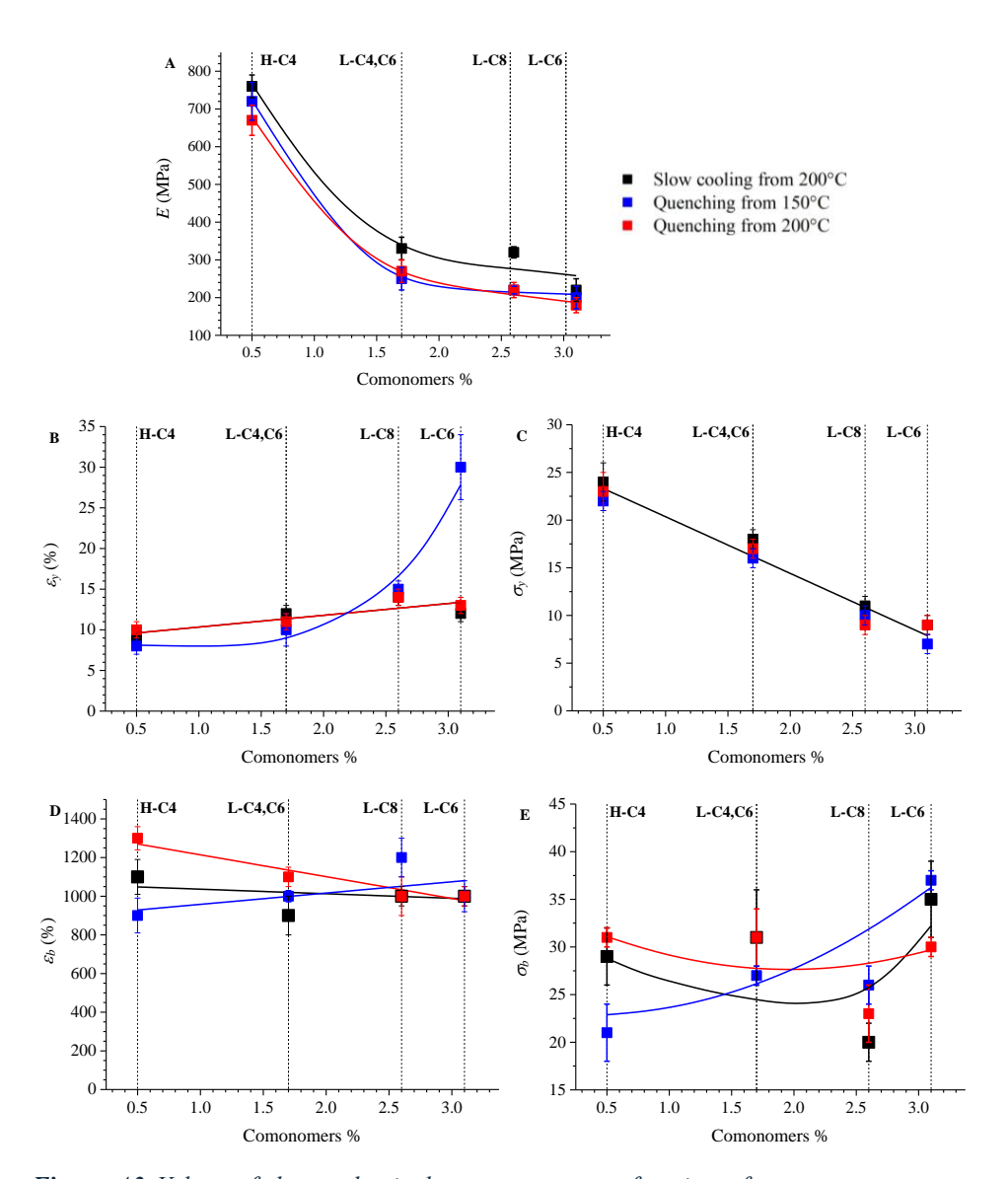


Figure A3 Values of the mechanical parameters as a function of comonomer content extracted from the stress-strain curves of compression-molded films of the PE samples, obtained through slow cooling from 200°C (black squares) and quenching from 150 (blue squares) and 200°C (red squares), after 30 min isotherm at the indicated temperatures. Young's Modulus (E, A), strain (ε_y, B) and stress (σ_y, C) at yielding, strain (ε_b, D) and stress (σ_b, E) at break.

Table A1 Mechanical parameters of the sample H-C4 extracted from stress-strain curves (Figure A1 (A)) after 10 min isotherm at the indicated temperatures.

| Cooling conditions | E (MPa) | σ_{y} ε_{y} (MPa) (%) | | σ _b (MPa) | ε _b (%) | WAXS (%) | |
|-------------------------|--------------|--|-------|-------------------------|-----------------------|----------|--|
| Slow cooling from 200°C | 800 ± 30 | 26 ± 2 | 9 ± 1 | 29 ± 4 | 1000 ± 70 | 82 | |
| Quenching from 150°C | 700 ± 30 | 23 ± 2 | 9 ± 1 | 30 ± 2 | 1200 ± 70 | 74 | |
| Quenching from 200°C | 690 ± 50 | 21 ± 1 | 6 ± 1 | 29 ± 2 | 1200 ± 70 | 72 | |

Table A2 Mechanical parameters of the sample H-C4 extracted from stress-strain curves (Figure A2 (A)) after 30 min isotherm at the indicated temperatures.

| Cooling conditions | E (MPa) | _ | | σ _b (MPa) | ε _b (%) | WAXS (%) | |
|----------------------------|--------------|----------|--------|-------------------------|-----------------------|----------|--|
| Slow cooling from 200°C | 760 ± 30 | 24 ± 2 | 9 ± 1 | 29 ± 3 | 1100 ± 90 | 79 | |
| Quenching from 150°C | 720 ± 50 | 22 ± 1 | 8 ± 1 | 21 ± 3 | 900 ± 90 | 74 | |
| Quenching from 200°C | 670 ± 40 | 23 ± 2 | 10 ± 1 | 31 ± 1 | 1300 ± 60 | 71 | |

Table A3 Mechanical parameters of the sample L-C4,C6 extracted from stress-strain curves (Figure A1 (B)) after 10 min isotherm at the indicated temperatures.

| Cooling conditions | E (MPa) | σ _y (MPa) | ε _y (%) | σ _b (MPa) | ε _b (%) | WAXS (%) | |
|----------------------------|--------------|-------------------------|-----------------------|-------------------------|-----------------------|----------|--|
| Slow cooling from 200°C | 300 ± 10 | 17 ± 1 | 10 ± 1 | 28 ± 3 | 900 ± 50 | 69 | |
| Quenching from 150°C | 200 ± 20 | 15 ± 1 | 8 ± 1 | 28 ± 3 | 1000 ± 50 | 60 | |
| Quenching from 200°C | 210 ± 50 | 17 ± 1 | 11 ± 1 | 31 ± 3 | 1100 ± 60 | 59 | |

Table A4 Mechanical parameters of the sample L-C4,C6 extracted from stress-strain curves (Figure A2 (B)) after 30 min isotherm at the indicated temperatures.

| Cooling conditions | E (MPa) | $ \sigma_{y} \qquad \varepsilon_{y} \\ (MPa) \qquad (\%) $ | | σ _b (MPa) | ε _b (%) | WAXS (%) | |
|----------------------------|------------|--|----------|-------------------------|-----------------------|----------|--|
| Slow cooling from 200°C | 330 ± 30 | 18 ± 1 | 12 ± 1 | 31 ± 5 | 900 ± 100 | 72 | |
| Quenching from 150°C | 250 ± 30 | 16 ± 1 | 10 ± 2 | 27 ± 1 | 1000 ± 30 | 64 | |
| Quenching from 200°C | 270 ± 30 | 17 ± 1 | 11 ± 1 | 31 ± 3 | 1100 ± 50 | 65 | |

Table A5 Mechanical parameters of the sample L-C8 extracted from stress-strain curves (Figure A1 (C)) after 10 min isotherm at the indicated temperatures.

| Cooling conditions | E (MPa) | $ \frac{\sigma_{y}}{(MPa)} \frac{\varepsilon_{y}}{(\%)} $ | | σ _b (MPa) | ε _b (%) | WAXS (%) | |
|----------------------------|--------------|--|--------|-------------------------|-----------------------|----------|--|
| Slow cooling from 200°C | 360 ± 15 | 12 ± 1 | 15 ± 2 | 24 ± 2 | 1200 ± 50 | 66 | |
| Quenching from 150°C | 210 ± 20 | 10 ± 1 | 15 ± 1 | 24 ± 1 | 1100 ± 20 | 52 | |
| Quenching from 200°C | 220 ± 20 | 11 ± 2 | 15 ± 1 | 28 ± 3 | 1300 ± 100 | 52 | |

Table A6 Mechanical parameters of the sample L-C8 extracted from stress-strain curves (Figure A2 (C)) after 30 min isotherm at the indicated temperatures.

| Cooling conditions | E (MPa) | _ | | σ _b (MPa) | ε _b (%) | WAXS (%) | |
|-------------------------|------------|------------|--------|-------------------------|-----------------------|----------|--|
| Slow cooling from 200°C | 320 ± 15 | 11 ± 1 | 14 ± 1 | 20 ± 2 | 1000 ± 50 | 65 | |
| Quenching from 150°C | 220 ± 10 | 10 ± 1 | 15 ± 1 | 26 ± 2 | 1200 ± 100 | 55 | |
| Quenching from 200°C | 220 ± 20 | 9 ± 1 | 14 ± 1 | 23 ± 3 | 1000 ± 100 | 56 | |

Table A7 Mechanical parameters of the sample L-C6 extracted from stress-strain curves (Figure A1 (\underline{D})) after 10 min isotherm at the indicated temperatures.

| Cooling conditions | E (MPa) | σ _y (MPa) | | | ε _b (%) | Xc WAXS (%) | |
|----------------------------|------------|-------------------------|--------|----------|-----------------------|-------------------|--|
| Slow cooling from 200°C | 210 ± 20 | 9 ± 1 | 16 ± 1 | 41 ± 2 | 1100 ± 80 | 63 | |
| Quenching from 150°C | 190 ± 20 | 8 ± 1 | 13 ± 1 | 37 ± 2 | 1100 ± 30 | 59 | |
| Quenching from 200°C | 200 ± 20 | 9 ± 1 | 17 ± 1 | 38 ± 4 | 1000 ± 50 | 55 | |

Table A8 Mechanical parameters of the sample L-C6 extracted from stress-strain curves (Figure A2 (\underline{D})) after 30 min isotherm at the indicated temperatures.

| Cooling conditions | E (MPa) | σ_{y} ε_{y} (MPa) (%) | | σ _b (MPa) | ε _b (%) | WAXS (%) | |
|----------------------------|--------------|--|----------|-------------------------|-----------------------|----------|--|
| Slow cooling from 200°C | 220 ± 30 | 9 ± 1 | 12 ± 1 | 35 ± 4 | 1000 ± 50 | 65 | |
| Quenching from 150°C | 200 ± 30 | 7 ± 1 | 30 ± 4 | 37 ± 1 | 1000 ± 80 | 59 | |
| Quenching from 200°C | 180 ± 20 | 9 ± 1 | 13 ± 1 | 30 ± 1 | 1000 ± 50 | 57 | |

Appendix A3

Structural analysis of compression-molded films of the samples obtained in different cooling conditions

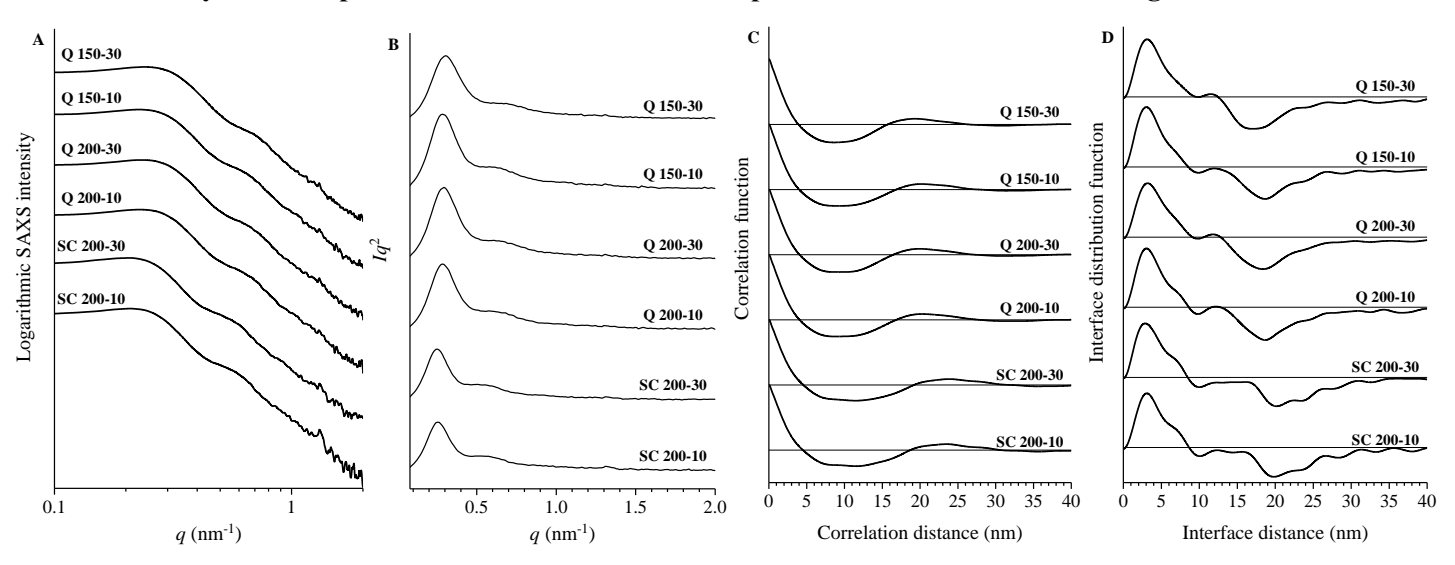


Figure A1 SAXS intensity profiles before (A) and after (B) Lorentz's factor correction, mono-dimensional Self-correlation function of electronic densities fluctuation CF (C) and Interface distribution function IDF (D) of compression-molded films of the sample H-C4 obtained under different cooling conditions. The samples are coded with names that specify the preparation conditions of the films: X Y-Z where X = SC (slow cooling) or Q (quenching) indicate the (slow or fast) cooling rate of the melt; Y stands for the temperature T_{max} reached in the melt, equal to 200 or 150 °C; the last number Z refers to the annealing time in min (t_{max}) of the melt at the indicated temperatures.

Table A1 Values of the lamellar periodicity (L) and thickness of amorphous (l_a) and crystalline (l_c) layers of lamellar stacks of the sample H-C4, deduced from SAXS data (Figure A1) through direct application of Bragg's law, the calculation of the monodimensional self-correlation function of electron density fluctuations (correlation function, CF) and the interface distribution function (IDF). The samples are coded with names that specify the preparation conditions of the films: X Y-Z where X= SC (slow cooling) or Q (quenching) indicate the (slow or fast) cooling rate of the melt; Y stands for the temperature T_{max} reached in the melt, equal to 200 or 150 °C; the last number Z refers to the annealing time in min (t_{max}) of the melt at the indicated temperatures.

| | Bragg | | | | | | | CF | | | | IDF | | | | |
|--------------------|---|----------------------------|------------------------------------|---------------------|--------------------------|-----------------------|---------------------|---------------------|-----------|---------------------|---------------------|--------------------------|-----------|---------------------|---------------------|--------------------------|
| Cooling conditions | <i>q</i> ₁ (nm ⁻¹) | <i>L</i> ₁ (nm) | q ₂ (nm ⁻¹) | L ₂ (nm) | x _c (WAXS) | Φ _c (%) | l _c (nm) | l _a (nm) | L (nm) | l _c (nm) | l _a (nm) | l _c /L (-) | L (nm) | l _c (nm) | l _a (nm) | l _e /L (-) |
| SC 200-10 | 0.254 | 24.7 | 0.503 | 24.9 | 0.82 | 0.79 | 19.6 | 5.1 | 23.5 | 18.9 | 4.6 | 0.81 | 19.8 | 16.7 | 3.1 | 0.84 |
| SC 200-30 | 0.254 | 24.7 | 0.502 | 25.0 | 0.79 | 0.76 | 18.8 | 5.9 | 23.9 | 19.3 | 4.6 | 0.80 | 20.2 | 17.3 | 2.9 | 0.86 |
| Q 150 10 | 0.287 | 21.9 | 0.582 | 21.6 | 0.74 | 0.71 | 15.5 | 6.4 | 20.2 | 15.9 | 4.3 | 0.77 | 18.7 | 15.6 | 3.0 | 0.84 |
| Q 150 30 | 0.304 | 20.7 | 0.642 | 19.6 | 0.72 | 0.69 | 14.2 | 6.5 | 19.5 | 15.1 | 4.4 | 0.78 | 17.0 | 13.9 | 3.1 | 0.82 |
| Q 200 10 | 0.284 | 22.1 | 0.572 | 21.9 | 0.72 | 0.69 | 15.2 | 6.9 | 20.2 | 15.8 | 4.4 | 0.78 | 18.7 | 15.7 | 3.03 | 0.84 |
| Q 200 30 | 0.294 | 21.6 | 0.602 | 20.9 | 0.74 | 0.71 | 15.1 | 6.2 | 19.9 | 15.5 | 4.4 | 0.78 | 17.0 | 13.9 | 3.1 | 0.82 |

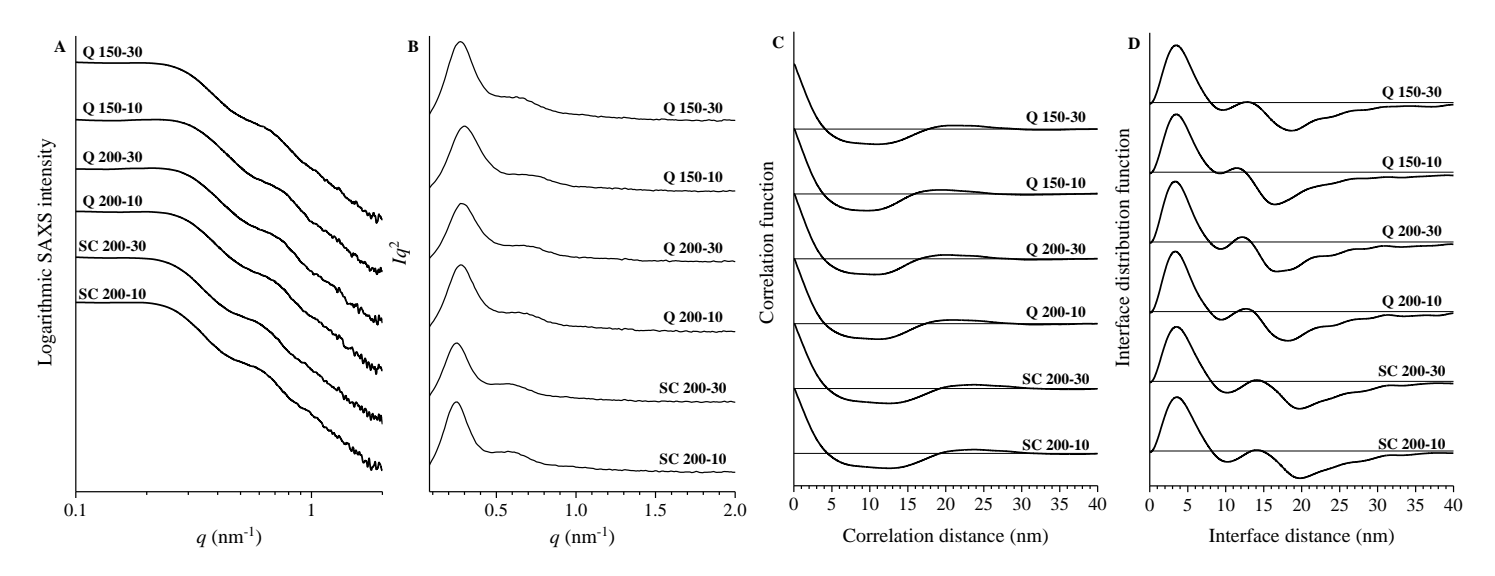


Figure A2 SAXS intensity profiles before (A) and after (B) Lorentz's factor correction, mono-dimensional Self-correlation function of electronic densities fluctuation CF (C) and Interface distribution function IDF (D) of compression-molded films of the sample L-C4,C6 obtained under different cooling conditions. The samples are coded with names that specify the preparation conditions of the films: X Y-Z where X = SC (slow cooling) or Q (quenching) indicate the (slow or fast) cooling rate of the melt; Y stands for the temperature T_{max} reached in the melt, equal to 200 or 150 °C; the last number Z refers to the annealing time in min (t_{max}) of the melt at the indicated temperatures.

Table A2 Values of the lamellar periodicity (L) and thickness of amorphous (l_a) and crystalline (l_c) layers of lamellar stacks of the sample L-C4,C6, deduced from SAXS data (Figure A1) through direct application of Bragg's law, the calculation of the monodimensional self-correlation function of electron density fluctuations (correlation function, CF) and the interface distribution function (IDF). The samples are coded with names that specify the preparation conditions of the films: X Y-Z where X= SC (slow cooling) or Q (quenching) indicate the (slow or fast) cooling rate of the melt; Y stands for the temperature T_{max} reached in the melt, equal to 200 or 150 °C; the last number Z refers to the annealing time in min (t_{max}) of the melt at the indicated temperatures.

| | Bragg | | | | | | | | | CF | | | ID | F | | |
|--------------------|------------------------------------|----------------------------|------------------------------------|---------------------|-----------------------|-----------------------|---------------------|------------|-----------|---------------------|---------------------|------------|-----------|---------------------|---------------------|--------------------------|
| Cooling conditions | q ₁ (nm ⁻¹) | <i>L</i> ₁ (nm) | q ₂ (nm ⁻¹) | L ₂ (nm) | x _c (WAXS) | Φ _c (%) | l _c (nm) | la (nm) | L (nm) | l _c (nm) | l _a (nm) | ldL (-) | L (nm) | l _c (nm) | l _a (nm) | l _o /L (-) |
| SC 200-10 | 0.254 | 24.7 | 0.572 | 21.9 | 0.69 | 0.65 | 16.2 | 8.5 | 23.9 | 19.3 | 4.6 | 0.81 | 19.8 | 16.2 | 3.6 | 0.84 |
| SC 200-30 | 0.254 | 24.7 | 0.572 | 21.95 | 0.72 | 0.69 | 17.0 | 7.8 | 23.9 | 19.3 | 4.6 | 0.81 | 19.7 | 16.2 | 3.5 | 0.82 |
| Q 150 10 | 0.304 | 20.6 | 0.662 | 19.0 | 0.6 | 0.56 | 11.6 | 9.1 | 19.5 | 15.1 | 4.3 | 0.77 | 16.5 | 13.0 | 3.5 | 0.79 |
| Q 150 30 | 0.274 | 22.9 | 0.623 | 20.2 | 0.64 | 0.60 | 13.8 | 9.1 | 20.9 | 16.7 | 4.2 | 0.79 | 18.7 | 15.2 | 3.5 | 0.81 |
| Q 200 10 | 0.274 | 22.9 | 0.642 | 19.6 | 0.59 | 0.55 | 12.6 | 10.3 | 20.9 | 16.5 | 4.4 | 0.79 | 18.2 | 14.8 | 3.3 | 0.87 |
| Q 200 30 | 0.274 | 22.9 | 0.672 | 18.7 | 0.65 | 0.61 | 14.03 | 8.9 | 20.1 | 15.8 | 4.3 | 0.79 | 16.7 | 13.4 | 3.4 | 0.80 |

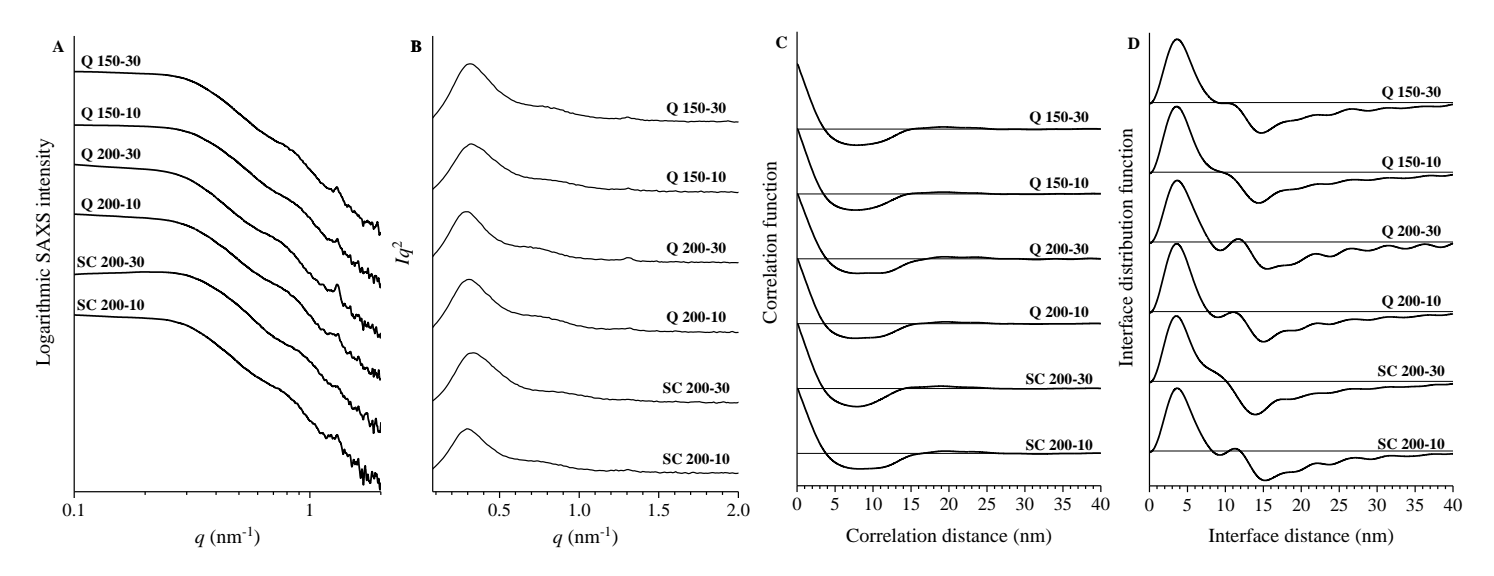


Figure A3 SAXS intensity profiles before (A) and after (B) Lorentz's factor correction, mono-dimensional Self-correlation function of electronic densities fluctuation CF (C) and Interface distribution function IDF (D) of compression-molded films of the sample L-C8 obtained under different cooling conditions. The samples are coded with names that specify the preparation conditions of the films: X Y-Z where X = SC (slow cooling) or Q (quenching) indicate the (slow or fast) cooling rate of the melt; Y stands for the temperature T_{max} reached in the melt, equal to 200 or 150 °C; the last number Z refers to the annealing time in min (t_{max}) of the melt at the indicated temperatures.

Table A3 Values of the lamellar periodicity (L) and thickness of amorphous (l_a) and crystalline (l_c) layers of lamellar stacks of the sample L-C8, deduced from SAXS data (Figure A1) through direct application of Bragg's law, the calculation of the monodimensional self-correlation function of electron density fluctuations (correlation function, CF) and the interface distribution function (IDF). The samples are coded with names that specify the preparation conditions of the films: X Y-Z where X= SC (slow cooling) or Q (quenching) indicate the (slow or fast) cooling rate of the melt; Y stands for the temperature T_{max} reached in the melt, equal to 200 or T 150 T 150

| | | | | - | Bragg | | | | | | CF | | | IDF | | |
|--------------------|------------------------------------|----------------------------|------------------------------------|---------------------|-----------------------|-----------------------|---------------------|---------------------|--------|---------------------|---------------------|-------------------|-----------|---------------------|---------------------|--------------------------|
| Cooling conditions | q ₁ (nm ⁻¹) | <i>L</i> ₁ (nm) | q ₂ (nm ⁻¹) | L ₂ (nm) | x _c (WAXS) | Φ _c (%) | l _c (nm) | l _a (nm) | L (nm) | l _c (nm) | l _a (nm) | <i>l√L</i> (-) | L (nm) | l _c (nm) | l _a (nm) | l _c /L (-) |
| SC 200-10 | 0.294 | 21.4 | 0.741 | 16.9 | 0.66 | 0.62 | 13.3 | 8.1 | 19.6 | 15.4 | 4.2 | 0.79 | 15.3 | 11.6 | 3.7 | 0.76 |
| SC 200-30 | 0.333 | 18.9 | 0.831 | 15.1 | 0.59 | 0.55 | 10.4 | 8.5 | 18.9 | 14.8 | 4.1 | 0.78 | 13.9 | 10.4 | 3.5 | 0.75 |
| Q 150 10 | 0.323 | 19.4 | 0.78 | 16.1 | 0.52 | 0.48 | 9.3 | 10.1 | 19.1 | 15.2 | 3.9 | 0.79 | 14.4 | 10.8 | 3.6 | 0.75 |
| Q 150 30 | 0.314 | 20.0 | 0.79 | 15.9 | 0.56 | 0.52 | 10.5 | 9.5 | 19.2 | 15.1 | 4.0 | 0.79 | 14.8 | 11.1 | 3.6 | 0.75 |
| Q 200 10 | 0.314 | 20 | 0.731 | 17.2 | 0.52 | 0.48 | 9.6 | 10.4 | 19.6 | 15.7 | 3.9 | 0.80 | 15.0 | 11.5 | 3.6 | 0.76 |
| Q 200 30 | 0.304 | 20.7 | 0.651 | 19.3 | 0.58 | 0.53 | 11.1 | 9.6 | 19.5 | 15.3 | 4.2 | 0.79 | 15.5 | 11.9 | 3.7 | 0.76 |

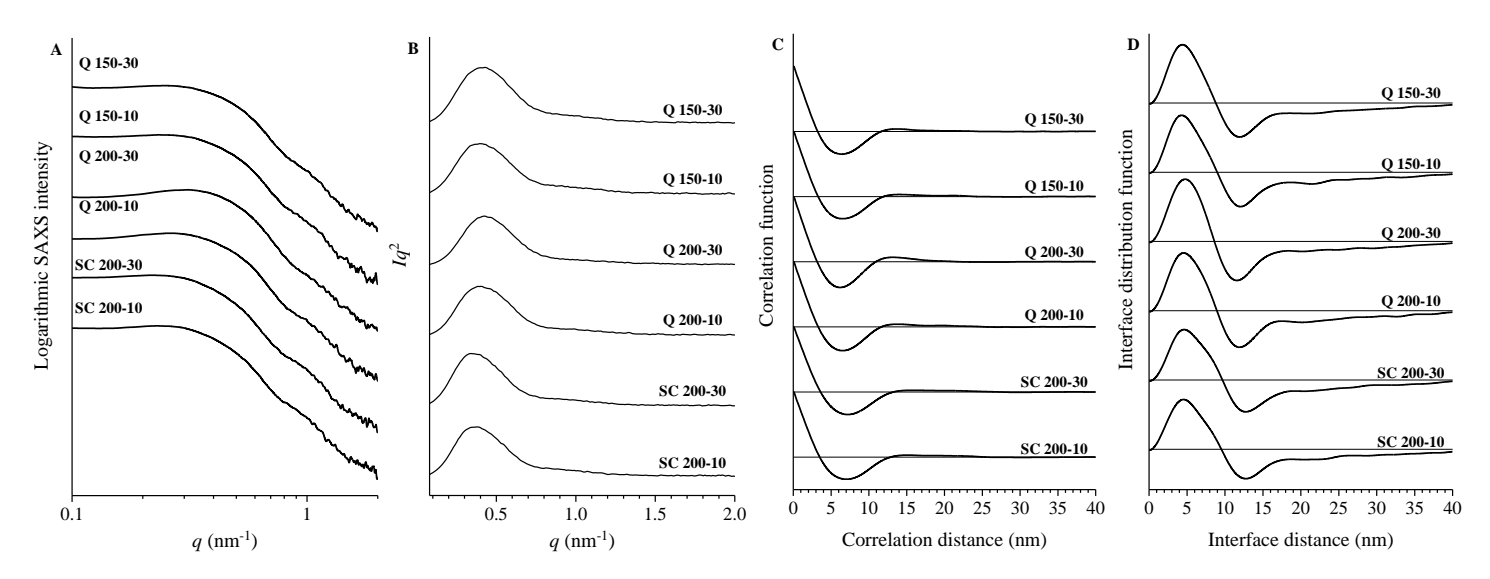


Figure A4 SAXS intensity profiles before (A) and after (B) Lorentz's factor correction, mono-dimensional Self-correlation function of electronic densities fluctuation CF (C) and Interface distribution function IDF (D) of compression-molded films of the sample L-C6 obtained under different cooling conditions. The samples are coded with names that specify the preparation conditions of the films: X Y-Z where X = SC (slow cooling) or Q (quenching) indicate the (slow or fast) cooling rate of the melt; Y stands for the temperature T_{max} reached in the melt, equal to 200 or 150 °C; the last number Z refers to the annealing time in min (t_{max}) of the melt at the indicated temperatures.

Table A4 Values of the lamellar periodicity (L) and thickness of amorphous (l_a) and crystalline (l_c) layers of lamellar stacks of the sample L-C6, deduced from SAXS data (Figure A1) through direct application of Bragg's law, the calculation of the mono-dimensional self-correlation function of electron density fluctuations (correlation function, CF) and the interface distribution function (IDF). The samples are coded with names that specify the preparation conditions of the films: X Y-Z where X=SC (slow cooling) or Q (quenching) indicate the (slow or fast) cooling rate of the melt; Y stands for the temperature T_{max} reached in the melt, equal to 200 or 150 °C; the last number Z refers to the annealing time in min (t_{max}) of the melt at the indicated temperatures.

| | Bragg | | | | | | CF IDF | | | | | | | | | |
|--------------------|------------------------|----------------------------|------------------------------------|----------------------------|--------------|-----------------------|---------------------|------------|--------|------------|------------|-------------|-----------|---------------------|------------|--------------------------|
| Cooling conditions | q1 (nm ⁻ | <i>L</i> ₁ (nm) | q ₂ (nm ⁻¹) | <i>L</i> ₂ (nm) | xc (WAXS) | Φ _c (%) | l _c (nm) | la (nm) | L (nm) | lc (nm) | la (nm) | lc/L (-) | L (nm) | l _c (nm) | la (nm) | l _c /L (-) |
| SC 200-10 | 0.38 | 16.5 | / | / | 0.63 | 0.59 | 9.8 | 6.8 | 15.2 | 10.8 | 4.4 | 0.71 | 12.8 | 8.2 | 4.6 | 0.64 |
| SC 200-30 | 0.343 | 18.3 | / | / | 0.521 | 0.48 | 8.8 | 9.5 | 15.8 | 11.3 | 4.6 | 0.71 | 12.8 | 8.1 | 4.6 | 0.64 |
| Q 150 10 | 0.4 | 15.7 | / | / | 0.57 | 0.53 | 8.3 | 7.4 | 14.0 | 9.8 | 4.2 | 0.70 | 12.1 | 7.8 | 4.3 | 0.64 |
| Q 150 30 | 0.43 | 14.6 | / | / | 0.507 | 0.47 | 6.8 | 7.8 | 13.9 | 9.7 | 4.2 | 0.70 | 11.9 | 7.6 | 4.4 | 0.63 |
| Q 200 10 | 0.39 | 16.1 | / | / | 0.59 | 0.55 | 8.9 | 7.2 | 13.9 | 9.6 | 4.3 | 0.69 | 11.9 | 7.4 | 4.6 | 0.62 |
| Q 200 30 | 0.42 | 14.9 | / | / | 0.506 | 0.46 | 6.9 | 8.0 | 13.3 | 9.0 | 4.2 | 0.68 | 11.6 | 6.8 | 4.8 | 0.59 |

Mechanical properties of compression-molded films of the blends obtained in different cooling conditions.

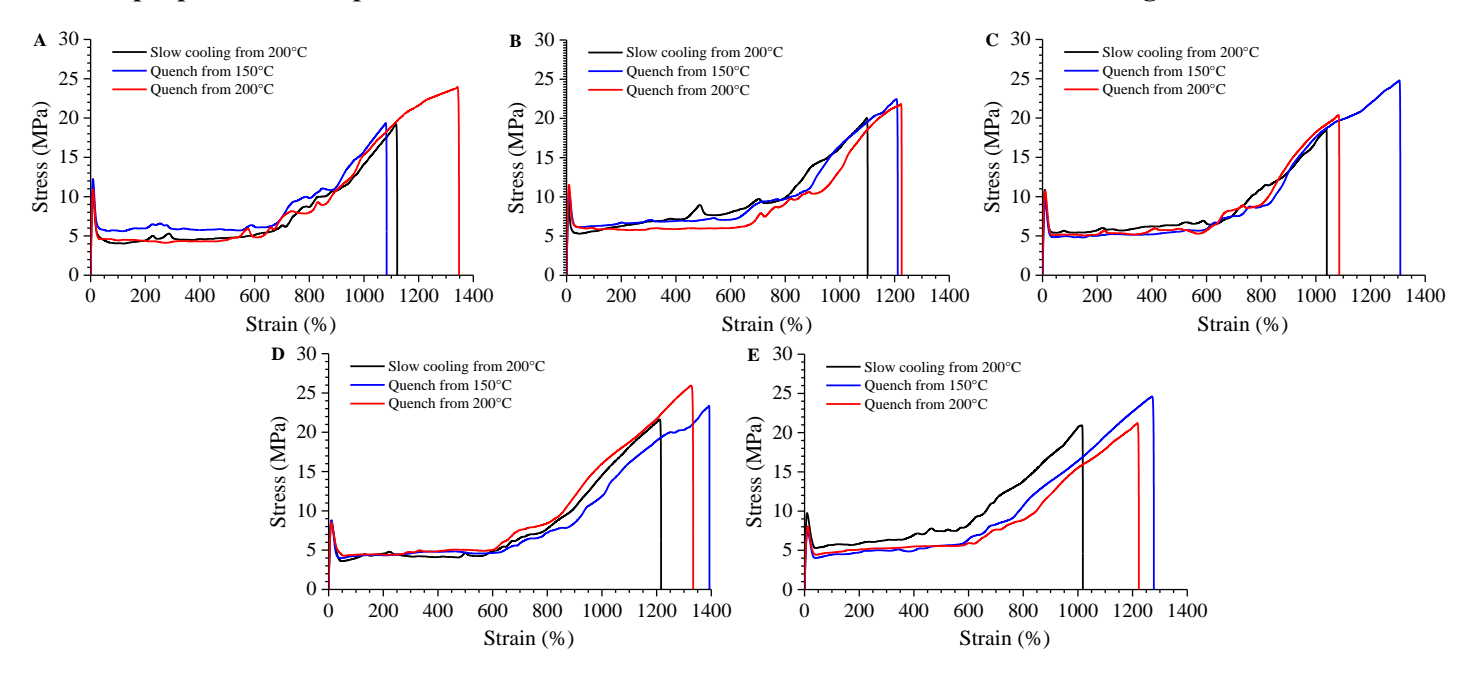


Figure A1 Stress-strain curves recorded on compression-molded films of the LLDPE/HDPE blends (A) 20L-80H, (B) 40L-60H, (C) 50L-50H, (D) 60L-40H, (E) 80L-20H, obtained through slow cooling from $T_{max} = 200^{\circ}$ C (black curve), quenching from $T_{max} = 150^{\circ}$ C (blue curve) and quenching from $T_{max} = 200^{\circ}$ C (red curve) after annealing the samples at T_{max} for $t_{max} = 10$ min.

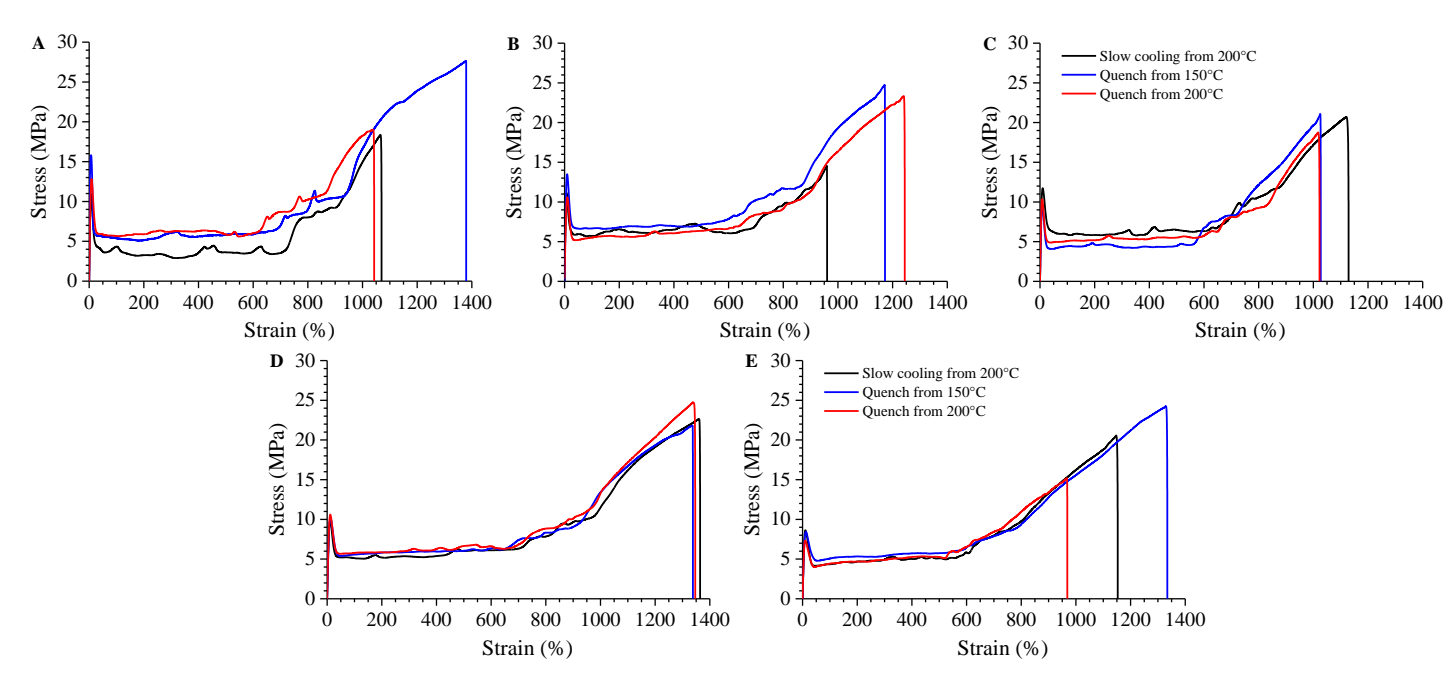


Figure A2 Stress-strain curves recorded on compression-molded films of the LLDPE/HDPE blends (A) 20L-80H, (B) 40L-60H, (C) 50L-50H, (D) 60L-40H, (E) 80L-20H, obtained through slow cooling from $T_{max} = 200^{\circ}$ C (black curve), quenching from $T_{max} = 150^{\circ}$ C (blue curve) and quenching from $T_{max} = 200^{\circ}$ C (red curve) after annealing the samples at T_{max} for $t_{max} = 30$ min.

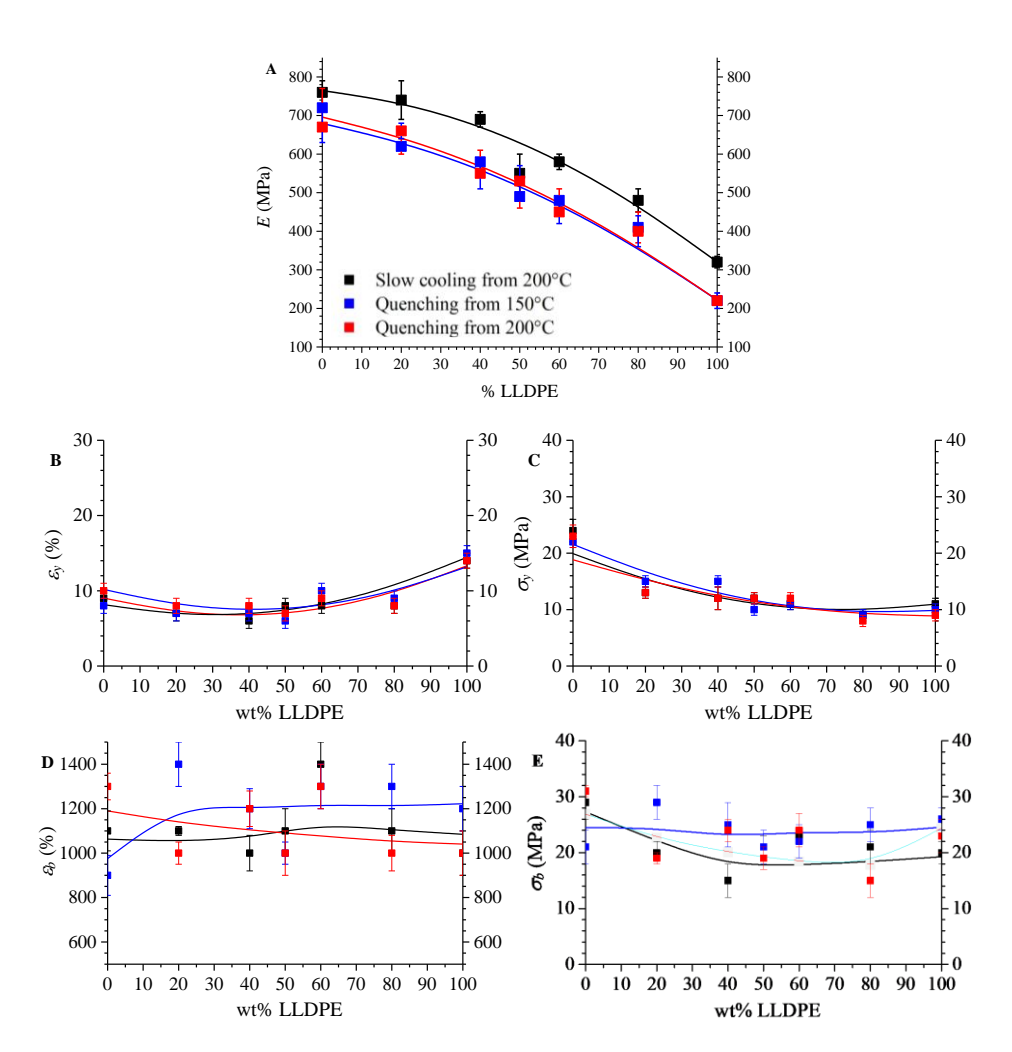


Figure A3 Mechanical parameters as a function of LLDPE (L-C8) content extracted from stress-strain curves of compression-molded films of the LLDPE-HDPE blends and neat components, obtained through slow cooling from $T_{max} = 200^{\circ}\text{C}$ (black squares), quenching from $T_{max} = 150^{\circ}\text{C}$ (blue squares) and quenching from $T_{max} = 200^{\circ}\text{C}$ (red squares) after annealing at T_{max} for $t_{max} = 30$ min. Young's Modulus (E)(A), strain (ε_y) (B) and stress (σ_y) (C) at yielding, strain (ε_b) (D) and stress (σ_b) (E) at break.

Table A1 Mechanical parameters of the LLDPE-HDPE blend 20L-80H extracted from stress-strain curves of Figure A1 (A), relative to compression molded films obtained by slow cooling from $T_{max} = 200$ °C and quenching from $T_{max} = 150$ and 200°C, after annealing at T_{max} for $t_{max} = 10$ min.

| Cooling conditions | E (MPa) | σ _y (MPa) | ε _y (%) | σ _b (MPa) | ε _b (%) |
|----------------------------|--------------|-------------------------|-----------------------|-------------------------|-----------------------|
| Slow cooling from 200°C | 760 ± 50 | 13 ± 1 | 7 ± 1 | 22 ± 3 | 1100 ± 100 |
| Quenching from 150°C | 630 ± 40 | 14 ± 1 | 7 ± 1 | 23 ± 3 | 1100 ± 80 |
| Quenching from 200°C | 650 ± 50 | 13 ± 1 | 7 ± 1 | 25 ± 1 | 1300 ± 100 |

Table A2 Mechanical parameters of the LLDPE-HDPE blend 20L-80H extracted from stress-strain curves of Figure A2 (A), relative to compression molded films obtained by slow cooling from $T_{max} = 200$ °C and quenching from $T_{max} = 150$ and 200°C, after annealing at T_{max} for $t_{max} = 30$ min.

| Cooling conditions | E (MPa) | σ _y (MPa) | ε _y (%) | σ _b (MPa) | ε _b (%) |
|----------------------------|--------------|-------------------------|-----------------------|-------------------------|-----------------------|
| Slow cooling from 200°C | 740 ± 50 | 13 ± 1 | 7 ± 1 | 20 ± 4 | 1100 ± 20 |
| Quenching from 150°C | 620 ± 20 | 15 ± 1 | 7 ± 1 | 29 ± 2 | 1400 ± 100 |
| Quenching from 200°C | 660 ± 20 | 13 ± 1 | 8 ± 1 | 19 ± 1 | 1200 ± 70 |

Table A3 Mechanical parameters of the LLDPE-HDPE blend 40L-60H extracted from stress-strain curves of Figure A1 (B), relative to compression molded films obtained by slow cooling from $T_{max} = 200$ °C and quenching from $T_{max} = 150$ and 200°C, after annealing at T_{max} for $t_{max} = 10$ min.

| Cooling conditions | E (MPa) | σ _y (MPa) | ε _y (%) | σ _b (MPa) | ε _b (%) |
|----------------------------|--------------|-------------------------|-----------------------|-------------------------|-----------------------|
| Slow cooling from 200°C | 720 ± 30 | 12 ± 2 | 5 ± 1 | 20 ± 1 | 1100 ± 20 |
| Quenching from 150°C | 530 ± 30 | 13 ± 1 | 7 ± 1 | 23 ± 2 | 1200 ± 100 |
| Quenching from 200°C | 550 ± 30 | 13 ± 1 | 8 ± 1 | 22 ± 1 | 1100 ± 40 |

Table A4 Mechanical parameters of the LLDPE-HDPE blend 40L-60H extracted from stress-strain curves of Figure A2 (B), relative to compression molded films obtained by slow cooling from T_{max} =200°C and quenching from T_{max} =150 and 200°C, after annealing at T_{max} for t_{max} = 30 min.

| Cooling conditions | E (MPa) | σ _y (MPa) | ε _y (%) | σ _b (MPa) | ε _b (%) |
|----------------------------|--------------|-------------------------|-----------------------|-------------------------|-----------------------|
| Slow cooling from 200°C | 690 ± 20 | 12 ± 2 | 6 ± 1 | 15 ± 3 | 1000 ± 80 |
| Quenching from 150°C | 580 ± 30 | 15 ± 1 | 7 ± 2 | 25 ± 4 | 1200 ± 90 |
| Quenching from 200°C | 550 ± 40 | 12 ± 2 | 8 ± 1 | 24 ± 2 | 1200 ± 80 |

Table A5 Mechanical parameters of the LLDPE-HDPE blend 50L-50H extracted from stress-strain curves of Figure A1 (C), relative to compression molded films obtained by slow cooling from $T_{max} = 200$ °C and quenching from $T_{max} = 150$ and 200°C, after annealing at T_{max} for $t_{max} = 10$ min.

| Cooling conditions | E (MPa) | σ _y (MPa) | ε _y (%) | σ _b (MPa) | ε _b (%) |
|----------------------------|--------------|-------------------------|-----------------------|-------------------------|-----------------------|
| Slow cooling from 200°C | 560 ± 50 | 12 ± 2 | 7 ± 1 | 19 ± 3 | 1000 ± 50 |
| Quenching from 150°C | 490 ± 40 | 11 ± 1 | 6 ± 1 | 25 ± 2 | 1300 ± 20 |
| Quenching from 200°C | 530 ± 30 | 12 ± 1 | 8 ± 1 | 21 ± 2 | 1100 ± 100 |

Table A6 Mechanical parameters of the LLDPE-HDPE blend 50L-50H extracted from stress-strain curves of Figure A2 (C), relative to compression molded films obtained by slow cooling from $T_{max} = 200$ °C and quenching from $T_{max} = 150$ and 200°C, after annealing at T_{max} for $t_{max} = 30$ min.

| Cooling conditions | E (MPa) | σ _y (MPa) | ε _y (%) | σ _b (MPa) | ε _b (%) |
|----------------------------|--------------|-------------------------|-----------------------|-------------------------|-----------------------|
| Slow cooling from 200°C | 550 ± 50 | 12 ± 1 | 8 ± 1 | 21 ± 2 | 1100 ± 100 |
| Quenching from 150°C | 490 ± 30 | 10 ± 1 | 6 ± 1 | 21 ± 3 | 1000 ± 50 |
| Quenching from 200°C | 530 ± 40 | 12 ± 1 | 7 ± 1 | 19 ± 2 | 1000 ± 100 |

Table A7 Mechanical parameters of the LLDPE-HDPE blend 60L-40H extracted from stress-strain curves of Figure A1 (D), relative to compression molded films obtained by slow cooling from $T_{max} = 200$ °C and quenching from $T_{max} = 150$ and 200°C, after annealing at T_{max} for $t_{max} = 10$ min.

| Cooling conditions | E (MPa) | σ _y (MPa) | ε _y (%) | σ _b (MPa) | ε _b (%) |
|----------------------------|------------|-------------------------|-----------------------|-------------------------|-----------------------|
| Slow cooling from 200°C | 540 ± 40 | 10 ± 1 | 7 ± 1 | 22 ± 1 | 1200 ± 20 |
| Quenching from 150°C | 470 ± 20 | 10 ± 1 | 8 ± 1 | 24 ± 3 | 1400 ± 100 |
| Quenching from 200°C | 450 ± 30 | 10 ± 1 | 8 ± 1 | 25 ± 2 | 1300 ± 80 |

Table A8 Mechanical parameters of the LLDPE-HDPE blend 60L-40H extracted from stress-strain curves of Figure A2 (D), relative to compression molded films obtained by slow cooling from $T_{max} = 200$ °C and quenching from $T_{max} = 150$ and 200°C, after annealing at T_{max} for $t_{max} = 30$ min.

| Cooling conditions | E (MPa) | σ _y (MPa) | ε _y (%) | σ _b (MPa) | ε _b (%) |
|----------------------------|------------|-------------------------|-----------------------|-------------------------|-----------------------|
| Slow cooling from 200°C | 580 ± 20 | 11 ± 1 | 8 ± 1 | 23 ± 1 | 1400 ± 100 |
| Quenching from 150°C | 480 ± 30 | 11 ± 1 | 10 ± 1 | 22 ± 3 | 1300 ± 100 |
| Quenching from 200°C | 450 ± 30 | 12 ± 1 | 9 ± 1 | 24 ± 3 | 1300 ± 100 |

Table A9 Mechanical parameters of the LLDPE-HDPE blend 80L-20H extracted from stress-strain curves of Figure A1 (E), relative to compression molded films obtained by slow cooling from $T_{max} = 200$ °C and quenching from $T_{max} = 150$ and 200°C, after annealing at T_{max} for $t_{max} = 10$ min.

| Cooling conditions | E (MPa) | σ _y (MPa) | ε _y (%) | σ _b (MPa) | ε _b (%) |
|----------------------------|--------------|-------------------------|-----------------------|-------------------------|-----------------------|
| Slow cooling from 200°C | 500 ± 30 | 10 ± 1 | 8 ± 1 | 21 ± 2 | 1000 ± 60 |
| Quenching from 150°C | 450 ± 50 | 8 ± 1 | 8 ± 1 | 25 ± 3 | 1300 ± 80 |
| Quenching from 200°C | 430 ± 20 | 9 ± 1 | 8 ± 1 | 22 ± 2 | 1200 ± 100 |

Table A10 Mechanical parameters of the LLDPE-HDPE blend 80L-20H extracted from stress-strain curves of Figure A2 (E), relative to compression molded films obtained by slow cooling from $T_{max} = 200$ °C and quenching from $T_{max} = 150$ and 200°C, after annealing at T_{max} for $t_{max} = 30$ min.

| Cooling conditions | E (MPa) | σ _y (MPa) | ε _y (%) | σ _b (MPa) | ε _b (%) |
|----------------------------|--------------|-------------------------|-----------------------|-------------------------|-----------------------|
| Slow cooling from 200°C | 480 ± 30 | 9 ± 1 | 8 ± 1 | 21 ± 3 | 1100 ± 100 |
| Quenching from 150°C | 410 ± 40 | 9 ± 1 | 9 ± 1 | 25 ± 3 | 1300 ± 100 |
| Quenching from 200°C | 400 ± 40 | 8 ± 1 | 8 ± 1 | 15 ± 3 | 1000 ± 80 |

Self-Nucleation and Annealing (SNA)

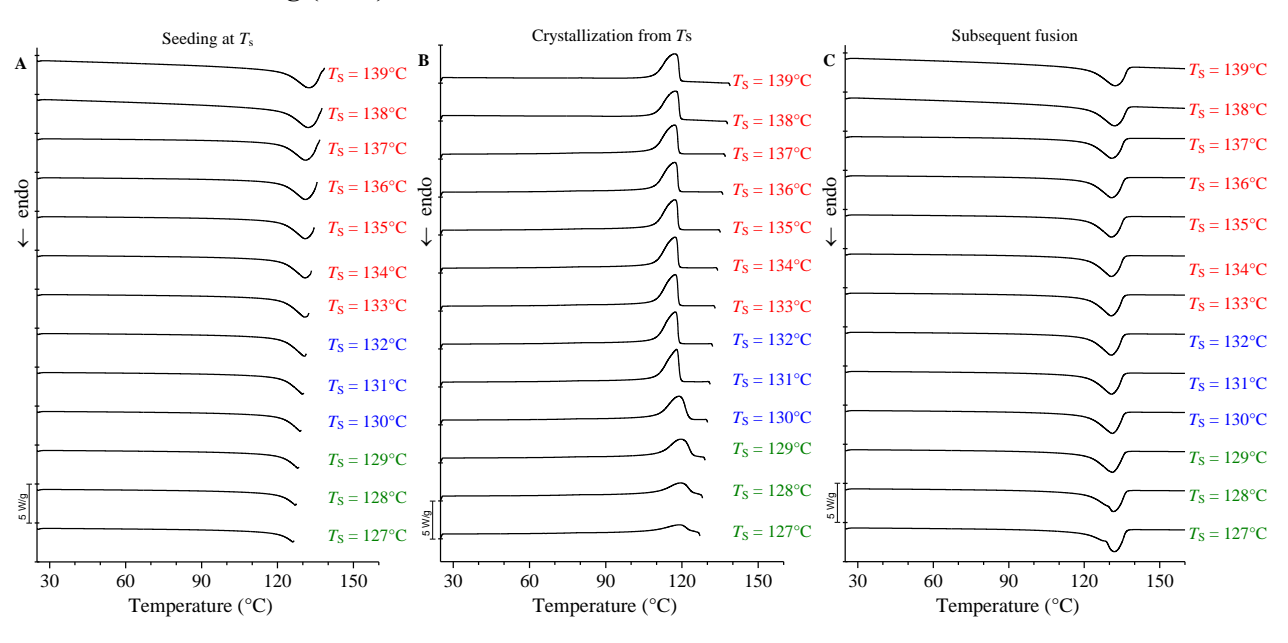


Figure A1 DSC heating scans recorded up to at seeding temperatures $T_s(A)$, in the successive cooling steps after 5 min isotherm at the indicated $T_s(B)$, and successive heating scans (C) for the sample H-C4. The scanning rate is 10 °C/min.

Table A1 Crystallization temperatures T_c and corresponding enthalpies ΔH_c of sample H-C4 extracted from cooling scans recorded after 5 minutes at the indicated seeding temperature T_s (step 4 of SNA protocol), melting temperature T_m and corresponding enthalpies ΔH_m extracted from subsequent heating (step 5 of SNA protocol).

| Seeding Temperature T _s (°C) | $T_{\rm c}$ recorded by cooling from $T_{\rm s}$ (°C) | $\Delta H_{\rm c}$ (J/g) | $T_{ m m}$ recorded by subsequent heating (°C) | $\Delta H_{ m m} \ ({ m J/g})$ |
|---|---|--------------------------|--|--------------------------------|
| 139 | 117.3 | 212.6 | 132.3 | 197.5 |
| 138 | 117.3 | 213.4 | 132.0 | 197.4 |
| 137 | 117.2 | 206.3 | 130.9 | 201.5 |
| 136 | 117.1 | 206.6 | 130.8 | 202.1 |
| 135 | 117.2 | 206.4 | 130.8 | 202.4 |
| 134 | 117.2 | 206.3 | 130.8 | 202.2 |
| 133 | 117.2 | 206.3 | 130.6 | 202.2 |
| 132 | 117.4 | 206.4 | 130.6 | 202.2 |
| 131 | 117.7 | 204.0 | 130.8 | 202.2 |
| 130 | 118.9 | 198.7 | 131.1 | 204.6 |
| 129 | 119.5 | 125.1 | 131.1 | 206.3 |
| 128 | 119.4 | 67.6 | 131.6 | 207.0 |
| 127 | 118.9 | 55.0 | 131.9 | 207.0 |

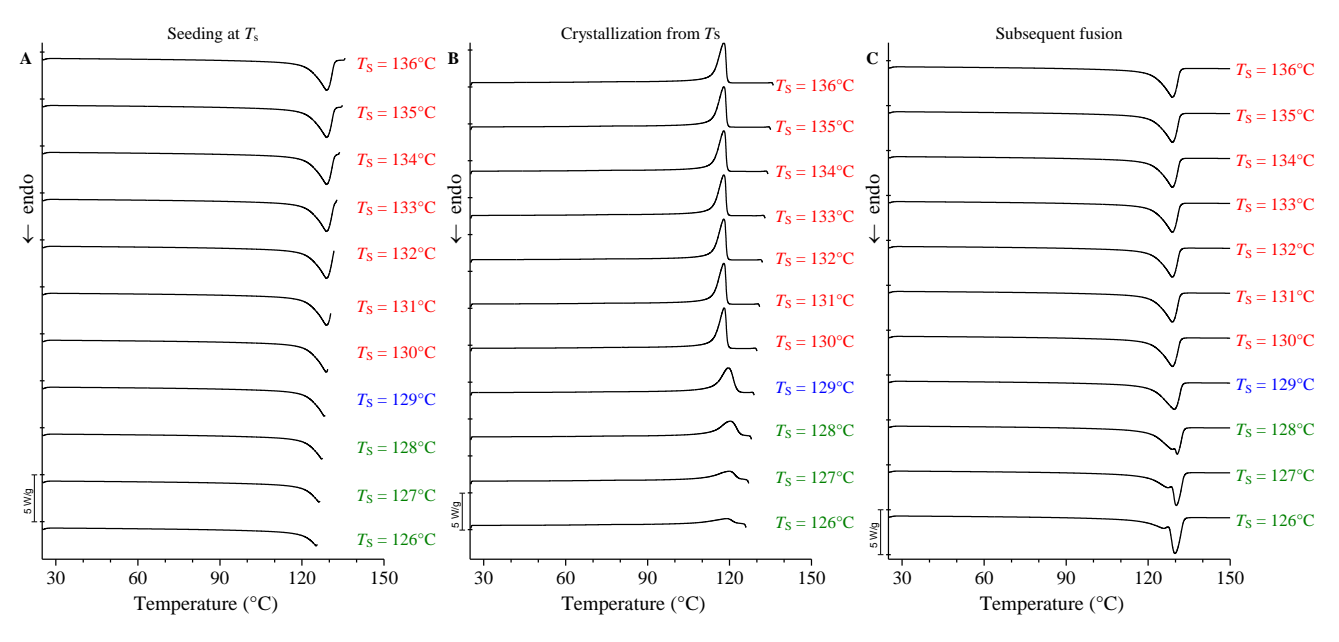


Figure A2 DSC heating scans recorded up to at seeding temperatures $T_s(A)$, in the successive cooling steps after 5 min isotherm at the indicated $T_s(B)$, and successive heating scans (C), for the blend 20L-80H. The scanning rate is 10 °C/min.

Table A2 Crystallization temperatures T_c and corresponding enthalpies ΔH_c of sample 20L-80H extracted from cooling scans recorded after 5 minutes at the indicated seeding temperature T_s (step 4 of SNA protocol), melting temperature T_m and corresponding enthalpies ΔH_m extracted from subsequent heating (step 5 of SNA protocol).

| Seeding Temperature T _s (°C) | $T_{\rm c}$ recorded by cooling from $T_{ m s}$ (°C) | $\Delta H_{ m c} \ ({ m J/g})$ | $T_{ m m}$ recorded by subsequent heating (°C) | $\Delta H_{ m m} \ m (J/g)$ |
|---|--|--------------------------------|--|------------------------------|
| 136 | 118.0 | 181.9 | 128.9 | 180.5 |
| 135 | 118.0 | 181.6 | 128.9 | 181.2 |
| 134 | 118.0 | 181.3 | 128.9 | 180.4 |
| 133 | 118.0 | 181.2 | 128.9 | 180.4 |
| 132 | 118.0 | 181.1 | 128.9 | 179.5 |
| 131 | 118.0 | 181.3 | 128.9 | 179.8 |
| 130 | 118.0 | 181.3 | 128.9 | 179.9 |
| 129 | 119.6 | 170.7 | 129.6 | 182.7 |
| 128 | 120.3 | 90.7 | 128.8, 130.6 | 184.1 |
| 127 | 119.9 | 64.9 | 127.4, 130.3 | 184.1 |
| 126 | 119.0 | 49.9 | 125.8, 129.8 | 183.9 |

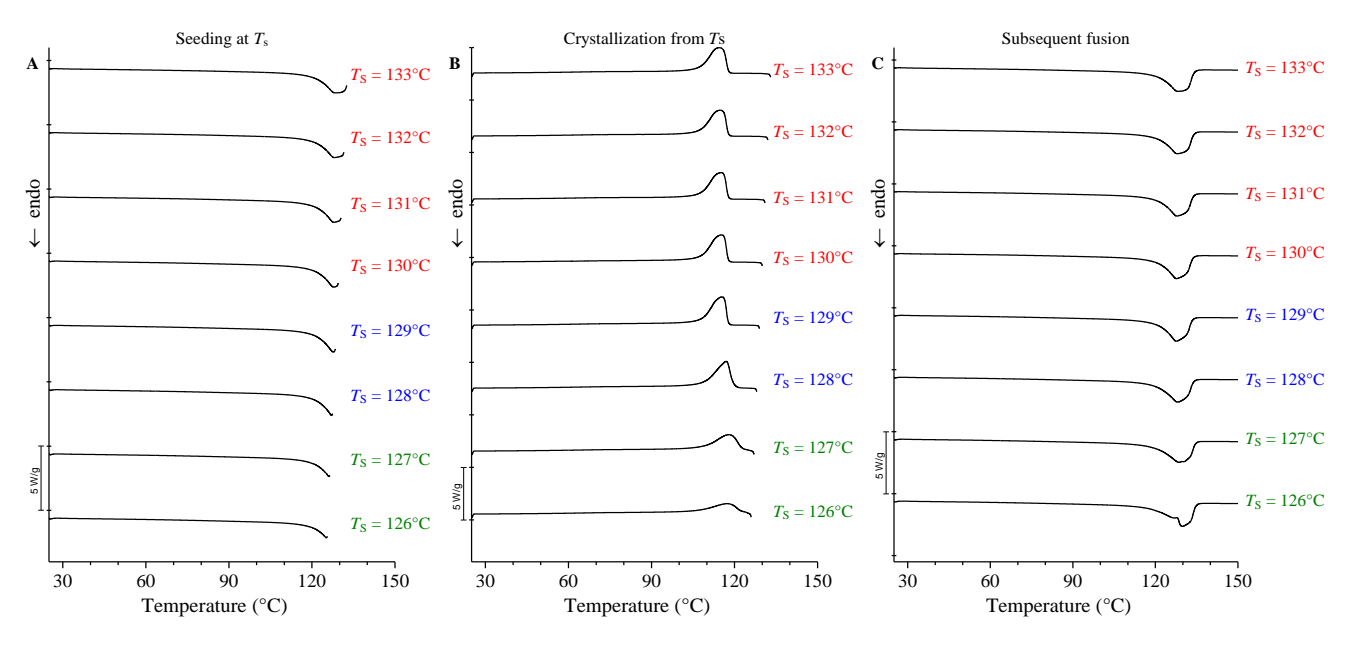


Figure A3 DSC heating scans recorded up to at seeding temperatures $T_s(A)$, in the successive cooling steps after 5 min isotherm at the indicated $T_s(B)$, and successive heating scans (C), for the blend 40L-60H. The scanning rate is 10 °C/min.

Table A3 Crystallization temperatures T_c and corresponding enthalpies ΔH_c of sample 40L-60H extracted from cooling scans recorded after 5 minutes at the indicated seeding temperature T_s (step 4 of SNA protocol), melting temperature T_m and corresponding enthalpies ΔH_m extracted from subsequent heating (step 5 of SNA protocol).

| Seeding Temperature T _s (°C) | $T_{\rm c}$ recorded by cooling from $T_{\rm s}$ (°C) | $\Delta H_{\rm c}$ (J/g) | $T_{\rm m}$ recorded by subsequent heating (°C) | $\Delta H_{ m m} \ ({ m J/g})$ |
|---|---|--------------------------|---|--------------------------------|
| 133 | 115.2 | 156.7 | 128.1 | 156.8 |
| 132 | 115.1 | 156.4 | 127.9 | 156.1 |
| 131 | 115.2 | 155.8 | 127.8 | 155.9 |
| 130 | 115.2 | 154.3 | 127.8 | 156.6 |
| 129 | 115.2 | 157.4 | 127.6 | 160.1 |
| 128 | 115.5 | 158.3 | 128.1 | 161.2 |
| 127 | 116.9 | 103.2 | 128.6, 130.3 | 162.7 |
| 126 | 118.0 | 72.1 | 126.9, 129.9 | 163.5 |

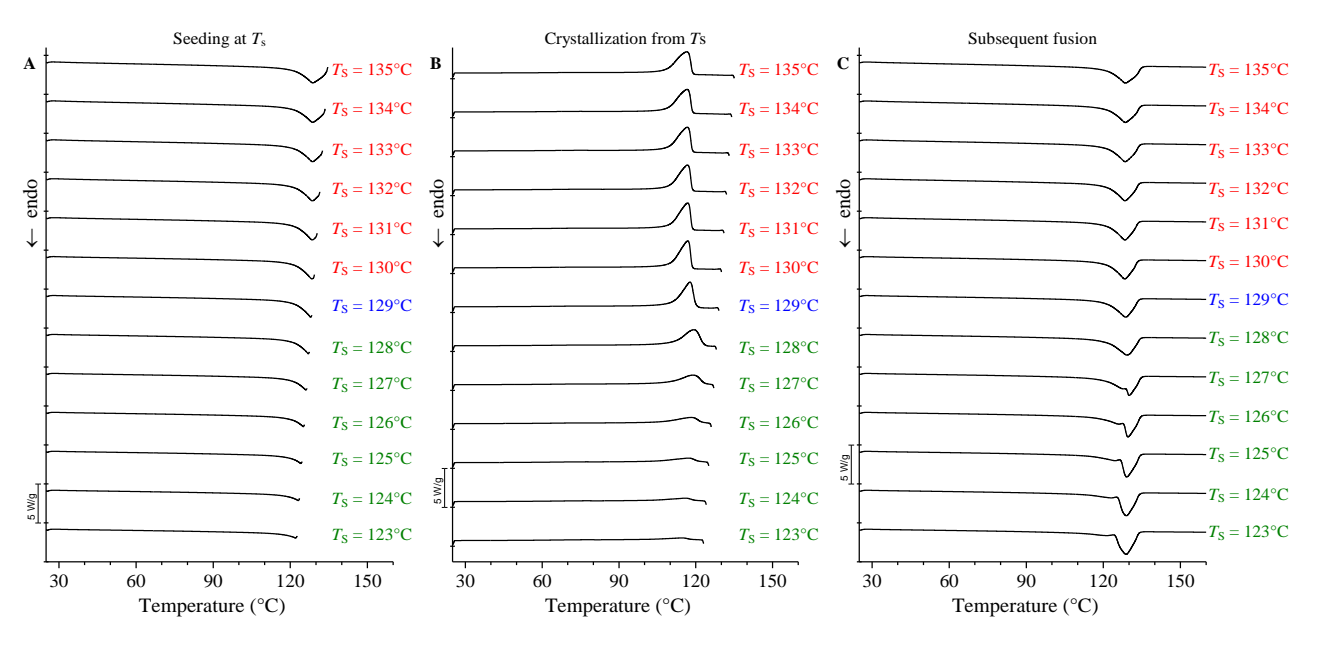


Figure A4 DSC heating scans recorded up to at seeding temperatures $T_s(A)$, in the successive cooling steps after 5 min isotherm at the indicated $T_s(B)$, and successive heating scans (C), for the blend 50L-50H. The scanning rate is 10 °C/min.

Table A4 Crystallization temperatures T_c and corresponding enthalpies ΔH_c of sample 50L-50H extracted from cooling scans recorded after 5 minutes at the indicated seeding temperature T_s (step 4 of SNA protocol), melting temperature T_m and corresponding enthalpies ΔH_m extracted from subsequent heating (step 5 of SNA protocol).

| Seeding Temperature T _s (°C) | $T_{\rm c}$ recorded by cooling from $T_{\rm s}$ (°C) | $\Delta H_{\rm c}$ (J/g) | T_{m} recorded by subsequent heating (°C) | $\Delta H_{ m m}$ (J/g) |
|---|---|--------------------------|--|-------------------------|
| 135 | 116.8 | 177.6 | 128.5 | 178.8 |
| 134 | 116.7 | 177.2 | 128.5 | 177.6 |
| 133 | 116.8 | 176.8 | 128.5 | 178.3 |
| 132 | 116.9 | 177.0 | 128.5 | 179.8 |
| 131 | 116.9 | 176.1 | 128.5 | 178.8 |
| 130 | 116.9 | 174.2 | 128.3 | 173.6 |
| 129 | 117.7 | 174.6 | 128.7 | 174.4 |
| 128 | 119.2 | 143.7 | 129.2 | 176.3 |
| 127 | 118.9 | 85.0 | 127.9, 130.0 | 177.6 |

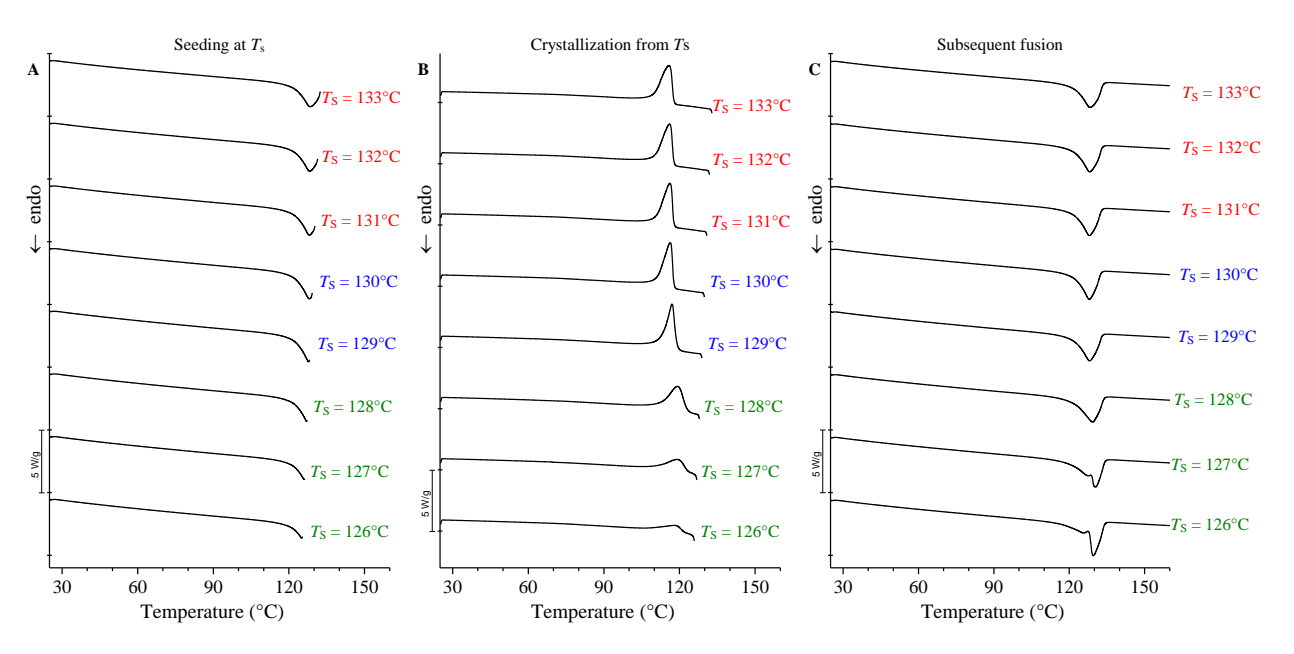


Figure A5DSC heating scans recorded up to at seeding temperatures $T_s(A)$, in the successive cooling steps after 5 min isotherm at the indicated $T_s(B)$, and successive heating scans (C), for the blend 60L-40H. The scanning rate is 10 °C/min.

Table A5 Crystallization temperatures T_c and corresponding enthalpies ΔH_c of sample 60L-40H extracted from cooling scans recorded after 5 minutes at the indicated seeding temperature T_s (step 4 of SNA protocol), melting temperature T_m and corresponding enthalpies ΔH_m extracted from subsequent heating (step 5 of SNA protocol).

| Seeding Temperature T _s (°C) | $T_{\rm c}$ recorded by cooling from $T_{\rm s}$ (°C) | $\Delta H_{\rm c}$ (J/g) | $T_{\rm m}$ recorded by subsequent heating (°C) | $\Delta H_{ m m} \ ({ m J/g})$ |
|---|---|--------------------------|---|--------------------------------|
| 133 | 116.1 | 177.4 | 128.3 | 181.7 |
| 132 | 116.1 | 178.7 | 128.1 | 183.6 |
| 131 | 116.1 | 179.8 | 128.1 | 184.2 |
| 130 | 116.3 | 180.6 | 128.1 | 185.4 |
| 129 | 117.0 | 175.7 | 128.1 | 198.1 |
| 128 | 119.2 | 109.8 | 129.2 | 189.6 |
| 127 | 119.1 | 51.5 | 127.6, 130.4 | 188.4 |
| 126 | 118.2 | 78.6 | 125.9, 129.6 | 186.6 |

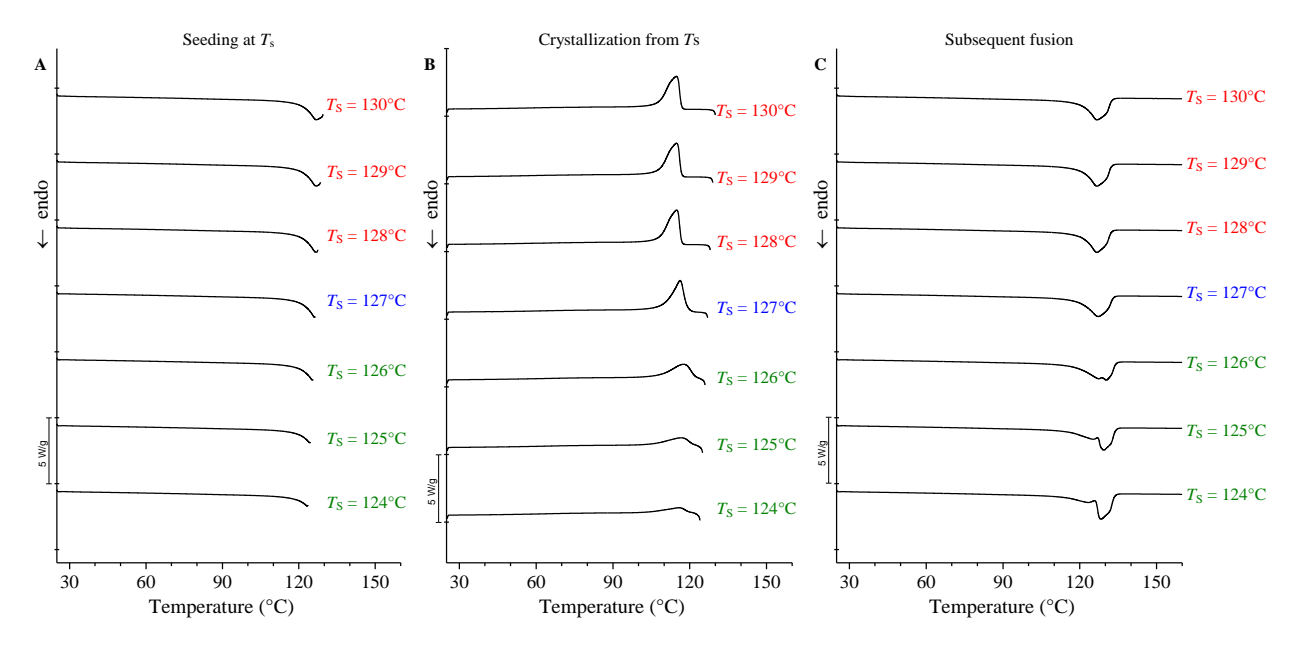


Figure DSC heating scans recorded up to at seeding temperatures $T_s(A)$, in the successive cooling steps after 5 min isotherm at the indicated $T_s(B)$, and successive heating scans (C), for the blend 80L-20H. The scanning rate is 10 °C/min.

Table A6 Crystallization temperatures T_c and corresponding enthalpies ΔH_c of sample 80L-20H extracted from cooling scans recorded after 5 minutes at the indicated seeding temperature T_s (step 4 of SNA protocol), melting temperature T_m and corresponding enthalpies ΔH_m extracted from subsequent heating (step 5 of SNA protocol).

| Seeding Temperature T _s (°C) | $T_{\rm c}$ recorded by cooling from $T_{\rm s}$ (°C) | $\Delta H_{\rm c}$ (J/g) | $T_{ m m}$ recorded by subsequent heating (°C) | $\Delta H_{ m m} \ ({ m J/g})$ |
|---|---|--------------------------|--|--------------------------------|
| 130 | 114.76 | 136.2 | 126.6 | 137.4 |
| 129 | 114.77 | 135.6 | 126.6 | 137.4 |
| 128 | 114.78 | 135.5 | 126.6 | 137.4 |
| 127 | 116.25 | 132.4 | 127.3 | 135.9 |
| 126 | 117.58 | 72.78 | 127.4, 130.3 | 138.0 |
| 125 | 116.52 | 61.2 | 125.2, 129.3 | 137.8 |
| 124 | 115.82 | 33.6 | 123.4, 128.3 | 139.2 |

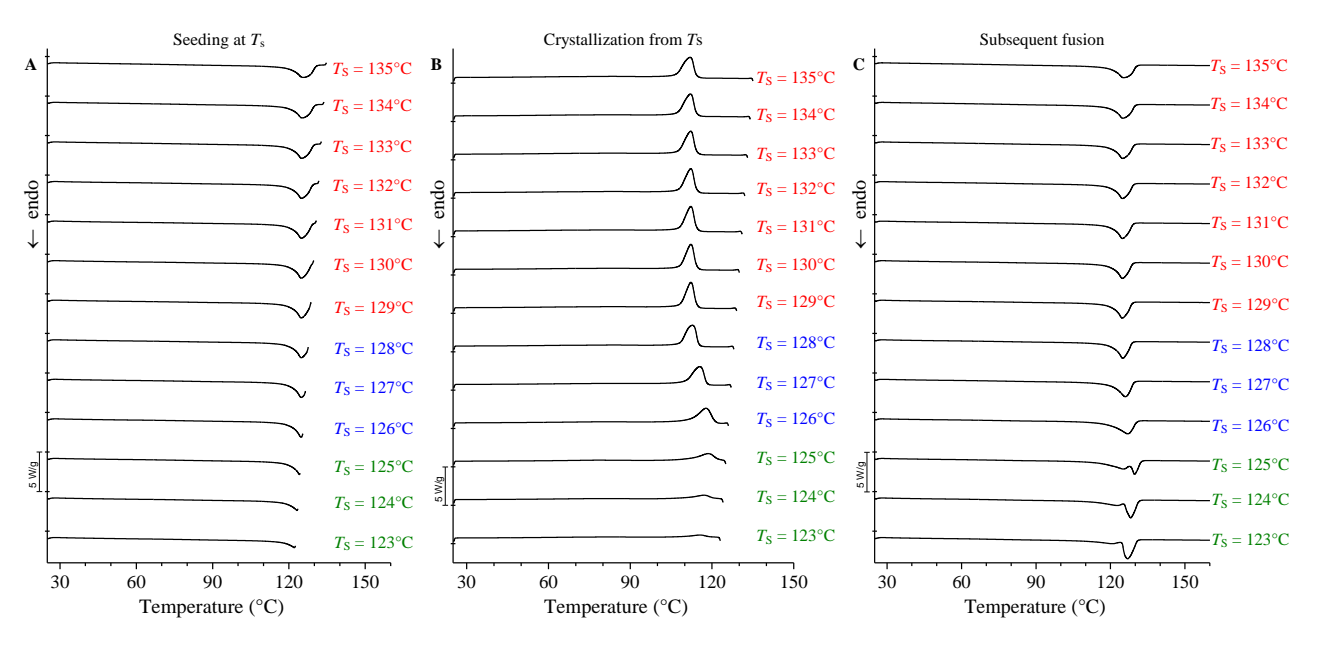


Figure A7 DSC heating scans recorded up to at seeding temperatures $T_s(A)$, in the successive cooling steps after 5 min isotherm at the indicated $T_s(B)$, and successive heating scans (C), for the sample L-C8. The scanning rate is 10 °C/min.

Table A7 Crystallization temperatures T_c and corresponding enthalpies ΔH_c of sample 40L-60H extracted from cooling scans recorded after 5 minutes at the indicated seeding temperature T_s (step 4 of SNA protocol), melting temperature T_m and corresponding enthalpies ΔH_m extracted from subsequent heating (step 5 of SNA protocol).

| Seeding Temperature T _s (°C) | $T_{\rm c}$ recorded by cooling from $T_{\rm s}$ (°C) | $\Delta H_{\rm c}$ (J/g) | $T_{ m m}$ recorded by subsequent heating (°C) | $\Delta H_{ m m} \ ({ m J/g})$ |
|---|---|--------------------------|--|--------------------------------|
| 135 | 112.1 | 132.7 | 125.3 | 130.6 |
| 134 | 112.5 | 132.1 | 124.9 | 130.9 |
| 133 | 112.2 | 132.1 | 124.9 | 129.9 |
| 132 | 112.2 | 131.6 | 124.8 | 128.1 |
| 131 | 112.2 | 130.9 | 124.7 | 128.7 |
| 130 | 112.2 | 131.2 | 124.7 | 129.1 |
| 129 | 112.2 | 131.4 | 124.7 | 127.4 |
| 128 | 112.8 | 131.2 | 124.9 | 128.4 |
| 127 | 115.4 | 129.5 | 125.9 | 130.0 |
| 126 | 117.9 | 108.5 | 126.9 | 130.1 |
| 125 | 118.6 | 52.0 | 125.4, 129.8 | 132.4 |
| 124 | 117.0 | 36.9 | 122.8, 128.2 | 132.8 |
| 123 | 115.5 | 29.8 | 120.8, 126.8 | 133.8 |

Thermal fractionation via Successive Self-Nucleation and Annealing (SSA)

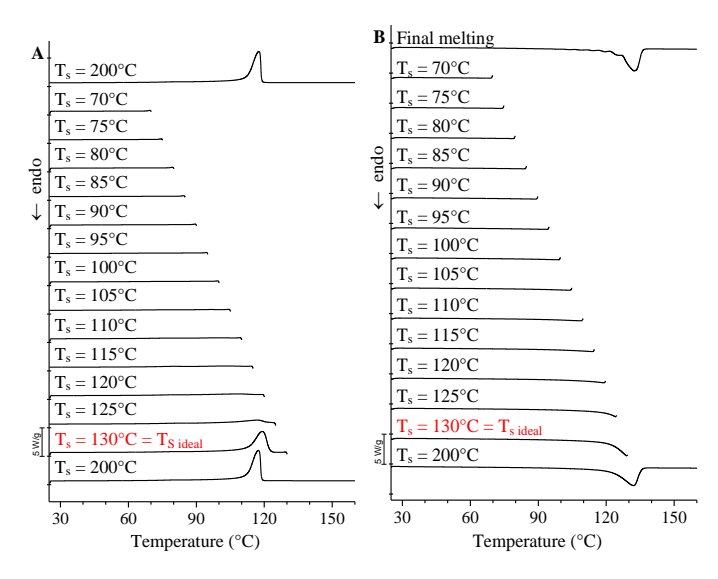


Figure A1 DSC scans recorded in the SNA protocol for the sample H-C4, during the DSC cooling steps from the selected T_s to 25 °C (A) and the successive heating scans (B). The scanning rate is 10°C/min.

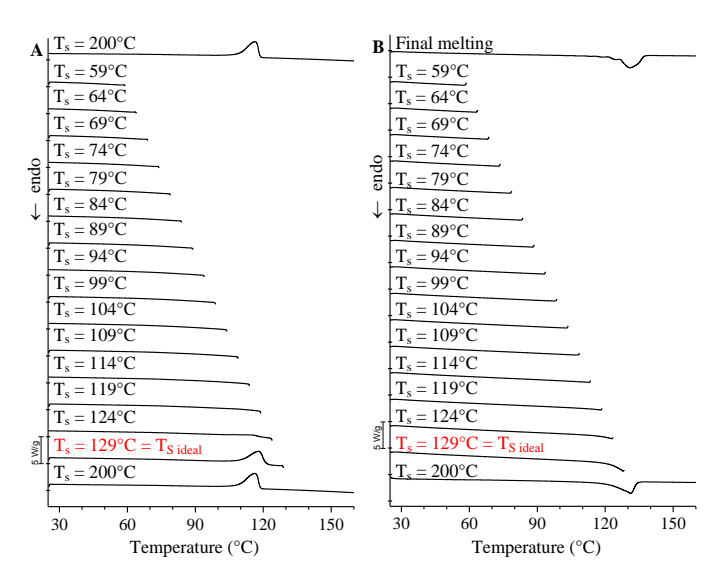


Figure A2 DSC scans recorded in the SNA protocol for the sample 50L-50H, during the DSC cooling steps from the selected T_s to 25 °C (A) and successive heating scans (B). The scanning rate is 10°C/min.

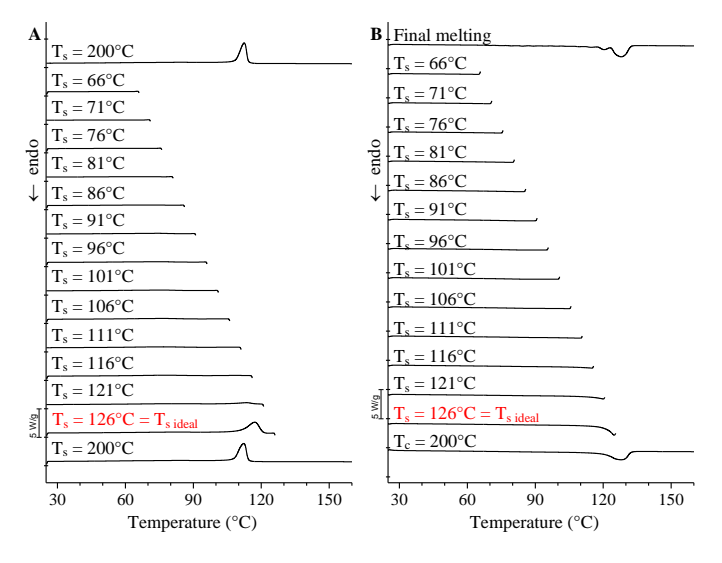


Figure A3 DSC scans recorded in the SNA protocol for the sample L-C8, during the DSC cooling steps from the selected T_s to 25 °C (A) and the successive heating scans. The scanning rate is 10°C/min.

High temperature and room temperature structural analysis at different $T_{\text{treatment}}$ and after fast cooling.

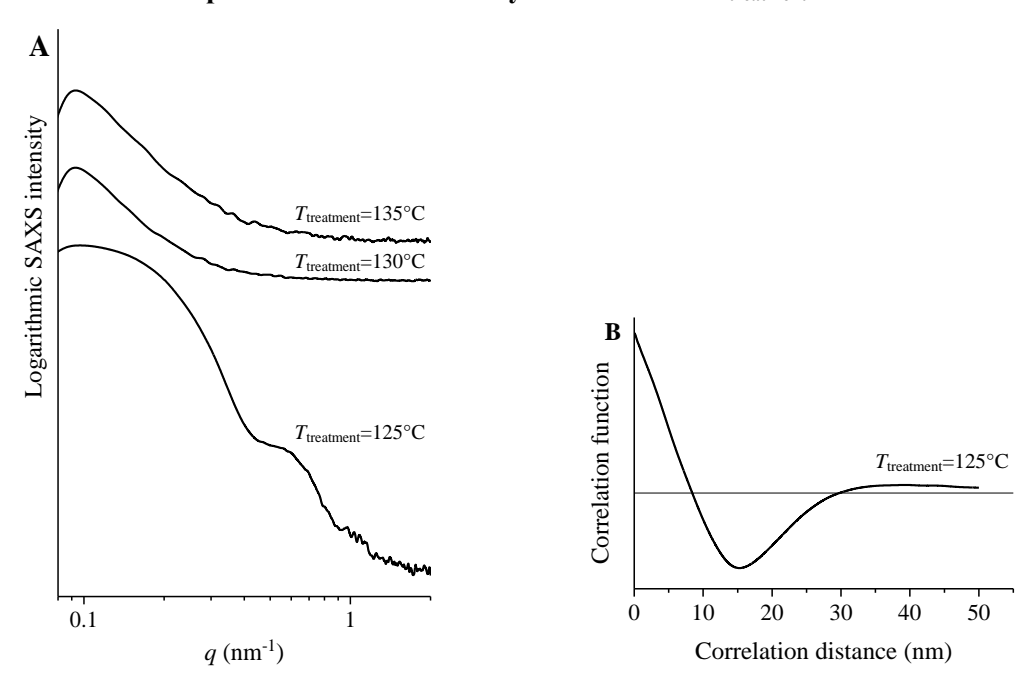


Figure A1 SAXS profiles (A) recorded at the indicated temperatures ($T_{treatment}$) and calculated mono-dimensional self-correlation function of electronic densities fluctuation (correlation function, CF) (B) of the sample H-C4.

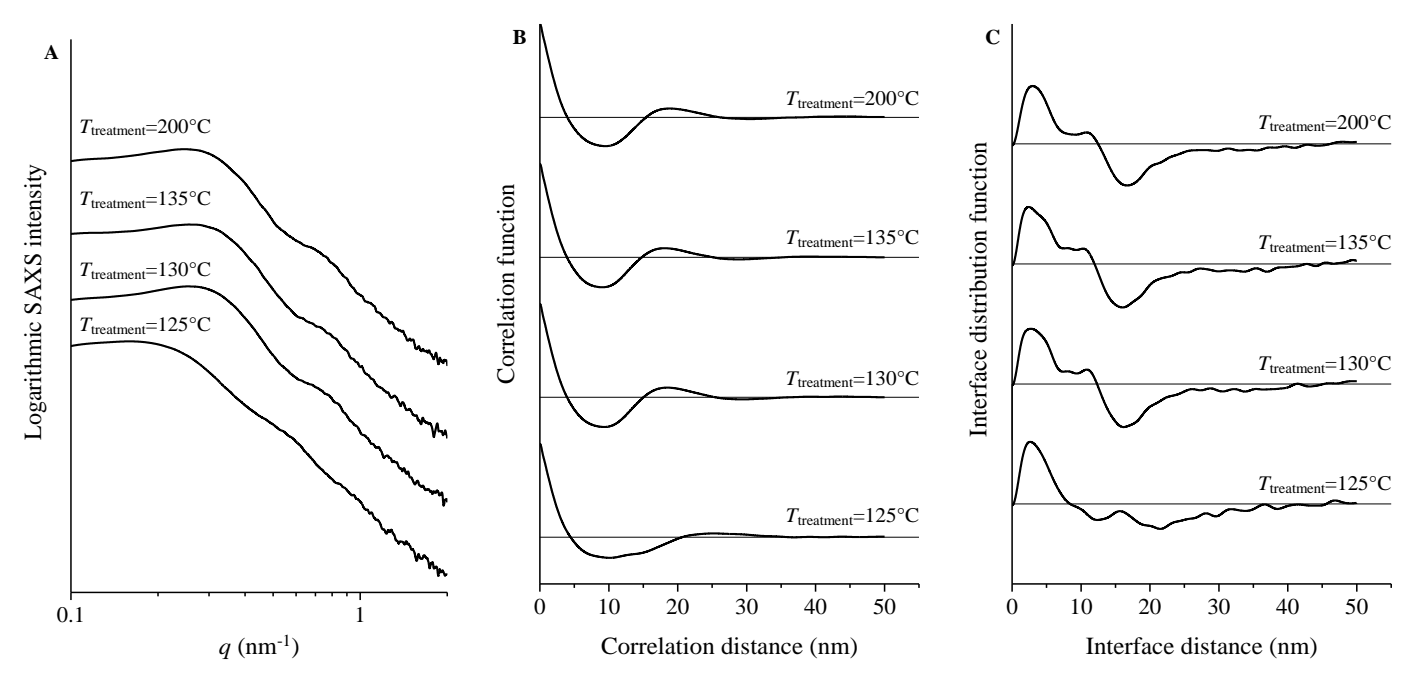


Figure A2 SAXS profiles (A) recorded at room temperature for heat treated specimens of the sample H-C4 for $t_{treatment} = 10$ min at the indicated temperatures ($T_{treatment}$), obtained by fast cooling (40 °C/min) to room temperature calculated monodimensional self-correlation function of electronic densities fluctuation (correlation function, (CF) (B) and Interface distribution function IDF (C).

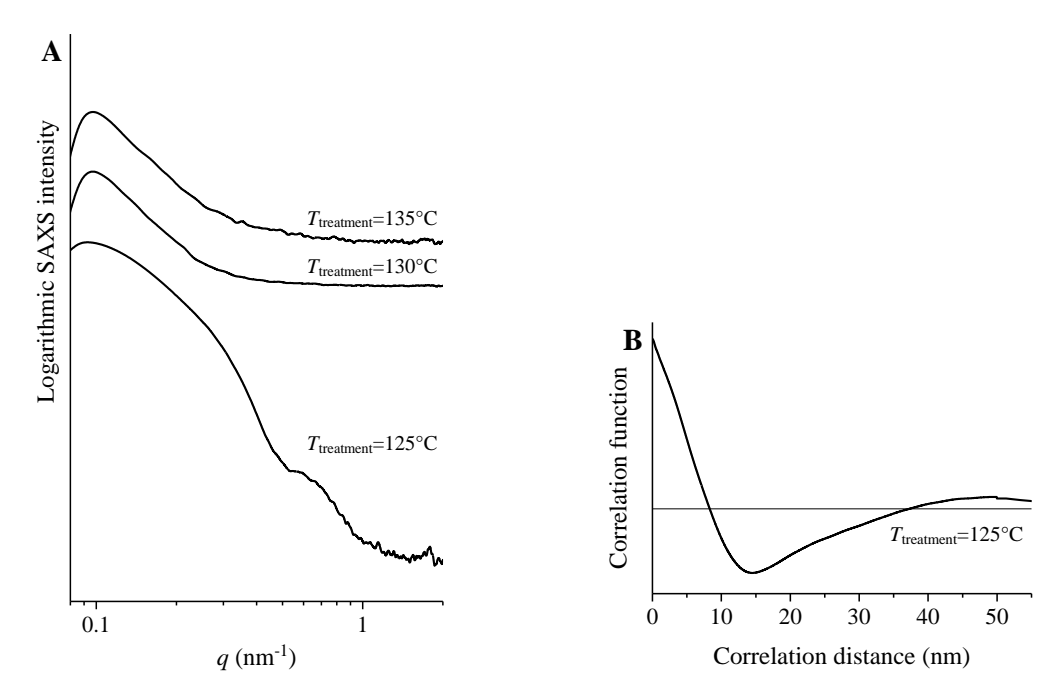


Figure A3 SAXS profiles (A) recorded at the indicated temperatures ($T_{treatment}$) and calculated mono-dimensional self-correlation function of electronic densities fluctuation (correlation function, CF) (B) of the sample L-C8.

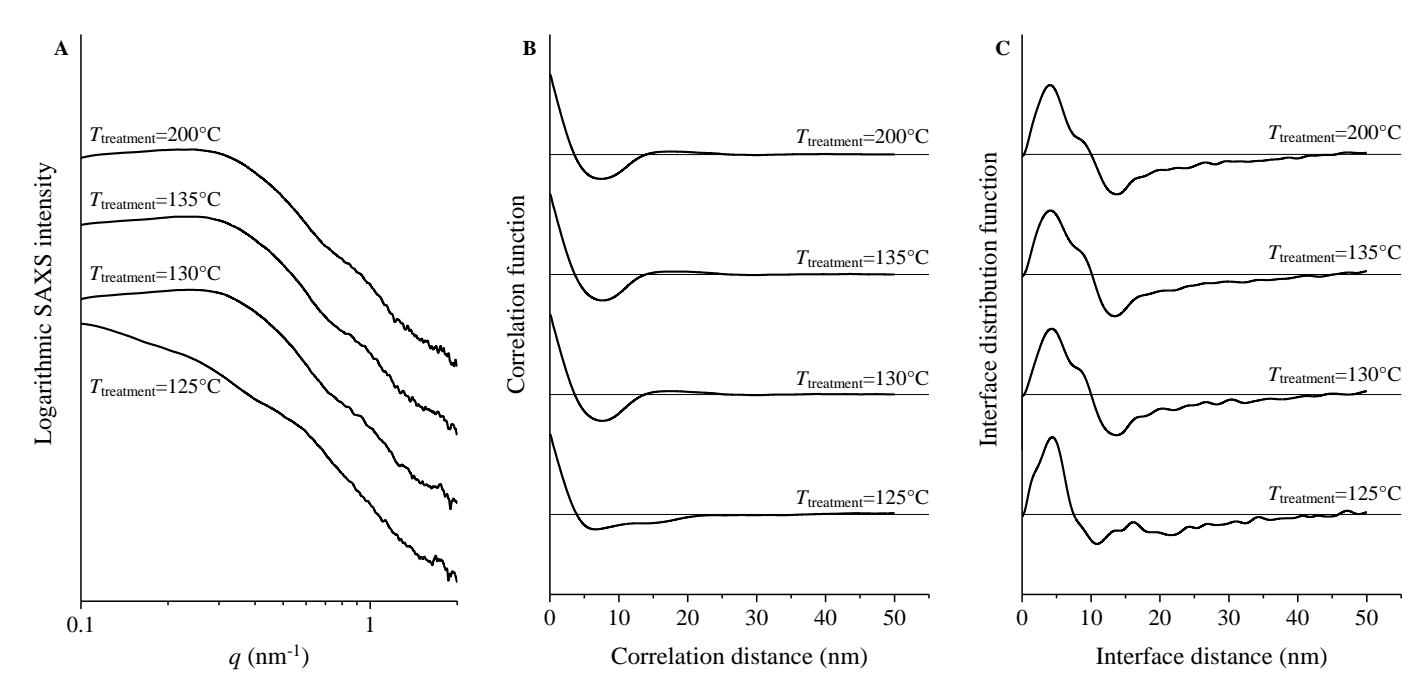


Figure A4 SAXS profiles (A) recorded at room temperature for heat treated specimens of the sample L-C8 for $t_{treatment} = 10$ min at the indicated temperatures ($T_{treatment}$), obtained by fast cooling (40 °C/min) to room temperature, calculated mono-dimensional self-correlation function of electronic densities fluctuation (correlation function, (CF) (B) and Interface distribution function IDF (C).

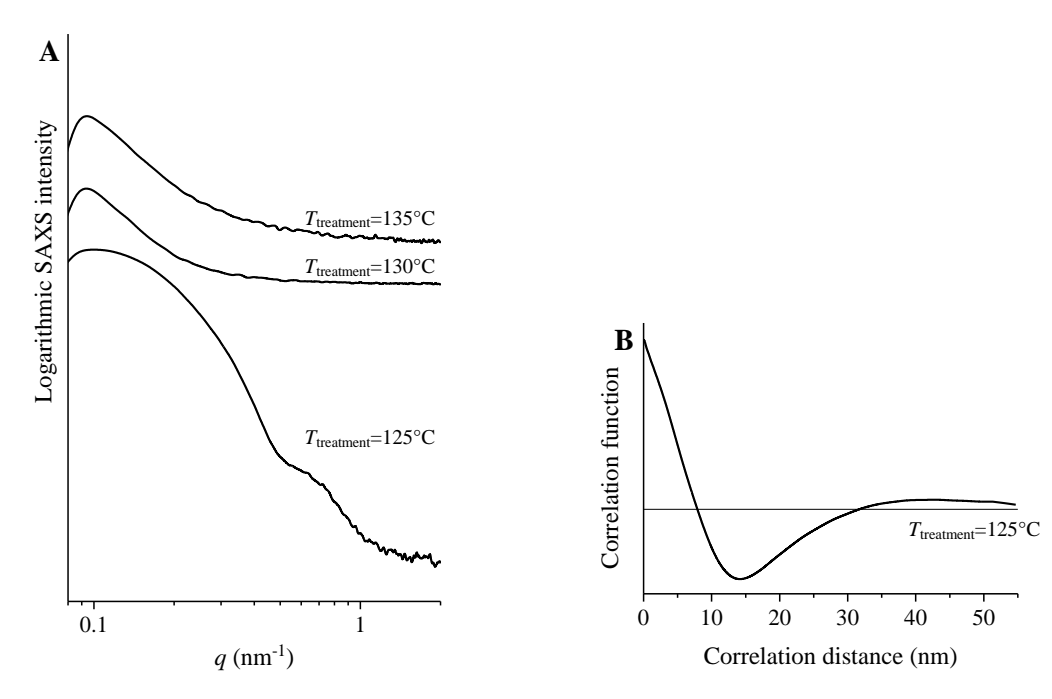


Figure A5 SAXS profiles (A) recorded at the indicated temperatures ($T_{treatment}$) and calculated mono-dimensional self-correlation function of electronic densities fluctuation (correlation function, CF) (B) of the blend 50L-50H.

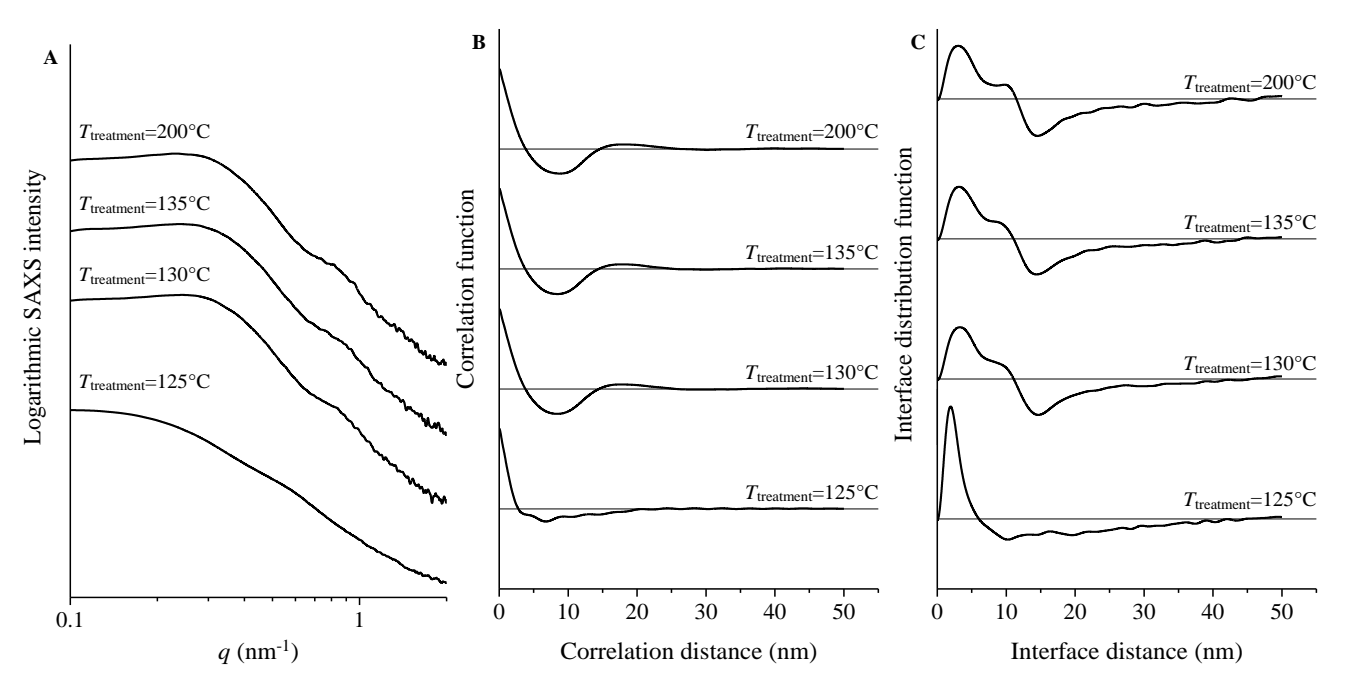


Figure A6 SAXS profiles (A) recorded at room temperature for heat treated specimens of the sample blend 50L-50H for $t_{treatment} = 10$ min at the indicated temperatures ($T_{treatment}$), obtained by fast cooling (40 °C/min) to room temperature, calculated mono-dimensional self-correlation function of electronic densities fluctuation (correlation function, (CF) (B) and Interface distribution function IDF (C).

Structural analysis after fast cooling from selected $T_{\text{treatment}}$ for different times

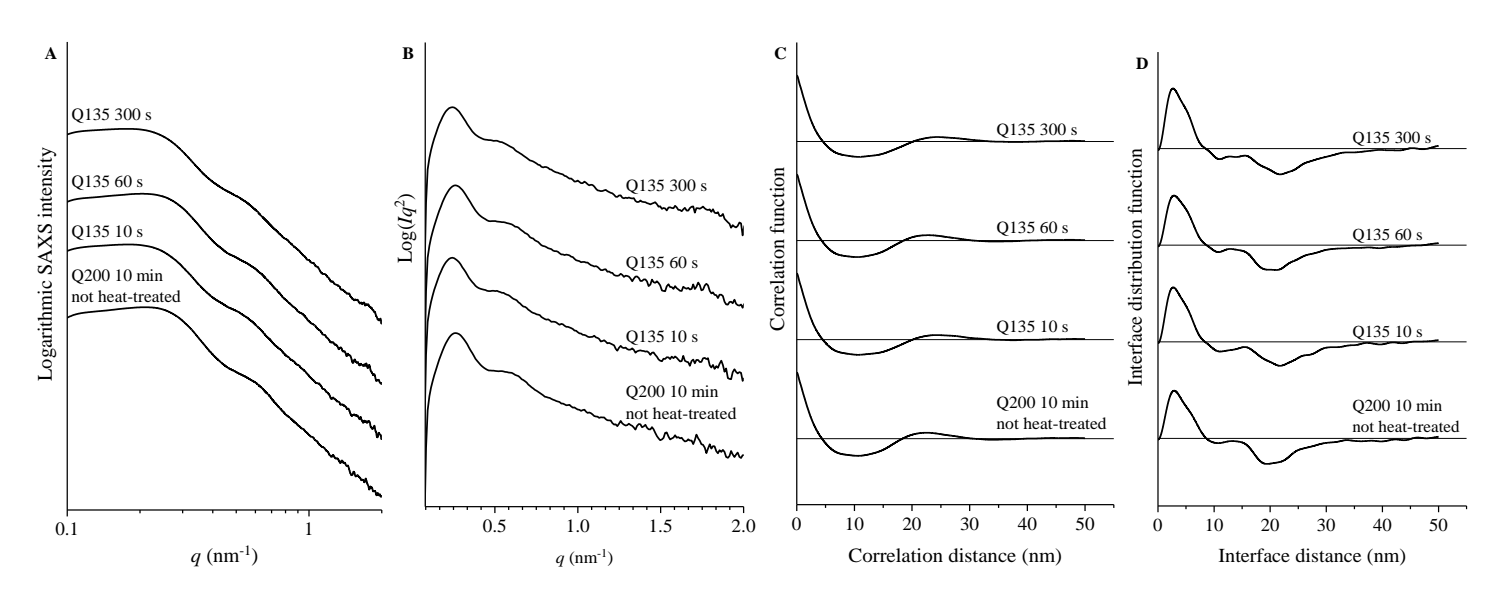


Figure A7 SAXS intensity profiles before (A) and after (B) correction for the Lorentz factor, Self-correlation function of electronic densities fluctuation CF (C) and Interface distribution function IDF (D) of the sample H-C4 obtained after fast cooling from $200^{\circ}C$ C and then heat treated at $T_{treatment}=135^{\circ}C$ for different times.

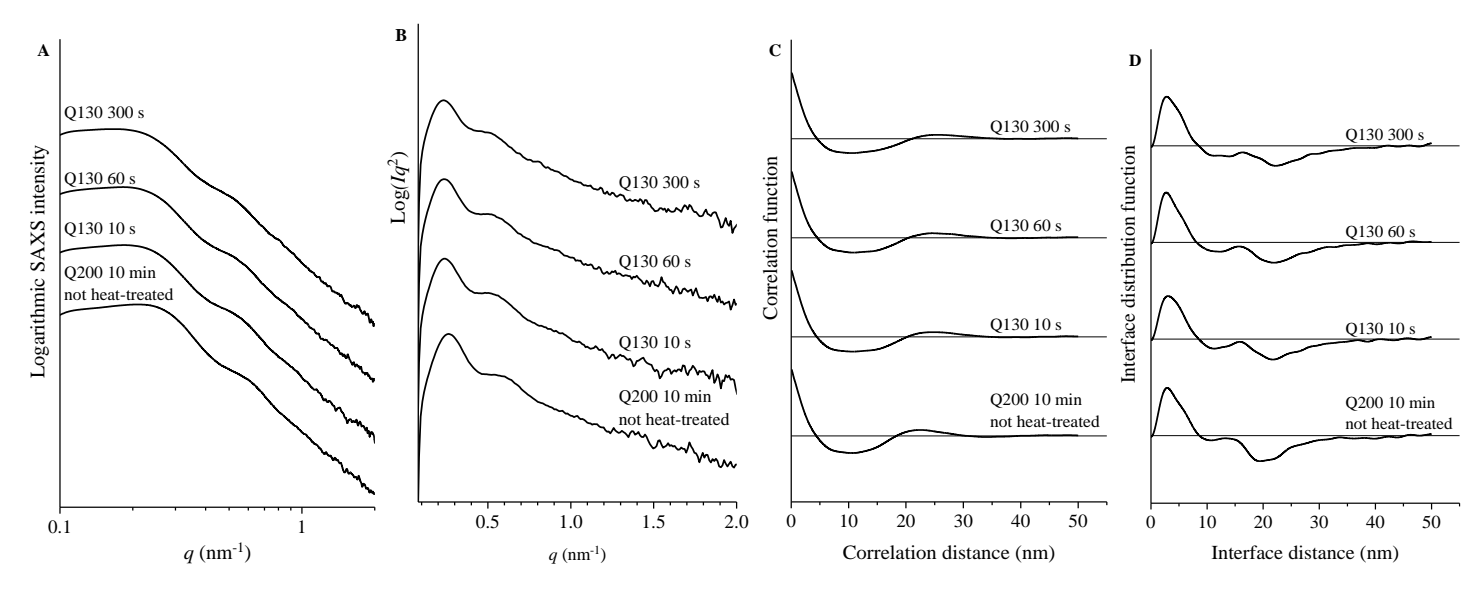


Figure A8 SAXS intensity profiles before (A) and after (B) correction for the Lorentz factor, Self-correlation function of electronic densities fluctuation CF(C) and Interface distribution function IDF(D) of the sample H-C4 obtained after fast cooling from $200^{\circ}C$ and then heat treated at $T_{treatment}=130^{\circ}C$ for different times.

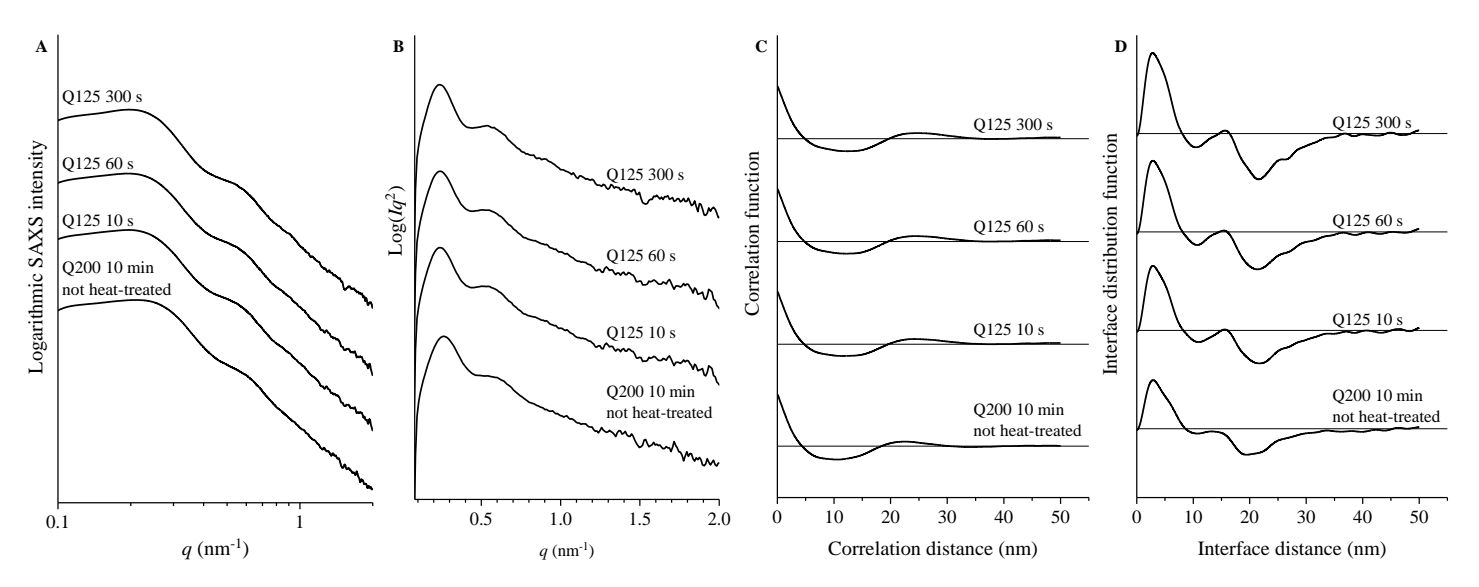


Figure A9 SAXS intensity profiles before (A) and after (B) correction for the Lorentz factor, Self-correlation function of electronic densities fluctuation CF (C) and Interface distribution function IDF (D) of the sample H-C4 obtained after fast cooling from 200°C C and then heat treated at $T_{treatment}=125$ °C for different times.

Table A1 Values of the lamellar periodicity (L) and thickness of amorphous (la) and crystalline (lc) layers of lamellar stacks of the sample H-C4, deduced from SAXS data (Figure A7A,B-A9A,B) through direct application of Bragg's law, the calculation of the self-correlation function of electron density fluctuations (correlation function, CF) and the interface distribution function (IDF).

| | | | | BRA | AGG | | | CF | | | IDF | | | | | |
|--------------------|------------------------------------|----------------------------|------------------------------------|---------------------|--------|-----------------------|---------------------|---------------------|--------|---------------------|---------------------|-------------------|-----------|---------------------|------------|--------------------------|
| t treatment | q ₁ (nm ⁻¹) | <i>L</i> ₁ (nm) | q ₂ (nm ⁻¹) | L ₂ (nm) | (WAXS) | Φ _c (%) | l _c (nm) | l _a (nm) | L (nm) | l _c (nm) | l _a (nm) | <i>l√L</i> (-) | L (nm) | l _c (nm) | la (nm) | l _c /L (-) |
| 600s at 200°C | 0.264 | 23.8 | 0.532 | 23.6 | 0.66 | 0.62 | 14.8 | 9.0 | 22.6 | 18.3 | 4.3 | 0.76 | 19.4 | 16.6 | 2.9 | 0.85 |
| 10s at 135°C | 0.244 | 25.7 | 0.513 | 24.5 | 0.67 | 0.63 | 16.3 | 9.4 | 24.1 | 19.9 | 4.2 | 0.83 | 21.8 | 19.1 | 2.7 | 0.88 |
| 60s at 135°C | 0.263 | 23.9 | 0.524 | 24.0 | 0.66 | 0.62 | 14.9 | 9.0 | 22.8 | 18.5 | 4.3 | 0.81 | 20.0 | 17.1 | 2.9 | 0.86 |
| 300s at 135°C | 0.244 | 25.7 | 0.512 | 24.5 | 0.66 | 0.62 | 16.0 | 9.7 | 24.5 | 20.1 | 4.3 | 0.82 | 21.8 | 19.1 | 2.7 | 0.88 |
| 10s at 130°C | 0.234 | 26.8 | 0.483 | 26.0 | 0.67 | 0.63 | 17.0 | 9.8 | 24.7 | 20.4 | 4.3 | 0.83 | 21.7 | 18.7 | 3.0 | 0.86 |
| 60s at 130°C | 0.234 | 26.8 | 0.493 | 25.5 | 0.67 | 0.63 | 17.0 | 9.8 | 24.6 | 20.4 | 4.2 | 0.83 | 21.9 | 19.2 | 2.7 | 0.87 |
| 300s at 130°C | 0.234 | 26.8 | 0.478 | 26.3 | 0.67 | 0.63 | 17.0 | 9.8 | 25.3 | 21.0 | 4.3 | 083 | 22.2 | 19.4 | 2.8 | 0.87 |
| 10s at 125°C | 0.244 | 25.7 | 0.522 | 24.1 | 0.65 | 0.61 | 15.7 | 10.0 | 24.1 | 19.7 | 4.4 | 0.82 | 21.7 | 18.9 | 2.8 | 0.87 |
| 60s at 125°C | 0.240 | 26.2 | 0.522 | 24.1 | 0.65 | 0.61 | 16.0 | 10.2 | 24.5 | 20.0 | 4.5 | 0.82 | 21.4 | 18.5 | 2.9 | 0.87 |
| 300s at 125°C | 0.234 | 26.8 | 0.532 | 23.6 | 0.63 | 0.59 | 15.9 | 10.9 | 24.6 | 20.0 | 4.6 | 0.81 | 21.6 | 18.8 | 2.8 | 0.87 |

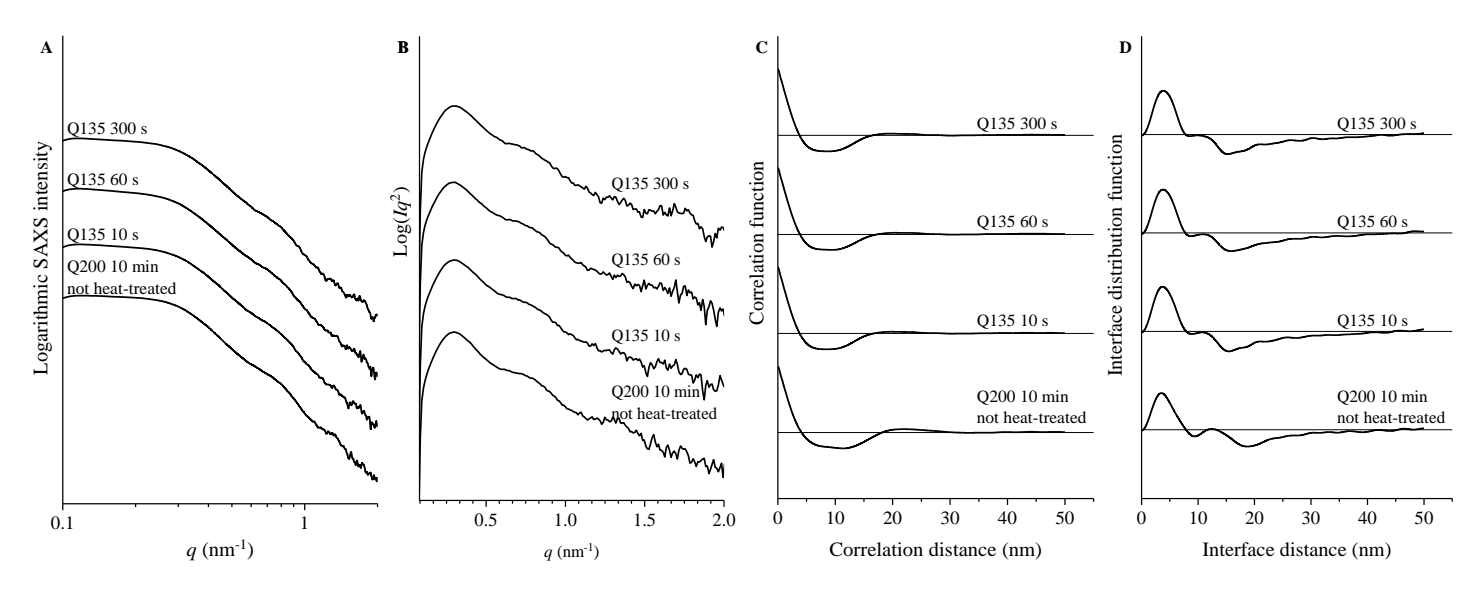


Figure A10 SAXS intensity profiles before (A) and after (B) correction for the Lorentz factor, Self-correlation function of electronic densities fluctuation CF (C) and Interface distribution function IDF (D) of the sample L-C8 obtained after fast cooling from 200°C C and then heat treated at $T_{treatment}=135$ °C for different times.

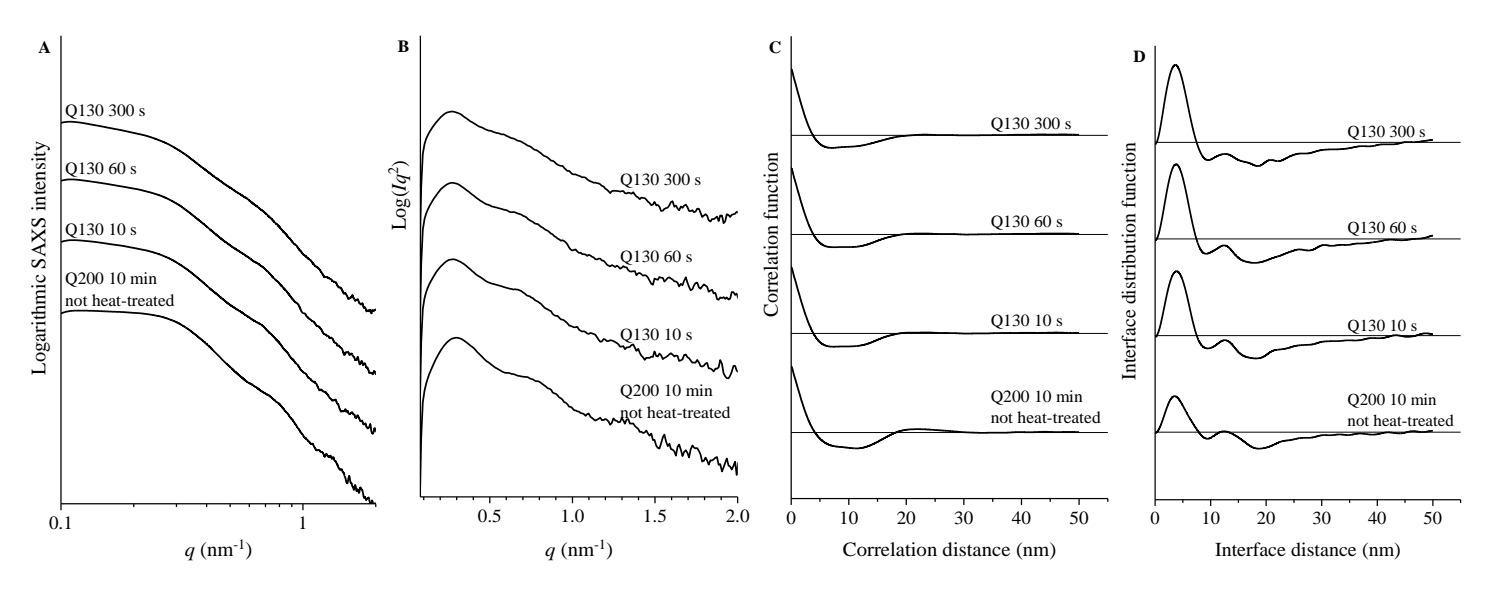


Figure A11 SAXS intensity profiles before (A) and after (B) correction for the Lorentz factor, Self-correlation function of electronic densities fluctuation CF (C) and Interface distribution function IDF (D) of the sample L-C8 obtained after fast cooling from 200°C C and then heat treated at $T_{treatment}$ =130°C for different times.

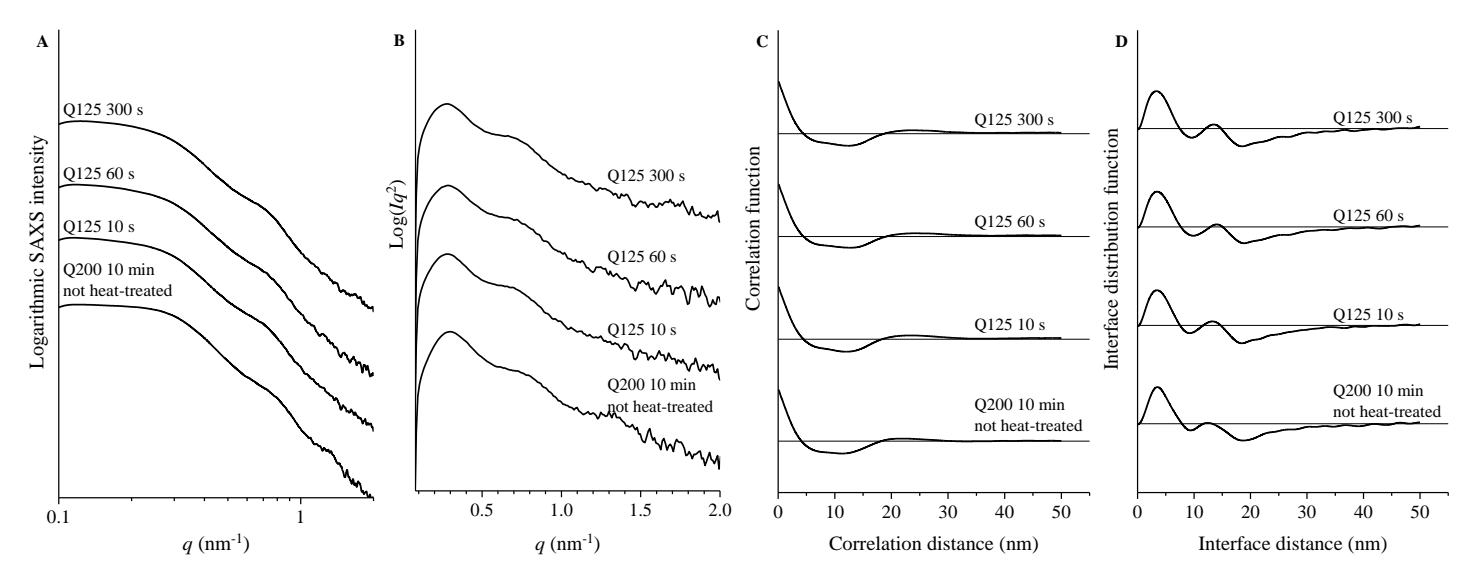


Figure A12 SAXS intensity profiles before (A) and after (B) correction for the Lorentz factor, Self-correlation function of electronic densities fluctuation CF (C) and Interface distribution function IDF (D) of the sample L-C8 obtained after fast cooling from 200°C C and then heat treated at T_{treatment}=125°C for different times.

Table A2 Values of the lamellar periodicity (L) and thickness of amorphous (la) and crystalline (lc) layers of lamellar stacks of the sample L-C8, deduced from SAXS data (Figure A10A,B-A12A,B) through direct application of Bragg's law, the calculation of the self-correlation function of electron density fluctuations (correlation function, CF) and the interface distribution function (IDF).

| | | | | C | CF | | IDF | | | | | | | | | |
|--------------------|------------------------------------|----------------------------|---------------------------|----------------------------|--------------|-----------------------|--------------------|------------|-----------|--------------------|------------|-------------|-----------|--------------------|------------------------|--------------------------|
| <i>t</i> treatment | q ₁ (nm ⁻¹) | <i>L</i> ₁ (nm) | q_2 (nm ⁻¹) | <i>L</i> ₂ (nm) | xc (WAXS) | Φ _c (%) | <i>l</i> c (nm) | la (nm) | L (nm) | <i>l</i> c (nm) | la (nm) | lc/L (-) | L (nm) | <i>l</i> c (nm) | l _a (nm) | l _c /L (-) |
| 600s at 200°C | 0.304 | 20.6 | 0.651 | 19.3 | 0.41 | 0.37 | 7.6 | 13.0 | 19.6 | 15.4 | 4.1 | 0.79 | 15.5 | 11.9 | 3.6 | 0.76 |
| 10s at 135°C | 0.294 | 21.4 | 0.684 | 18.4 | 0.39 | 0.36 | 7.6 | 13.7 | 19.6 | 15.5 | 4.1 | 0.79 | 15.5 | 11.8 | 3.7 | 0.76 |
| 60s at 135°C | 0.304 | 20.6 | 0.652 | 19.3 | 0.44 | 0.40 | 8.3 | 12.3 | 20.3 | 16.5 | 4.1 | 0.80 | 15.9 | 12.1 | 3.8 | 0.76 |
| 300s at 135°C | 0.304 | 20.6 | 0.642 | 19.6 | 0.40 | 0.36 | 7.5 | 13.1 | 19.6 | 15.4 | 4.2 | 0.79 | 15.3 | 11.4 | 3.9 | 0.75 |
| 10s at 130°C | 0.283 | 22.2 | 0.671 | 18.7 | 0.42 | 0.38 | 8.5 | 13.7 | 23.4 | 19.4 | 4.0 | 0.83 | 18.2 | 14.3 | 3.9 | 0.79 |
| 60s at 130°C | 0.273 | 23.0 | 0.653 | 19.2 | 0.41 | 0.37 | 8.5 | 14.5 | 22.8 | 18.8 | 4.0 | 0.83 | 17.9 | 14.1 | 3.8 | 0.79 |
| 300s at 130°C | 0.274 | 22.9 | / | / | 0.40 | 0.36 | 8.3 | 14.6 | 23.3 | 19.4 | 3.9 | 0.83 | 18.5 | 14.8 | 3.7 | 0.80 |
| 10s at 125°C | 0.284 | 22.1 | 0.692 | 18.2 | 0.42 | 0.38 | 8.4 | 13.7 | 22.2 | 18.1 | 4.1 | 0.82 | 17.1 | 13.2 | 3.9 | 0.77 |
| 60s at 125°C | 0.284 | 22.1 | 0.721 | 17.4 | 0.41 | 0.37 | 8.3 | 13.8 | 23.5 | 19.4 | 4.1 | 0.83 | 16.8 | 12.9 | 3.9 | 0.77 |
| 300s at 125°C | 0.278 | 22.6 | 0.662 | 18.9 | 0.41 | 0.37 | 8.4 | 14.2 | 23.4 | 19.2 | 4.2 | 0.82 | 17.2 | 13.3 | 3.9 | 0.77 |

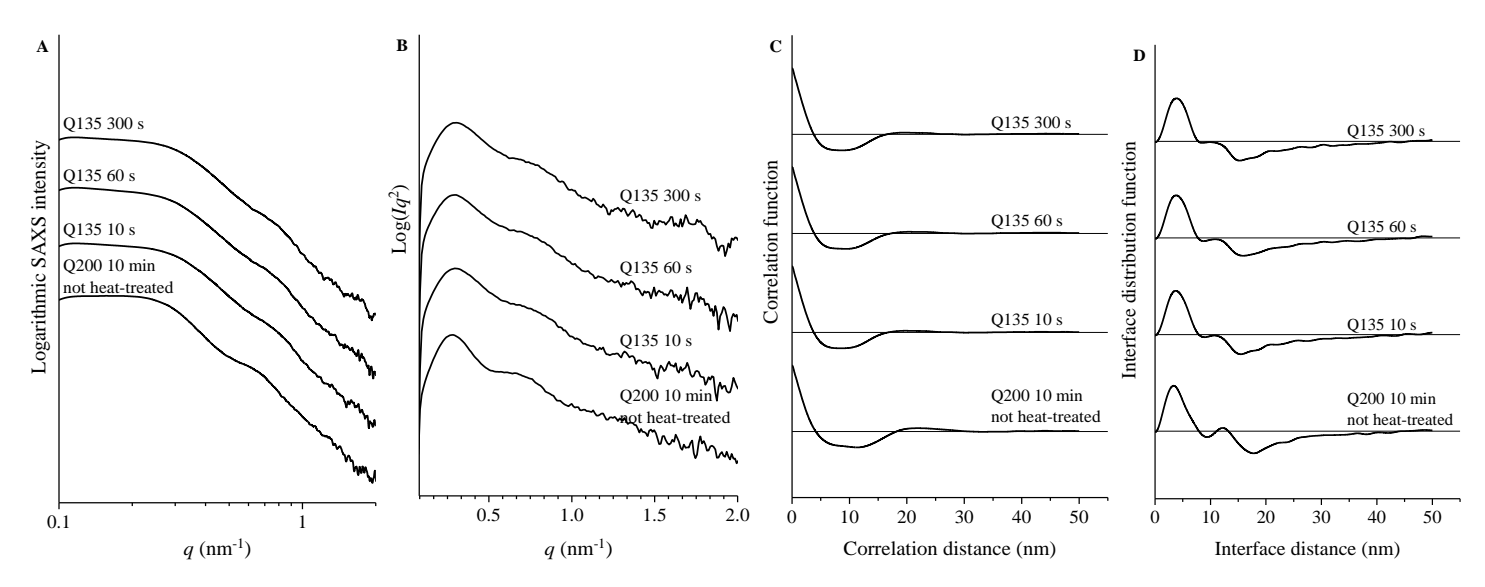


Figure A13 SAXS intensity profiles before (A) and after (B) correction for the Lorentz factor, Self-correlation function of electronic densities fluctuation CF (C) and Interface distribution function IDF (D) of the blend 50L-50H obtained after fast cooling from 200°C and C and then heat treated at $T_{treatment}$ =135°C for different times.

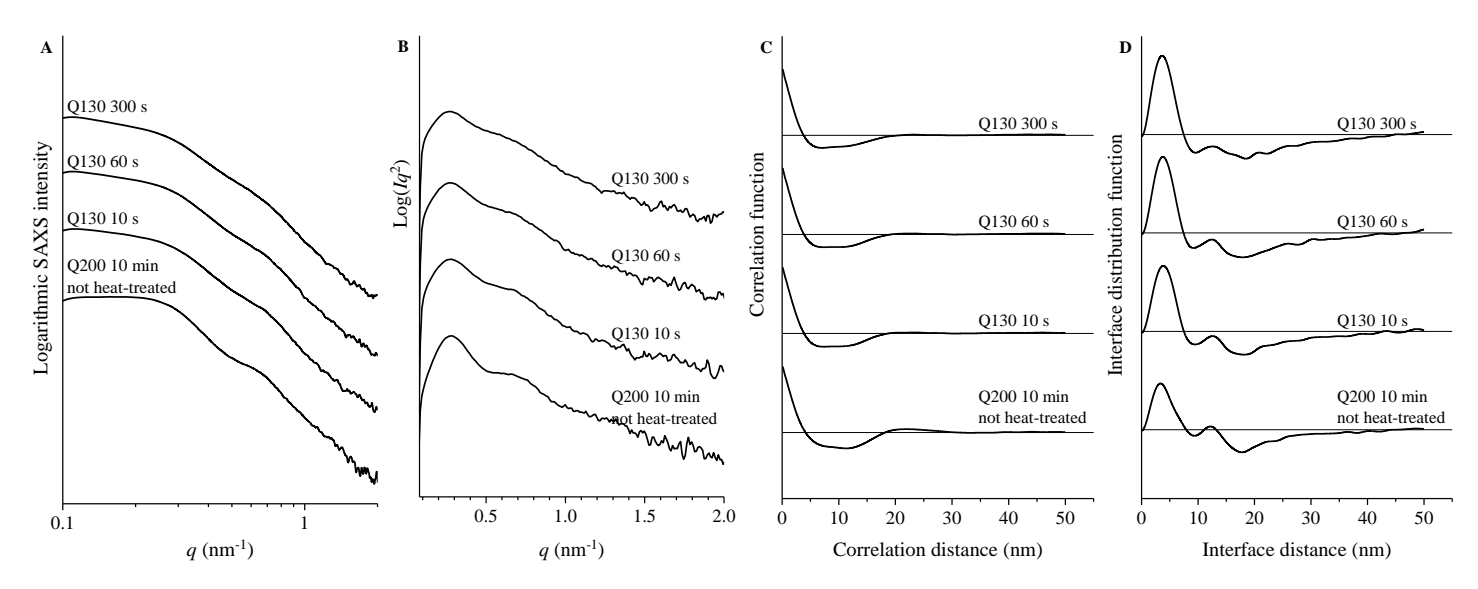


Figure A14 SAXS intensity profiles before (A) and after (B) correction for the Lorentz factor, Self-correlation function of electronic densities fluctuation CF (C) and Interface distribution function IDF (D) of the blend 50L-50H obtained after fast cooling from 200°C and then heat treated at T_{treatment}=130°C for different times.

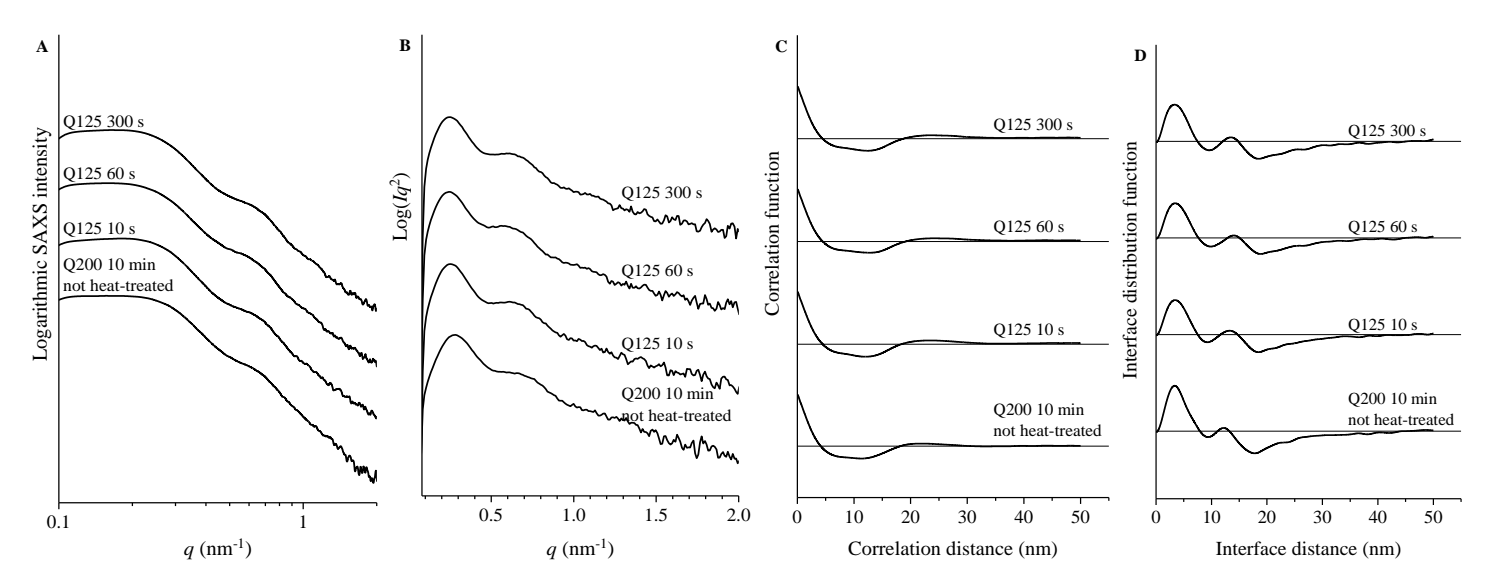


Figure A15 SAXS intensity profiles before (A) and after (B) correction for the Lorentz factor, Self-correlation function of electronic densities fluctuation CF (C) and Interface distribution function IDF (D) of the blend 50L-50H obtained after fast cooling from 200°C and then heat treated at T_{treatment}=125°C for different times.

Table A3 Values of the lamellar periodicity (L) and thickness of amorphous (la) and crystalline (lc) layers of lamellar stacks of the blend 50L-50H, deduced from SAXS data (Figure A10A,B-A12A,B)through direct application of Bragg's law, the calculation of the self-correlation function of electron density fluctuations (correlation function, CF) and the interface distribution function (IDF).

| | | | | | (| CF | | IDF | | | | | | | | |
|------------------------|------------------------------------|----------------------------|------------------------------------|---------------------|--------------------------|-----------------------|---------------------|---------------------|--------|---------------------|---------------------|-------------|--------|---------------------|---------------------|--------------------------|
| t _{treatment} | q ₁ (nm ⁻¹) | <i>L</i> ₁ (nm) | q ₂ (nm ⁻¹) | L ₂ (nm) | x _c (WAXS) | Φ _c (%) | l _c (nm) | l _a (nm) | L (nm) | l _c (nm) | l _a (nm) | l₀/L (-) | L (nm) | l _c (nm) | l _a (nm) | l _c /L (-) |
| 600s at 200°C | 0.284 | 22.1 | 0.611 | 20.6 | 0.53 | 0.49 | 10.8 | 11.3 | 22.1 | 17.9 | 4.2 | 0.81 | 18.7 | 15.2 | 3.5 | 0.81 |
| 10s at 135°C | 0.294 | 21.4 | 0.689 | 18.2 | 0.50 | 0.46 | 9.9 | 11.4 | 22.1 | 17.9 | 4.2 | 0.81 | 15.5 | 11.7 | 3.8 | 0.76 |
| 60s at 135°C | 0.304 | 20.7 | 0.652 | 19.3 | 0.51 | 0.47 | 9.7 | 10.9 | 22.1 | 17.8 | 4.3 | 0.80 | 15.9 | 12.1 | 3.8 | 0.76 |
| 300s at 135°C | 0.304 | 20.7 | 0.642 | 19.6 | 0.51 | 0.47 | 9.8 | 10.8 | 22.2 | 17.8 | 4.4 | 0.80 | 15.3 | 11.5 | 3.8 | 0.75 |
| 10s at 130°C | 0.284 | 22.1 | 0.762 | 16.5 | 0.51 | 0.47 | 10.4 | 11.7 | 23.3 | 19.0 | 4.3 | 0.81 | 18.2 | 14.3 | 3.9 | 0.79 |
| 60s at 130°C | 0.274 | 22.9 | / | / | 0.51 | 0.47 | 10.9 | 12.0 | 22.8 | 18.7 | 4.1 | 0.82 | 17.9 | 14.1 | 3.8 | 0.79 |
| 300s at 130°C | 0.274 | 22.9 | / | / | 0.51 | 0.47 | 10.8 | 12.1 | 23.3 | 19.2 | 4.1 | 0.82 | 18.5 | 14.9 | 3.6 | 0.80 |
| 10s at 125°C | 0.254 | 24.7 | 0.612 | 20.5 | 0.51 | 0.47 | 11.7 | 13.0 | 23.4 | 19.0 | 4.4 | 0.81 | 18.5 | 15.0 | 3.5 | 0.81 |
| 60s at 125°C | 0.244 | 25.7 | 0.585 | 21.5 | 0.51 | 0.47 | 12.1 | 13.6 | 24.0 | 19.8 | 4.2 | 0.81 | 18.9 | 15.4 | 3.5 | 0.82 |
| 300s at 125°C | 0.247 | 25.4 | 0.612 | 20.5 | 0.51 | 0.47 | 12.0 | 13.4 | 23.5 | 19.1 | 4.4 | 0.81 | 18.5 | 15.2 | 3.3 | 0.82 |

Appendix A8

In-situ structural analysis at different $T_{\text{treatment}}$.

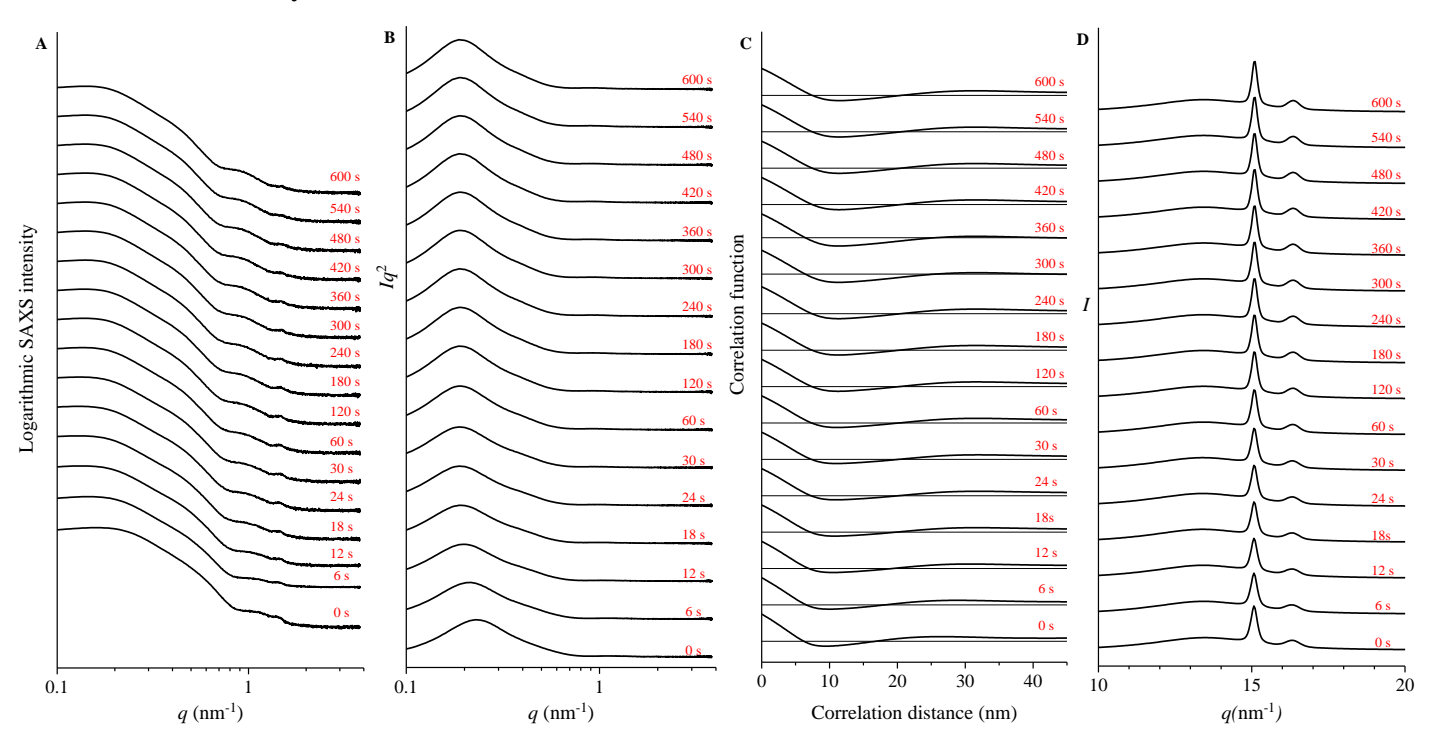


Figure A1 SAXS intensity profiles before (A) and after (B) correction for the Lorentz factor, mono-dimensional Self-correlation function of electronic densities fluctuation CF (C) and WAXS profiles (D) of the sample L-C8 obtained during 600 s of isothermal treatment at $T_{treatment}$ =120°C at the indicated times.

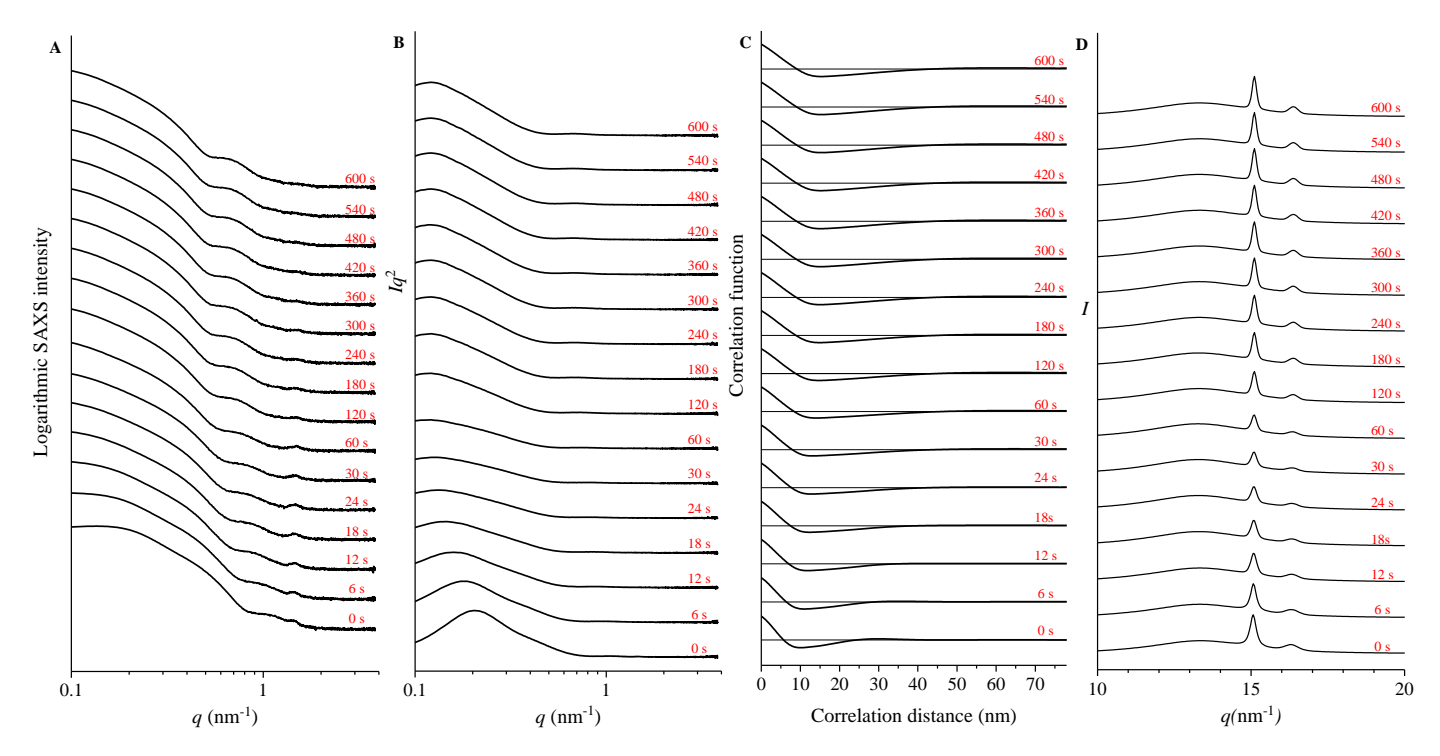


Figure A2 SAXS intensity profiles before (A) and after (B) correction for the Lorentz factor, mono-dimensional Self-correlation function of electronic densities fluctuation CF (C) and WAXS profiles (D) of the sample L-C8 obtained during 600 s of isothermal treatment at $T_{treatment}$ =125°C at the indicated times.

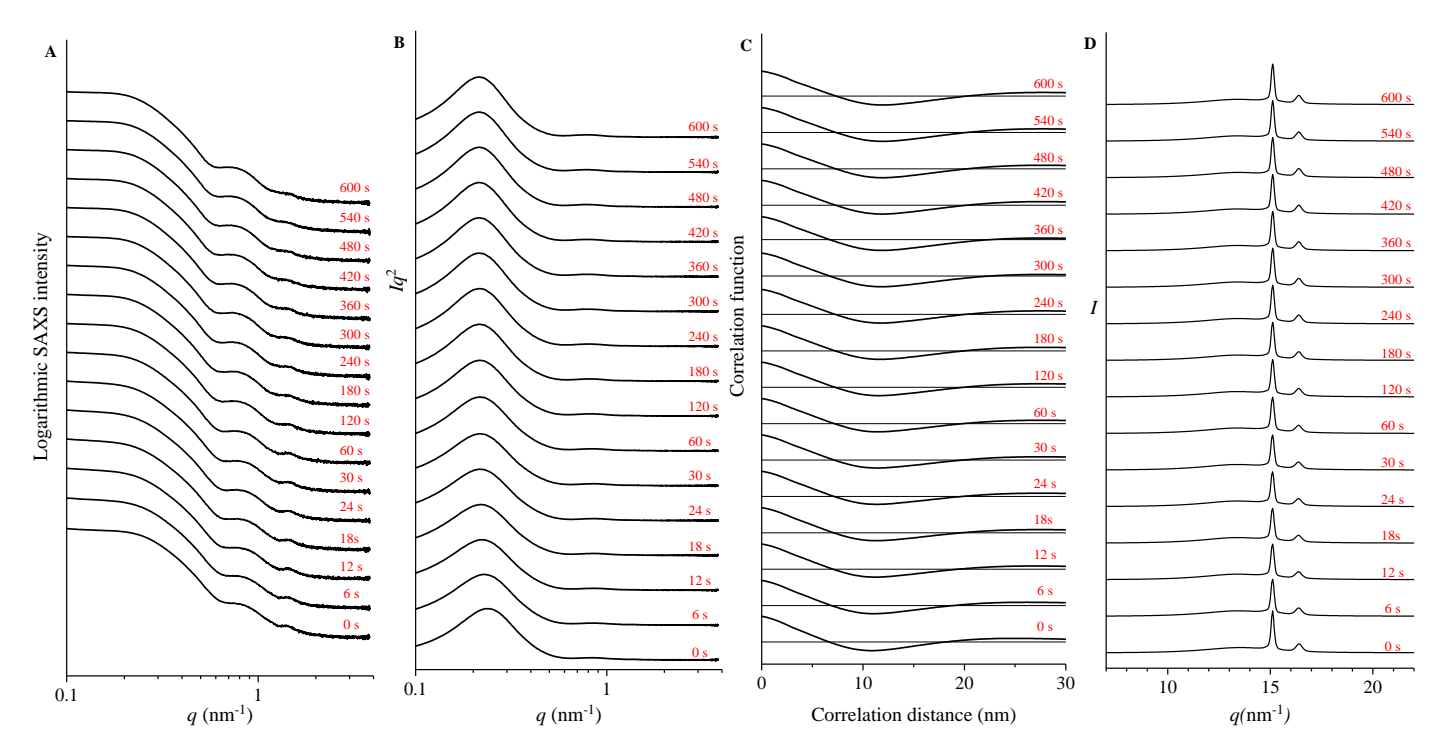


Figure A3 SAXS intensity profiles before (A) and after (B) correction for the Lorentz factor, mono-dimensional Self-correlation function of electronic densities fluctuation CF (C) and WAXS profiles (D) of the blend 50L-50H obtained during 600 s of isothermal treatment at $T_{treatment}$ =120°C at the indicated times.

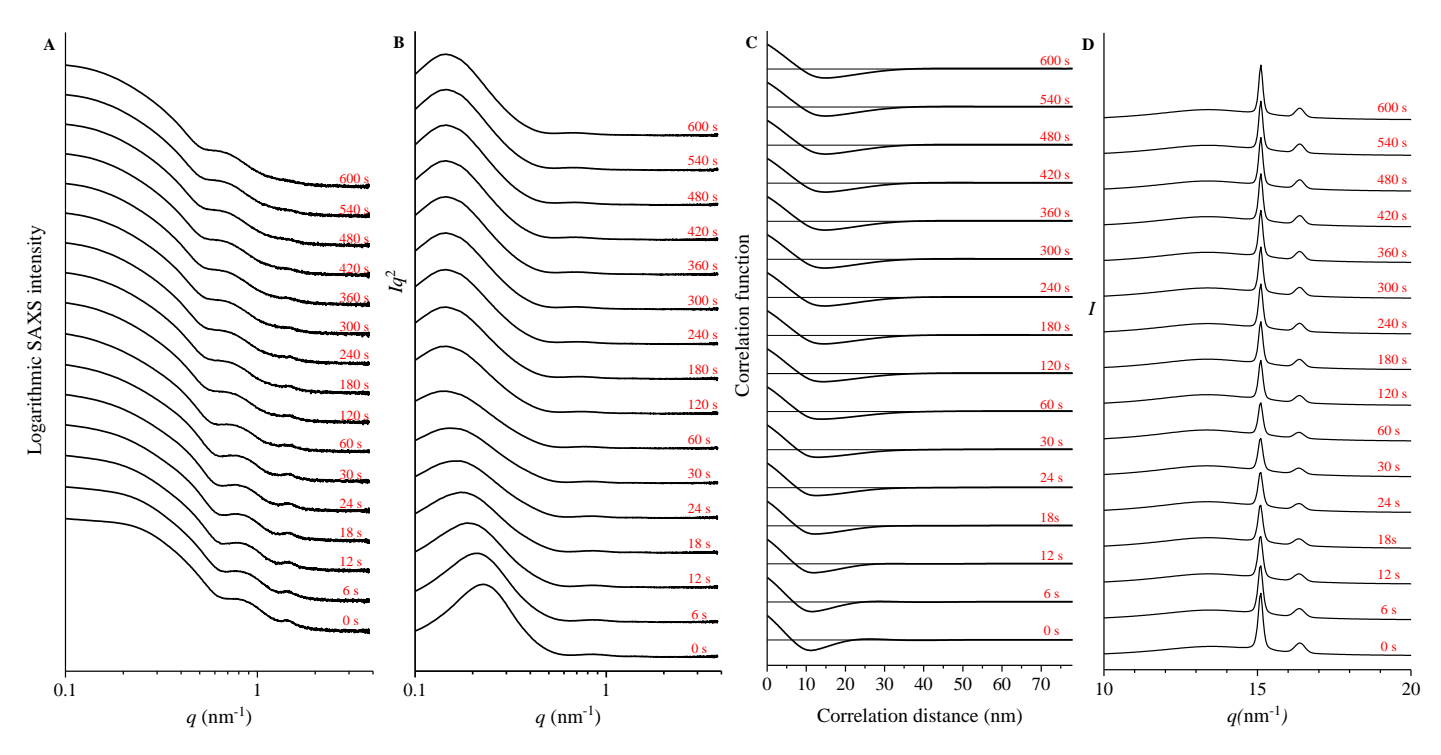


Figure A4 SAXS intensity profiles before (A) and after (B) correction for the Lorentz factor, mono-dimensional Self-correlation function of electronic densities fluctuation CF (C) and WAXS profiles (D) of the blend 50L-50H obtained during 600 s of isothermal treatment at $T_{treatment}$ =125°C at the indicated times.

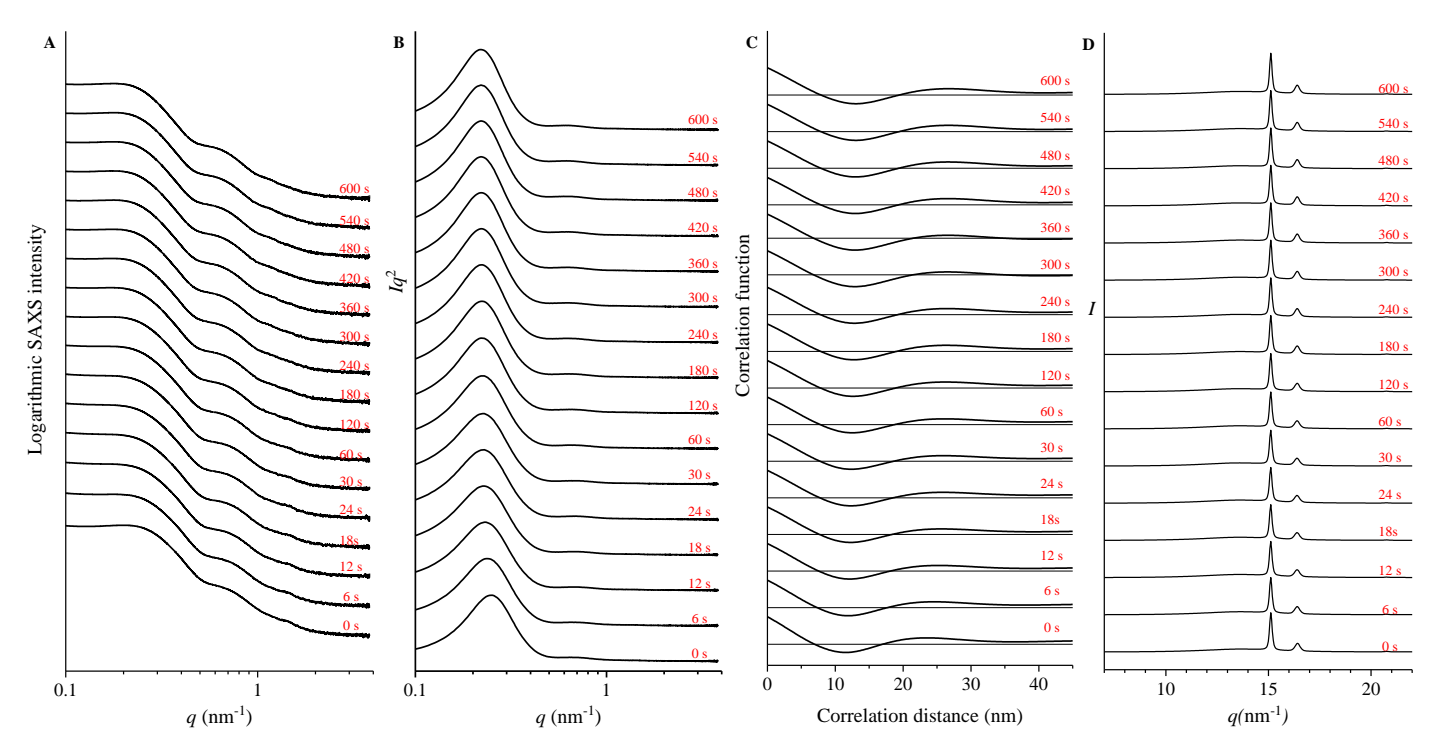


Figure A5 SAXS intensity profiles before (A) and after (B) correction for the Lorentz factor, mono-dimensional Self-correlation function of electronic densities fluctuation CF(C) and WAXS profiles (D) of the sample H-C4 obtained during 600 s of isothermal treatment at $T_{treatment}=120^{\circ}C$ at the indicated times.

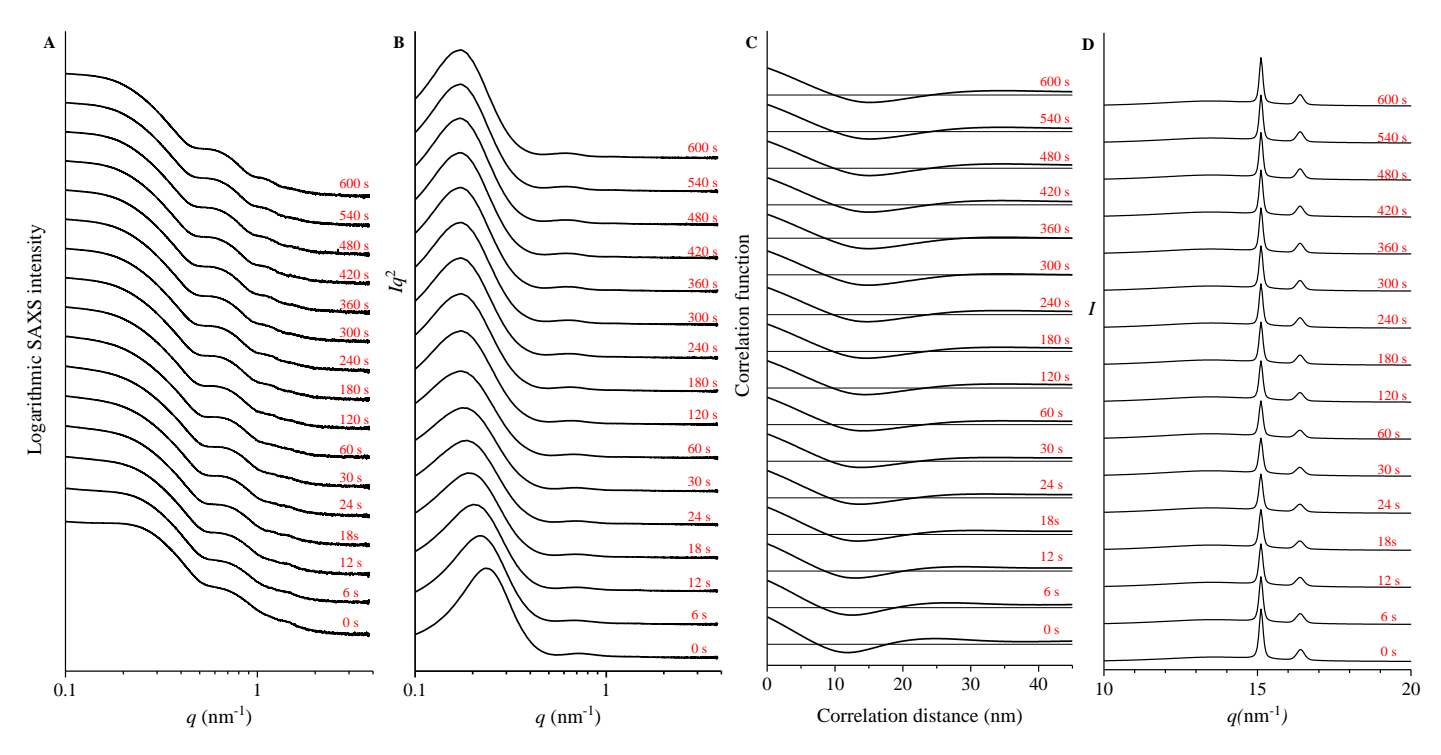


Figure A6 SAXS intensity profiles before (A) and after (B) correction for the Lorentz factor, mono-dimensional Self-correlation function of electronic densities fluctuation CF(C) and WAXS profiles (D) of the sample H-C4 obtained during 600 s of isothermal treatment at $T_{treatment}=125^{\circ}C$ at the indicated times.

Appendix A9

In-situ structural analysis during biaxial stretching in semi-solid state.

1D-SAXS/1D-WAXS profiles collected for the sample L-C8 during biaxial stretching until reaching rupture.

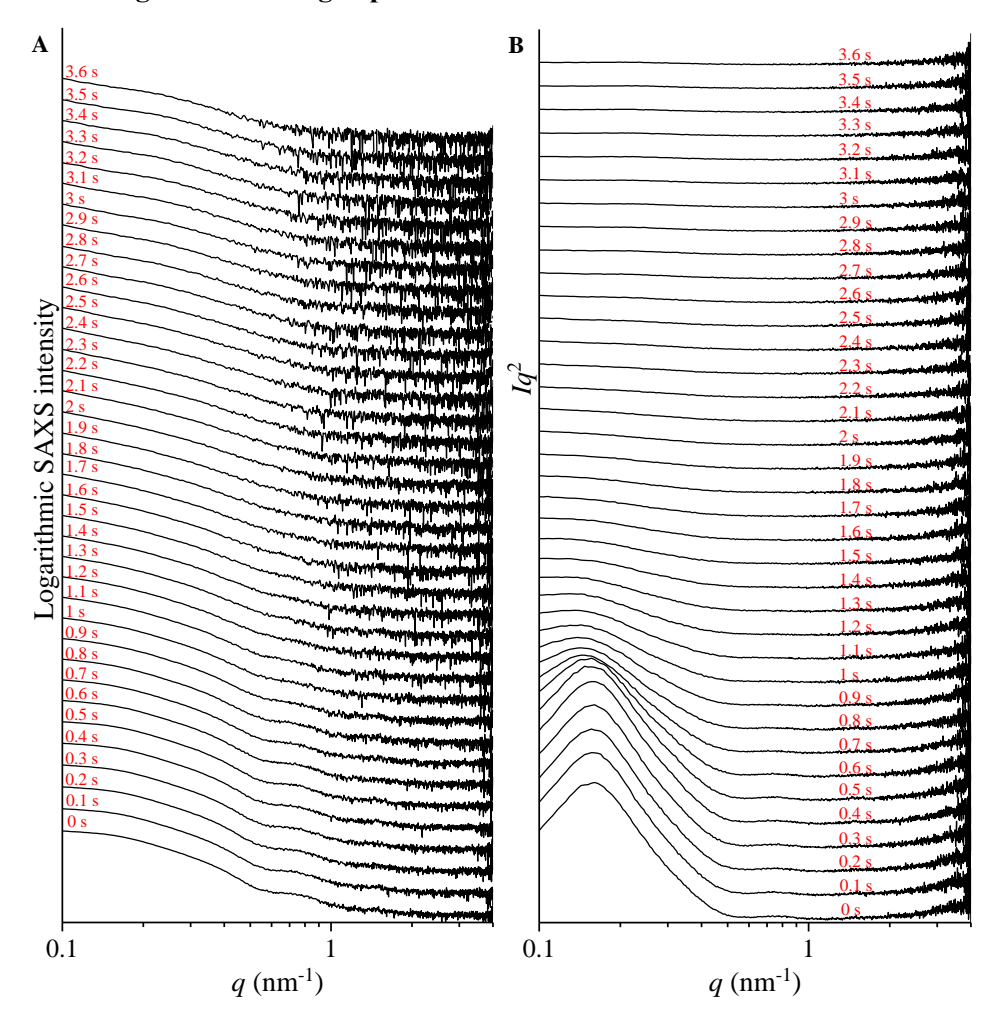


Figure A1 SAXS profiles before (A) and after (B) correction for the Lorentz's factor of sample L-C8 obtained during biaxial stretching until rupture at different times, at the $T_{tentering}$ =117°C.

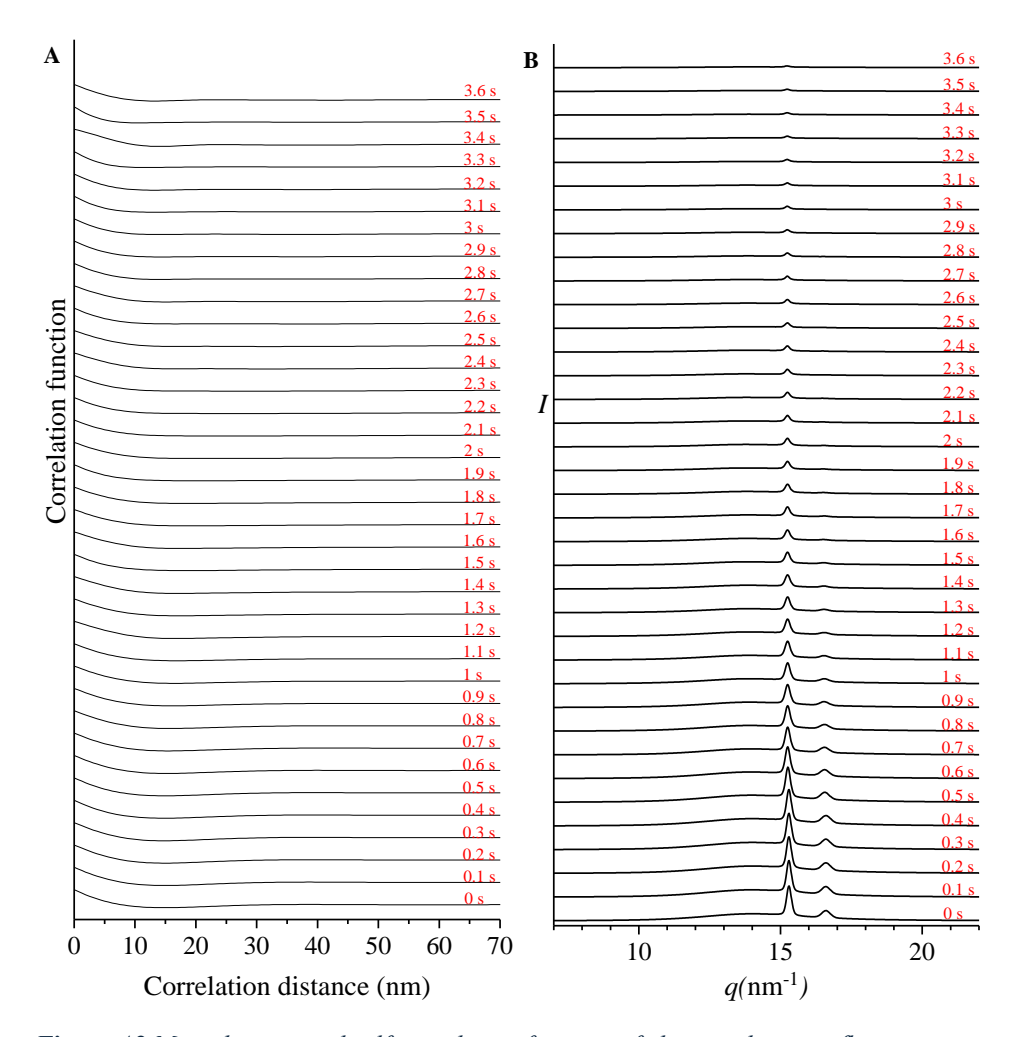
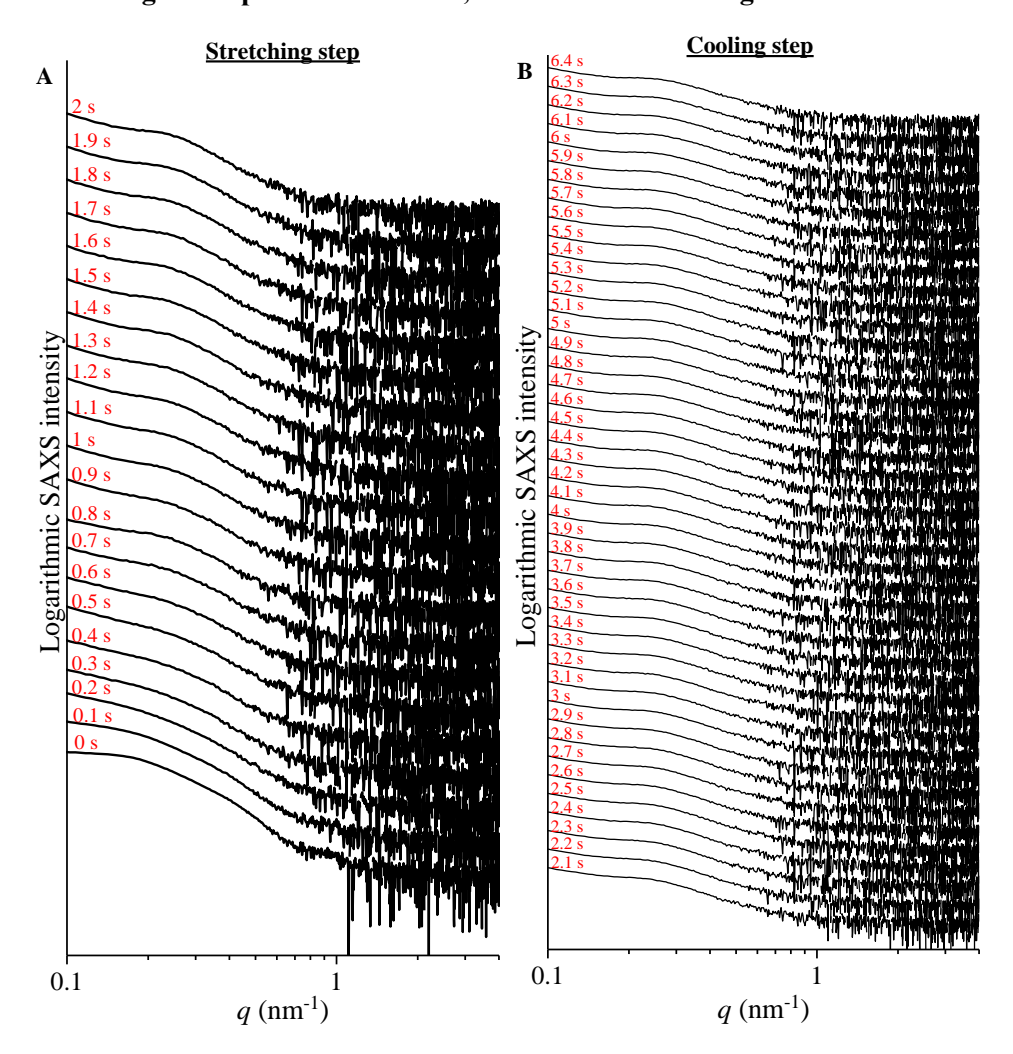


Figure A2 Monodimensional self-correlation function of electron densities fluctuation (correlation function, CF) (A) and WAXS profiles (B) of sample L-C8 obtained during biaxial stretching until rupture at different times, at the $T_{tentering}$ =117°C.

1D-SAXS/1D-WAXS profiles collected for the sample L-C8 during biaxial stretching until specific draw ratio, and successive cooling.



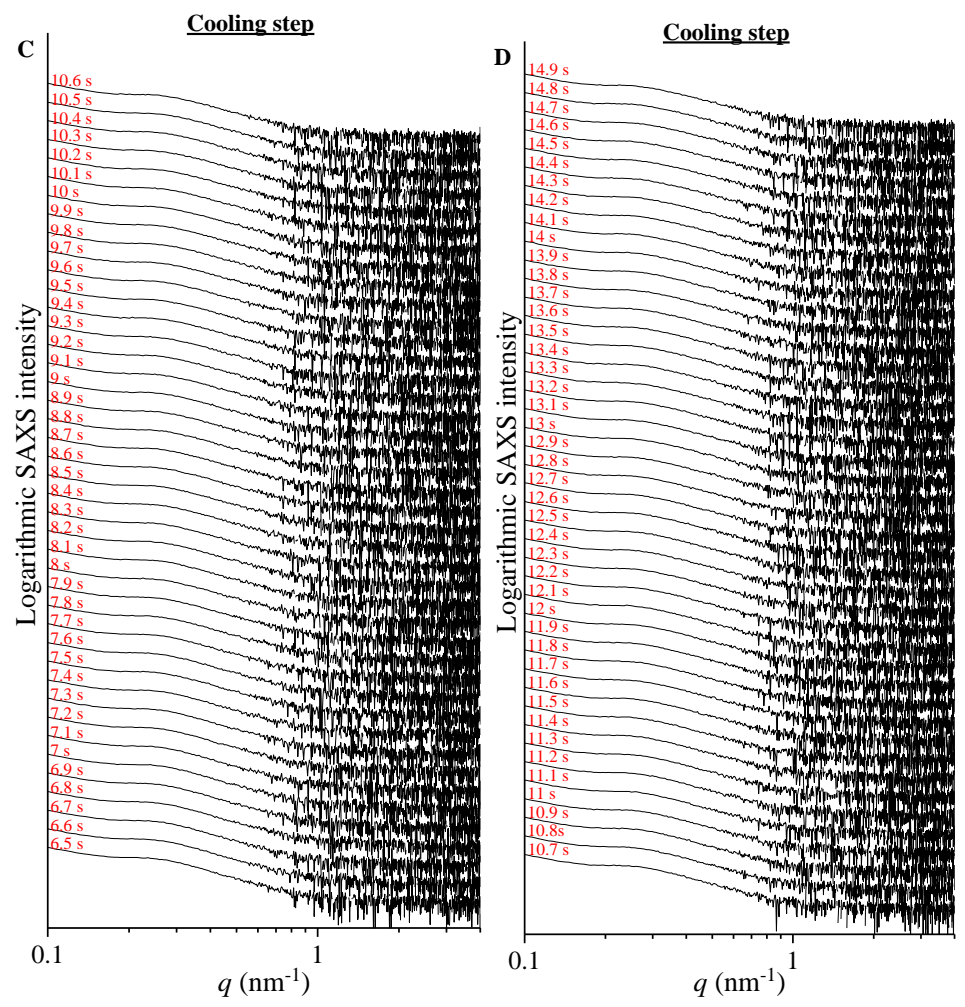
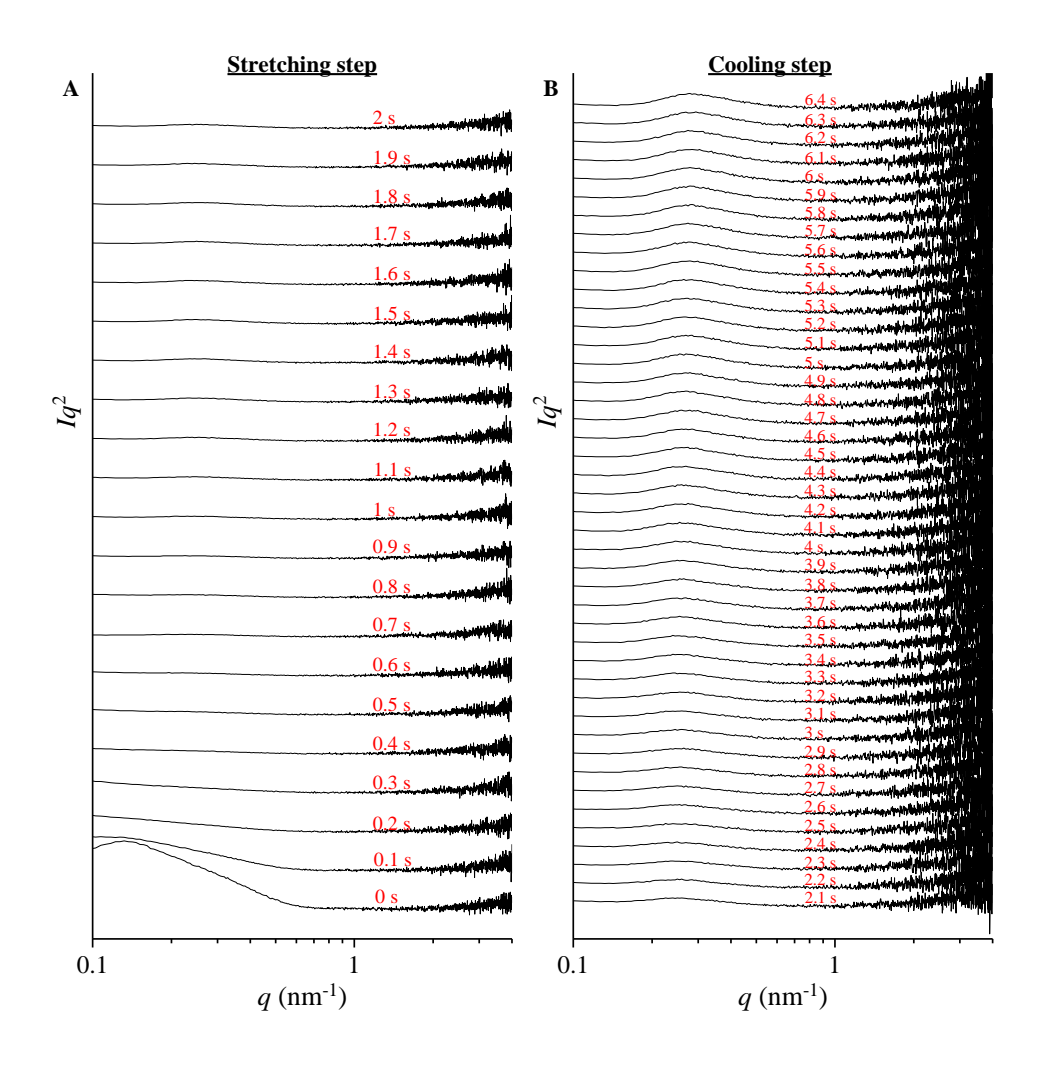


Figure A3 SAXS profiles of the sample L-C8 sample collected during biaxial stretching until reaching a draw ratio of 2x2, at the temperature $T_{tentering}$ =114°C (lapsed time 2 s) (A) and during cooling from $T_{tentering}$ (B-D). Data are collected every 0.1 s.



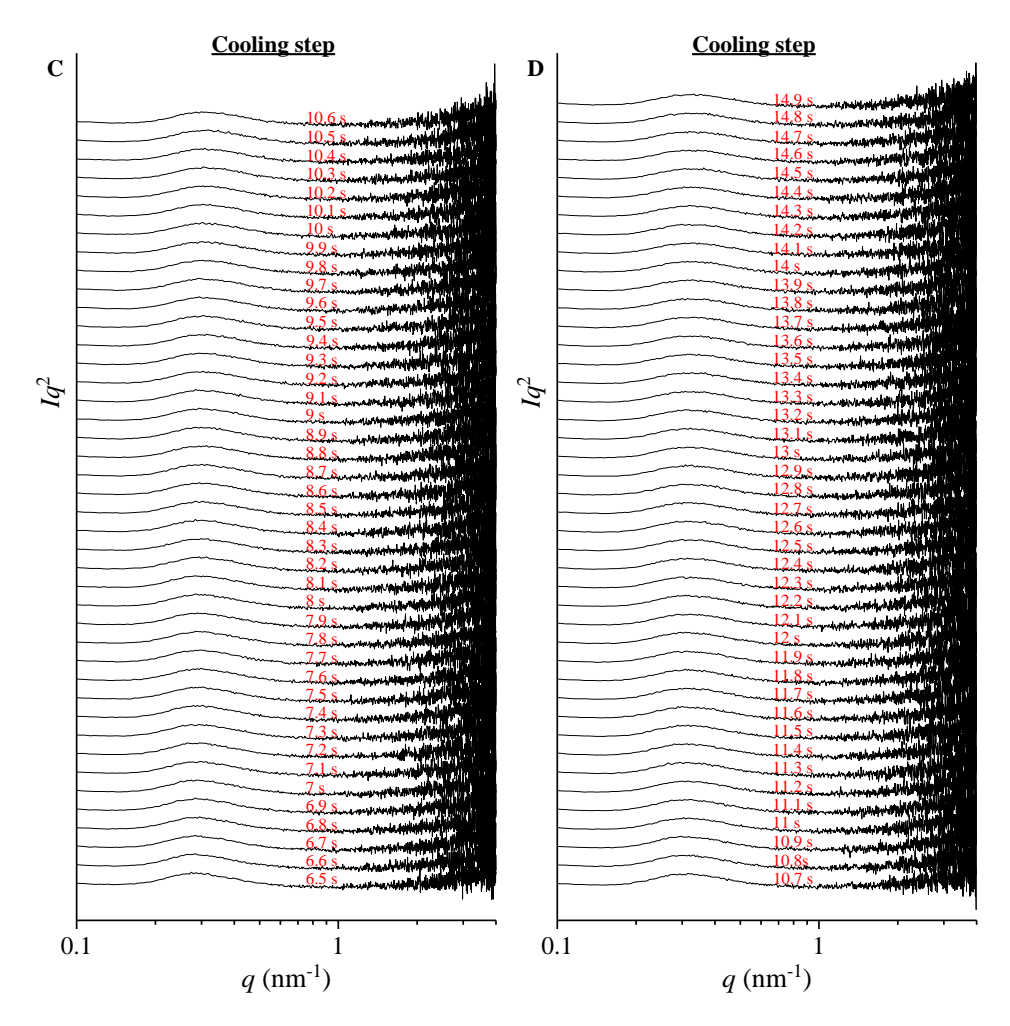
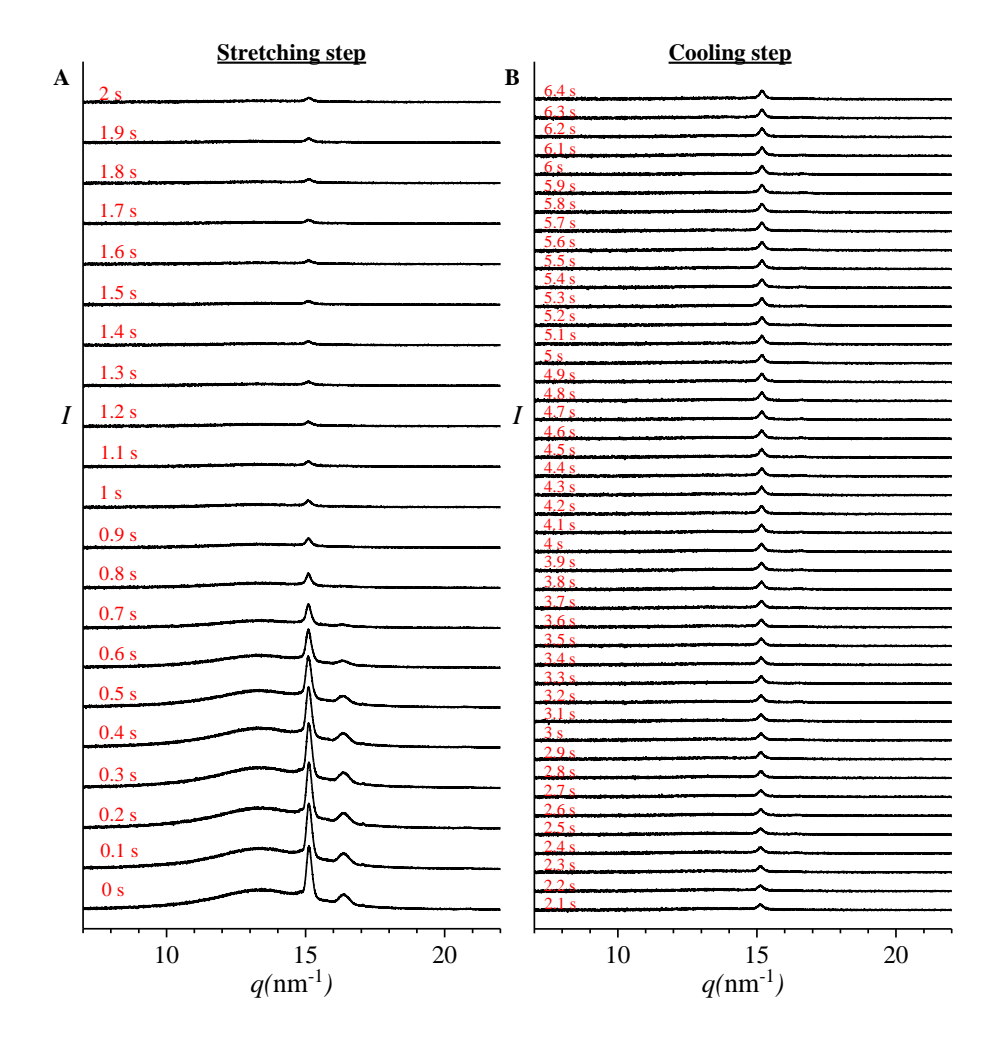


Figure A4 SAXS intensity profiles after correction for the Lorentz's factor collected for the sample L-C8 during biaxial stretching until reaching a draw ratio of 2x2, at the temperature $T_{tentering}$ =114°C (lapsed time 2 s) (A) and during successive cooling from $T_{tentering}$ (B-D). Data are collected every 0.1 s.



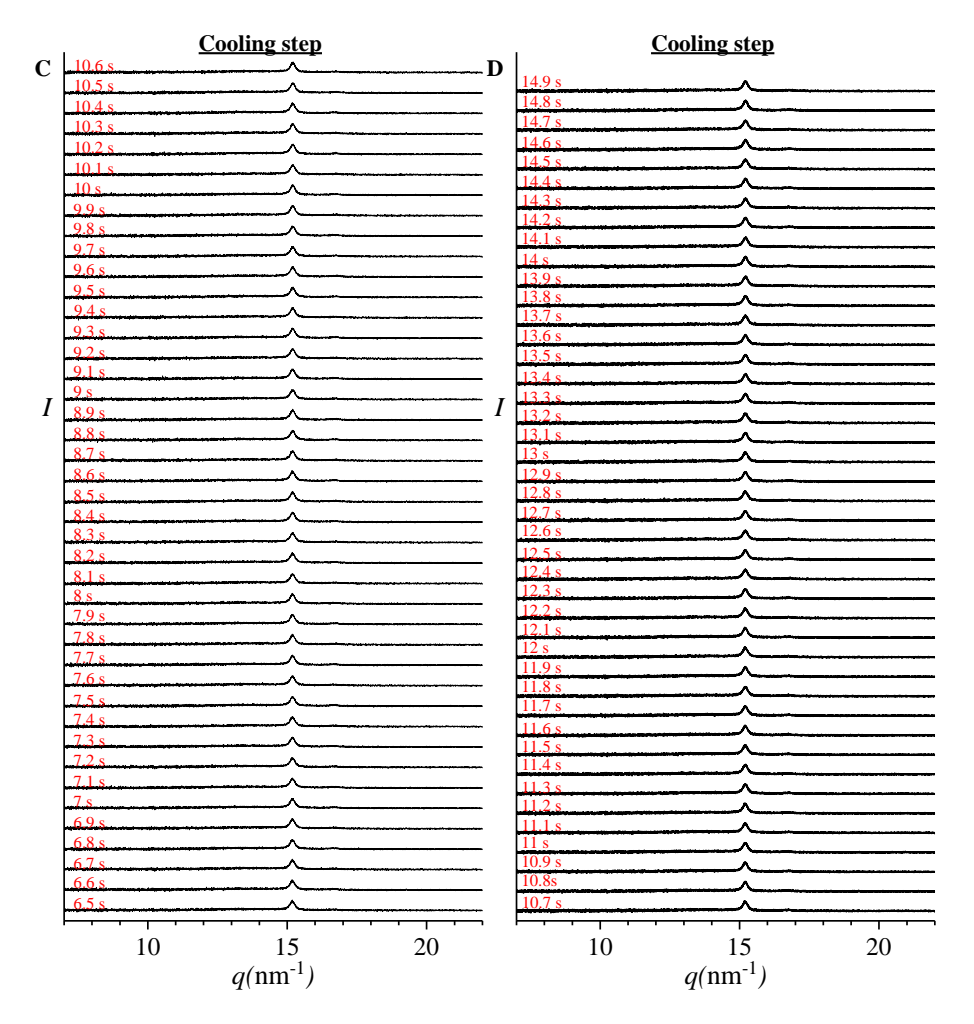


Figure A5 WAXS profiles of the sample L-C8 obtained by radial integration of 2D-WAXS patterns collected during biaxial stretching until reaching a draw ratio of 6x6 at $T_{tentering}$ =118°C (lapsed time 2 s) (A) and during successive cooling from $T_{tentering}$ (B,C,D). Data are collect every 0.1 s.